About the Cover

Nathan Renfro's article in this issue describes how exposing blue zircon to long-wave UV radiation causes them to turn brown, and how this color modification can be reversed. The 7.95 ct blue zircon ring on the cover is set in 18K white gold and surrounded by 2.43 carats of rubies. It is shown alongside a similar ring with a 5.46 ct tanzanite center stone. Both were designed by Loretta Castoro of Los Angeles for her KissMe collection. Photo by Kevin Schumacher, courtesy of Loretta Castoro.

FSC® www.fsc.org
MIX
Paper from responsible sources
FSC® C006300

pg. 223

pg. 248

pg. 253

pg. 280

Charting the Increasing Availability
and Quality of CVD Synthetic Diamonds

Welcome to the Fall 2016 *Gems & Gemology*! This issue brings together synthetic diamonds grown by the chemical vapor deposition (CVD) process, a reversible color modification of zircon, and a rich vein of locality articles including sapphires from Russia, a new Madagascar deposit of the rare gem grandidierite, Vietnamese peridot, and Indonesian cultured pearls.

Our lead article, by Drs. Sally Eaton-Magaña and James Shigley, reviews the characteristics and key identifying features of CVD synthetic diamonds based on the study of several hundred faceted examples examined by GIA between 2003 and 2016. This comprehensive summary

"GIA researchers review several hundred CVD synthetics produced between 2003 and 2016."

shows how the volume and quality of CVD diamonds changed from what the authors term the "pre-commercial" phase prior to 2008, to the range and color of material available in today's jewelry marketplace.

Our second paper, by Nathan Renfro, might be of great use to jewelers wishing to restore blue zircons that clients have inadvertently altered to unattractive brown. This "ugly duckling" transformation results from accidental exposure to long-wave ultraviolet radiation from tanning beds or other UV lights. The author explores the nature of this change using spectroscopy to confirm whether exposure to visible light might restore the zircons' blue color.

Next, a team of Russian researchers headed by Svetlana Yuryevna Buravleva describes a new deposit of translucent to semitransparent, blue to pinkish blue sapphire crystals and corundum-bearing rocks at Sutara, in the Jewish Autonomous Region of the Russian Far East. The authors postulate that this deposit formed by metasomatism of the contact zone between carbonate rocks and pegmatite veins.

In our fourth article, lead author Dr. Delphine Bruyère reports on a new occurrence of the rare gem grandidierite in southern Madagascar and provides a gemological characterization of the material, which occurs as bluish green to greenish blue crystals measuring up to 15 centimeters in length. Their analysis confirms that this new locality provides some of the purest grandidierite yet found and will likely be of great interest to museums and collectors.

In our penultimate paper, Dr. Nguyen Thi Minh Thuyet and colleagues review the gemological and geochemical characteristics of peridot from Vietnam's Central Highlands, noting similarities with material that originates from xenoliths in alkaline basalts from other localities.

In our final article, visit a pearl farm in the pristine waters off the Indonesian island of Lombok, where a team of researchers and industry professionals led by GIA's Nicholas Sturman capture the recovery of bead-cultured and non-bead-cultured pearls from gold-lipped oysters.

As always, our Lab Notes, Micro-World and Gem News International entries are filled with the latest updates from around the world.

You can also meet the editors and take advantage of special offers on subscriptions and back issues at the *G&G* booth in the publicly accessible Galleria section (middle floor) of the Tucson Convention Center during the AGTA show, January 31–February 5, 2017. We would be delighted to see you.

We hope you enjoy our Fall issue!

Duncan Pay | Editor-in-Chief | dpay@gia.edu

OBSERVATIONS ON CVD-GROWN SYNTHETIC DIAMONDS: A REVIEW

Sally Eaton-Magaña and James E. Shigley

This article presents statistical data and distinctive features from several hundred faceted CVD-grown synthetic diamonds examined by GIA researchers from 2003 through June 2016. This study, the first comprehensive summary published on such a large number of gem-quality CVD synthetics, describes the reliable means of identifying them, with a focus on material currently marketed for jewelry use. Most CVD synthetic diamonds analyzed by GIA have been in the near-colorless or pink color ranges, with clarity grades comparable to those of their natural counterparts. Faceted CVD samples are generally 2 ct or less, though the sizes are increasing. They can be identified by their distinctive fluorescence pattern using the DiamondView imaging instrument, and by the detection of the silicon-vacancy defect using photoluminescence (PL) spectroscopy. Some visual gemological characteristics provide indicators, but not definitive proof, of CVD origin.

Synthetic diamonds grown by the high-pressure, high-temperature (HPHT) process have been commercially available since the early 1990s. Perhaps several thousand faceted HPHT synthetics have been examined to date by gemological researchers; these specimens have been the subject of widespread coverage in *Gems & Gemology* and other trade publications. But gem-quality diamonds grown by chemical vapor deposition (CVD), which produces tabular crystals that are colorless or evenly colored, are of more recent manufacture. For these products, the range of observations and number of samples examined are more limited. While CVD growth technology has progressed significantly in recent years, with improvements in crystal size and quality, the use of these synthetics in the jewelry trade is still limited. The CVD material examined by GIA has generally contained minor amounts of microscopic inclusions. Therefore, the gemological identification of this material relies on the observation of weak, low-order, banded anomalous birefringence (i.e., "strain patterns"); ultraviolet fluorescence reactions with atypical colors, as seen with DiamondView imaging; and spectral features recorded mainly using

photoluminescence (PL) spectroscopy. *G&G* has published a number of articles on the detection of CVD synthetic diamonds over the past decade.

This article presents statistical information and distinctive identification features based on a review of data from all the faceted CVD synthetic diamonds examined so far by GIA. Because no summary has been published on such a large number of CVD samples, we describe the most diagnostic means of identification, with an emphasis on the material currently being sold for jewelry use. We analyzed data gathered by GIA staff, principally at the New York and Carlsbad laboratories, on all CVD synthetic diamonds examined from 2003 through June 2016; additionally, we cite one CVD synthetic submitted after that date—a 5.19 ct "near-colorless" sample. Of this sample set, 60% were in the colorless to near-colorless to very light brown range (D–N) and 24% were in the "pink" color range (figure 1). The remaining 16% showed other colors, including gray, yellow, and brown. The samples were purchased by GIA on the market or from manufacturers, loaned or donated by manufacturers, or submitted to GIA for identification or grading reports. To the best of our knowledge, this data set of several hundred samples is representative of the gem-quality CVD material available in the trade.

Many of these samples have been described in detail in previous articles (Wang et al., 2003, 2007, 2010, 2012) and in *G&G*'s Lab Notes section (e.g.,

---

Figure 1. These near-colorless and Fancy Vivid purplish pink samples are representative of most CVD synthetic diamonds examined by GIA. The pink round brilliant weighs 0.48 ct. Photo by Robert Weldon/GIA.

Wang and Moses, 2008; Wang and Moe, 2010; Ardon et al., 2013; Wang et al., 2013; Ardon and Wang, 2014; Moe et al., 2014). Whereas earlier studies examined small batches of CVD synthetic diamonds from specific manufacturers, which were likely to have been grown using a similar recipe, the goal of the present study is to investigate trends in the distinctive features seen among CVD synthetic diamonds from multiple sources over the past 13 years.

This article traces the evolution of gem-quality CVD technology from what we term the "pre-commercial" phase of 2003–2008. During this period, many advances occurred but the products were very much in the development stage in terms of crystal size and quality and were not widely available to the public. Since 2008, CVD synthetic diamonds of improved color and quality have gone into limited commercial production, though GIA's laboratory still receives only a small quantity—both disclosed and undisclosed—from the trade. Of the CVD samples surveyed, 75% date from 2013 or later.

While the past decade has also seen advances in CVD technology aimed toward non-gemological applications such as quantum computing (Twitchen et al., 2016), we limit our observations to gem-quality CVD synthetics and the data set of material examined by GIA. Angus (2014) provides an excellent retrospective of the evolution of CVD growth prior to the "gem-quality" era covered here.

The synthetic diamonds discussed in this article are from only a few known manufacturers. In the past, GIA solicited samples from Apollo Diamond Inc. (which sold its technology to Scio Diamond Technology of Greenville, South Carolina, in 2011) and from the Gemesis Corporation of Bradenton, Florida (Wang et al., 2003, 2007, 2010, 2012). Some of the samples submitted to GIA's laboratory are from other manufacturers, such as Washington Diamond or the Diamond Foundry, but not all the makers of our study samples are known, as many specimens submitted for grading reports came from third-party clients.
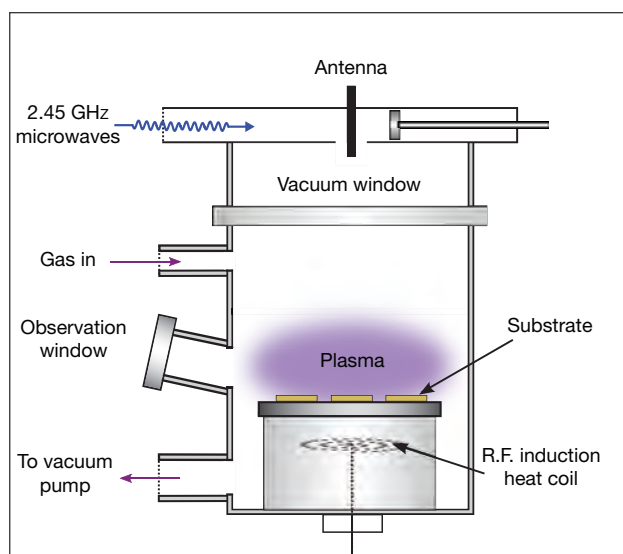
Figure 2. This diagram shows some of the key components of a microwave-plasma CVD reactor. Depending on the reactor size, growth parameters, and desired crystal quality, the growth area beneath the plasma can range from 2 to 20 cm in diameter. This large growth area means that several CVD crystals can be produced during a single run.

CVD SYNTHETIC DIAMOND GROWTH

The CVD process involves diamond growth at moderate temperatures (700–1300°C) but very low pressures of less than 1 atmosphere in a vacuum

Figure 3. An as-grown 4.52 ct CVD-grown crystal with a graphitized outer edge and a brownish color (left), a CVD synthetic diamond crystal laser-cut to a 1.91 ct cylinder (center), and a 0.40 ct near-colorless, heat-treated CVD round brilliant (right). Note these are three separate samples at different post-growth stages and should not be interpreted as a progression of the same sample. Photo by C.D. Mengason.

chamber (Angus and Hayman, 1988; Butler et al., 2009; Nad et al., 2015). In 1952, William G. Eversole at Union Carbide created tiny synthetic diamonds using the low-pressure, comparatively low-temperature method of CVD growth. Many of the early research efforts focused on (1) the "thermodynamic paradox" of growing diamond outside its stability zone and (2) exploring the chemical composition to suppress the simultaneous growth of graphite and the associated necessity of atomic hydrogen (Angus and Hayman, 1988; Angus, 2014). Single-crystal, gem-quality CVD synthetic diamond was once considered a "holy grail" within the research community. A half-century of investigation between CVD's early beginnings in 1952 until it advanced sufficiently that it became a research focus at GIA in 2003 (Wang et al., 2003) made that once-ambitious goal a reality.

Square-shaped tabular single crystals up to approximately 13.5 ct can now be grown several at a time (Meng et al., 2012), at relatively fast growth rates up to 0.2 mm/hr (figure 2). Because growth occurs in a heated mixture of a hydrocarbon gas (such as methane, CH_4) and hydrogen, the major impurity found in the resulting diamond crystals is hydrogen unless some other type of atom (such as nitrogen or silicon) is intentionally or unintentionally introduced into the gas mixture (Othman et al., 2014; Prieske and Vollertsen, 2016). Within the vacuum chamber, activation of the gas by an energy source (typically a microwave plasma) breaks apart the gas molecules to release carbon atoms. These atoms are drawn down toward the cooler substrate (typically flat, square-shaped seed plates) that consists of natural or, more typically, synthetic diamond. CVD synthetic diamond crystals are cubic in shape because they are often grown on a (100)-oriented diamond substrate: A different orientation of the substrate would yield a different crystal form. These "as-grown" tablets typically undergo laser cutting to remove the outer edge of the crystal, followed by standard gem polishing techniques (figure 3). Single-crystal diamond growth progresses, layer by layer on top of the seed plate, to form the tabular crystal. A slower growth process generally results in colorless crystals of very high purity and low defect content; however, the growth chemistry of many mass-produced CVD synthetics is manipulated by adding nitrogen or oxygen to the gas mixture to improve crystal quality (Liang et al., 2009), or they are treated at HPHT conditions afterward to remove any brown coloration. The tabular crystal shape generally limits the faceting styles used to manufacture gem-

TABLE 1. Timeline of gem-quality CVD synthetics.

Year	Representative sample	Colors	Clarity	Weight (ct)	Distinguishing features	Reference
2003		Mostly light brown, some yellow, dark brown, pinkish brown	VS_1–SI_2	0.14–1.11	Black inclusions or pinpoints, orangy red DiamondView, 596/597 nm doublet and SiV in PL, 3123 cm^{-1} in IR. No post-growth treatment.	Wang et al., 2003
2007		Near-colorless: E–M "Pink": brown-pink, brownish orange pink	VVS_1–I_1	0.14–1.20[a]	Black inclusions or pinpoints, pink/purple DiamondView; pink color from undetermined absorption band at ~520 nm; 3123 cm^{-1} peak is absent or weak; 596/597 nm doublet absent, SiV not always present in pink CVD samples.	Wang et al., 2007
2010		Pink to purplish pink	VVS_2–SI_2	0.27–0.72	Black inclusions or pinpoints, orange fluorescence in LW and SWUV; IR spectroscopic features at 3123, 1502, 1450, and 1344 cm^{-1}, and SiV at 737 nm in PL.	Wang et al., 2010
2012		F–L	IF–VS_2	0.24–0.90	Majority were HPHT-treated after growth, and IR spectra resembled HPHT-treated material. None had 3123 cm^{-1} center in IR. Presence of SiV center at 737 nm in PL and DiamondView features.	Wang et al., 2012
2016 (YTD; current client-submitted CVD samples)		D–J; orangy pink to purplish pink	VVS_1–VS_2	0.03–5.19	Presence of SiV center in PL. In the DiamondView, samples show increased evidence of multiple growth events, in which manufacturer grows a CVD layer, stops the growth process, presumably polishes away polycrystalline growth, and restarts growth process.	

[a] Tabular crystal

quality material. With the table facet of the cut stone as the upper surface of the crystal, the manufacturer has a small table-to-culet distance that may limit the choice of faceted shape.

CVD synthetic diamonds have important non-jewelry uses in laser and electronic components, in optical windows, and as blades in cutting tools. These and other high-tech applications are the major driving force behind efforts to improve the growth process (Butler et al., 2009).

ANALYSIS OF EXISTING DATA

This study focuses on data obtained previously from two important categories of material, which appear to involve different post-growth color treatments. The first are the colorless to near-colorless to very light brown samples whose color grades fall within the D–N range of the GIA color scale; for brevity, these will be collectively referred to as "near-color-less." Wang et al. (2012) concluded that these specimens were typically low-nitrogen type IIa synthetic diamonds and commonly subjected to HPHT anneal-ing to remove a brownish color component (figure 1).

The second group are type IIa "pink" samples (including brownish pink, pink, orangy pink, purplish pink, and a few red to pinkish orange); according to Wang et al. (2010), their colors are predominantly the result of post-growth annealing and irradiation of light brown starting material (again, see figure 1).

For these two groups, we will summarize quality factors, basic gemological properties, ultraviolet fluo-rescence reactions, and key spectral features based on information gathered when the samples were examined. In some instances, not all data types were collected on a particular CVD sample for various reasons: time constraints, the lack of certain instrument capabilities at the time, or the need to limit data collection to the client-requested grading service requirements. In the following discussion, therefore, the percentage of samples for which that data was collected will be clearly indicated. Nonetheless, the information from GIA's internal records reported here represents the most substantial set of observations published to date on gem-quality CVD synthetic diamonds. Table 1 presents a brief timeline and summary of CVD syn-thetics examined by GIA.

Weight Distribution of CVD Synthetics, 2003–2016

Legend:
- > 2.00 ct
- 1.01–2.00 ct
- 0.76–1.00 ct
- 0.51–0.75 ct
- 0.26–0.50 ct
- < 0.25 ct

Y-axis: PERCENTAGE OF CVD SAMPLES EXAMINED (0%–100%)

X-axis categories: 2003–2008, 2009, 2010–2011, 2012, 2013, 2014, 2015, 2016 (Jan.-June)
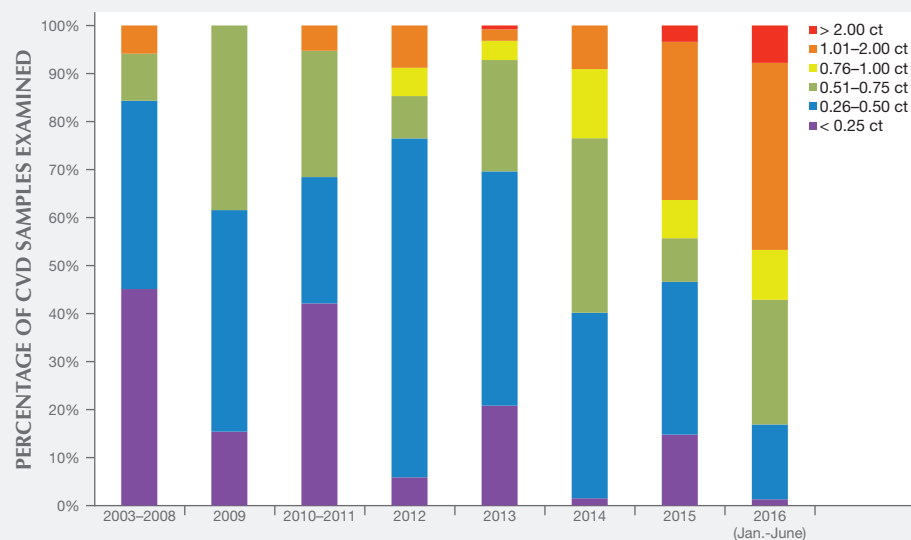
Figure 4. The carat weight distribution of CVD synthetic diamonds analyzed by GIA from 2003 through September 2016. In the "pre-commercial" era (2003–2008), the samples were donated or loaned to GIA by manufacturers. In later years, the samples were a mixture of donated samples and those submitted by clients. The years 2010 and 2011 are combined because of the decrease in production that resulted when a major manufacturer, Apollo, was acquired by Scio. This chart clearly illustrates the increasing size of CVD synthetic diamonds in the marketplace.

Other observations, such as short-wave fluorescence, strain pattern between crossed polarizers, and near-infrared absorption spectroscopy, have not been routinely collected or reported (for exceptions, see Wang et al., 2003, 2007, 2010, 2012), and they are not discussed in detail here. Also, it should be noted that during the "commercial" period beginning in 2009, the instrumentation and data collection conditions used were consistent both over time and between GIA's different laboratory locations.

We noted no significant differences in characteristics between the CVD samples sourced directly from the manufacturers and those submitted by GIA laboratory clients. The information presented here is strictly limited to material examined at GIA, which might not represent all of the goods available within the gem trade.

ANALYSIS OF QUALITY GRADING FACTORS

Carat Weight. Most of the faceted CVD synthetics examined by GIA fell in the 0.25–0.50 ct range (38%), with some larger than 1 ct (15%). In the pre-commercial era, samples below 0.25 ct were the most frequently examined. Between 2009 and 2013, the majority were in the 0.25–0.50 ct range. Since 2014, most have been larger than 0.50 ct (figure 4). This weight restriction is principally due to the tabular shape and the size of the as-grown crystals, which have influenced the choice of faceting styles and, in early material, the cut stone proportions.

A few *G&G* Lab Notes have chronicled the increasing carat size of CVD material. Wang and Moe (2010) revealed the first client-submitted sample larger than 1 carat (1.05 ct, with G color and I_1 clarity). Wang et al. (2013) reported on a 2.16 ct CVD synthetic (J/K color, SI_2 clarity). In June 2015, the Carlsbad laboratory graded a 2.51 ct sample (H color, I_2 clarity). In October 2015, the New York laboratory graded a 3.23 ct round brilliant (I color, VS_2) clarity. In September 2016, GIA identified the largest CVD synthetic it has examined to date, a 5.19 ct cushion modified brilliant cut (J color, VS_2 clarity; Law, 2016). Figure 5 shows some milestones in carat weight of CVD synthetics examined by GIA through the years.

Cut. The overwhelming majority of the faceted CVD synthetics were round brilliants (83%). Other styles included rectangle (3%), cut-cornered rectangle (3%), and emerald cut (4%). Many manufacturers seem to have chosen to facet the material as round brilliants because of the popularity of this style, even though "fancy" shapes would have retained slightly more weight from the original crystal.

The cut grades for the CVD round brilliants were comparable with their natural counterparts, with 85% judged as having an Excellent cut. The cut grade parameter of most interest was the depth percentage (the ratio of depth to average diameter); a low value would indicate the CVD synthetics were cut with lower than optimal pavilion or crown angles. As CVD synthetics are grown layer by layer, a shallow cut was once con-

CVD SYNTHETIC DIAMOND SIZE MILESTONES*
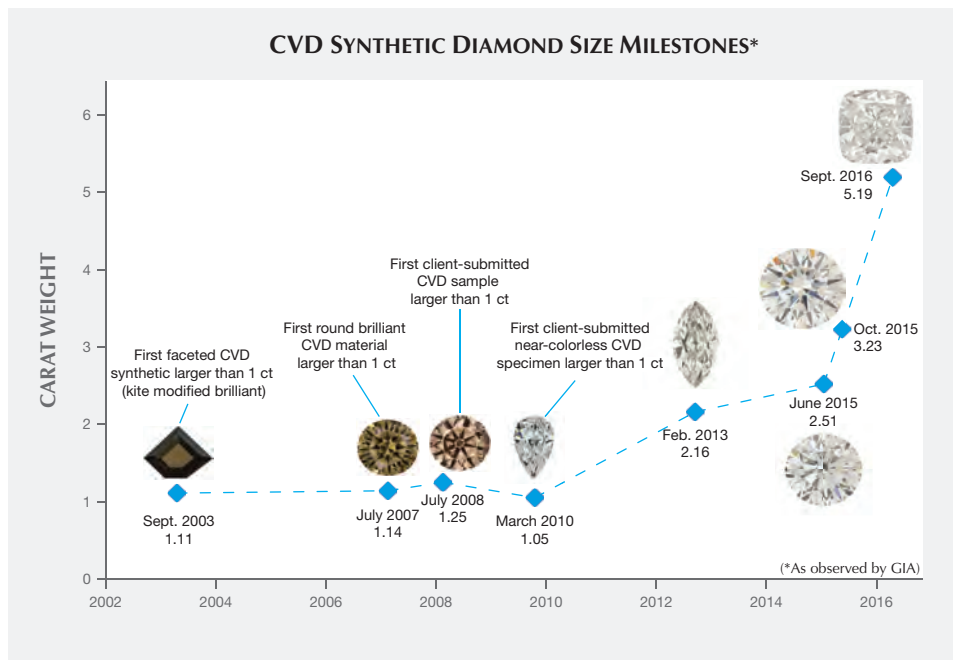
Figure 5. There have been several size milestones since GIA began examining CVD synthetics. The first CVD sample greater than 1 carat was reported in September 2003; a 5.19 ct near-colorless round brilliant, examined in September 2016, is the largest graded by GIA to date (Wang et al., 2003; Wang and Moses, 2008; Wang and Moe, 2010; Wang et al., 2013; Dieck et al., 2015; Law, 2016).

sidered a possible indicator of CVD material (Wang et al., 2003). However, no discernible trend of this kind has been detected since 2007. Over these years, the CVD samples have demonstrated a consistent range of depth percentage, with the vast majority judged as Excellent for this parameter. Among those that fell outside of the Excellent range, most had higher depth

percentages—an indicator that they were being cut with thicker girdles or larger crown or pavilion angles.

Color. Over the years, most CVD synthetics have been within the "near-colorless" category (figure 6): 67% in the G–J range, 21% in the D–F range, 10% in the K–N range, and only 1% in the split-grade range

DISTRIBUTION OF MAJOR COLORS OF CVD SYNTHETICS, 2003–2016
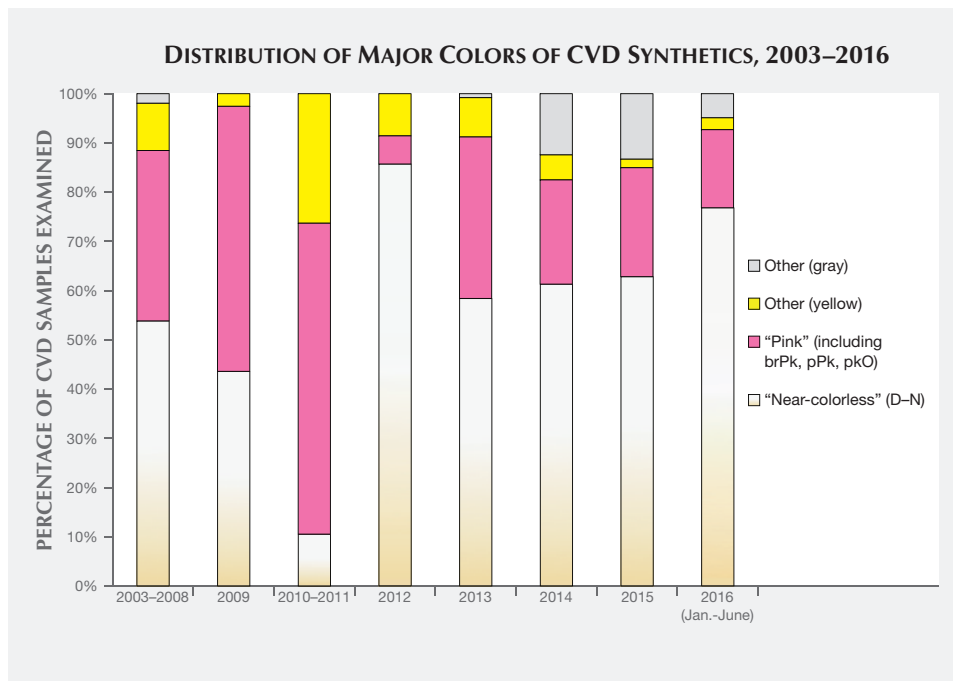
Figure 6. The color distribution of CVD synthetic diamonds analyzed by GIA by year. The samples were grouped in the "near-colorless" range (D–N) and in the "pink" range (which included brownish pink, purplish pink, and pinkish orange). Among the few remaining samples, the majority had a yellow or gray color. As in figure 4, the years 2003–2008 and 2010–2011 are combined.

While CVD-grown diamond samples in colors other than pink have been examined by GIA over the years (figure A-1), these have not been submitted in significant quantities, and the individual colors do not appear to be commercially important.

Fancy-color brown CVD samples (some with orange or yellow modifiers) have been submitted by clients or manufacturers, particularly between 2003 and 2008. The brown color is attributed to non-diamond carbon inclusions and/or internal extended defects such as dislocations rather than the plastic deformation that causes brown coloration in natural diamonds (Wang et al., 2003).

Fancy-color yellow CVD samples (some with brown or orange modifiers) have been graded as well. The yellow color is ascribed to accidental or deliberate incorporation of nitrogen (e.g., Moe et al., 2014). These diamonds have nitrogen concentrations up to 12.5 ppm (e.g., figure A-1B and Ardon et al., 2013).

GIA has graded a few blue CVD synthetics in which the color is derived from irradiation (Ardon and Wang, 2014). In irradiated CVD-grown diamonds, as with irradiated natural diamonds, a strong GR1 absorption is created. This absorption has a sharp line at 741.2 nm and related absorption in the visible region; the latter imparts a green to blue color.

An interesting CVD creation is a pink-to-blue color change caused by massive quantities of intentional silicon doping (D'Haenens-Johansson et al., 2015). This is several orders of magnitude greater than the doping typically observed in CVD-grown diamonds and creates very strong SiV absorption. These heavily silicon-doped samples exhibit a color change from a stable light pink to an unstable blue. The pink-to-blue color change is caused by a charge-transfer effect between SiV^- and SiV^0 (D'Haenens-Johansson et al., 2015). The blue is created by strong absorption of the SiV^0 center. This center exhibits a sharp absorption line at 946 nm within the NIR, together with absorption, which extends into the visible region and becomes less intense at shorter wavelengths. This color origin is similar to the cause of blue color in type IIb diamond in which the boron-related absorption starting in the IR shows decreasing intensity from the red end of the visible spectrum to the blue, causing the blue color. Pink is the stable color, and this is the color provided on the grading report.

More gray-colored samples have been submitted in recent years. Several of these had a depth of color that was nominally within the K–N range of the D-to-Z scale, but these received a fancy color grade since the dominant color was gray and not yellow or brown. It is likely that the manufacturer intended these to be near-colorless, falling on the D-to-Z scale.

The identification criteria for these colored CVD samples are similar to those for the near-colorless and pink material: a combination of spectroscopic and gemological evidence such as the presence of silicon and the growth features observed with the DiamondView.

Besides color, the other quality factors of carat weight, shape, and clarity are consistent with those previously described for the "near-colorless" and "pink" CVD synthetics.

Figure A-1. CVD samples have occasionally been submitted in colors besides pink. A: 0.46 ct Fancy Dark orangy brown, as-grown (Wang et al., 2007). B: 0.27 ct Fancy Deep brownish greenish yellow, colored by 12 ppm of type Ib nitrogen. C: 0.43 ct Fancy Deep greenish blue, irradiated (Ardon and Wang, 2014). D: 0.31 ct Very Light gray, treated. Photos by Jian Xin (Jae) Liao.
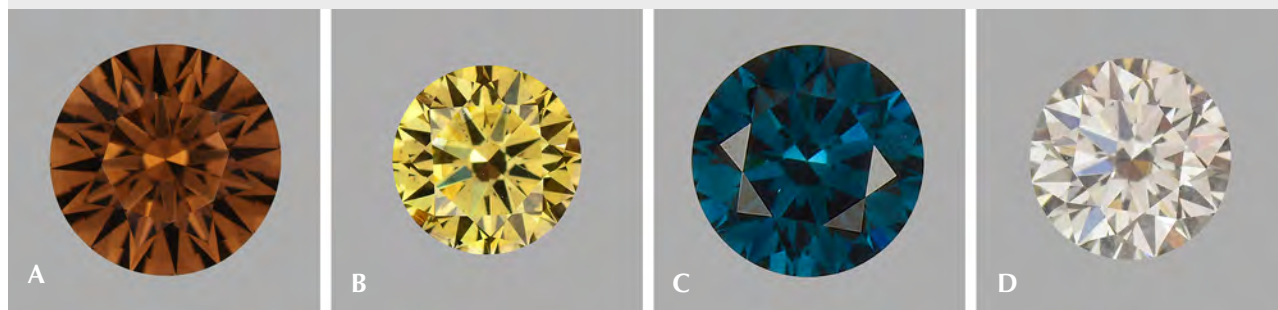
(O to Z on the D-to-Z scale). These percentages have not shifted dramatically over time.

Wang et al. (2012) concluded that Gemesis products in the "near-colorless" range had been HPHT-treated after growth. Based on spectroscopic analysis, the conclusion applies to most CVD synthetics in this color range, regardless of manufacturer. The lower color grades on the D-to-Z scale are caused by either a
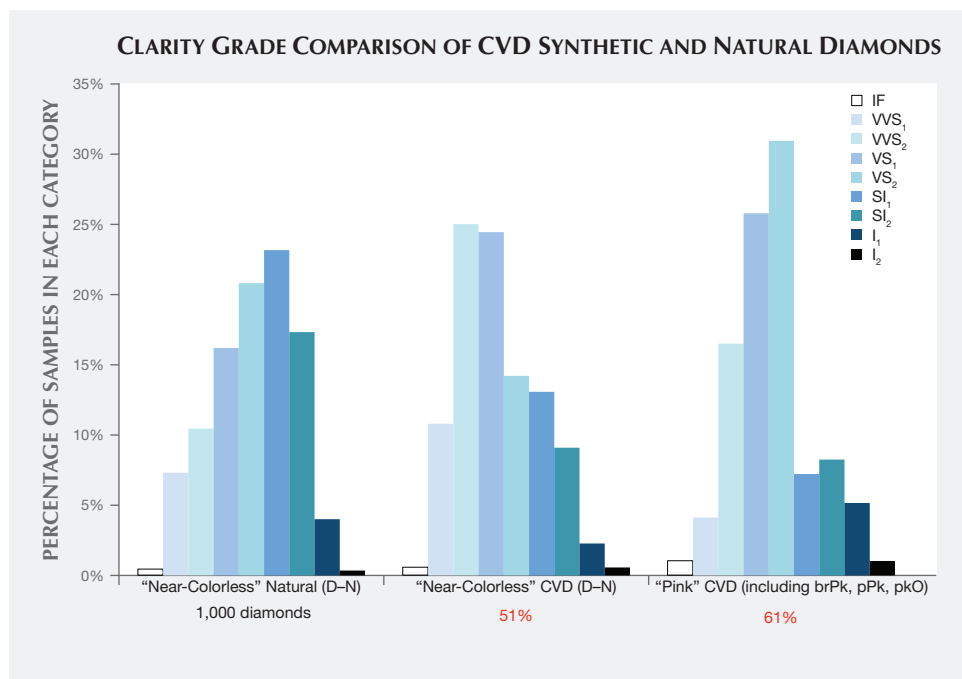
Figure 7. The clarity grade distribution for "near-colorless" (D–N) natural diamonds along with CVD samples in the "near-colorless" and "pink" ranges. The natural diamonds are within a similar weight range and were chosen randomly from the GIA database and their distribution was plotted (left graph), with a plurality receiving SI_1 grades. A plurality of the near-colorless CVD synthetics had VVS_2 clarity grades, while a plurality of the pinks were VS_2. The percentages shown in red represent the portion of samples with data available for that color range.

yellow color from type Ib (i.e., single substitutional) nitrogen-related optical defects or a brown appearance due to extended defects (such as vacancy-related com-

In Brief

- Since 2003, CVD synthetic gem diamonds observed by GIA have increased significantly in size and quantity. Most of the samples submitted are still near-colorless or have pink hues.

- Although CVD synthetics have evolved rapidly in the last decade, they are reliably identified within gemological laboratories based on distinct spectroscopic features and growth characteristics.

- Near-colorless CVD synthetic melee have been examined by GIA, a trend that is likely to continue. Many gemological laboratories (including GIA) now offer melee sorting services to detect both CVD and HPHT synthetic diamonds and treated diamonds.

plexes). The post-growth treatment is presumably used to remove a brown or yellow color component so the material can obtain a better color grade.

The vast majority of the fancy-color CVD synthetic diamonds are within the pink range. Their hues include a variety of color descriptions such as pinkish brown, brownish pink, pink, purplish pink, and orangy pink, with one specimen described as red. Among the "pink" CVD synthetics, most fell in the

pink (28%) to orangy pink (17%) to purplish pink (27%) range; these colors are due to multiple post-growth treatments, including HPHT annealing, irradiation, and low-temperature annealing (Wang et al., 2010). Except for a few samples (discussed in Wang et al., 2007; D'Haenens-Johansson et al., 2015), the "pink" color of the remaining CVD samples is attributed to nitrogen-vacancy (NV) centers (e.g., Wang et al., 2010). The colors are very similar to those of treated natural diamonds, treated HPHT synthetic diamonds, and rare type IIa Golconda-type untreated natural diamonds (table 2).

During the pre-commercial years and again more recently, GIA has graded CVD samples in other colors such as yellow and gray, and less frequently fancy brown and blue. These colors, which do not appear to be commercially important at present, are discussed briefly in box A.

Clarity. The CVD samples span nearly the entire clarity scale, but most received grades in the VVS_2/VS_1 range. The clarity characteristics and grades for 1,000 randomly selected natural D–N diamonds submitted for grading reports were surveyed for comparison (figure 7). The median clarity of the CVD samples was slightly higher than for natural diamonds: VVS_2/VS_1 for "near-colorless" CVD, VS_1/VS_2 for "pink" CVD, and VS_2/SI_1 for near-colorless natural diamonds. This trend is not surprising, since the very controlled growth environment and growth chemistry of the

TABLE 2. Characteristics of natural, treated, HPHT synthetic, and CVD synthetic pink diamonds.

Sample	Type IIa natural diamonds (i.e., rare Golconda pinks; compiled from unpublished data)[a]	Treated natural diamond (Wang et al., 2005)	Treated HPHT synthetics (Shigley et al., 2004)	Pre-commercial CVD synthetics (Wang et al., 2007)	Treated CVD synthetics (Wang et al., 2010)
Center responsible for pink color	NV centers	NV centers	NV centers	~520 nm band	NV centers
Reported treatment	Not applicable	HPHT annealing, irradiation, LPLT annealing	Irradiation, LPLT annealing	Not reported	HPHT annealing, irradiation
Color	Pale color, occasionally higher saturation	Strongly saturated purple-red to orangy red	Moderately to intensely saturated pink with orange, brown, or purple components	Moderately saturated pink with brown or orange components	Strongly saturated pink, sometimes with purplish component
Clarity	Not reported	Not reported	I–VVS (mostly I and VS)	SI–VVS	VS–VVS
Clarity characteristics	Consistent with natural diamonds	Color zoning, graphitized natural inclusions	Color zoning, metallic inclusions	Pinpoints, clouds	Pinpoints and small black inclusions with irregular shapes
Fluorescence reaction: Long-wave UV	Weak to very strong orange, sometimes yellow or blue	Combinations of yellow, green, and orange, sometimes blue	Moderate to strong orange or orangy red	Weak to moderate orange to orangy yellow	Moderate to strong orange
Fluorescence reaction: Short-wave UV	Weak to very strong orange, sometimes yellow or blue	Moderate to strong orange and yellow	Weak to strong orange	Very weak to weak orange to orangy yellow	Moderate to strong orange
Phosphorescence	None	None	Weak orange of short duration in 16%	None	None
DiamondView imaging	Orange to red	Orange-red fluorescence with complex growth patterns	Orange luminescence, synthetic growth sectors observed[c]	Strong reddish orange fluorescence, some showed banded structure	Strong orange or orangy red fluorescence, with a banded structure
Observation between crossed polarizers	Tatami strain, typically with low-order interference colors	Weak to moderately intense strain in banded patterns with low-order interference colors	Weak strain patterns	Irregular patterns with high-order interference colors	Low to very high-order interference colors; sometimes tatami
Diamond type	Type IIa	Type IaAB (typically A>B)	Nominally type IIa, low Ib component	Nominally type IIa, low Ib component	Nominally type IIa, low Ib component
Mid-IR spectra[b]	Only 1332 cm^{-1} peak	Strong 1450 (H1a), ~1360 (platelets), weak 1344 cm^{-1}	Low 1344 cm^{-1}	Strong 3123, weak 1344 cm^{-1}	Weak peaks at 3123, 3107,1450 (H1a), 1405, 1344 cm^{-1}; bands at ~1130, 1295 cm^{-1}
Near-IR spectra[b]	Not reported	Peaks at 10140 (H2), 6170, 5165 (H1c), and 4935 cm^{-1} (H1b)	Not reported	Strong peaks at 7804, 7353, and 6425 cm^{-1}	Peaks at 6902 and 5892 cm^{-1}
UV-Vis absorption[b]	NV centers, sometimes ~270 nm band, H3, GR1	Strong N3, H3, and NV centers; weak ND1, GR1, and peak at 594 nm (i.e., 595 nm center)	Strong NV centers, also 595 nm and GR1	Broad absorption band centered at ~270 and ~520 nm; weak 637 peak	Strong NV peaks; GR1, 737 nm doublet, 595 nm, and ND1 peaks
PL spectra[b]	H3, NV centers, GR1	Strong H3, NV centers; also H4, 588 and 594 nm, and GR1	Strong NV centers, also 693 nm band due to nickel	Strong H3, NV centers, 737 doublet, numerous weak peaks from 847 to 956 nm using 830 nm laser excitation	Weak N3, strong NV centers, most show 737 nm doublet; also peaks at 796.9, 806.4, 949.5 nm
Other		"Green transmitter" to visible light	Fe, Ni, Co (and possibly Cu) detected by EDXRF		

[a] Table does not include natural pink diamonds colored by 550 nm band.
[b] See text (or references) for more details regarding peak assignments; not all peaks mentioned in original references are repeated here.
[c] Image collected using cathodoluminescence; results are comparable to DiamondView imaging.

CVD process leads to fewer inclusions and other visible clarity characteristics. As GIA generally examines only the material that CVD manufacturers decide is worthy of cutting, samples submitted to GIA

GRADE-SETTING CLARITY CHARACTERISTICS IN CVD SYNTHETICS AND NATURALS

Legend:
- "Near–colorless" natural (D–N)
- "Near–colorless" CVD (D–N)
- "Pink" CVD (including brPk, pPk, R, pkO)
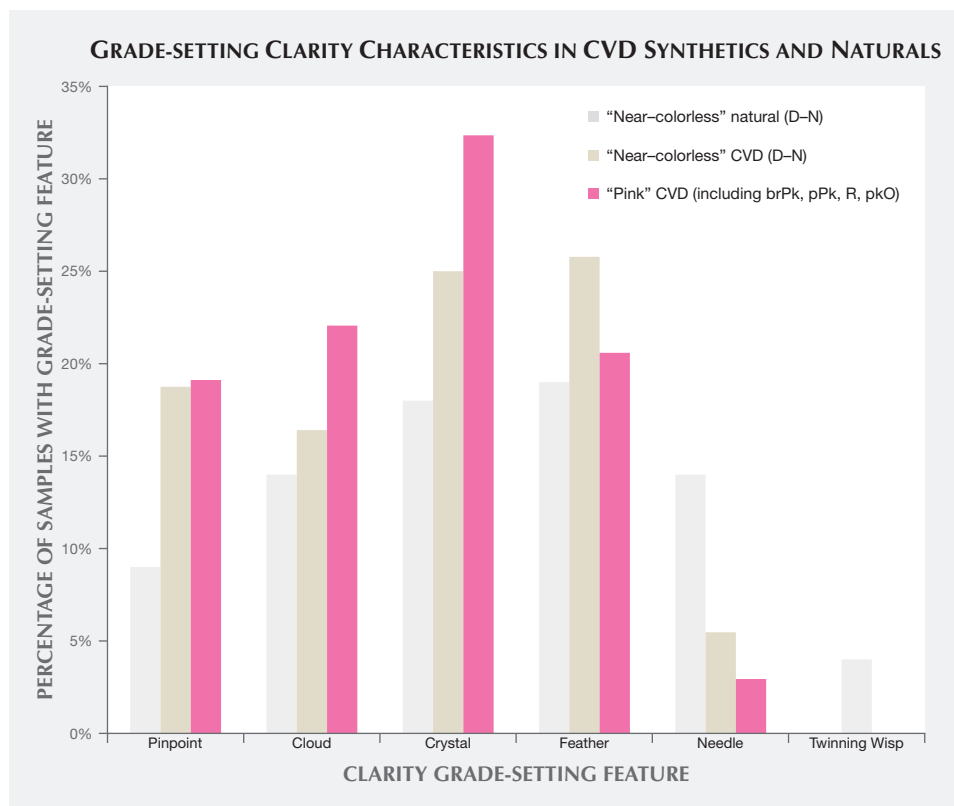
Figure 8. Distribution of the grade-setting clarity characteristic for 1,000 "near-colorless" (D–N) natural diamonds is shown with "near-colorless" and "pink" CVD samples. The natural diamonds (also shown in figure 7) are within a similar weight range. They were chosen at random from the GIA database and their distribution was plotted. Grade-setting characteristics with very low overall percentages within the data set (such as a knot or chip) were not included, so the total is slightly less than 100%.

are likely to reflect what is available within the trade but may not be representative of the manufacturing output.

Clarity grading of diamonds often involves the determination of the "grade-setting" clarity feature. This is the characteristic that determines the clarity grade. For example, a diamond might have a large feather and a few sparse pinpoints; while both would be listed as inclusions, the feather would be considered the "grade setter." A number of different grade-setting clarity characteristics were found in these CVD samples, as shown in figure 8. None of these characteristics would be diagnostic of this material for identification purposes, however. Certain manufacturers laser-inscribe a distinctive name or number on the girdle of their faceted goods as a recognition aid (figure 9).

The most common grade-setting inclusions for CVD synthetic diamonds were identified by GIA diamond graders as clouds, pinpoints, crystals, and needles; these inclusions were often mentioned in previous articles (Wang et al., 2003, 2007, 2010, and 2012). In most cases, these characteristics were black graphitic inclusions of various sizes (e.g., figure 10) or tiny pinpoints of non-diamond carbon that clustered together to form clouds. Wang et al. (2007, 2012) mentioned radial fractures surrounding larger inclusions;

graders reported these as feathers if they reached the surface.

Despite their very different growth environments and histories, natural and CVD synthetic diamonds have clarity characteristics that are roughly comparable, at least in terms of size, number, location, nature, and relief. Therefore, GIA graders can use the same clarity terms for either. For example, a colorless

Figure 9. Most CVD manufacturers inscribe their products as laboratory-grown on the girdle, as in this photo. Similarly, all samples identified as synthetic diamonds leave GIA with an identifying inscription of "Laboratory Grown." Photo by Sally Eaton-Magaña.

NATURAL	CVD SYNTHETIC
Pinpoint A	B
Cloud C	D
Crystal E	F
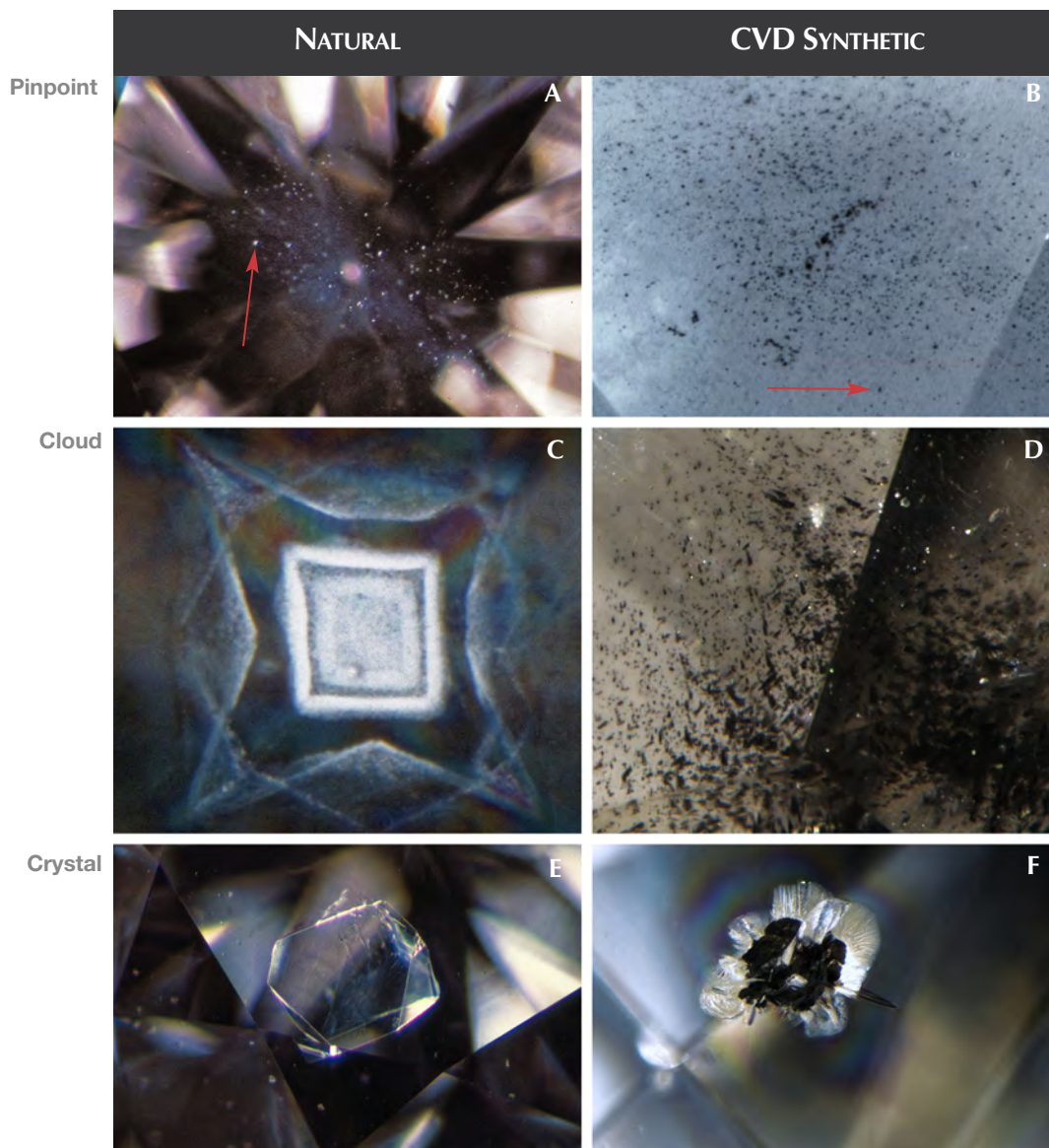
Figure 10. Non-diamond carbon inclusions are the most common type observed in CVD synthetics; here they are compared with carbon inclusions in natural material. While these inclusion images are representative of natural and CVD-grown material, natural diamonds can also show black inclusions that resemble the non-diamond carbon material observed in some CVD-grown diamonds. A and B show pinpoint inclusions (the red arrows indicate individual pinpoints), C and D show clouds, and E and F show crystals. Photomicrographs by John I. Koivula (A and E), Sally Eaton-Magaña (B and D), Nathan Renfro (C), and Jonathan Muyal (F).

foreign mineral in a natural diamond and a black inclusion of non-diamond carbon would both be described as a "crystal" by a grader (figure 10). A cloud is a cluster of pinpoints (tiny crystals that appear as specks at 10× magnification), while a crystal is solid mineral, larger than a pinpoint, contained within the diamond. A feather is an internal fracture visible at 10× magnification, and a needle is a thin crystal seen at 10× magnification. These clarity characteristics are annotated on internal GIA records as crystals, pinpoints, and clouds (among other designations) and are plotted accordingly for the client. On GIA synthetic diamond grading reports, they are not individually listed as crystals, clouds, or pinpoints, but collectively described under the umbrella term of

"growth remnant." Although similar terminology may be used, there are rare instances in which inclusions provide definitive evidence of diamond origin, such as metal platelets and garnet crystal inclusions.

It is interesting to note that twinning wisp inclusions, the grade-setting feature in 4% of the randomly selected natural diamonds, were not observed in any CVD synthetics. Twinning wisps are inclusions formed through an orientation change in the crystal structure during growth. Although twinning has been encountered in experimental CVD synthetics (Butler and Oleynik, 2008), such a change in the growth structure is unlikely to occur in current gem-quality CVD synthetics, as it would tend to lead to polycrystalline growth, something manufacturers wish to avoid.
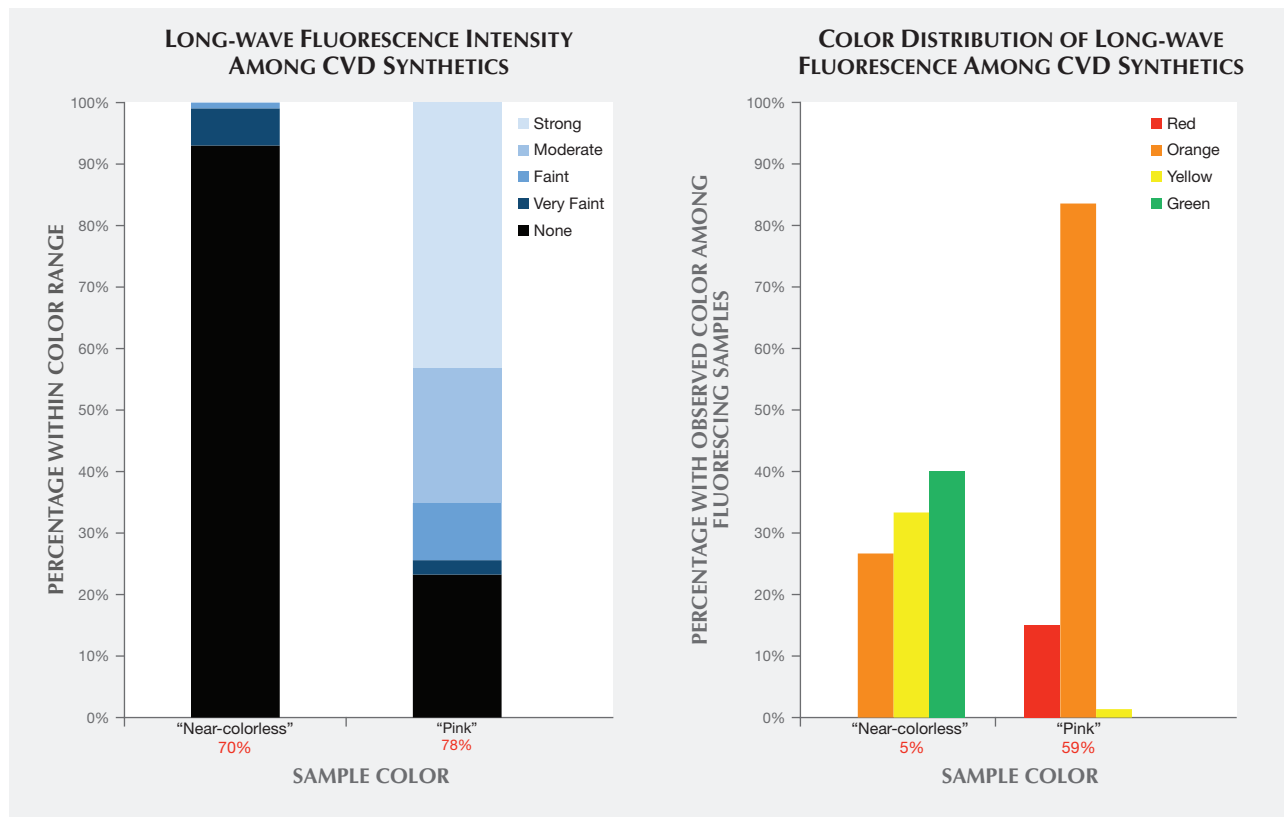
Figure 11. The "near-colorless" and "pink" CVD synthetics showed distinctly different reactions to long-wave fluorescence. Nearly all of the "near-colorless" samples showed no reaction, while most "pink" CVD synthetics showed moderate to strong long-wave fluorescence (orange or red) due to post-growth treatment that created NV defect centers. The percentages shown in red represent the portion of samples with data available for that color range.

ANALYSIS OF OTHER GEMOLOGICAL PROPERTIES

Long-Wave Fluorescence. The observation of ultraviolet fluorescence has been an important and practical means of distinguishing natural diamonds from HPHT-grown synthetics. The determination is based on differences in fluorescence colors, intensities, and patterns (and in some cases the occurrence of persistent phosphorescence among HPHT synthetics). UV fluorescence is also important for recognizing CVD-grown material.

The bar graphs in figure 11 illustrate the fluorescence reactions to long-wave ultraviolet radiation from a standard gemological UV lamp. Most of the "near-colorless" samples displayed no fluorescence intensity, while the "pink" samples tended to display stronger reactions. The distinguishing feature for both groups was the high incidence of orange and red fluorescence colors. Both of these colors, along with green, are extremely uncommon fluorescence reactions among natural, untreated diamonds.

Near-Colorless Material. All CVD samples submitted to GIA for synthetic diamond grading reports are measured for the intensity of their fluorescence reaction to a long-wave UV source using a proprietary device. Only 7% of the "near-colorless" CVD synthetics had measurable (faint to very faint) fluorescence; the remainder had "none." This is a far lower rate of fluorescent samples than observed among natural diamonds. Moses et al. (1997) reported that 35% of natural diamonds in the same "near-colorless" color range had detectable fluorescence, and that 99% of the fluorescence reactions were blue due to the N3 optical defect. By contrast, the small percentage of CVD synthetic diamonds with detectable fluorescence emitted orange, green, and yellow colors. Further investigation reveals that only the pre-commercial goods (2003–2008) showed orange fluorescence, while a few stones from 2010 and 2012 fluoresced yellow and green. The yellow to orange fluorescence is principally attributed to NV centers, and the green fluorescence to the H3 defect (Dobrinets et al., 2013).

DiamondView Fluorescence Color of CVD Synthetics

Figure legend:
- Blue
- Greenish blue
- Green
- Yellowish green
- Yellowish orange
- Orange
- Reddish orange
- Red
- Yellow + purple
- Pink + purple

Y-axis: PERCENTAGE WITHIN COLOR CATEGORY

X-axis categories: "Near-colorless" CVD (D–N) 85%, "Pink" CVD 94%

X-axis label: FLUORESCENCE COLOR
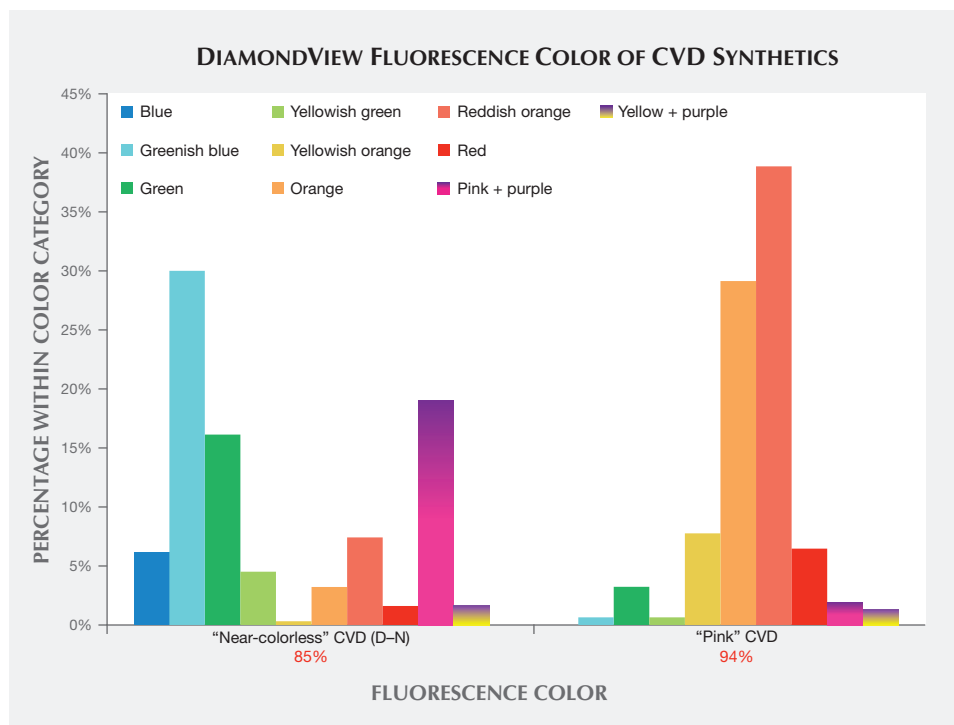
Figure 12. Due to the various growth and treatment histories for "near-color-less" synthetic diamonds—as-grown or HPHT-treated, grown slowly or quickly, grown with low accidental amounts of nitrogen or deliberately high amounts of silicon—the CVD samples show a variety of Diamond-View fluorescence colors. Most "pink" CVD synthetics are treated after growth to create high concentrations of NV centers; as a result, their fluorescence images are dominated by yellowish orange to red colors. The percentages shown in red represent the portion of samples with data available for that color range.

None of the "near-colorless" CVD samples tested since 2013 had detectable long-wave fluorescence, indicating that the ever-evolving CVD process is no longer producing crystals that display observable fluorescence. It is unknown whether this trend represents a normal advancement in growth technology or a deliberate effort to remove a potentially identifying feature.

Pink Material. Due to the presence of NV defect centers acquired during post-growth treatment, the majority of "pink" CVD synthetics showed moderate to strong fluorescence, typically with orange or red colors. Only 23% had no reaction to long-wave UV. By contrast, 16% of the natural "pink" diamonds had no reaction to long-wave UV (King et al., 2002). Among those natural diamonds with observed fluorescence, the vast majority gave a blue reaction, while the remainder showed an orange color. Only a very small percentage (<1%) of natural pink diamonds derive their color from NV centers, and it is this small percentage that showed orange rather than blue fluorescence. Another trend among pink CVD synthetics in recent years is the increasing percentage of samples showing no fluorescence reaction. Before 2012, nearly all pink CVD synthetics tested had observable fluorescence; since 2013, fluorescence has been observed in only 68% of them. Other color origins for pink CVD synthetics include a ~520 nm band (Wang et al., 2007) or

high silicon impurities (see box A); such material has also been submitted to the GIA labs.

DiamondView Imaging. For the past two decades, the DiamondView fluorescence imaging instrument has been a principal tool of major gemological laboratories. The design of the sample holder allows diamonds to be positioned and examined in various orientations, and the fluorescence reactions can be observed in real time. Because of the very short wavelength and intensity of the ultraviolet excitation source, fluorescence is created in diamonds at locations just beneath facet surfaces, producing a distinct reaction. Although many CVD synthetics showed no reaction to a standard long-wave UV light source, *all* diamonds—including all CVD synthetics—show some observable reaction to the high-intensity, high-energy UV source of the DiamondView.

Differences in UV fluorescence colors and patterns in diamonds provide the basis for DiamondView analysis (Welbourn et al., 1996). Because of their unique growth environment and tabular crystal shape, CVD synthetic diamonds exhibit distinctive fluorescence reactions under the DiamondView. Figure 12 presents a histogram of the fluorescence colors observed in CVD samples using the DiamondView. The "near-colorless" samples on the left side of the figure exhibited a range of fluorescence colors, each due to a particular optical defect in the diamond lat-
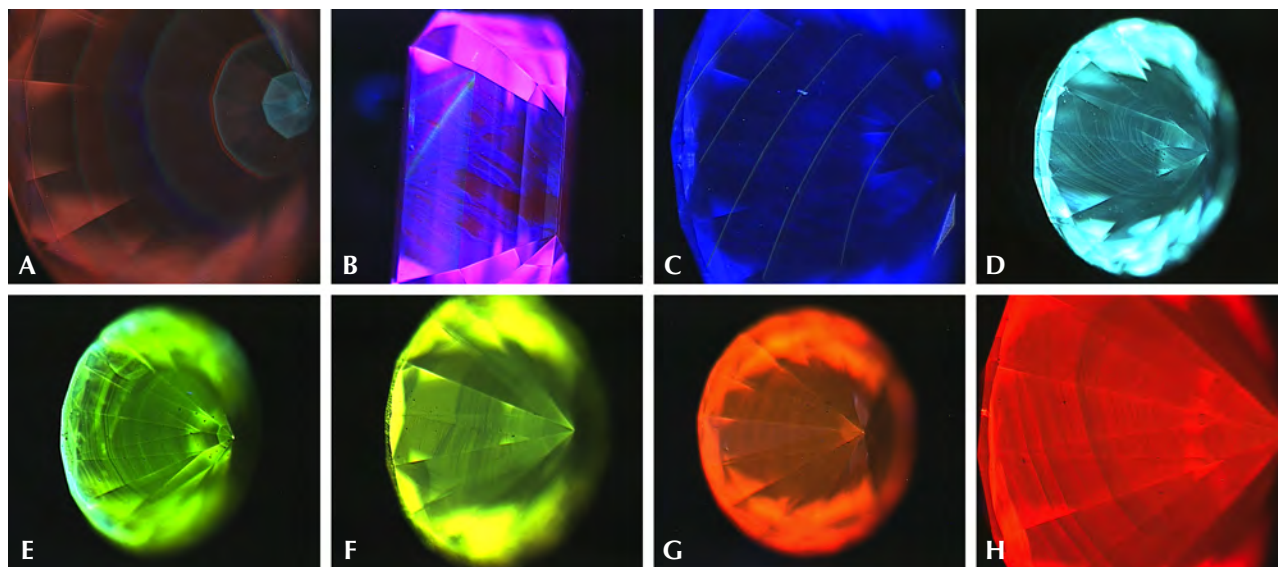
Figure 13. CVD synthetics can produce a rainbow of fluorescence colors and a wide variety of growth features when observed in the DiamondView. Images B and D show the most common fluorescence reactions among "near colorless" CVD material, while G and H are typical among "pink" CVD samples. Most of the images show multiple striations of the fluorescence, best seen in pavilion view.

tice. By contrast, the "pink" samples displayed predominantly yellowish orange, orange, reddish orange, or red fluorescence reactions, which all appear to be the result of just the NV optical defect. Figure 13 shows the variety of colors and growth features that can be seen in CVD synthetic diamonds using the DiamondView.

Growth Features. As shown in figure 13, the fluorescence observed in the DiamondView is usually not distributed evenly. Thin striations of the luminescence are often visible (e.g., images D–H; see Martineau et al., 2004), especially through the pavilion facets. As mentioned earlier, CVD diamond growth takes place layer by layer on the top surface of the growing crystal. Minor or temporary disruptions in diamond formation can result in planes within the crystal where the fluorescing optical defects can become concentrated, and these are visible as striations.

In figure 13, images A and C illustrate a trend seen by GIA researchers in the last few years: a series of parallel bands, likely indicating interruptions during the CVD growth sequence. If a CVD specimen is grown for too long, single-crystal growth becomes polycrystalline growth (Nad et al., 2015). The only remedy is to stop the growth process, remove the crystal from the reactor, and polish away the nongem polycrystalline diamond. The sample can then

be returned to the reactor for the growth process to resume. The chemical composition within the gas phase and on the diamond surface is slightly different at start-up than when the reactor has reached a steady-state condition. Thus, the fluorescence is slightly different within this initial growth layer, as indicated by the evenly spaced luminescence bands (figure 13C). The interruption in growth is recorded as a distinct line in the fluorescence pattern. Such banded fluorescence patterns are not seen in natural diamonds in GIA's labs or elsewhere (e.g., Mokuno et al., 2005; Nad et al., 2015).

Fluorescence Color in "Near-Colorless" CVD Synthetics. For the most part, the fluorescence colors seen in figure 13 originate from particular optical defects in the diamond lattice. The "near-colorless" CVD synthetic diamonds show a variety of fluorescence reactions due to the variety of growth and treatment histories for synthetic diamonds in this range—as-grown or HPHT-treated, grown slowly or quickly, grown with low accidental amounts of nitrogen or deliberately high amounts of silicon. The blue reaction, seen in about 5% of near-colorless material (figure 13C), is likely due to luminescence from bundles of structural dislocations (termed band A in the scientific literature; see Martineau et al., 2004). The greenish blue color is the most common obser-

TABLE 3. Major defect centers and their spectral band positions within CVD synthetics, observed by Vis-NIR absorption, PL, and IR absorption spectroscopy.[a]

Position			Principally observed in:	% of analyzed CVD synthetics in which peak is observed in PL, Vis-NIR, or IR
Wavelength (nm) in Vis-NIR and/or PL spectra	Wavenumber (cm⁻¹) in IR spectra	Designation (Configuration)		
	3123	$(NVH)^0$	Split-grade, pink colors	31%
	3107	(N_3VH)	Pink to purplish pink	33%
	3032		Pink colors	23%
	2947		Pink colors	12%
	1502	(N_i)[b]	Purplish pink	5%
	1450	H1a $(N_{2,i})$	Pink colors	20%
	1344	$(N_s)^0$	Pink colors	45%
	1332	$(N_s)^+$	Split-grade, pink colors	46%
388		Irradiation center[c]	PL: D–N, purplish pink	7%
467			PL: D–N	10%
496		H4 $(N_4V_2)^0$	UV-Vis: brownish pink; PL: split-grade, pink colors	26%
503.2		H3 $(NVN)^0$	UV-Vis: Pink colors; PL: All color grades	65%
503.5		3H (C_i)	PL: All color grades	27%
535			PL: D–N; brownish pink	16%
540			PL: D–N; brownish pink	17%
543			PL: D–N; brownish pink	31%
562/563			PL: D–N; brownish pink	15%
575		$(NV)^0$	UV-Vis: Pink colors; PL: All color grades	100%
595		Irradiation center	UV-Vis: Pink colors	24%
596/597			Exclusive to as-grown CVD; PL: D–N; brownish pink	21%
637		$(NV)^-$	UV-Vis: Pink colors; PL: All color grades	97%
736.7/736.9		$(SiV)^-$	UV-Vis: All color grades; PL: All color grades	91%
741.2		GR1 $(V)^0$	UV-Vis: pink colors	20%
777			PL: D–N, purplish pink	12%
850			PL: D–N, brownish pink, pink	16%
870			PL: pink colors	9%
910			PL: brownish pink	6%
946.5		$(SiV)^0$	PL: D–N	6%
952			PL: D–N; brownish pink	20%
986		H2 $(NVN)^-$	PL: pink colors	39%

[a]*The optical centers appearing in more than 50% of the CVD diamonds surveyed are shown in blue.*
[b]*Subscript* i *designates interstitial; subscript* s *designates substitutional.*
[c]*Zaitsev (2003, p. 338)*

vation among HPHT-treated CVD samples (figure 13D; Wang et al., 2012). The greenish fluorescence is ascribed to H3 centers (figure 13E; Wang et al., 2012).

The pink fluorescence alongside regions of purple mottling of dislocation bundles (figure 13B; see Wang et al., 2007) is observed in CVD synthetic diamonds in the "near-colorless" range and in a few pinks. These CVD synthetics showed the 596/597 nm doublet in their PL spectra. This indicates that the samples with the pink/purple DiamondView reaction are likely as-grown and were not subjected to additional treatment (see the "Photoluminescence Spectroscopy" section below).

Recently, several "near-colorless" CVD Diamond-View images resembling the one in figure 13C (Eaton-Magaña, 2014) have displayed a pattern of dislocation

networks and a deep blue color, which appears rather similar to some DiamondView images of natural diamond. The striations and distinctive colors, such as the pink/purple mottling in figure 13B or the light greenish blue in figure 13D, are not observed. The growth features in the deep blue fluorescing areas closely resemble the dislocation networks commonly associated with natural diamonds. This similarity illustrates the need for vigilance with *all* diamonds and confirms the importance of using more than one feature to identify a stone.

Fluorescence Color in "Pink" CVD Synthetics. As most pink CVD samples are treated after growth to create high concentrations of NV centers (the defect responsible for the pink color), it is not surprising that colors related to NV centers dominate the DiamondView fluorescence reactions. The yellowish orange to red reactions are due to the NV centers: the NV^0 zero-phonon line (ZPL) at 575 nm and the NV^- ZPL at 637 nm. The specific fluorescence color observed varies based on the relative concentrations of NV^0 and NV^- centers.

SPECTROSCOPIC PROPERTIES

With so few diagnostic visual gemological properties (namely the lack of color zoning or distinctive inclusions, but the presence of unusual fluorescence colors and banded strain patterns), spectroscopic techniques are essential for CVD detection in a gemological laboratory. These methods allow quick identification of diamonds as type IIa (such as using a DiamondCheck or DiamondSure instrument) and therefore as potential CVD synthetics. (Near-colorless type Ia diamond, which represents the vast majority of natural diamonds, still cannot be produced by the CVD technique.) Secondly, among the specimens identified as potential CVD synthetics, a combination of features in visible/near-infrared (Vis-NIR) absorption, Fourier-transform infrared absorption (FTIR), and PL spectroscopy will aid in definitive identification of CVD origin. Therefore, positive identification of CVD synthetics is best accomplished by a major gemological laboratory that maintains a database of information on known natural, treated, and synthetic diamonds and sees a sufficient quantity of goods to spot emerging trends.

In the following discussion, the optical defects responsible for spectral features are indicated as either known or unknown to scientists. As an aid for the reader, table 3 summarizes the spectral features recorded by Vis-NIR, FTIR, and PL spectroscopy. We

VIS-NIR ABSORPTION SPECTRA
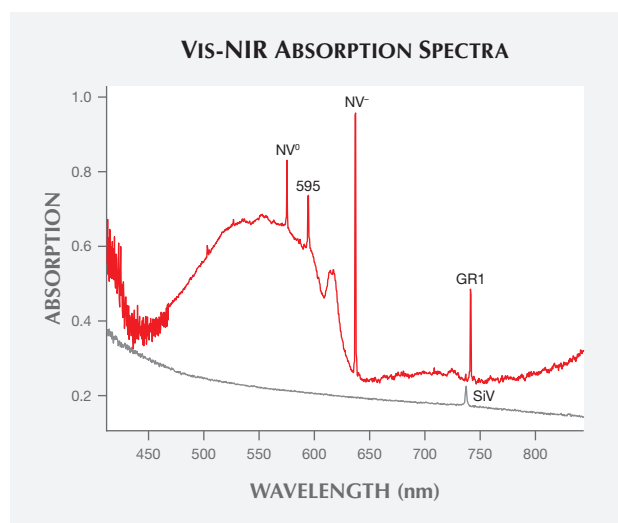
Figure 14. These Vis-NIR absorption spectra were recorded for a 0.60 ct Fancy Vivid purple-pink CVD synthetic (red trace) and a 0.45 ct I-color CVD synthetic (gray trace). The pink specimen shows peaks due to strong NV centers at 575 and 637 nm along with their sidebands and irradiation (GR1 and 595 nm features). This is indicative of post-growth color treatment. The near-colorless sample shows only a small silicon-vacancy (SiV) defect peak, a feature almost exclusive to CVD synthetics. Also note that all Vis-NIR absorption spectra were collected at liquid nitrogen temperature.

will focus solely on analyzing the presence or absence of the spectral feature. The relative intensity of the spectral peak will not be considered for this discussion because it is influenced by the size of the sample, the facet design and shape, and the path length of light travel within the material, among other factors.

In plotting these spectra, it was more illustrative to separate the "pinks" into brownish pink, pink, and purplish pink to show the progression in several spectroscopic properties with color and the different types of post-growth treatment. In other words, there were three categories: (1) HPHT decolorization treatment or no treatment for the "near-colorless" CVD synthetics, (2) no treatment or a growth method not commonly seen for the brownish pinks (e.g., Wang et al., 2007), and (3) HPHT annealing/irradiation/LPLT annealing for the pinks and purplish pinks.

Vis-NIR Spectroscopy. Figure 14 shows representative visible absorption spectra of a "near-colorless" and a "pink" CVD synthetic diamond. For the former, the lack of spectral features (and coloration) is typical of high-color type IIa diamonds. By contrast,

Vis-NIR Absorption Spectral Features

Legend:
- 503.2 nm (H3)
- 575 nm (NV⁰)
- 595 nm (Irradiation)
- 637 nm (NV⁻)
- 737 nm (SiV)
- 741 nm (GR1)

Y-axis: PERCENT INCIDENCE WITHIN COLOR GRADE (0% to 100%)

X-axis (SAMPLE COLOR):
- "Near-colorless" (D–N) 24%
- Brownish pink 95%
- Pink 100%
- Purplish pink 100%
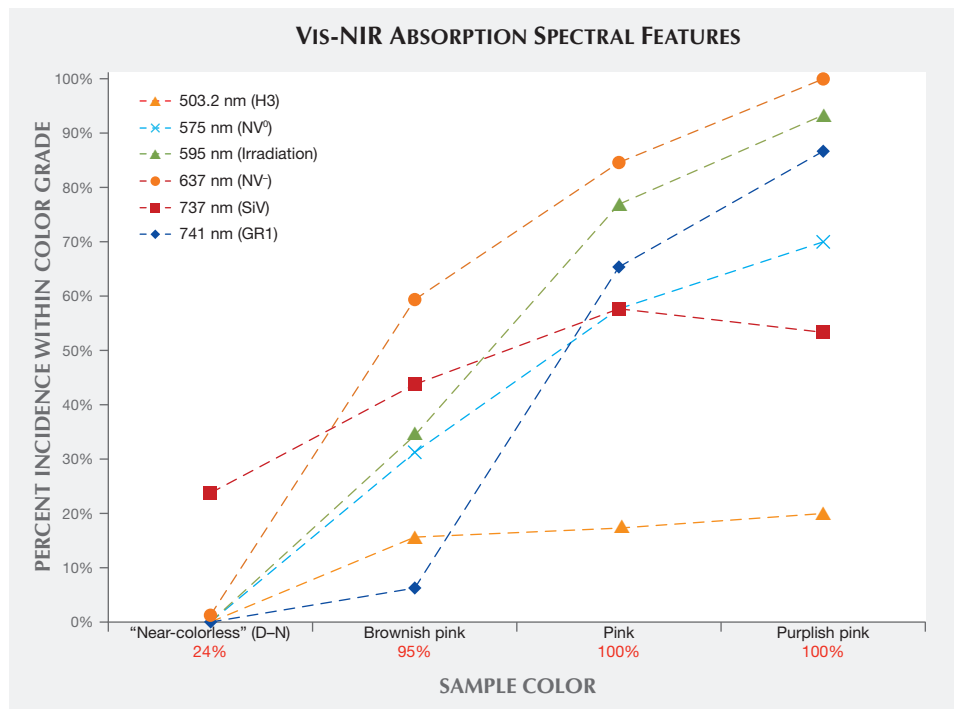
Figure 15. The distribution of samples in each color range in which UV-Vis-NIR absorption spectroscopy detected a specific optical center. The data points for each category are linked by tie lines to emphasize the changing percentages of the particular defect in samples from each category. For example, among the brownish pink CVD samples analyzed at GIA whose Vis-NIR absorption spectra were available and examined for this survey, 16% showed the H3 center and 31% showed the NV^0 center. The percentages shown in red represent the portion of samples with data available for that color range.

the "pink" samples typically exhibit several sharp absorption bands, including several that are due to nitrogen-containing optical defects. Their Vis-NIR spectra appear quite similar to those of treated pink natural diamonds, illustrating the need for multiple measurement techniques and gemological observations to confirm an identification. Figure 15 shows how often these spectral features occur in the CVD synthetic diamonds from this study. Despite the fact that the samples are type II, nitrogen impurities are present in low concentrations (generally below the detection limit of FTIR absorption spectroscopy, so that the sample is still considered a type IIa diamond), and their visible spectra display features that originate from nitrogen-containing optical defects. These features indicate a small amount of nitrogen in the gas mixture during diamond synthesis.

As expected, Vis-NIR spectra for "near-colorless" CVD synthetic diamonds are nearly featureless. Only a small percentage of these samples show the silicon peak at 737 nm, and the silicon-vacancy (SiV) absorbance in these samples is too weak to noticeably affect their color. As color progresses from the "near-colorless" to the "pink" range, there is a much higher incidence of nitrogen-related spectral features, including NV⁻ (at 637 nm), NV⁰ (575 nm), and H3 (503.2 nm).

The brownish pink CVD samples were occasionally as-grown, with high concentrations of silicon, or the pink color was derived from an absorption band centered at approximately 520 nm (Wang et al., 2007,

Khan et al., 2009, Khan et al., 2010) rather than high concentrations of NV centers at 575 and 637 nm.

The post-growth treatment that creates the pink and purplish pink colors usually involves a combination of irradiation and annealing. As expected, the irradiation-related optical defects (the GR1 and 595 nm centers) and related absorption features are significantly higher for these samples.

Infrared (IR) Absorption Spectroscopy. IR absorption spectroscopy is most useful in separating type IIa "near-colorless" diamonds—and therefore CVD and HPHT synthetics—from type Ia, which represent the vast majority of natural diamonds. (This is the basis of GIA's DiamondCheck instrument.) In addition, several features in the IR spectra indicate CVD origin or provide an indication of post-growth color treatment. Figure 16 shows representative IR absorption spectra of two CVD samples: as-grown "near-colorless" and treated "pink." With post-growth treatment, the 3123 cm⁻¹ peak becomes dramatically weaker, while both the 3107 cm⁻¹ peak and the H1a peak at 1450 cm⁻¹ are created. As shown in the figure, the detected features are generally quite weak.

Nitrogen concentrations at the atomic-parts-per-million (ppma) level of detection may be calculated using IR spectra. Nitrogen concentrations were determined using a customized algorithm derived at the Diamond Trading Company (DTC) Research Centre in Maidenhead, UK (from Kiflawi et al., 1994;

FTIR Absorption Spectra
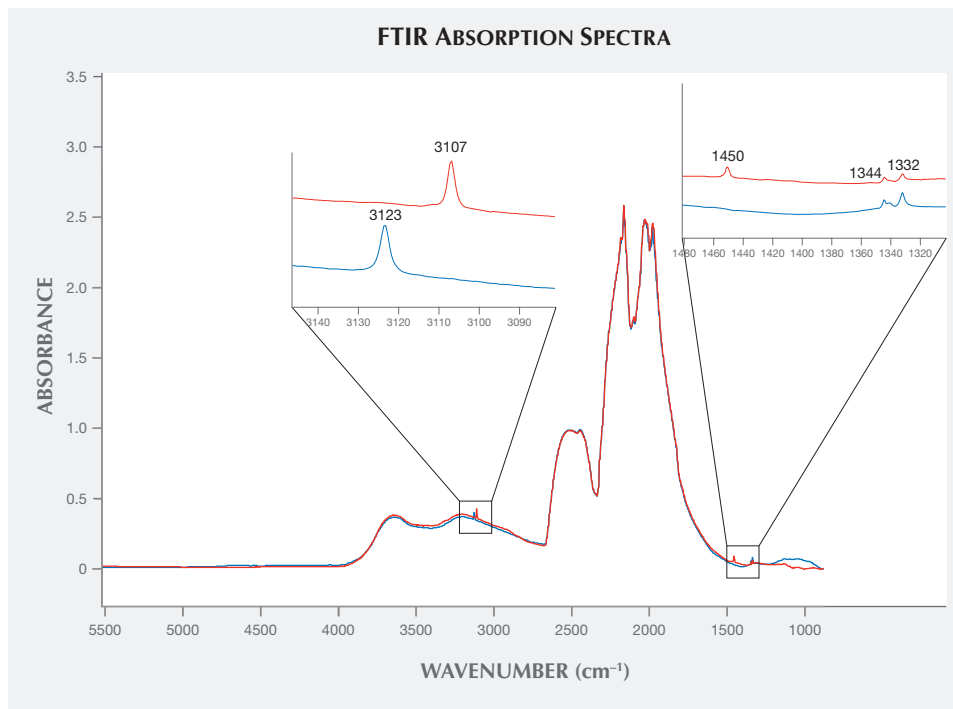
Figure 16. IR spectra of a treated 0.67 ct Fancy Vivid purple-pink CVD sample (red trace) and an as-grown 0.50 ct, N-color CVD synthetic (blue trace). With post-growth treatment, the 3123 cm^{-1} peak is reduced or eliminated, while the 3107 cm^{-1} peak and the H1a peak at 1450 cm^{-1} are created. The significant spectral features between about 1700 and 2700 cm^{-1} are intrinsic to the IR spectra of all diamonds.

Boyd et al., 1994, 1995). Most "near-colorless" CVD-grown diamonds had no detectable nitrogen aggregates in their IR spectra, indicating nitrogen concentrations of less than 1 ppm. The treated pink, as-grown brown-pink, and O-to-Z samples (which are all nominally type IIa) showed weak absorption at 1344 and 1332 cm^{-1}, indicating the presence of 1 to 5 ppm of substitutional nitrogen.

Figure 17 shows the incidence of particular features seen in the mid-IR spectra of the CVD samples. De-
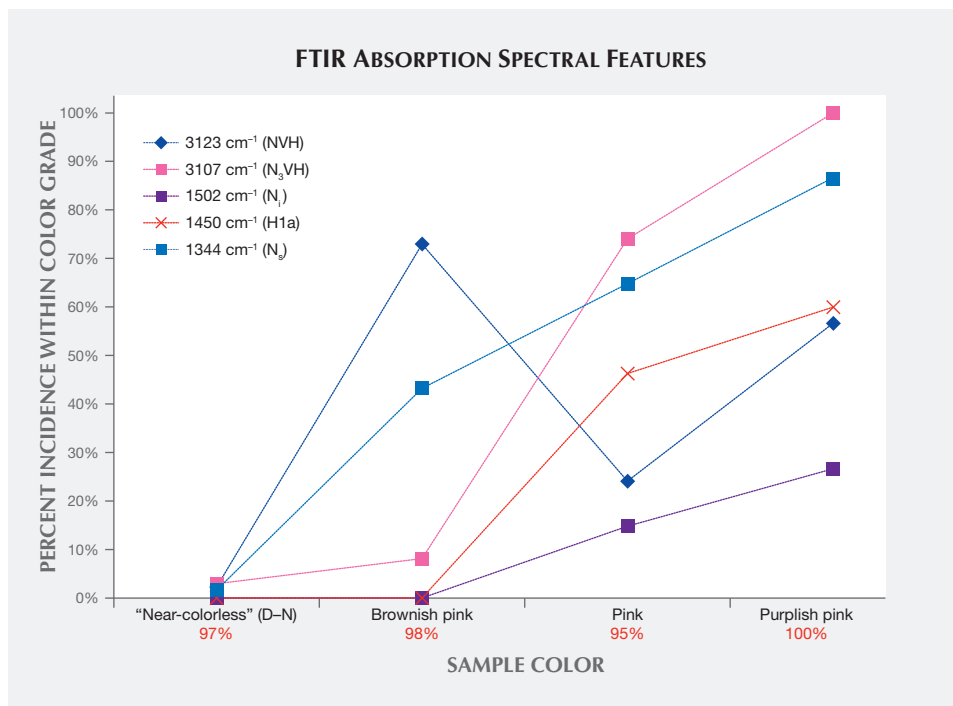
Figure 17. This chart shows the distribution of samples in each CVD synthetic color range where a specific optical center was detected by infrared absorption spectroscopy. The percentages shown in red represent the portion of samples with data available for that color range.

spite the fact that this CVD material is type IIa (indicating a very low nitrogen concentration), all of the nonintrinsic peaks included in figure 17 originate from various nitrogen-containing optical defects.

Photoluminescence (PL) Spectroscopy. PL spectroscopy is a very sensitive analytical technique that can detect optical defects at much lower concentrations than absorption spectroscopy. Therefore, the PL method (where spectral features are excited by incident laser light) is capable of detecting optical centers in diamond when Vis-NIR absorption is not. PL is a vital technique for gemological laboratories in determining diamond origin and color origin, and CVD synthetics are no exception. Figure 18 shows representative PL spectra for two near-colorless CVD samples: one that did not undergo post-growth color treatment (as evidenced by the 596/597 nm doublet) and one that was HPHT annealed, which had a much lower concentration of NV centers and no 596/597 nm doublet. Both show a very small but detectable peak related to the SiV⁻ center. The 596/597 nm doublet has never been reported in natural diamond, HPHT-treated CVD synthetics, or CVD synthetics that have undergone multiple treatment steps. It is considered a reliable indicator that

a CVD specimen has not undergone HPHT treatment (Wang et al., 2010, 2012).

The SiV⁻ doublet at 736.6 and 736.9 nm is a strong indicator of CVD growth; the center is seen very rarely in natural diamonds and occasionally in HPHT synthetics (Breeding and Wang, 2008). Other features, such as the presence of the 596/597 nm doublet, indicate that the CVD sample did not undergo any color treatment, while the H2 center is an indicator of post-growth treatment (figure 19). With synthetic diamonds, however, the jewelry trade makes no distinction in market value between as-grown and treated products.

Figure 19 shows the incidence of selected features in the PL spectra based on sample color. In this figure, the percentage of CVD-grown diamonds with the 596/597 nm doublet decreases as the color progresses from "near-colorless" to brownish pink to pink. This also provides an estimate of the percentage that have not undergone post-growth treatment. Among "near-colorless" samples, 30% have the 596/597 nm doublet, indicating that the remaining 70% were likely HPHT-annealed. The pink samples showed a higher percentage of H2, H3, and H4 centers due to high-temperature heating during post-growth treatment for these color ranges.

PHOTOLUMINESCENCE SPECTRA
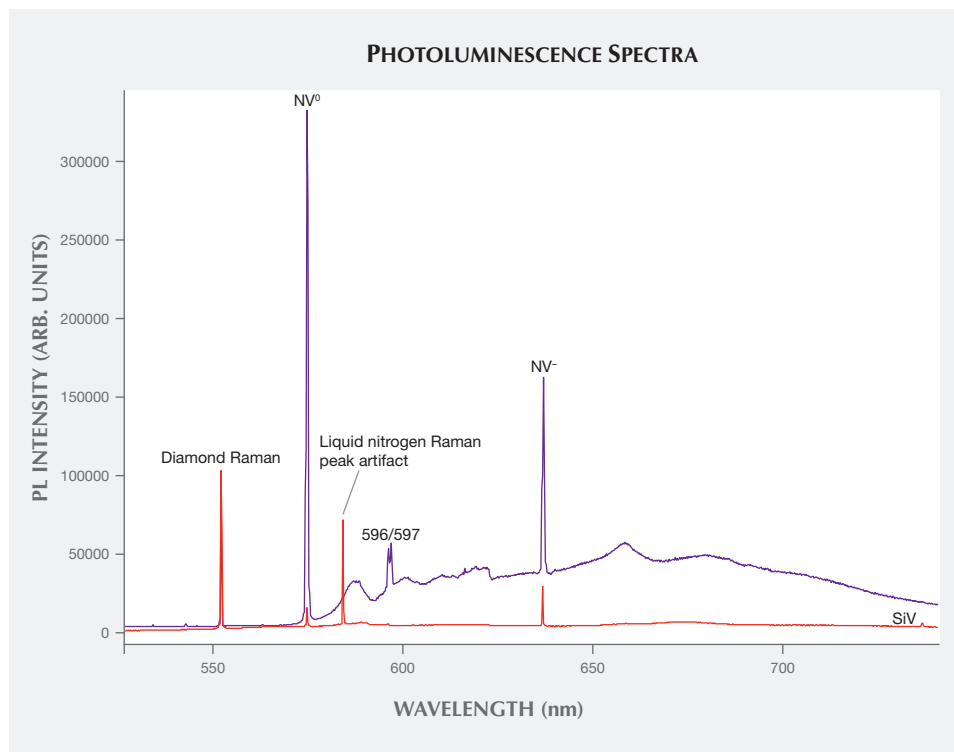
Figure 18. These PL spectra were recorded for an as-grown 0.26 ct I-color CVD synthetic (purple trace) and an HPHT-treated 0.30 ct H-color CVD synthetic (red trace). The spectra are scaled vertically so that their diamond Raman peaks at 1333 cm⁻¹ (552.4 nm) are equivalent in intensity. Key diagnostic spectral features of CVD material include the SiV⁻ doublet at 736.6 and 736.9 nm in most samples and the 596/597 nm doublet in as-grown material. Also note that all PL spectra were collected at liquid nitrogen temperature.

DISTRIBUTION OF PL SPECTRAL FEATURES
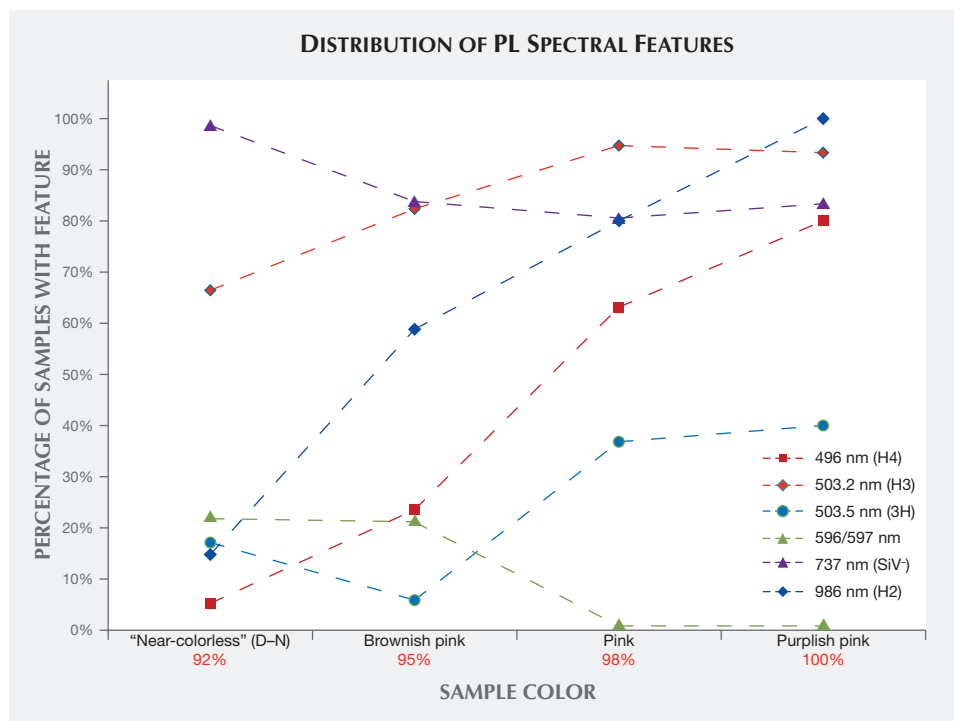
Figure 19. The distribution of spectral features in each of the four color ranges of CVD synthetics, as detected by PL spectroscopy. Other optical centers that had nearly 100% incidence across all colors—though at drastically different intensities, such as NV^0 and NV^-—are not included. The percentages shown in red represent the portion of samples with data available for that color range.

CRITERIA FOR THE GEMOLOGIST

There are no reliable visual factors to help identify potential CVD synthetics. The size of the cut stone is not diagnostic: Most CVD synthetic diamonds are below 0.75 ct, and (except for one recent sample) all those surveyed by GIA have weighed less than 4 ct. The color appearance and the cause of the pink color are not diagnostic for the majority, though the pink color in CVD synthetics is usually more saturated than in natural pink diamonds.

There are several distinctive features gemologists may use to recognize in order to identify potential CVD synthetics, though none should be relied upon as the sole means of identification.

1. Orange-to-red fluorescence reaction to a standard UV lamp in pink specimens derives from NV centers, indicating that the diamond is either a rare Golconda-type natural diamond, a treated natural diamond, or an HPHT or CVD synthetic (table 2). Although the vast majority of "near-colorless" CVD synthetics do not show observable long-wave fluorescence, some older material shows fluorescence colors (such as green) that are quite rare among natural colorless diamonds. In a gemological laboratory, the presence of striated fluorescence corresponding to multiple growth layers in Diamond-View images provides additional confirmation

of CVD growth, but its absence does not eliminate the possibility of CVD origin.

2. CVD samples span the clarity scale, but those observed by GIA's laboratory trend toward higher clarity grades. The small inclusions most often encountered are clouds, pinpoints, and black "crystals." Similar clarity features are found in both natural and CVD synthetics. These inclusions are generally not diagnostic for identification purposes, despite the very different diamond formation environments.

3. Type II diamonds—samples that are UV transparent or show no detectable nitrogen in their FTIR absorption spectra—should always be sent to a laboratory for testing.

4. Major CVD manufacturers inscribe the synthetic diamond's origin on the girdle (e.g., "Lab Grown"). But note that the lack of an inscription does not necessarily indicate a natural stone.

5. A strain pattern viewed in the polariscope or a microscope configured with crossed polarizing filters (e.g., figure 20) can help distinguish CVD synthetics from HPHT synthetics, as the latter show extremely low levels of strain (e.g., figure 7 in D'Haenens-Johansson et al., 2015b).

Gem-testing laboratories need to maintain a full complement of gemological, imaging, and spec-
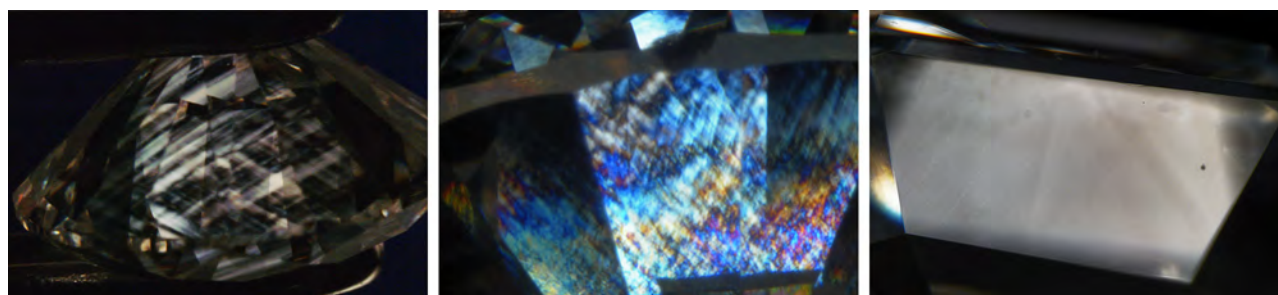
Figure 20. Viewed in crossed polarizers, CVD synthetics (left and center) show higher-order interference colors than those generally seen in type IIa natural diamonds (though this observation is not sufficient for a reliable identification). Viewing in crossed polarizers also distinguishes CVD from HPHT synthetics, which tend to display extremely low levels of strain (right). Shown in these photos are a 0.53 ct G-color CVD synthetic diamond (left), a 2.51 ct H-color CVD synthetic (center) and a 0.46 ct D-color HPHT synthetic (right).

troscopy instrumentation, including a DiamondView imaging microscope, an FTIR absorption spectrometer, and a photoluminescence spectrometer equipped with several lasers to distinguish diamond origin and treatments. Additionally, they must have access to CVD specimens that are representative of products available in the trade and maintain a database of information on their properties. They must be constantly on the lookout for emerging trends that deviate from standard detection criteria for natural, treated, or synthetic diamonds. Gem laboratories must also operate under the assumption that today's reliable criteria may not be applicable in the future and find alternative methods to ensure that identification keeps pace with the manufacturers' technology.

FUTURE
Melee. In recent years, several gemological laboratories (including GIA's) have established melee sorting services for colorless to near-colorless diamonds to separate natural stones from those that are potentially treated or synthetic. Therefore, both colored melee (through grading reports) and colorless melee (through sorting) can be screened for synthetics. Yet melee-size CVD synthetic diamonds have not been routinely submitted to GIA for examination. Based on our own observations and discussions with manufacturers, there is little evidence of CVD-grown melee in the marketplace. We have recently examined some CVD melee (e.g., figure 21) and anticipate that melee-size CVD material will become more available in the future (Poon et al., 2016). There have been reports that CVD melee is being manufactured in India, and this supply might become more prevalent in the coming years (W. Wang, pers. comm., 2016). HPHT-grown melee will likely remain more common than CVD-grown material, since yellow samples that can be fashioned as melee are easy to produce by this method. Although colorless natural melee is more abundant, HPHT-grown synthetic diamonds are currently in limited supply.

Without our own data or any published information, it is difficult to know the extent of HPHT and CVD synthetic diamond melee in the marketplace. Because of the availability of natural colorless melee, pink CVD melee is more likely to be produced (e.g.,

Figure 21. These five CVD melee were recently examined by GIA. All are in the near-colorless range, weigh 0.02–0.04 ct, and show a similar range of DiamondView colors as larger CVD-grown diamonds. The images for only B and C show the striations typical of CVD growth, once again indicating the need to rely on a combination of data and observations, such as the unusual DiamondView colors of these melee and their IR and PL spectra, that confirm CVD synthetic origin.
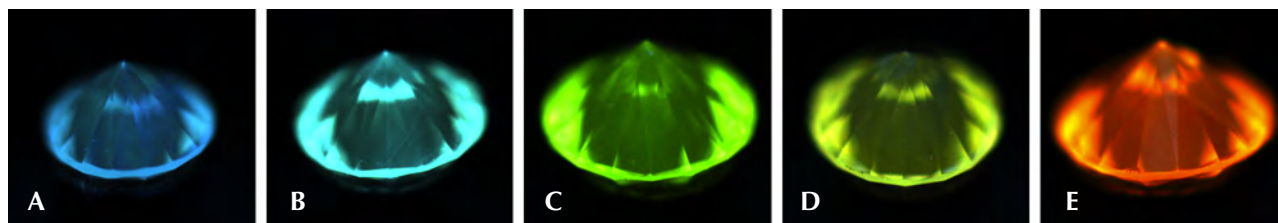
Kitawaki et al., 2010). If this is the case, pink CVD melee are not being submitted to GIA, which accepts colored diamonds of melee size for origin reports.

Outlook. Several features seen in early CVD synthetics have become less relevant in recent years. CVD-specific peaks such as 3123 cm^{-1} in IR absorption spectra and the 596/597 nm doublet in PL spectra were common in early products. Most CVD material today has undergone at least one round of post-growth treatment (either HPHT annealing or a combination of irradiation and annealing), so these early features are rarely observed. Likewise, it is possible that today's criteria will no longer be applicable in a few years. Growth techniques are rapidly progressing due to research by CVD manufacturers for gem purposes and high-tech applications.

At present, the reliable identification criteria for undisclosed client-submitted samples have been established by examining CVD synthetics from known manufacturers: for instance, the presence of the SiV peak in Vis-NIR absorption or PL spectroscopy, and synthetic growth features as observed by Diamond-View luminescence imaging.

While quality factors such as color, the cut grade of round brilliants, and clarity have been fairly consistent in CVD synthetics over the last several years, carat weight has risen. The number of samples submitted to GIA dwindled during 2010–2011, when Apollo Diamond Inc. was acquired by Scio, but has increased dramatically since then as Scio and other manufacturers have ramped up their production. Gemesis added CVD synthetics to their offerings in 2012 (Wang et al., 2012), and more companies have starting selling their own manufactured products.

It is likely that the range of CVD synthetic colors will continue to expand and the sizes will increase. In September 2016, GIA's Hong Kong laboratory graded a 5.19 ct J-color CVD synthetic—the largest submitted to GIA thus far (Law, 2016). Also, there have been unique CVD synthetics with interesting optical characteristics, such as samples with a reversible color change between pink and blue due to a charge-transfer effect caused by high amounts of incorporated silicon (D'Haenens-Johansson et al., 2015; see also box A). We also expect the quantity of CVD synthetics submitted for grading reports to increase in the coming years. Figure 22 shows the percentage of CVD synthetics within the data set from this study divided by year. There was a marked increase in CVD samples examined by GIA between 2012 and 2013, and this trend should continue to increase as new CVD diamond manufacturers (e.g., Bates, 2015) release their products.

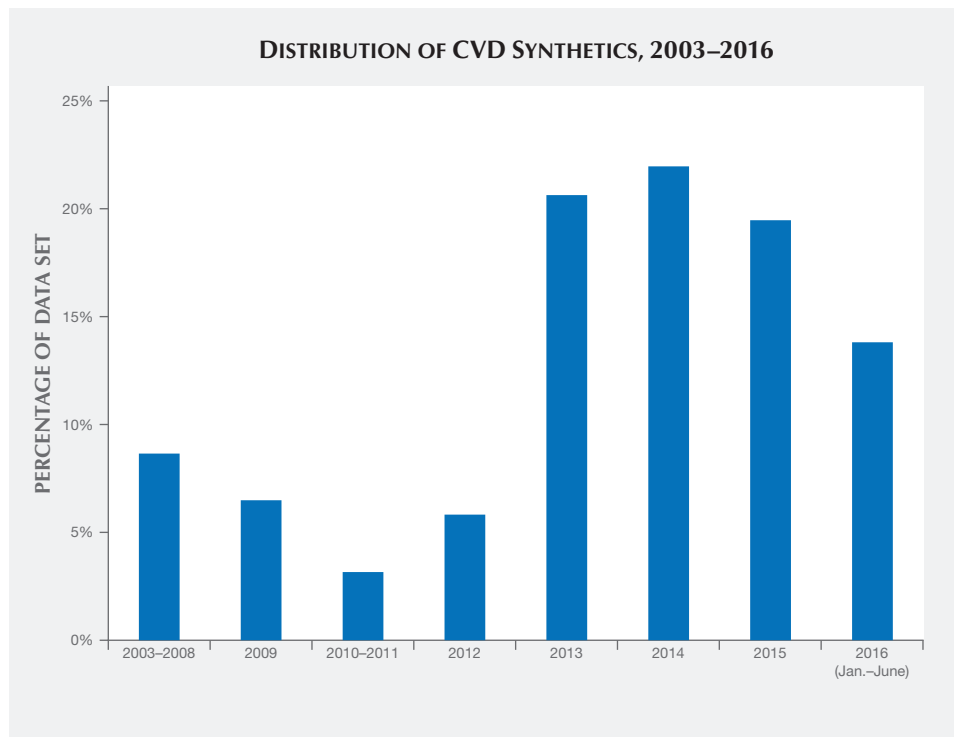**DISTRIBUTION OF CVD SYNTHETICS, 2003–2016**

Figure 22. This plot shows the distribution of the CVD samples comprising the data set, separated by year. The majority of the samples are from the last several years, when client submissions significantly increased.

CONCLUSIONS

Today the CVD process is used to produce high-color (or fancy color) and high-clarity type II synthetic diamonds up to several carats in size that are likely to be visually indistinguishable from polished natural diamonds. These CVD synthetics may display ultraviolet fluorescence reactions and inclusion features that would be unusual within natural diamonds. Ad-ditionally, the results described in this article illustrate how the samples all exhibited spectroscopic features that were quite different from those occurring in similar natural gem diamonds. Based on the use of analytical instruments and access to our large database of gemological information, the synthetic diamonds examined to date by GIA's laboratory can be readily identified.

ABOUT THE AUTHORS
Dr. Eaton-Magaña is a research scientist, and Dr. Shigley is a distinguished research fellow, at GIA in Carlsbad, California.

REFERENCES

Angus J.C. (2014) Diamond synthesis by chemical vapor deposition: The early years. *Diamond and Related Materials*, Vol. 49, pp. 77–86, http://dx.doi.org/10.1016/j.diamond.2014.08.004

Angus J.C., Hayman C.C. (1988) Low-pressure, metastable growth of diamond and "diamondlike" phases. *Science*, Vol. 241, No. 4868, pp. 913–921.

Ardon T., Wang W. (2014) Lab Notes: Heavily irradiated CVD synthetic diamond. *G&G*, Vol. 50, No. 3, pp. 240–241.

Ardon T., Allen T., Breeding C.M. (2013) Lab Notes: CVD-grown synthetic diamond with aggregated nitrogen impurities. *G&G*, Vol. 49, No. 1, pp. 47–49.

Bates R. (2015) The lab-grown diamond producer backed by Leonardo DiCaprio. *JCK Online*, Nov. 11, www.jckonline.com/blogs/cutting-remarks/2016/01/20/lab-grown-diamond-producer-backed-leonardo-dicaprio

Boyd S.R, Kiflawi I., Woods G.S. (1994) The relationship between infrared absorption and the A defect concentration in diamond. *Philosophical Magazine Part B*, Vol. 69, No. 6, pp. 1149–1153, http://dx.doi.org/10.1080/01418639408240185

——— (1995) Infrared absorption by the B nitrogen aggregate in diamond. *Philosophical Magazine Part B*, Vol. 72, No. 3, pp. 351–361, http://dx.doi.org/10.1080/13642819508239089

Breeding C.M., Wang W. (2008) Occurrence of the Si-V defect center in natural colorless gem diamonds. *Diamond and Related Materials*, Vol. 17, No. 7–10, pp. 1335–1344, http://dx.doi.org/10.1016/j.diamond.2008.01.075

Butler J.E., Oleynik I. (2008) A mechanism for crystal twinning in the growth of diamond by chemical vapour deposition. *Philosophical Transactions of the Royal Society A*, Vol. 366, No. 1863, pp. 295– 310, http://dx.doi.org/10.1098/rsta.2007.2152

Butler J.E., Mankelevich Y.A., Cheesman A., Ma J., Ashfold M.N.R. (2009) Understanding the chemical vapor deposition of diamond: Recent progress. *Journal of Physics: Condensed Matter*, Vol. 21, No. 36, pp. 364201-1–364201-20, http://dx.doi.org/10.1088/0953-8984/21/36/364201

D'Haenens-Johansson U.F.S., Ardon T., Wang W. (2015) CVD synthetic gem diamonds with high silicon-vacancy concentrations. *Conference on New Diamond and Nano Carbons*, Shizuoka, Japan, May 2015.

Dieck C., Loudin L., D'Haenens-Johansson U.F.S. (2015) Lab Notes: Two large CVD-grown synthetic diamonds tested by GIA. *G&G*, Vol. 51, No. 4, pp. 437–439.

Dobrinets I.A., Vins V.G., Zaitsev A.M. (2013) *HPHT-Treated Diamonds: Diamonds Forever*. Springer, Heidelberg, Germany.

Eaton-Magaña S. (2014) Lab Notes: CVD synthetic diamond with unusual DiamondView image. *G&G*, Vol. 50, No. 1, pp. 67–68.

Khan R.U.A., Martineau P.M. Cann B.L., Newton M.E., Twitchen D.J. (2009) Charge transfer effects, thermo and photochromism in single crystal CVD synthetic diamond. *Journal of Physics: Condensed Matter*, Vol. 21, pp. 364214-1–364214-9

Khan R.U.A., Martineau P.M., Cann B.L., Newton M.E., Dhillon H.K., Twitchen D.J. (2010) Color alterations in CVD synthetic diamond with heat and UV exposure: Implications for color grading and identification. *G&G*, Vol. 46, No. 1, pp. 18–26, http://dx.doi.org/10.5741/GEMS.46.1.18

Kiflawi I., Mayer A.E., Spear P.M., van Wyk J.A., Woods G.S. (1994) Infrared absorption by the single nitrogen and A defect centres in diamond. *Philosophical Magazine Part B*, Vol. 69, No. 6, pp. 1141–1147, http://dx.doi.org/10.1080/01418639408240184

King J.M., Shigley J.E., Guhin S.S., Gelb T.H., Hall M. (2002) Characterization and grading of natural-color pink diamonds. *G&G*, Vol. 38, No. 2, pp. 128–147, http://dx.doi.org/10.5741/GEMS.38.2.128

Kitawaki H., Abduriyim A., Kawano J., Okano M. (2010) Gem News International: Treated CVD-grown pink synthetic diamond melee. *G&G*, Vol. 46, No. 1, pp. 68–69.

Law B. (2016) Lab Notes: CVD synthetic diamond over 5 carats identified by GIA. *G&G*, Vol. 52, No. 4, http://www.gia.edu/gems-gemology/winter-2016-labnotes-CVD-synthetic-diamond-over-5-carats-identified

Liang Q., Yan C.-S., Meng Y. Lai J., Krasnicki S., Mao H.-K., Hemley R.J. (2009) Recent advances in high-growth rate single-crystal CVD diamond. *Diamond and Related Materials*, Vol. 18, No. 5–8, pp. 698–703, http://dx.doi.org/10.1016/j.diamond.2008.12.002

Martineau P.M., Lawson S.C., Taylor A.J., Quinn S.J., Evans D.J.F., Crowder M.J. (2004) Identification of synthetic diamond grown

using chemical vapor deposition (CVD). *G&G*, Vol. 40, No.1, pp. 2–25, http://dx.doi.org/10.5741/GEMS.40.1.2

Moe K.S., Wang W., D'Haenens-Johansson U.F.S. (2014) Lab Notes: Yellow CVD synthetic diamond. *G&G*, Vol. 50, No. 2, pp. 154–155.

Mokuno Y., Chayahara A., Soda Y., Horino Y., Fujimori N. (2005) Synthesizing single-crystal diamond by repetition of high rate homoepitaxial growth by microwave plasma CVD. *Diamond and Related Materials*, Vol. 14, No. 11/12, pp. 1743–1746, http://dx.doi.org/10.1016/j.diamond.2005.09.020

Moses T.M., Reinitz I.M., Johnson M.L., King J.M., Shigley J.E. (1997) A contribution to understanding the effect of blue fluorescence on the appearance of diamonds. *G&G*, Vol. 33, No. 4, pp. 244–259, http://dx.doi.org/10.5741/GEMS.33.4.244

Nad S., Gu Y., Asmussen J. (2015) Growth strategies for large and high quality single crystal diamond substrates. *Diamond and Related Materials*, Vol. 60, pp. 26–34, http://dx.doi.org/10.1016/j.diamond.2015.09.018

Othman M.Z., May P.W., Fox N.A., Heard P.J. (2014) Incorporation of lithium and nitrogen into CVD diamond thin films. *Diamond and Related Materials*, Vol. 44, pp. 1–7, http://dx.doi.org/10.1016/j.diamond.2014.02.001

Poon T., Lo C., Law B. (2016) Lab Notes: Ring with a CVD synthetic melee. *G&G*, Vol. 52, No. 1, pp. 75–76.

Prieske M., Vollertsen F. (2016) In situ incorporation of silicon into a CVD diamond layer deposited under atmospheric conditions. *Diamond and Related Materials*, Vol. 65, pp. 47–52, http://dx.doi.org/10.1016/j.diamond.2016.01.021

Shigley J.E., McClure S.F., Breeding C.M., Shen A.H.-T., Muhlmeister S.M. (2004) Lab-grown colored diamonds from Chatham Created Gems. *G&G*, Vol. 40, No. 2, pp. 128–145, http://dx.doi.org/10.5741/GEMS.40.2.128

Twitchen D.J., Markham M.L., Scarsbrook G.A. (2016) Diamond sensors, detectors, and quantum devices. U.S. Patent 9249526.

Wang W., Moe K.S. (2010) Lab Notes: CVD synthetic diamond over one carat. *G&G*, Vol. 46, No. 2, pp. 143–144.

Wang W., Moses T.M. (2008) Lab Notes: Gem-quality CVD synthetic diamond with traces of boron. *G&G*, Vol. 44, No. 2, pp. 158–159.

Wang W., Moses T., Linares R., Shigley J.E., Hall M., Butler J.E. (2003) Gem-quality synthetic diamonds grown by a chemical vapor deposition (CVD) method. *G&G*, Vol. 39, No. 4, pp. 268–283, http://dx.doi.org/10.5741/GEMS.39.4.268

Wang W., Smith C.P., Hall M.S., Breeding C.M., Moses T.M. (2005) Treated-color pink-to-red diamonds from Lucent Diamonds Inc. *G&G*, Vol. 41, No. 1, pp. 6–19, http://dx.doi.org/10.5741/GEMS.41.1.6

Wang W., Hall M.S., Moe K.S., Tower J., Moses T.M. (2007) Latest-generation CVD-grown synthetic diamonds from Apollo Diamond Inc. *G&G*, Vol. 43, No. 4, pp. 294–312, http://dx.doi.org/10.5741/GEMS.43.4.294

Wang W., Doering P., Tower J., Lu R., Eaton-Magaña S., Johnson P., Emerson E., Moses T.M. (2010) Strongly colored pink CVD lab-grown diamonds. *G&G*, Vol. 46, No. 1, pp. 4–17, http://dx.doi.org/10.5741/GEMS.46.1.4

Wang W., D'Haenens-Johansson U.F.S., Johnson P., Moe K.S., Emerson E., Newton M.E., Moses T.M. (2012) CVD synthetic diamonds from Gemesis Corp. *G&G*, Vol. 48, No. 2, pp. 80–97, http://dx.doi.org/10.5741/GEMS.48.2.80

Wang W., Moe K.S., Yeung S.F., D'Haenens-Johansson U.F.S. (2013) Lab Notes: Very large CVD-grown synthetic diamond. *G&G*, Vol. 49, No. 1, p. 50.

Zaitsev A.M. (2003) *Optical Properties of Diamond: A Data Handbook*. Springer-Verlag, Berlin.

For online access to all issues of GEMS & GEMOLOGY from 1934 to the present, visit:

gia.edu/gems-gemology

Reversible Color Modification of Blue Zircon by Long-Wave Ultraviolet Radiation

Nathan D. Renfro

Exposing blue zircon to long-wave ultraviolet (LWUV) radiation introduces a brown coloration, resulting in a somewhat unattractive, much less valuable gemstone. Common sources of accidental long-wave radiation that can affect mounted faceted blue zircons are tanning beds and UV lights used to apply acrylic fingernails. To determine if the LWUV-induced brown color in zircon is completely and easily reversible, quantitative UV-visible spectroscopy was used to measure the difference in absorption before and after LWUV exposure. This study explored the nature of the UV-induced color-causing defect to establish whether subsequent exposure to visible light would completely restore the blue color. Spectroscopic examination showed that blue color in zircon is due to a broad absorption band in the ordinary ray, starting at 500 nm and centered at approximately 650 nm. LWUV exposure induced absorption features, including a broad band centered at 485 nm that was responsible for the brown color.

Zirconium silicate ($ZrSiO_4$), better known as zircon, is prized for its brilliance, vibrant color, and high clarity. Though commonly thought of as a colorless diamond simulant, this tetragonal mineral occurs in several countries in a wide variety of colors. Zircon has been described as having unusual tenebrescent properties (McClure, 2011) and as changing color when irradiated (McClure et al., 2001). Blue zircon (figure 1) is produced by heat treating brown material to 900–1000°C in a reducing atmosphere (Smith and Balmer, 2009); within the gem trade, all blue zircon is presumed to be heat treated. In recent years, at least two anonymous gem dealers attending the Tucson gem shows have reported to the author that customers returned blue zircons because they had changed to an unattractive brown color (Renfro, 2013). Further inquiry revealed that the zircons had been inadvertently exposed to long-wave ultraviolet (LWUV) radiation, either in a tanning bed or under a UV lamp that cures the epoxy resin used to apply acrylic fingernails. The gem dealers' main concern was returning the stones to their vivid blue color. One of these stones was reportedly restored to the desired blue, while the status of the other is unknown.

In the case of a blue zircon that turned brown (Koivula and Misiorowski, 1986), the blue color was restored by placing the stone near an incandescent

In Brief

- Zircon is a popular gem that occurs in several colors.
- Gem-quality blue zircon can turn brown from accidental long-wave UV (LWUV) exposure.
- LWUV-induced brown color can be removed by exposure to an incandescent light source, restoring the blue color.

light bulb for a couple of hours. The more recent reports from the gem dealers prompted the current investigation, in which blue zircons presumed to be heat treated were exposed to LWUV radiation to induce a brown color. The color change was observed and quantitatively measured to determine whether the color could be completely restored.

Figure 1. Blue zircon, a popular gemstone due to its vibrant color, results from the heat treatment of brown material that contains traces of uranium (Rossman, 1981). Photo by Robert Weldon/GIA, courtesy of Artinian Gems.

MATERIALS AND METHODS

Eleven faceted blue zircons (figure 2) of unknown geographic origin, presumed to be heat-treated material, were studied for color observation before and after exposure to LWUV radiation. A 350 mW, 365 nm LED light source (a GIA prototype that only emits LWUV light) was used at a distance of approx-imately 1 cm for varying durations. In addition to the 11 faceted stones, one optically oriented wafer (Thomas, 2009) of blue zircon from Cambodia (figure 3) was used for quantitative spectroscopic examination to determine the nature of the color-modifying defect introduced by LWUV exposure. Using an aluminum sample holder with a 3 mm aperture, the au-
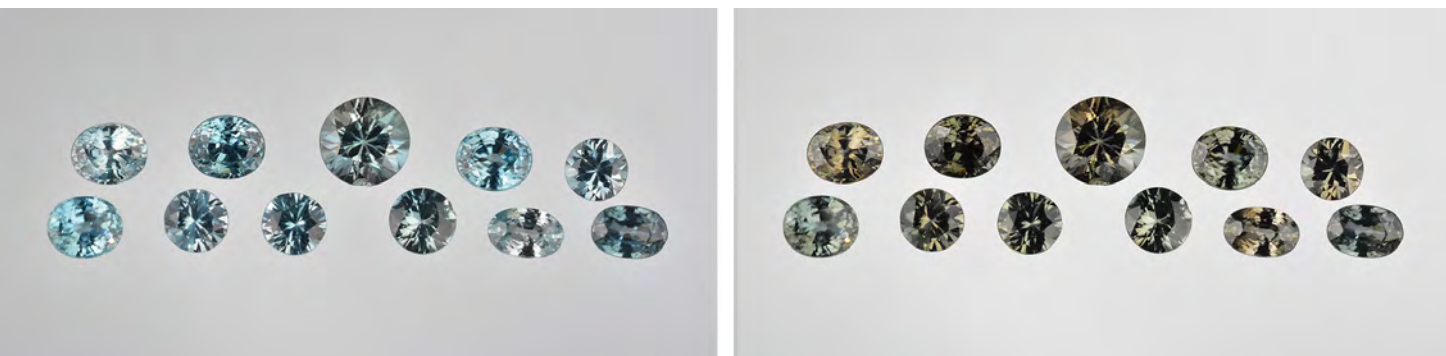
Figure 2. These 11 faceted zircons of unknown origin (left), weighing between 0.62 and 1.96 ct, all showed a brown face-up color after several minutes of LWUV radiation exposure (right). Photos by C.D. Mengason.

thor measured the visible spectrum of the oriented wafer at regular 30-second intervals of LWUV exposure using a Perkin Elmer Lambda 950 scanning spectrophotometer with a data interval of 1 nm. Baseline correction for reflection loss was performed on the blue zircon wafer's spectra by measuring a thin oriented wafer of colorless zircon and subtracting the reflection loss of the colorless sample from the blue zircon spectra.

Differential spectra were used to determine the nature of the LWUV-induced defect by subtracting the original absorption spectra from the spectra measured after maximum LWUV exposure. CIE $L^*a^*b^*$ color space coordinates were calculated from the baseline-corrected spectra to produce an accurate swatch representative of the color produced by the chromophores in the zircon in both the ordinary (o) and extraordinary (e) rays at LWUV exposure intervals of 30 seconds. The brown color was removed by exposing the samples to an approximately 22 W incandescent light source at a distance of approximately 1 cm.
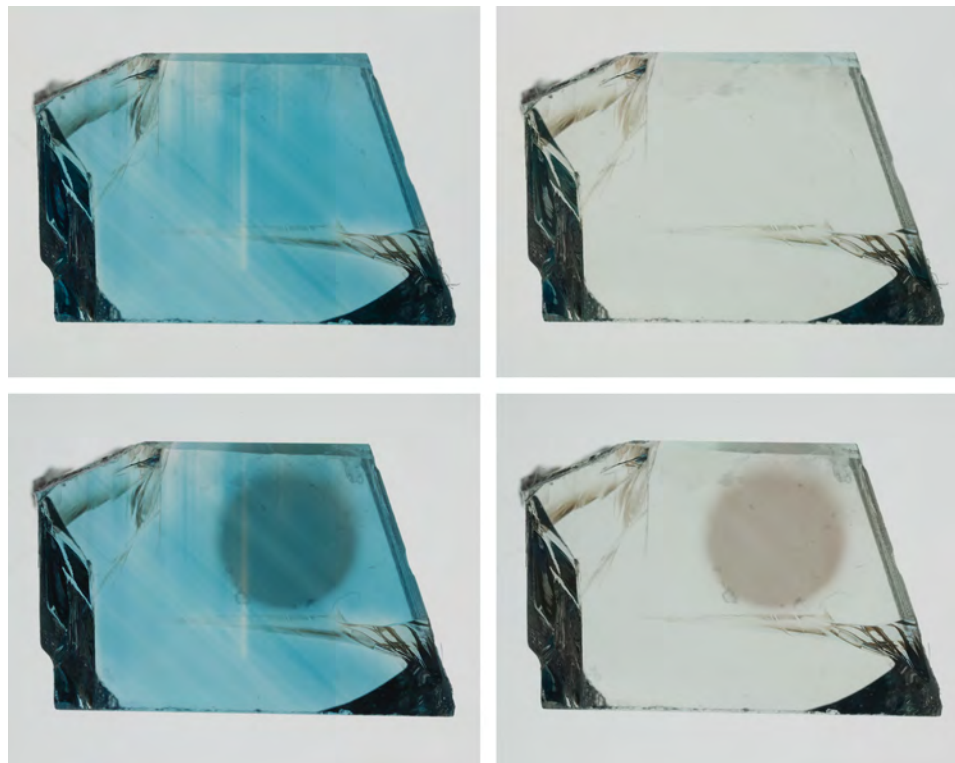
Figure 3. This 6.67 × 10.56 × 5.17 mm optically oriented wafer of blue zircon was used for spectroscopic examination of the LWUV-induced brown color, seen here using plane-polarized light. The photos show the ordinary (o) ray on the left and the extraordinary (e) ray on the right. The photos on the top were taken prior to LWUV exposure. The 3 mm circular brown spot in the bottom images is the localized area that was exposed to LWUV while the immediate area around the spot was masked by an aluminum sample plate. Here it is unmasked to illustrate the color before and after five minutes of LWUV color modification.
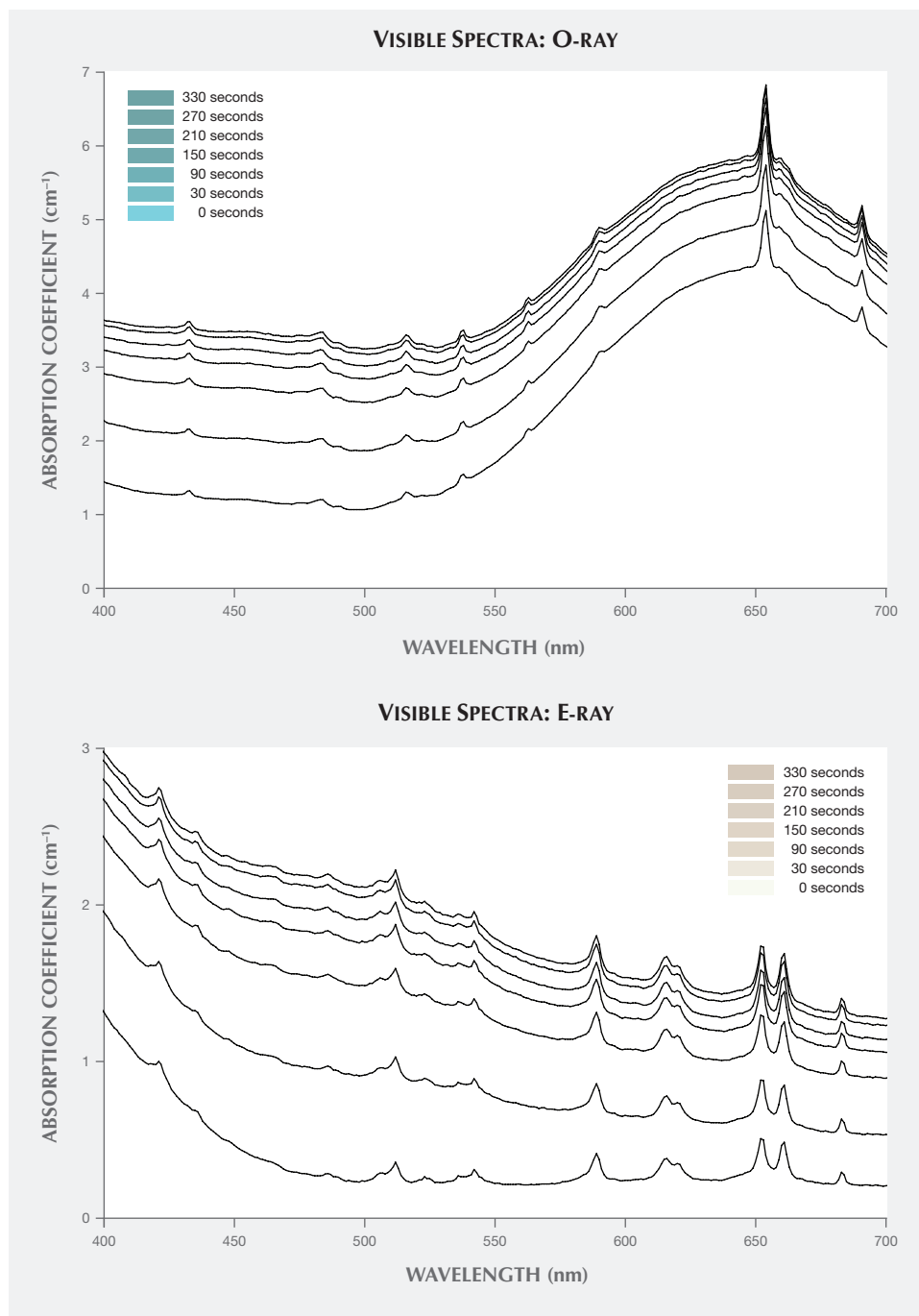
Figure 4. The polarized visible spectra of the blue zircon wafer were measured following 30-second LWUV exposure intervals up to 330 seconds, when a brown color was fully induced. The color swatches were calculated from the collected spectra to show the progressive change in color over time in the o- (top) and e-(bottom) rays of the zircon sample. The spectra were measured at 30-second intervals, but here half of the traces are removed for clarity.

RESULTS AND DISCUSSION

Exposure to LWUV Radiation. Blue color in zircon is attributed to a broad absorption band in the o-ray centered at approximately 650 nm, which is caused by U^{4+} replacing Zr^{4+} atoms in the crystal lattice (http://minerals.gps.caltech.edu/FILES/Visible/zircon/Index.html). The e-ray in blue zircon is colorless, and the o-ray is blue (again, see figure 3). LWUV radiation exposure measured at regular 30-second intervals revealed near-complete saturation of the defect in both the o- and e- rays after just over five minutes (figure 4). The differential spectra of the ordinary and extraordinary rays, calculated by subtracting the spectra measured before LWUV exposure from the spectra measured after 330 seconds of LWUV exposure, revealed broad absorption bands that imparted a brown

VISIBLE DIFFERENTIAL SPECTRA
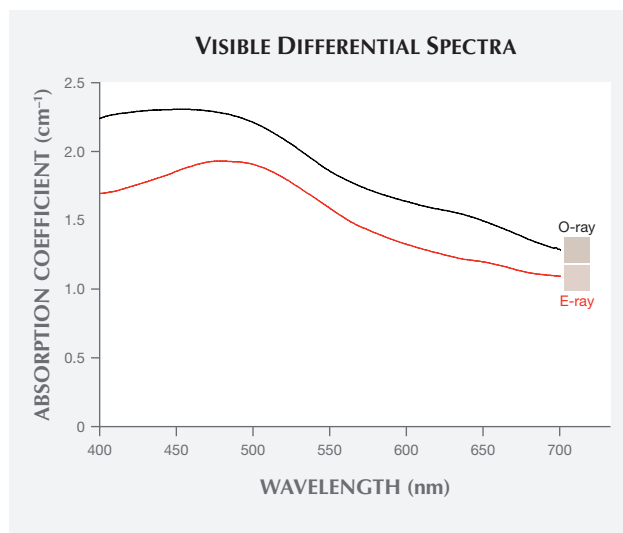
Figure 5. Differential spectroscopy was used to determine the absorption contribution of the LWUV-induced defect at maximum saturation. The author subtracted the original visible spectrum from the one measured after 330 seconds of LWUV exposure. The defect responsible for the brown color is primarily characterized by a broadband absorption centered at approximately 485 nm. The color swatches to the right of the plot lines were produced from the differential spectrum in each polarization to show the color contribution from the change in absorption spectra of the LWUV-induced defect alone.

component in both rays (figure 5). This explains the overall murky brown color observed in the faceted stones viewed face-up, where the o- and e-rays are mixed (again, see figure 2, right). After 330 seconds of exposure, there was effectively no change in the absorption measured, indicating complete saturation of the brown LWUV-induced defect.

Removing the LWUV-Induced Defect. To determine how long it should take to restore this sample's blue color using an incandescent light source, the blue zircon's visible spectrum was measured three times: in the initial state (red trace), after LWUV exposure (blue trace), and after incandescent light exposure (black trace) at a distance of 1 cm. The absorbance observed at 485 nm was then measured at regular 10-minute intervals until there was no further change in the absorbance. The data collected showed the decay of the brown color (figure 6), indicating complete reversal after approximately 20 minutes.

To confirm that the brown color could be completely removed, the visible spectrum taken before LWUV exposure was compared to the spectrum taken

BROWN COLOR DECAY AT 485 NM
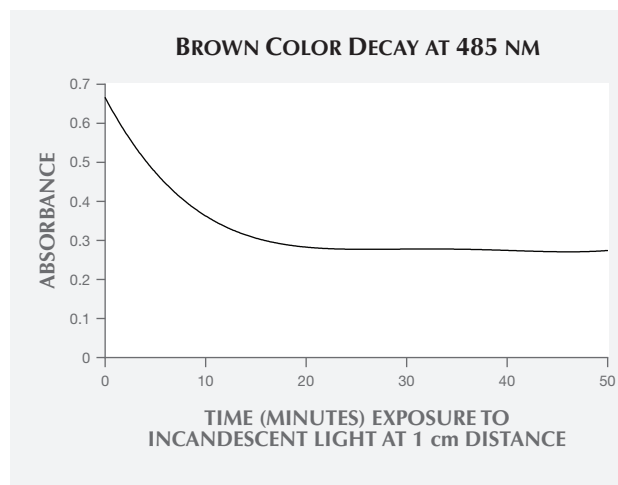
Figure 6. After saturation with the LWUV-induced brown defect, the sample was exposed to an approximately 22 W incandescent bulb at a distance of 1 cm. Plotting the absorption measured at 485 nm over 10-minute intervals shows a rapid initial decrease in absorbance and near-complete removal of the LWUV-induced brown color in just over 20 minutes.

after the color reversal by incandescent light. The two spectra were identical, proof that incandescent illumination can restore the material to its original state (figure 7). When the sample was left in a dark environment for one week after LWUV exposure, the brown color remained until the sample was once

Figure 7. These three visible spectra of the o-ray show the blue zircon sample at its initial state (red trace), after LWUV exposure (blue trace), and after one hour of exposure to incandescent light (black trace). Because the initial and final traces essentially overlay each other, we know the blue color has been completely restored and the induced brown color has been removed.

VISIBLE SPECTRA OF O-RAY COLOR MODIFICATION CYCLE
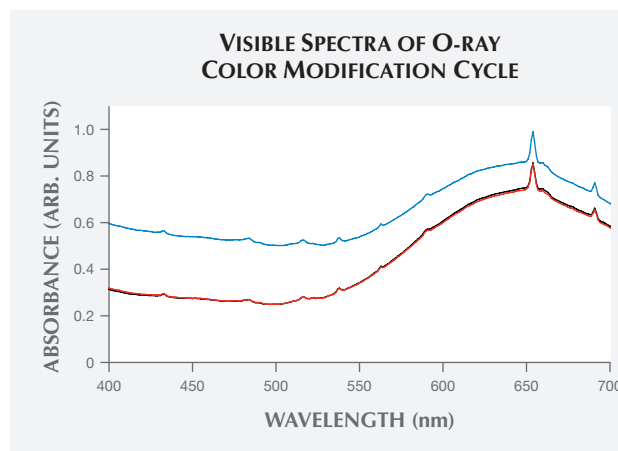
Figure 8. Brilliant and doubly refractive, blue zircon is a favorite among jewelry buyers. This 7.95 ct blue zircon ring designed by Loretta Castoro, also shown on the cover, is set in 18K white gold and contains 2.43 carats of rubies. Photo by Kevin Schumacher.

again exposed to the 22 W incandescent lamp. The sample was also placed near an incandescent light source, with all visible light blocked to see if the low-temperature radiant heat from the lamp would remove the brown color without interference from the light. Over one hour later, the brown color was still present in the sample. After the sample was returned to its blue state, it was also subjected to one minute of short-wave UV using a DiamondView instrument; no perceptible change in color occurred. Similar testing conducted on the 11 faceted stones yielded the same color change and reversal.

CONCLUSIONS

Blue zircon (figure 8) displays an interesting reversible color modification, with long-wave UV exposure turning the material brown in less than six minutes. In this study, the blue color was completely restored to all samples by exposing the stone to an incandescent source for about 20 minutes. Dealers should caution clients who purchase blue zircon to avoid LWUV sources. If such exposure does occur, they can inform their clients that the color change appears to be easily and completely reversible through the use of incandescent lighting.

ABOUT THE AUTHOR
Mr. Renfro is the analytical manager of the gem identification department, and microscopist of the inclusion research department, at GIA in Carlsbad, California.

REFERENCES

Koivula J.I., Misiorowski E., Eds. (1986) Gem News: Undesirable color change in blue zircon. *G&G*, Vol. 22, No. 2, pp. 188–189.

McClure S.F. (2011) Lab Notes: Tenebrescent zircon. *G&G*, Vol. 47, No. 4, pp. 314–315.

McClure S.F., Moses T.M., Koivula J.I. (2001) Gem News International: U.S. Postal Service irradiation process may affect some gemstones. *G&G*, Vol. 37, No. 4, pp. 326–328.

Renfro N.D. (2013) Reversible color modification of blue zircon by long wave ultraviolet radiation. *GSA Abstracts with Programs*, Vol. 45, No. 7, Abstract No. 226600.

Rossman G.R.(1981) Color in gems: The new technologies. *G&G*, Vol. 17, No. 2, pp. 60–71, http://dx.doi.org/10.5741/GEMS.17.2.60

Smith M., Balmer W. (2009) Gem News International: Zircon mining in Cambodia. *G&G*, Vol. 45, No. 2, pp. 152–154.

Thomas T. (2009) Corundum c-axis device for sample preparation. *GIA Ongoing Research*, June 8, http://www.gia.edu/ongoing-research/corundum-c-axis-device-for-sample-preparation

SAPPHIRES FROM THE SUTARA PLACER IN THE RUSSIAN FAR EAST

Svetlana Yuryevna Buravleva, Sergey Zakharovich Smirnov, Vera Alekseevna Pakhomova, and Dmitrii Gennadyevich Fedoseev

From 2009 to 2011, sapphire crystals and corundum-bearing rocks were discovered at Sutara, in the Jewish Autonomous Region of the Russian Far East. These sapphires are typically translucent to semitransparent and blue to pinkish blue. Most of the crystals are heavily included and display prominent growth zoning, twinning planes, and abundant exsolution lamellae. Their primary fluid inclusions contain diaspore crystals and a low-density CO_2-CH_4 mixture. These inclusions indicate that sapphire mineralization occurred by means of low-density aqueous-carbonic fluids, which were able to carry significant concentrations of alumina. These fluids may have formed as a result of thermal impact of granitic magma on carbonate country rocks. The authors consider Sutara a metamorphic occurrence that formed as a result of diffusive and metasomatic processes at a region of contact between carbonate rocks and pegmatite veins.

Sapphire deposits are widespread throughout Southeast Asia and Africa (Peretti et al., 2008; Schwarz et al., 2008; Shor and Weldon, 2009; Khoi et al., 2011; Dharmaratne et al., 2012). Russia's only placer deposit of gem-quality sapphire is at Nezametnoya (Pakhomova et al., 2006). Another Russian source of sapphire (figure 1) lies along the Sutara River, in the Jewish Autonomous Region bordering China (figure 2). The earliest discovery of corundum there came about as a result of gold mining (Shaposhnikov, 1945). In 1943, geologists discovered gray and blue sapphire fragments in the alluvium of the Sutara River, but they showed little interest because gold mining was more important at the time. Scientific studies of the sapphire's mineral associations, genesis, and gemological characteristics were not performed before the mine was closed in 2005.

From 2009 to 2011, the authors conducted field-work searching for gem-quality sapphire in the basin of the Sutara River. Corundum-bearing rock samples and sapphire crystals were discovered at the outer limits of the area (Pakhomova et al., 2009). Cabochon-grade sapphire from Sutara (figure 3) recently underwent gemological and mineralogical study at the Far East Geological Institute, Far Eastern Branch of the Russian Academy of Sciences (FEGI FEB RAS) in Vladivostok.

GEOLOGY AND OCCURRENCE

The bedrock of the Sutara mining region consists of early Cambrian siltstones, sandstones, gneiss, marbles, marbleized limestones, and crystal slates that

Figure 1. Sapphire fragments from Sutara ranging from 0.6 to 4.4 ct. Photo by Svetlana Buravleva.

Figure 2. The Sutara mine district is located in the Jewish Autonomous Region (Russian Far East), approximately 36 km (22 miles) southeast of the town of Obluche and about 200 km (124 miles) west of the city of Birobidzhan. Source: www.google.ru/maps.

interstratify with clay slates, carbonate, and graphitic rocks (figure 4). Intrusive rocks are present as biotite granites, biotite and tourmaline leucogranites, veins of granitic pegmatites, and aplites.

In Brief

- Between 2009 and 2011, the authors discovered sapphire crystals and corundum-bearing rocks in the Russian Far East.

- Primary (syngenetic) inclusions in the corundum consisted of diaspore crystals and a CO_2-CH_4 mixture.

- Low-density aqueous-carbonic fluids may have formed as a result of thermal impact of granitic magma on carbonate country rocks.

Early research by Shaposhnikov (1945) identified four sources of corundum in Sutara, two of which occur in carbonaceous rocks and in veins of intruding light-colored granites of a late Paleozoic complex. The others occur in terrigenous-carbonaceous rocks intruded by early Paleozoic granites.

Investigation of corundum mineralization (Shaposhnikov, 1945; Kovrizhnykh, 1993) showed that carbonate rocks contact with granites and pegmatites. Gray and light gray granites, medium- and

fine-grained, which are sometimes aplitic (figure 5), consist of microcline, microperthite, oligoclase, quartz, and biotite; muscovite is less common. Secondary minerals are zircon, apatite, magnetite, and titanite. Carbonate rocks in contact with granites became marble, and serpentinites developed in the exo-

Figure 3. These 14.07 and 14.52 ct sapphire cabochons are from Sutara, Russia. Photo by Svetlana Buravleva.

Figure 4. This simplified geologic map shows the primary and secondary (alluvial) sapphire occurrences discovered in the basin of the Sutara River. The basement is composed of metamorphosed carbonate rocks, intruded by granite and pegmatite. Adapted from Vaskin (1999).

contact zone. In the ophicalcites, forsterite-bearing bodies are present. Similar associations are found as xenoliths in granites.

Ophicalcites and serpentinites contain yellow forsterite, greenish phlogopite, tremolite, actinolite, and serpentine, sometimes creating ribboned structures. Secondary minerals of these rocks are calcite, talc, chlorite, and scapolite. Microscopic examina-

tion shows that the forsterite has been substantially converted to serpentine, which is present as fibrous chrysotile and needle-like antigorite.

Plagioclasites (anorthosites) formed thin veins (from a few centimeters to a few meters thick) in the serpentinites, filling a transitional zone from granites to ophicalcites. Plagioclasites consist primarily of white plagioclase (anorthite) aggregates with minor

Figure 5. Schematic cross-section I. This illustration shows the primary corundum occurrence within the contact between light-colored granites and marbles. Corundum plagioclasites consist of white plagioclase (anorthite), biotite, muscovite, and single sapphire crystals.

Legend (Figure 5):
- Marble
- Serpentinite (ophicalcite)
- Forsterite-bearing rock
- Microdiorite
- Light-colored granite
- Corundum plagioclasite

amounts of biotite and muscovite (about 5%). Sapphires occur as single translucent crystals of blue and pale purple color up to 1.5 cm in size, associated with plagioclase.

Bedrock exposures of corundum-bearing rocks (figure 6) were found in the Sutara district by Shaposhnikov in 1943. Here, two-mica granites break through quartz-micaceous slates with lenses of carbonate rocks. Within the contact of granites, a gradual transition from granites to pegmatites is observed. Carbonate rocks occur at a contact skarn that is defined by the presence of almandine (60%),

muscovite (30%), and epidote and chlorite (10%). In other sites outside the contact, the ophicalcites and serpentinites developed in a similar fashion.

On contact with carbonate rocks, pegmatites became desilicated and formed single well-formed bipyramidal crystals of corundum. Lenses ranging from 10 to 20 cm wide are visible, represented by near-monomineral varieties of corundum-bearing rocks with small amounts of margarite, vermiculite, and diaspore filling the interstices between the corundum crystals (figure 7).

The secondary (alluvial) sapphire occurrence was
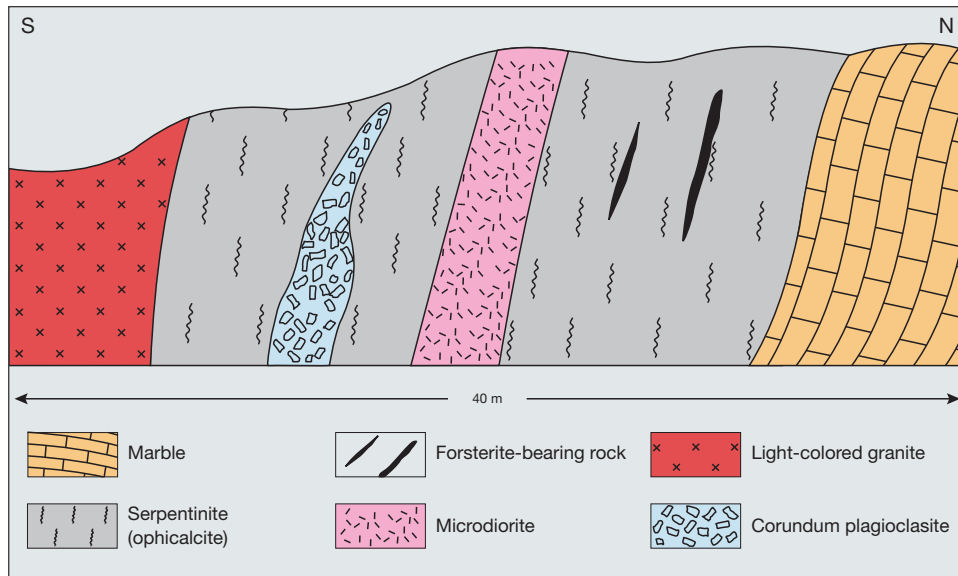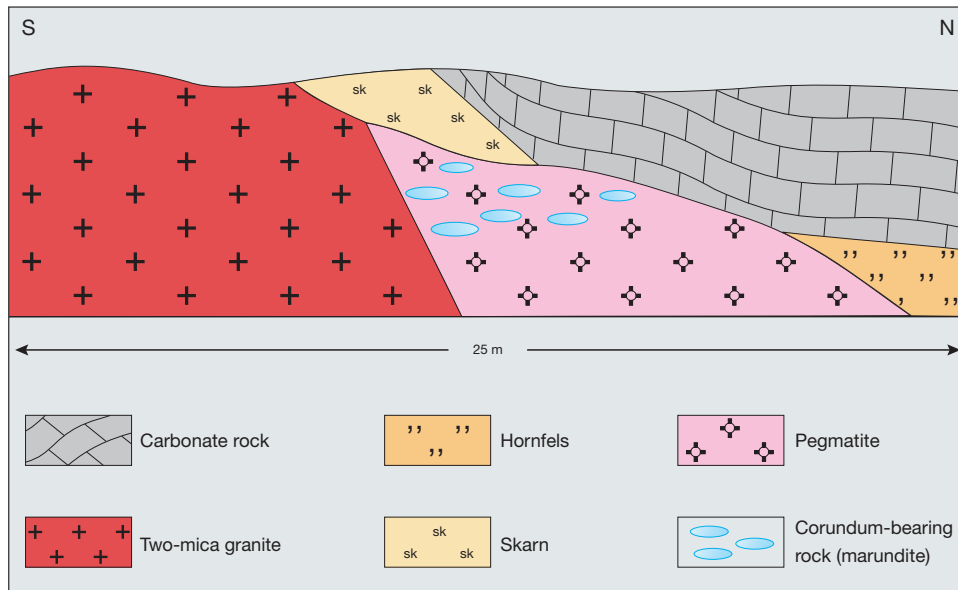

Figure 6. Schematic cross-section II. This illustration shows the primary corundum occurrence at the contact zone of pegmatite and carbonate rocks. Lenses of corundum-bearing rocks consist of brittle mica (margarite) between the corundum crystals.

Legend (Figure 6):
- Carbonate rock
- Two-mica granite
- Hornfels
- Skarn
- Pegmatite
- Corundum-bearing rock (marundite)

Figure 7. This corundum-bearing rock sample from Sutara (2.8 × 2.0 cm) contains 70–90% corundum; the remainder is mostly mica (margarite). Photo by Svetlana Buravleva.

discovered in the basin of the Sutara River. The alluvium consists of a sapphire- and garnet-bearing layer above the bedrock that contains sand, pebbles, and boulders.

MATERIALS AND METHODS

We examined 139 samples (primary and alluvial) collected during three visits to the Sutara mine between 2009 and 2011. These consisted of five cut sapphires (up to 65.5 ct; figures 8 and 17), 57 rough specimens (up to 33 ct), 34 windowed sapphires, 18 thin sections of corundum-bearing rocks, and 25 parallel plates of the corundum-bearing rocks cut and polished for spectroscopy.

Standard gemological testing was performed at the gemological laboratory of the FEGI FEB RAS. A refractometer was used to measure refractive index and birefringence. Fluorescence was observed with long- and short-wave UV lamps (365 and 254 nm, respectively) in a darkened room. We measured carat weights with Sartorius jewelry scales and determined specific gravity hydrostatically. Internal features were observed with a standard gemological microscope and a Nikon Eclipse LV100 POL polarizing microscope.

Inclusions in 17 samples were analyzed by Raman spectroscopy using a Horiba LabRAM HR 800 spectrometer coupled with a Si-based charge-coupled device (CCD) detector and a Melles Griot 514 nm Ar⁺ green laser. These analyses were performed at the V.S. Sobolev Institute of Geology and Mineralogy, Siberian Branch of the Russian Academy of Sciences (IGM SB RAS, Novosibirsk).

Quantitative chemical analyses on a total of 67 spots were carried out on seven parallel-plated sapphires and four corundum-bearing rocks using a JEOL JXA-8100 electron microprobe at the Primorye Shared Analytical Center for Local Elemental and Isotope Analysis in Vladivostok. Three wavelength-dispersive spectrometers with LIF, PET, TAP, and LDE2 crystal analyzers in the microprobe and an Inca energy-dispersive X-ray spectrometer were used. Analyses were performed under the following conditions: 20 kV accelerating voltage, 10 nA beam current, and 1 μm spot size. Detection limits for TiO_2 and Fe_2O_3 were 0.05 wt.%.

Trace element chemical data of seven alluvial sapphires were measured quantitatively by inductively coupled plasma–mass spectrometry (ICP-MS) at the Primorye Center using an Agilent 7500c mass spectrometer. Laser ablation was not used. Samples were melted with lithium metaborate ($LiBO_2$) on platinum melting pots. Detection limits were typically 0.01–0.05 parts per million by weight (ppmw) for the solid component. Calibration solutions for ICP-MS were prepared from multi-element certified solutions. For defined elements, the following isotopes were chosen: ^9Be, ^{45}Sc, ^{51}V, ^{52}Cr, ^{59}Co, ^{60}Ni, ^{63}Cu, ^{66}Zn, ^{71}Ga, ^{85}Rb, ^{88}Sr, ^{89}Y, ^{90}Zr, ^{93}Nb, ^{118}Sn, ^{133}Cs, ^{139}La, ^{140}Ce, ^{141}Pr, ^{146}Nd, ^{181}Ta, ^{232}Th, ^{182}W, and ^{208}Pb. The plasma conditions of the ICP-MS were optimized to an intensity of CeO/Ce 156/140<0.750% and Ce++/Ce+ 70/140<2%. This was achieved using the following parameters: plasma gas flow (Ar) of 15.0 liters per

Figure 8. This 2.22 ct sapphire cabochon is one of the samples from Sutara. Photo by Svetlana Buravleva.
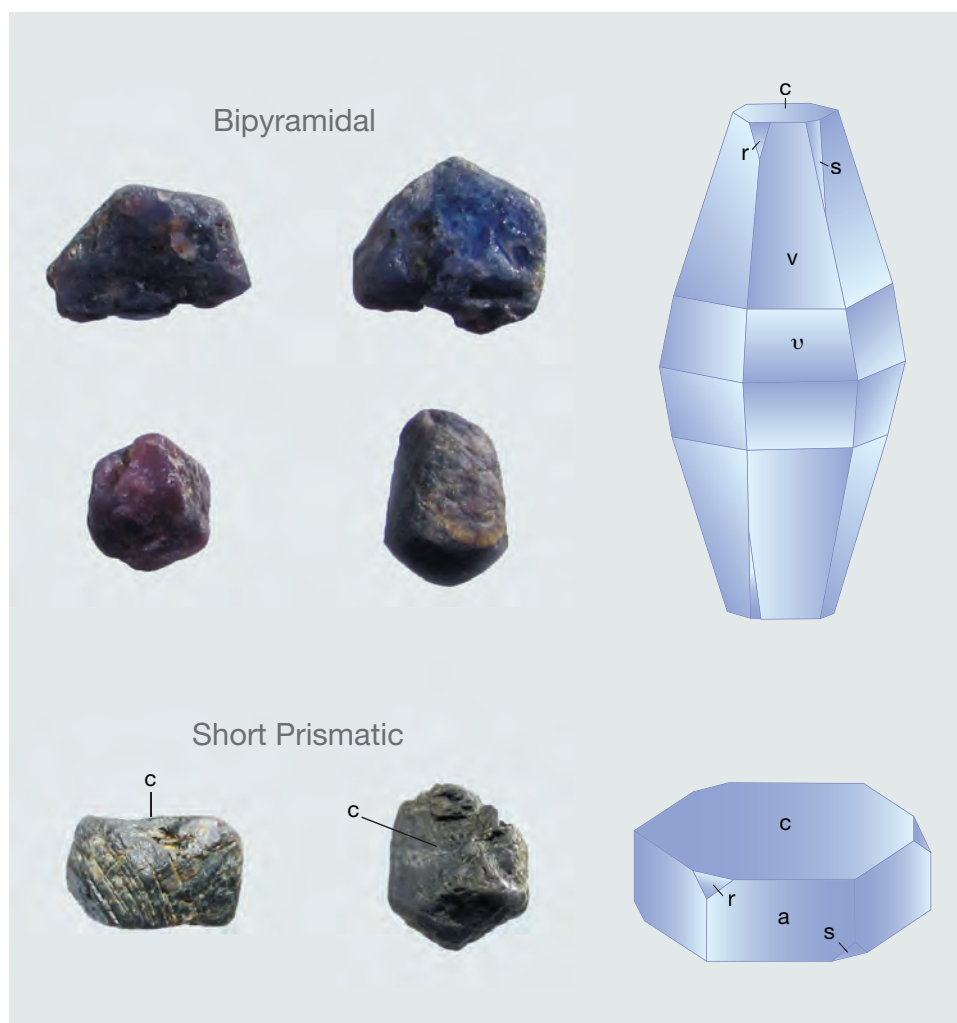
Figure 9. These Sutara sapphire crystals show bipyramidal (four samples) and short prismatic (one sample) forms. The bipyramidal crystals are dominated by υ faces with various combinations of c, r, s, and v; they do not show a faces. The short prismatic forms consist of various combinations of c, a, r, and s faces (Schwarz et al., 2008). Photos by Svetlana Buravleva.

minute, nebulizer gas flow (Ar) of 1.14–1.19 liters per minute, and auxiliary gas flow (Ar) of 1.0 liter per minute. Sensitivity was tuned using Agilent tuning solution, containing 10 mg/l ^{140}Ce, ^{59}Co, ^{7}Li, ^{205}Tl, and ^{89}Y. The background signal was controlled by measuring the signal intensity of ^{45}Sc in Agilent tuning solution, since scandium is absent in it. The intensity of the ^{45}Sc signal was <70 counts per second, with an integration time of 0.1 seconds.

Elemental analyses of five alluvial sapphires were measured quantitatively by inductively coupled plasma–atomic emission spectroscopy (ICP-AES) at the Primorye Center using an iCAP 6500 Duo spectrometer. This instrument combines an Echelle optical spectrometer with a semiconductive CID detector and a system for radial and axial observations of a plasma charge. Detection limits in the solution were typically 0.01–0.07 ppm (Al = 0.07, Ti = 0.002, Fe = 0.005, Ca = 0.011, Mg = 0.012, Mn = 0.001, K = 0.031,

Na = 0.128, P = 0.053). For the determination of aluminum, we used a multivariate calibration solution of aluminum; to determine the remaining elements, we used Merck Certipur ICP multi-element standard solution IV as well as multi-element calibration standard-4. The material was carried to the ICP by Ar gas with the following parameters: plasma gas flow (Ar) of 12.0 liters per minute, nebulizer gas flow (Ar) of 0.6 liters per minute, auxiliary gas flow (Ar) of 0.5 liters per minute, and RF power of 1150 W. Sensitivity was again tuned using Agilent tuning solution.

GEMOLOGICAL PROPERTIES

Alluvial sapphires from Sutara are found as euhedral bipyramidal crystals or broken pieces, some weighing more than 65 ct. They display bipyramidal or short barrel habits, mainly with a combination of hexagonal prism a and basal pinacoid c faces (figure 9). Most bipyramidal crystal fragments showed υ and

TABLE 1. Gemological characteristics of sapphires from Sutara, Russia.

Property	Gray sapphires from type 1 corundum-bearing rock	Blue sapphires from type 2 corundum-bearing rock	Alluvial sapphires
Color	Colorless, gray, bluish gray, and black	Colorless, blue, and bluish white	Blue, gray, bicolored pink and blue, violetish blue, and purplish pink
Color zoning	Irregular gray and white color patches	Irregular blue and white color patches	Strong color zoning is common. Some have patches of pink and blue colors.
Refractive Indices	n_o = 1.768–1.770 n_e = 1.760–1.762	n_o = 1.767–1.770 n_e = 1.759–1.762	n_o = 1.768–1.770 n_e = 1.758–1.760
Birefringence	0.008	0.008	0.010
Specific gravity	3.98–4.00	3.98–4.00	3.98–4.02
Optic character	Uniaxial negative	Uniaxial negative	Uniaxial negative
Fluorescence[a]	Inert to both LW and SW	Inert to both LW and SW	*Blue, gray, bicolored pink and blue, and violetish blue:* Inert to both LW and SW *Purplish pink:* LW: Moderate to strong red SW: Inert to weak red
Internal features	• Rutile needles, plagioclase, margarite, ilmenite, spinel, and pyrrhotite • Primary and secondary liquid-gas inclusions • Growth zoning, parting, fractures, and lamellar twinning	• Rutile needles, plagioclase, apatite, xenotime, muscovite, margarite, and boehmite • Primary and secondary liquid-gas inclusions • Growth zoning, parting, fractures, and lamellar twinning	• Rutile needles, zircon, biotite, monazite, xenotime, plagioclase, ilmenite, pyrite, and spinel • Primary and secondary liquid-gas inclusions • Growth zoning, parting, fractures, lamellar twinning, and trapiche stars

[a]LW = long-wave ultraviolet radiation, SW = short-wave ultraviolet radiation

v faces. We observed *c* in combination with *r* and *s* faces. In the short prismatic crystals, basal pinacoid *c* and hexagonal prism *a* were dominant, with small *r* and *s* faces. Almost all of these crystals were characterized by polysynthetic twinning observed with a microscope. The colors observed ranged from blue, gray, bicolored pink and blue, violetish blue, yellowish, and purplish pink, varying in tone from very light to dark (again, see figure 1).

Some of the sapphires demonstrated strong dichroism. The samples' clarity ranged from semi-transparent to translucent and opaque. Their color pattern was often zoned and spotty (figure 10). Some of the gray samples showed silky patches and six-rayed trapiche-like patterns with oriented micro-inclusions, particularly rutile needles (figure 11).

The corundum-bearing rocks are classified here as type 1 and type 2 (table 1). Type 1 contains opaque gray, bluish gray, and black sapphire crystals; type 2

consists of blue and white zoned sapphire crystals (see figure 12). Both types are represented by almost monomineral varieties consisting of 70–90% sapphire crystals exhibiting a hexagonal prism shape.

Mineral Inclusions. The alluvial sapphires contained various mineral inclusions such as rutile, zircon, biotite, monazite, xenotime, plagioclase, ilmenite, pyrite, and spinel. Zircon, rutile, and biotite were the most common. These inclusions were identified by both Raman spectroscopy and electron microprobe analysis. Rutile usually occurred as short, dark three-dimensional networks of oriented needles (figure 13) or slightly brown irregular forms. Biotite occurred as single dark brown tabular crystals up to 70 μm in size.

Zircon inclusions were transparent, well-developed prismatic crystals measuring up to 30 μm, clustered in groups or compact agglomerations. Monazite occurred in irregular, slightly rounded forms up to 20
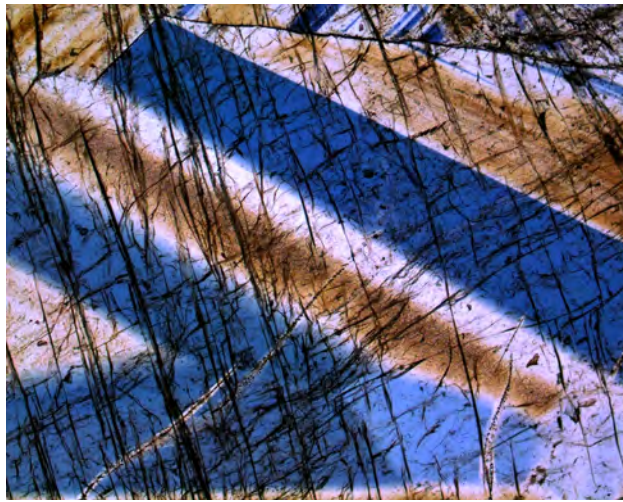
Figure 10. Multiple directions of growth zoning are often found in the Sutara sapphires. Photomicrograph by Svetlana Buravleva; transmitted light, field of view 1.10 mm.

Figure 11. This 7.2 ct sapphire with a trapiche-like pattern clearly displays the host's hexagonal symmetry (11.6 × 8.0 mm). Photo by Svetlana Buravleva.

μm in size. They were colorless, transparent, and associated with zircon crystals. Xenotime crystals up to 100 μm were transparent and nearly colorless, while others were slightly green. They were associated with zircon and monazite crystals (figure 14, left).

Plagioclase, identified by Raman spectrometry, was observed as well-developed transparent crystals (figure 14, center). Electron microprobe analysis established that the plagioclase corresponded to andesine in composition.

Spinel was a rare mineral inclusion. Identified by electron microprobe as small Fe- and Mg-rich inclusions up to 10 μm in size, it was not visible during microscopic examination of the samples.
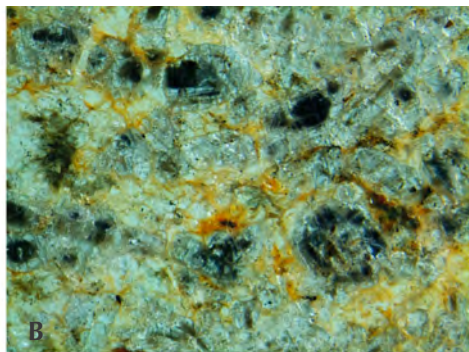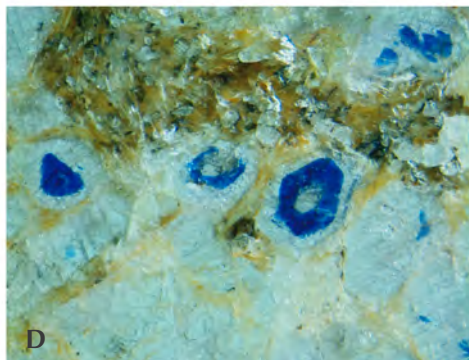
Figure 12. Corundum-bearing rocks, with mica filling the interstices between sapphire crystals, are represented by two types. Top: the first type 1 sample (left) and a parallel plate cut from it (right). Bottom: the second type 2 sample and the parallel plate cut from it. Photos and photomicrographs by Svetlana Buravleva; photomicrograph field of view 11 mm.

Figure 13. An example of oriented rutile needles in the Sutara sapphires. Photomicrograph by Svetlana Buravleva; field of view 0.55 mm.

In general, the primary and alluvial samples showed a similar range of mineral inclusions. Corundum from the primary occurrence also contained pyrrhotite (type 1), apatite, muscovite, and rarely boehmite (type 2).

Fluid Inclusions. Fluid inclusions in sapphires from primary and alluvial occurrences are similar. The study of syngenetic inclusions makes it possible to obtain accurate information on the conditions of mineral crystallization.

TABLE 2. Electron microprobe analyses (in wt.%) of two sapphires from the primary occurrence at Sutara, Russia.

Oxide	Type 1[a]	Type 2[b]
Al_2O_3	98.30 ± 0.16	98.78 ± 0.19
Fe_2O_3	0.65 ± 0.28	bdl[c]
TiO_2	bdl	0.22 ± 0.04
Total	**98.95**	**99.00**

[a]*Corundum-bearing rock with gray sapphires.*
[b]*Corundum-bearing rock with blue sapphires.*
[c]*bdl = below detection limit.*
Detection limits for TiO_2 and Fe_2O_3 are 0.05 wt.%.

Primary (syngenetic) inclusions (figure 14, right) were analyzed by Raman spectrometry. They consisted of diaspore, with a very strong peak at 448 cm^{-1}; carbon dioxide, with peaks at 1284 and 1387 cm^{-1}; and methane, with a 2914 cm^{-1} peak (figure 15). The molecular ratios of carbon dioxide and methane were 0.989 and 0.011, respectively. Diaspore also occurs as the solid phase in three-phase inclusions, as in Sri Lankan sapphire (Schmetzer and Medenbach, 1988). Primary and secondary gas-liquid fluid inclusions were encountered frequently. Gas in the form of carbon dioxide showed peaks at 1284 and 1385 cm^{-1}.

Chemical Composition. In sapphires from corundum-bearing rocks, electron microprobe analyses revealed concentrations of the chromophores Ti and Fe. Gray sapphires had an Fe_2O_3 concentration of approximately 0.37–0.93 wt.% (table 2). Blue sapphires contained Fe_2O_3 below the detection limit of 0.05 wt.%.

**TABLE 3.** Chemical composition by ICP-AES (in wt.%) of alluvial sapphires from Sutara, Russia.

Oxide	Pink		Blue		
	C-2	C-3	C-6	C-7	C-8
Al_2O_3	98.65	91.10	97.30	98.25	91.15
TiO_2	0.09	0.08	0.09	0.07	0.10
Fe_2O_3	1.15	1.31	1.14	1.09	1.22
CaO	0.11	0.16	0.13	0.10	0.17
MgO	0.09	0.13	0.11	0.09	0.14
MnO	0.01	0.02	0.01	0.01	0.02
K_2O	0.46	0.62	0.54	0.43	0.66
Na_2O	0.36	0.51	0.42	0.36	0.56
Total	**100.94**	**93.94**	**99.75**	**100.45**	**94.05**

Note: Detection limits in the solution are typically 1×10^{-6} to 7×10^{-6} wt.% (0.01–0.07 ppm).
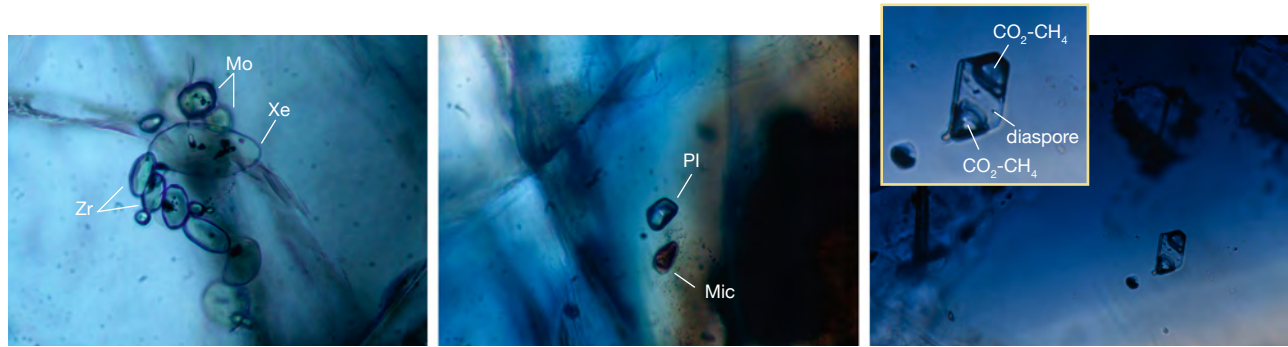
Figure 14. Left: Monazite (Mo), zircon (Zr), and xenotime (Xe) in the Sutara sapphires. Center: Transparent plagio-clase (Pl) and mica (Mic) in the Sutara sapphires. Right: These primary fluid inclusions in sapphire contain diaspore crystals and a low-density CO_2-CH_4 mixture. Photomicrographs by Svetlana Buravleva; field of view 0.22 mm.

In the blue sapphires, the TiO_2 concentration was approximately 0.11–0.26 wt.%. Type 1 gray sapphires from the primary occurrence had TiO_2 below the detection limit.

TABLE 4. Trace element composition (in ppmw) of alluvial sapphire from Sutara, Russia, measured by ICP-MS.

Trace element	Pink			Gray	Blue		
	C-1	C-2	C-3	C-5	C-6	C-7	C-8
Be	0.28	0.12	0.08	0.60	0.06	0.07	0.10
Sc	2.40	0.99	1.96	1.62	1.92	1.42	1.99
V	36.49	37.71	61.58	34.99	32.37	36.85	42.30
Cr	203.50	202.10	260.90	209.90	181.90	201.20	220.60
Co	0.71	0.55	0.77	0.38	0.58	0.45	0.85
Ni	5.13	2.11	2.43	2.87	1.75	2.33	3.99
Cu	bdl	bdl	bdl	bdl	bdl	bdl	bdl
Zn	16.10	18.73	13.95	34.94	16.90	10.08	8.60
Ga	69.09	74.57	93.47	75.69	76.57	73.52	75.32
Rb	7.78	5.64	8.23	5.84	4.75	5.44	8.20
Sr	9.42	8.47	10.65	8.15	11.81	8.11	11.49
Y	23.67	16.68	36.89	5.61	14.50	43.60	48.06
Zr	96.11	69.27	134.20	44.32	150.00	245.80	187.70
Nb	0.63	0.40	0.70	0.45	1.02	0.64	0.89
Sn	0.82	1.89	4.88	1.89	0.52	0.01	0.07
Cs	1.24	0.08	0.09	0.42	0.09	0.08	0.09
Ba	132.30	97.24	153.00	106.80	120.30	100.90	155.00
La	18.57	22.40	24.12	2.40	17.35	32.35	42.04
Ce	40.87	46.58	50.49	4.70	38.50	69.39	90.59
Pr	4.89	5.57	6.09	0.64	4.68	7.88	10.57
Nd	19.28	21.06	23.59	3.04	17.96	30.44	41.87
Ta	0.20	0.51	0.13	0.53	0.06	0.44	2.18
W	0.44	0.33	0.47	0.52	1.10	0.50	1.51
Pb	4.43	8.96	6.92	9.98	4.60	3.82	3.67
Th	6.28	7.77	8.07	1.22	7.86	13.57	13.89

Note: bdl = below detection limit. Detection limits are typically 0.01–0.05 ppmw for the solid component.

RAMAN SPECTRA
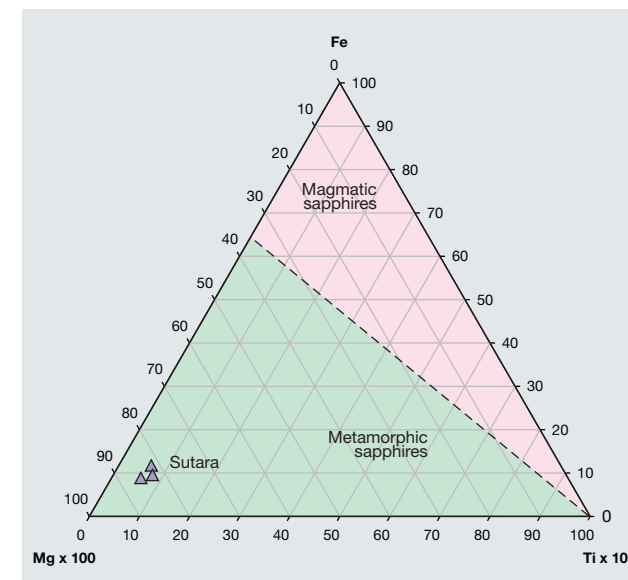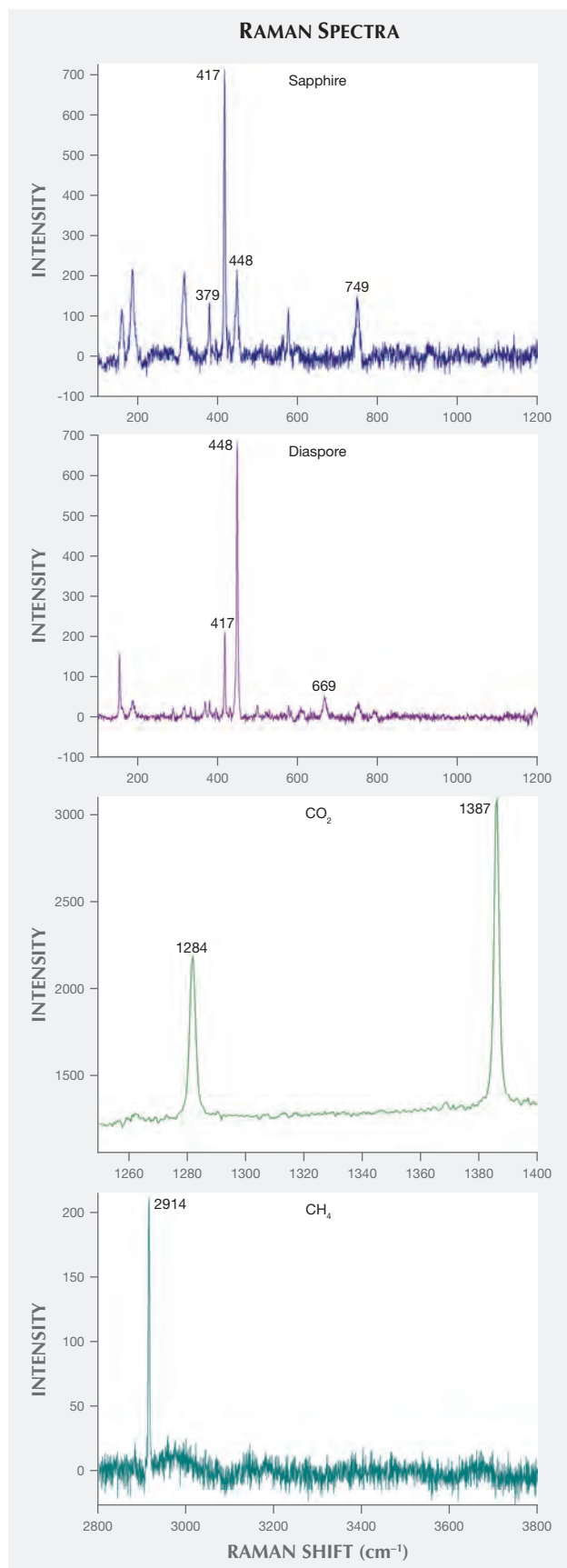
Figure 16. This ternary diagram shows the relative percentages of the elements Fe, Mg, and Ti (in ppmw) in blue alluvial sapphires from Sutara. Modified from Peucat et al. (2007).

Both the pink and blue alluvial sapphires had a relatively high Fe_2O_3 concentration, ranging from 1.09 to 1.31 wt.% (table 3). Their TiO_2 concentration ranged from 0.07 to 0.10 wt.%.

ICP-MS data of trace elements in the alluvial sapphires are shown in table 4. Cr was abundant, with concentrations above 200 ppm (0.02 wt.%). The V concentration was generally low, from 32 to 61 ppm. Ga content ranged from 69 to 93 ppm. The detection limit was 0.01–0.05 ppm. Gray sapphire had the lowest concentrations of most trace elements.

Trace element chemical data of alluvial sapphires measured by ICP-MS revealed high concentrations, compared to sapphire in general, of Zr (44.32–245.80 ppmw), Cr (181.9–260.9 ppmw), Th (1.22–13.89 ppmw), La (2.40–42.04 ppmw), Ce (4.7–90.59 ppmw), Nd (3.04–41.87 ppmw), Y (5.61–48.06 ppmw), V

Figure 15. Raman spectra of the primary syngenetic inclusion in sapphire in figure 14, right. The sapphire host displayed a peak at 417 cm⁻¹, while the primary inclusion consisted of a diaspore crystal with a peak at 448 cm⁻¹, carbon dioxide (CO_2) with peaks at 1284 and 1387 cm⁻¹, and methane (CH_4) with a peak at 2914 cm⁻¹. Raman spectra were collected with a 514 nm laser.

(32.37–61.58 ppmw), and Pr (0.64–10.57 ppmw). Many of these trace elements might be the result of contamination by inclusions.

DISCUSSION

Peucat et al. (2007) showed that differences in the composition of trace elements exist between magmatic and metamorphic corundum. He developed Fe-Mg-Ti diagrams, which also separate magmatic and metamorphic fields based on contrasting Fe/Mg ratios (figure 16). High Mg values are found in metamorphic sapphires only. Concentrations of Mg, Ti, and Fe (table 3) in the blue alluvial sapphires indicated metamorphic origin of Sutara corundum. Sapphires from Sutara plot in the metamorphic field. Their high Mg content is in agreement with the high Mg content of the carbonate rocks.

The geochemical characteristics of this corundum from Sutara are high total rare earth element (REE) contents and enrichment with Ba, Rb, and Sr compared to sapphires in general (Peretti et al., 2008). Thus, the main factor in the formation of this corundum mineralization is deep fluids enriched by Al, Ti, Zr, Ba, Sr, V, Cl, and REE.

Sapphires from the primary and alluvial occurrences at Sutara have similar inclusions. The syngenetic inclusions' composition can be determined using Raman spectrometry. These inclusions contain diaspore crystals and a low-density CO_2-CH_4 mixture. This fluid supposedly formed as a result of thermal impact of granitic magma on carbonate country rocks. Primary and secondary gas-liquid fluid inclusions were encountered frequently in this study, with gas present as carbon dioxide. These inclusions indicate that sapphire mineralization occurred with the participation of low-density aqueous-carbonic fluids, which carried significant concentrations of alumina. This alumina can be sufficient for sapphire crystallization.

The paragenetic sequence of the inclusions is plagioclase, diaspore, and margarite. Diaspore and margarite formed after the retrograde hydration of corundum and the plagioclase, respectively. Corundum forms through a metasomatic process of desilication. The interaction between the pegmatites and the dolomite-containing carbonates at moderate temperatures, together with the participation of aqueous-carbonic fluid, caused this desilication.

The formation of large sapphire crystals in the corundum-bearing rocks at Sutara could result from the recrystallization of early plagioclase-corundum associations when plagioclase was substituted by margarite.

Figure 17. This silver pendant contains a 65.5 ct sapphire cabochon from Sutara. Photo by Svetlana Buravleva, courtesy of A. Kurnosov.

CONCLUSIONS

The Nezametnoye deposit is Russia's only placer deposit of jewelry-grade corundum, and the Russian jewelry market must therefore rely on sapphires and rubies from other parts of the world, most of which are treated by a variety of methods. This shortage of domestic material has prompted geologists to investigate localities previously considered unpromising. Corundum crystals were discovered in the Sutara gold mining district of the Russian Far East in 1943, but scientific studies were not carried out until recently, when the authors conducted field research in the area. We found alluvial blue, gray, bicolored pink and blue, violetish blue, and purplish pink cabochon-grade sapphires, along with corundum-bearing rocks. Sapphires—both alluvial and from corundum-bearing rocks—often feature blue and white zones. Some finished samples are more than 65 carats; most of the

crystals are heavily included with rutile needles, zircon, and biotite.

This corundum mineralization formed as the result of contact between pegmatite veins and dolomite-containing carbonate rocks, with the participation of aqueous-carbonic fluid. While only cabochon-grade material (figures 3 and 17) was found in the Russian Far East pegmatite veins, carbonaceous rocks and products of their metamorphism with sapphire-bearing potential are widely distributed. This presents further prospects of finding new sapphire occurrences in the future.

ABOUT THE AUTHORS

Ms. Buravleva (s_buravleva@yahoo.com) is a gemologist, Dr. Pakhomova is a senior researcher in geology, and Mr. Fedoseev is an engineer at the Far East Geological Institute, Far Eastern Branch of the Russian Academy of Sciences (FEGI FEB RAS) in Vladivostok. Dr. Smirnov is senior researcher in geology at the V.S. Sobolev Institute of Geology and Mineralogy, Siberian Branch of the Russian Academy of Sciences (IGM SB RAS) in Novosibirsk.

REFERENCES

Dharmaratne P.G.R., Premasiri H.M.R., Dillimuni D. (2012) Sapphires from Thammannawa, Kataragama Area, Sri Lanka. *G&G*, Vol. 48, No. 2, pp. 98–107, http://dx.doi.org/10.5741/GEMS.48.2.98

Khoi N.N., Sutthirat C., Tuan D.A., Nam N.V., Thuyet N.T.M., Nhung N.T. (2011) Ruby and sapphire from the Tan Huong–Truc Lau Area, Yen Bai Province, northern Vietnam. *G&G*, Vol. 47, No. 3, pp. 182–195, http://dx.doi.org/10.5741/GEMS.47.3.182

Kovrizhnykh Y.B. (1993) Corundum formations of the Russian Far East. Report on fieldwork results for corundum. *Far East Geological Department,* Vol I, pp. 34–41.

Pakhomova V., Zalishchak B., Tishkina V., Lapina M., Karmanov N. (2006) Mineral and melt inclusions in sapphires as an indicator of conditions of their formation and origin (Primorsky Region of the Russian Far East). *The Australian Gemmologist*, Vol. 22, No. 11, pp. 508–511.

Pakhomova V., Buravleva S., Kurnosov A., Zalishchak B., Tishkina V., Fedoseev D., Zharchenco S., Mouzhevsky D., Ushkova M. (2009) Corundums and Marundites of the Sutara deposit (The Russian Far East). *The Journal of the Gemmological Association of Hong Kong*, Vol. 30, pp. 47–49.

Peretti A., Peretti F., Kanpraphai A., Bieri W.P., Hametner K., Günther D. (2008) Winza rubies identified. *Contributions to Gemology*, No. 7, Second Edition. GRS Gemresearch Swisslab, Switzerland, 97 pp.

Peucat J.J., Ruffault P., Fritsch E., Bouhnik-Le Coz M., Simonet C., Lasnier B. (2007) Ga/Mg ratio as a new geochemical tool to differentiate magmatic from metamorphic blue sapphires. *Lithos*, Vol. 98, pp. 261–274, http://dx.doi.org/10.1016/j.lithos.2007.05.001

Schmetzer K., Medenbach O. (1988) Examination of three-phase inclusions in colorless, yellow, and blue sapphires from Sri Lanka. *G&G*, Vol. 24, No. 2, pp. 107–111, http://dx.doi.org/10.5741/GEMS.24.2.107

Schwarz D., Pardieu V., Saul J.M., Schmetzer K., Laurs B.M., Giuliani G., Klemm L., Malsy A-K., Erel E., Hauzenberger C., Du Toit G., Fallick A.E., Ohnenstetter D. (2008) Rubies and sapphires from Winza, Central Tanzania. *G&G*, Vol. 44, No. 4, pp. 322–347, http://dx.doi.org/10.5741/GEMS.44.4.322

Shaposhnikov E.Y. (1945) Corundum mineralization of the Sutara mine. Report on fieldwork results for corundum in 1943 and 1944 in the Sutara Mine district (Birsky Region of the Jewish Autonomous District of the Khabarovsky Krai). *Far East Geological Department,* 103 pp.

Shor R., Weldon R. (2009) Ruby and sapphire production and distribution: A quarter century of change. *G&G*, Vol. 45, No. 4, pp. 236–259, http://dx.doi.org/10.5741/GEMS.45.4.236

Vaskin A.F. (1999) State geological map of the Russian Federation. 1: 200 000, VSEGEL, St. Petersburg, 196 pp.

GEMS & GEMOLOGY

CONGRATULATIONS

This year, hundreds of readers participated in the 2016 *Gems & Gemology* Challenge. Entries arrived from around the world, as readers tested their gemological knowledge by answering questions listed in the Spring 2016 issue. Those who earned a score of 75% or better received a GIA Certificate of Completion recognizing their achievement. The participants who scored a perfect 100% are listed below.

G&G Challenge Winners

Australia
Barbara Wodecki

Canada
Diane Gauthier

Italy
Chiara Piussi

United States
Andrea Blake

Lisa A. Marsh-Vetter

Paul Mattlin

Daniel Novak

Lydia Pringle

Jana Smith

Abba Steinfeld

Starla Turner

Clifton Young

Answers

See pages 66–67 of the Spring 2016 issue for the questions.

1 (d), 2 (a), 3 (c), 4 (b), 5 (a), 6 (c), 7 (d), 8 (b), 9 (c), 10 (d), 11 (b), 12 (c), 13 (a), 14 (a), 15 (b), 16 (d), 17 (a), 18 (d), 19 (c), 20 (b), 21 (d), 22 (a), 23 (c), 24 (b), 25 (a)

A New Deposit of Gem-Quality Grandidierite In Madagascar

Delphine Bruyère, Claude Delor, Julien Raoul, Rufin Rakotondranaivo, Guillaume Wille, Nicolas Maubec, and Abdeltif Lahfid

A new deposit of grandidierite, considered one of the world's rarest gems, has been discovered in southern Madagascar. The new deposit is outside the town of Tranomaro, near the original locality of Andrahomana. It occurs in the form of strong bluish green to greenish blue translucent to transparent crystals measuring up to 15 × 7 × 3 cm. Grandidierite is the magnesium end member in the solid-solution series with ominelite as the iron end member. The studied samples have a very low Fe/(Mg + Fe) ratio. This confirms that the Tranomaro deposit, together with Johnsburg in New York State, provides the purest grandidierite ever found. The crystals host inclusions of Cl-apatite, zircon, and monazite. The paragenesis also includes plagioclase, phlogopite, enstatite, diopside, dravite, and sapphirine (locally as gem-quality crystals). Transparent crystals have been faceted, yielding small but eye-clean jewelry-quality gems.

Named after French naturalist Alfred Grandidier (1836–1912), grandidierite is an extremely rare orthorhombic Mg-Fe aluminous borosilicate with the formula $(Mg,Fe)Al_3(BO_3)(SiO_4)O_2$ (Lacroix, 1902, 1922a,b). The material was first discovered at the cliffs of Andrahomana, on the southern coast of Madagascar. Grandidierite is described as a bluish green to greenish blue mineral (figure 1); the blue component increases with Fe content. It is transparent to translucent with a pale yellow to colorless, greenish blue, and blue trichroism. The larger elongate euhedral orthorhombic crystals, which may measure up to 8 cm, are often strongly corroded.

Since its discovery, grandidierite has been found as a rare accessory mineral in aluminous boron-rich pegmatite; in aplite, gneiss, and crystalline rock associated with charnockite; and in rock subjected to local high-temperature, low-pressure metamorphism (contact aureoles and xenoliths). In addition to Madagascar, it has been reported from New Zealand (Black, 1970), Norway (Krogh, 1975), Suriname (de Roever and Kieft, 1976), Algeria (Fabriès et al., 1976), Italy (van Bergen, 1980), Malawi (Haslam, 1980), India (Grew, 1983), the United States (Rowley, 1987; Grew et al., 1991), Canada (Lonker, 1988), Antarctica (Carson et al., 1995), the Czech Republic (Cempírek et al., 2010), and other localities. Yet gem-quality grandidierite is extremely rare. Facetable gem material larger than a millimeter has only been found in Madagascar and Sri Lanka; the latter is the source of a clean faceted specimen weighing 0.29 ct (Schmetzer et al., 2003).

Figure 1. This 0.11 ct round brilliant grandidierite is from a new deposit near the town of Tranomaro, in southern Madagascar. Photo by Delphine Bruyère.
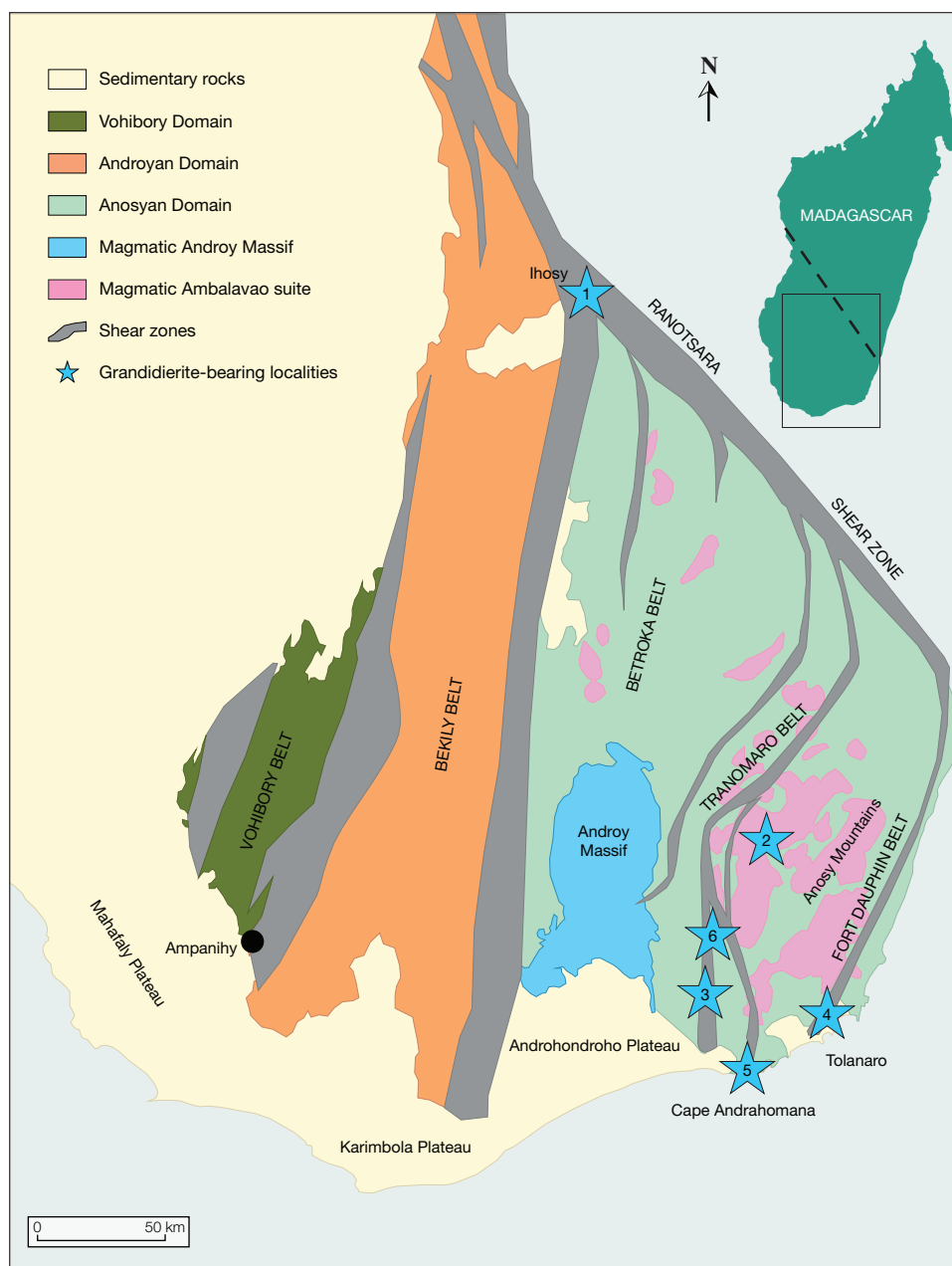
Figure 2. A map of Madagascar south of the Ranotsara shear zone showing the location of grandidierite-bearing deposits. 1: Ihosy, 2: Esira, 3: Vohibola, 4: Nampoana, 5: Andrahomana, 6: Tranomaro (this study). Modified after Razakamanana et al. (2010) and Roig et al. (2012).

The type locality described by Lacroix (1902) was visited in 1960 by C. Mignot, who was unable to find additional grandidierite at the site (Béhier, 1960a,b), as the small pegmatite was depleted. Since then, grandidierite has been reported in a few other localities in southern Madagascar that have also since been depleted. The present study focuses on a new deposit discovered in May 2014 near Tranomaro, close to the original locality of Andrahomana (figure 2). The aim of this study is to determine the material's properties and to evaluate its gem potential.

GEOLOGICAL BACKGROUND

The crystalline bedrock of Madagascar is described in terms of six geodynamic blocks that define the constituent elements of the Precambrian Shield; these are, from southwest to northeast, the Vohibory, Androyan-Anosyan, Ikalamavony, Antananarivo, Antongil-Masora, and Bemarivo domains. As the result of a major five-year (2007–2012) study funded by the World Bank, the Precambrian geology of Madagascar has been reinterpreted. The Antongil-Masora and Antananarivo domains are now considered part

of an even larger craton—the Greater Dharwar craton—that encompassed part of present-day India and Madagascar and was consolidated approximately 2.45–2.5 billion years ago (Tucker et al., 2012). The Ranotsara shear zone marks the approximate boundary between the Archean crust to the north and a more recent basement to the south. The Androyen-Anosyen domain of southern Madagascar is indeed a continental terrane of Paleoproterozoic age (1.8–2.0 billion years ago). It was accreted to the Vohibory domain, an oceanic terrane of early Neoproterozoic age, in Cryogenian time (about 0.62–0.64 billion years ago). A first deformation (600–650 Ma) gave rise to recumbent isoclinal folds and a regional shallow-dipping foliation, with a second deformation (500–530 Ma) producing steep north-south-trending shear zones that separate five gneissic tectonic belts. The last episode of Madagascar's Neoproterozoic geodynamic evolution is marked by the alkaline magmatism of the Ambalavao suite, which forms major batholitic intrusions (up to 1400 km²). Numerous pegmatitic vein intrusions associated with this episode are directly related to gem and rare earth element (REE) mineralization. A final magmatic activ

In Brief

- A new deposit of gem-quality grandidierite was discovered in May 2014 in southern Madagascar.
- The very low Fe/(Mg + Fe) ratio makes these crystals, together with samples from Johnsburg in New York State, the purest grandidierite ever found.
- The ratio of gem-quality crystals is about 1 in 10,000.
- A few dozen rough transparent crystals have been faceted, yielding small but eye-clean jewelry-quality gems, including fewer than 10 that are above 1 carat.

ity during the Cretaceous period is expressed by the megavolcanic Androy Massif.

A grandidierite-bearing pegmatite is found in the Anosyan domain (again, see figure 2). At Cape Andrahomana, where grandidierite was first described, it was associated with quartz, microcline, red almandine, pleonaste, andalusite, and biotite in a pegmatite and an aplite (Lacroix, 1922a,b). Grandidierite was also found 30 km to the north, near Vohibola, in association with serendibite and sinhalite in a diopsidite-bearing paragneiss (Razakamanana et al., 2010). It was associated with quartz in the Nampoana quarry near

Tolanaro (Farges, 2001) and at Sakatelo, Ampamatoa, Marotrana, and Sahakondra, near Esira (McKie, 1965; Farges, 2001). It was also found in association with serendibite and tourmaline in anatectic gneiss near Ihosy (Nicollet, 1990). These reports relate only microscopic crystals of grandidierite, and the Lacroix finding from a century ago remains the only one of gemological interest. Grandidierite was recently reported from a mine near Tolanaro, with no further information yet (Vertriest et al., 2015).

LOCATION AND MINING

A new deposit of grandidierite was discovered in May 2014 by two of the authors and their mining team, about 15 km from the village of Tranomaro. The area is located in the Amboasary district of southern Madagascar's Anosy region (again, see figure 2), 60 km northwest of Cape Andrahomana. Access from Tolanaro is via a 60 km paved road west to Amboasary Atsimo, followed by a rough, unpaved 50 km road north to Tranomaro that requires a four-wheel-drive vehicle. Final access from the village of Tranomaro to the deposit is half a day by foot only. Security is a problem because bandits operate throughout the region.

Mining is done by hand due to the locality's remote location, its limited production, and its irregular, discontinuous veins in opposition to large linear veins. The deposit itself extends over a few acres. The weathered pegmatite is exploited by near-surface artisanal and small-scale mining (figure 3). Using spades and pickaxes, about 12 miners dig holes up to a depth of 15 meters. These open-air corridors crosscut two grandidierite-bearing veins separated by 30 cm to a few meters. The uppermost tunnel is called "Vein 1," while the deeper one is "Vein 2." The rough blue crystals are manually extracted and sorted on-site. The workers carefully remove the valuable mineral specimens to avoid damaging them. Between May 2014 and March 2016, 800 kg of rough specimens were produced. Mining is still in progress as of this writing.

MATERIALS AND METHODS

Using standard gemological methods, we tested a dozen grandidierite crystals from the two veins near Tranomaro for pleochroism, fluorescence reaction, and specific gravity at the French Geological Survey (BRGM) in Orléans, France. After the samples were prepared as polished thin sections, we observed them under a polarizing microscope. The crystals' chemi-

Figure 3. At the new deposit in Madagascar, grandidierite is exploited by artisanal and small-scale mining (left), and rough crystals are sorted on-site (right). Photos by Rufin Rakotondranaivo.

cal homogeneity was investigated with a scanning electron microscope (SEM) on sections that had been carbon coated under vacuum (approximately 20 nm thick). The observations were performed on a Tescan Mira3 XMU field-emission scanning electron microscope (FE-SEM) at 15 kV, and the SEM images were collected using a doped YAG scintillator-type backscattered electron (BSE) detector. Energy-dispersive spectra were obtained by an EDAX TEAM EDS system with an Apollo XPP silicon drift detector.

A Cameca SXFive electron microprobe was used to investigate the grandidierite's chemical composition, including boron content. The standards were boron nitride (B-Kα), Al_2O_3 (Al-Kα), orthoclase (K-Kα), $MnTiO_3$ (Mn-Kα, Ti-Kα), andradite (Si-Kα, Ca-Kα), Fe_2O_3 (Fe-Kα), MgO (Mg-Kα), UO_2 (U-Mβ), and ThO_2 (Th-Mα). All analyses were performed at an acceleration voltage of 15 kV and a beam current of 20 nA. Count time was 10 s for Mg, Al, Si, K, and Ca; 20 s for Ti; 30 s for Fe and Mn; 60 s for Th and U; and 480 s for B. A $\varphi\rho(Z)$ method was chosen for data correction. B-Kα intensity was measured in peak area integration mode, while boron intensity was calibrated with a boron nitride reference sample (coated together with the grandidierite samples). The chemical composition is expressed as atoms per formula units (apfu) based on nine atoms of oxygen.

To confirm the mineral identification, powdered samples and thin sections were analyzed by X-ray diffraction (XRD) and Raman microspectroscopy, respectively. The XRD analyses were performed on randomly oriented powders using soda-lime capillaries 0.5 mm in diameter; they were carried out from 6° to 75° 2θ on a Bruker D8 Advance diffractometer with Cu-Kα radiation (λ=1.5418 Å, 40 kV, and 40 mA) and a Lynx-Eye 1D detector, using a step size of 0.04° 2θ and a step time of 1,920 seconds. Bruker's Diffrac Plus Eva software was chosen for the data analysis. In addition, Raman measurements were performed on polished thin sections with a Renishaw inVia Reflex system coupled to a Leica DM2500 microscope with a 100× objective (numerical aperture = 0.9). The Raman scattering was excited by a 514 nm diode-pumped solid-state (DPSS) laser, and the spectrometer was calibrated using the 520.5 cm^{-1} line of a silicon standard before each measurement session. Several acquisitions were accumulated to improve the signal-to-noise ratio. Raman spectra of at least 10 spots on each crystal were recorded to ensure the consistency of the data.

RESULTS AND DISCUSSION

Optical and Physical Properties. The Tranomaro samples consisted of strong bluish green to greenish blue euhedral crystals measuring up to 15 × 7 × 3 cm and weighing 930 g (figure 4). They were typically stubby, and perfect terminations were rare. The samples were generally translucent and only rarely transparent. Although smooth-edged, the crystals showed flat, well-formed faces locally striated following the {100} cleavage. The thickest crystals were opaque, while the thinner transparent crystals were pleochroic, displaying a deep greenish blue color when polarized light was perpendicular to the c-axis (figure 5, left) and a pale yellow to almost colorless hue when the polarized light was parallel to the c-axis (figure 5, right).
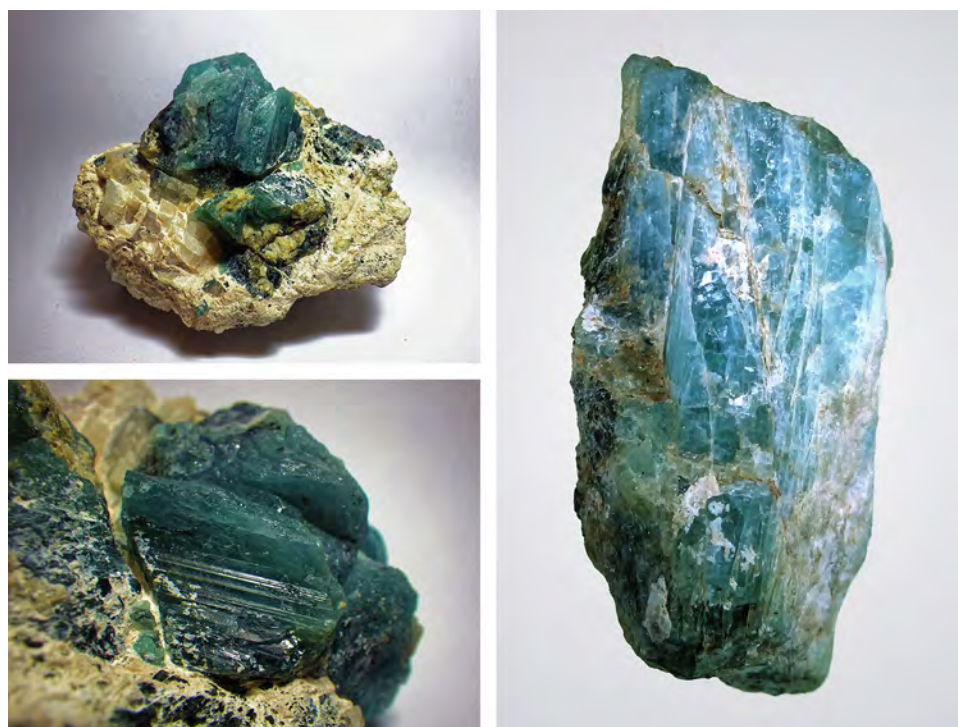
Figure 4. Rough crystals of grandidierite from southern Madagascar, near Tranomaro. Left: A translucent euhedral crystal (top, 53 × 39 mm) with a close-up view of cleavage planes (bottom). Right: An opaque crystal 45 mm in height along the c-axis and weighing 39.7 g. Photos by Julien Raoul (top left and bottom left) and Delphine Bruyère (right).

No fluorescence was observed under either short- or long-wave UV radiation (254 and 365 nm, respectively). The specific gravity of the small pure crystals was established at 3.01 ± 0.02, while that of a rough 39.7 g crystal (figure 4, right), probably influenced by mineral inclusions, was 2.88 ± 0.02. The density of the eye-clean crystals was consistent with Lacroix (1902), which gave a value of 2.99 g/cm³.

Although the new deposit at Tranomaro was discovered only 80 km northwest of the type locality, there were some slight differences. The recently mined crystals had the same optical properties, but a typically stubby rather than elongated habit. Thin sections observed under the polarizing microscope revealed colorless crystals with a good {100} cleavage. The pleochroism observed visually was not seen in thin section. The crystals were homogenous (without zoning) under both the optical and electron microscopes, and they showed fractures. The minerals were birefringent, with a pink-violet-green color of
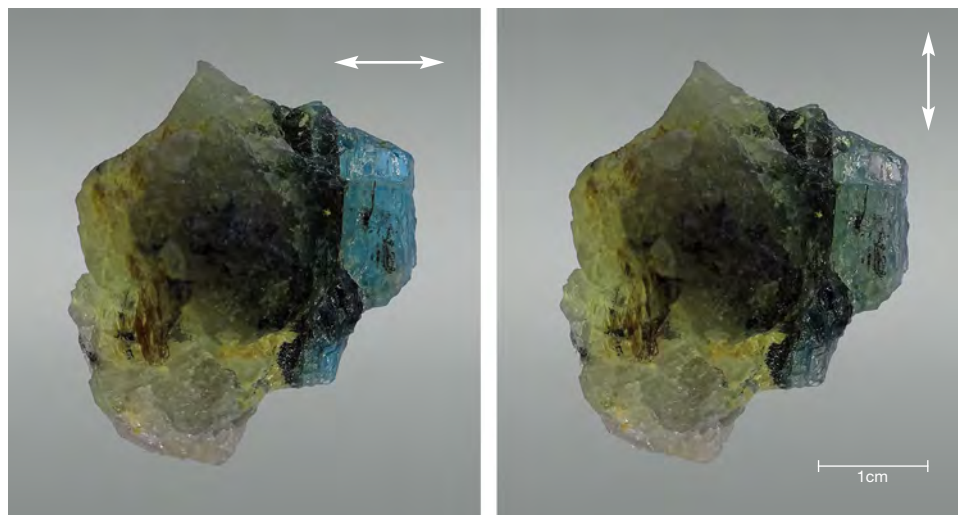
Figure 5. This grandidierite associated with white plagioclase and black Mn oxides, shown under polarized daylight-equivalent light, exhibits pleochroism. Polarized light perpendicular to the c-axis reveals a deep greenish blue color (left). When the polarized light is parallel to the c-axis, the stone appears pale yellow and almost colorless (right). Arrows indicate the orientation of the polarization plane. Photos by Delphine Bruyère.
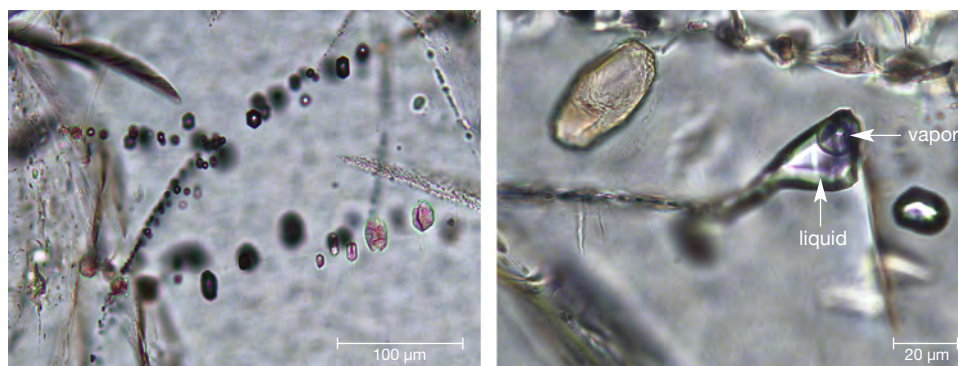
Figure 6. Inclusions in grandidierite from Tranomaro. Left: Euhedral dipyramidal tetragonal crystals, confirmed by microprobe analyses as zircon. Field of view 0.42 mm. Right: A two-phase liquid-vapor fluid inclusion. Field of view 0.18 mm. Photomicrographs by Delphine Bruyère.

the second to third orders. Samples from Vein 1 showed lines of birefringent euhedral mineral inclusions 2–40 µm long (figure 6), some with a dipyramidal tetragonal habit consistent with zircon. A few two-phase liquid-vapor fluid inclusions were also present.

Mineral Identification. The XRD patterns of grandidierite from Tranomaro were compared with those obtained on samples from Tolanaro by Stephenson and Moore (1968). Despite the new material's different habit and specific gravity, no shift was observed in the XRD pattern.

The Raman spectra from the two veins (figure 7) were also similar and revealed several bands that appeared to be characteristic of grandidierite (Maestrati, 1989; Schmetzer et al., 2003; http://rruff.info/R050196). Based on the literature about similar minerals, we propose to relate the spectrum to the mineral structure. Stephenson and Moore (1968) determined that the structure of grandidierite is made up of BO_3 triangles; SiO_4 tetrahedra; distorted AlO_5, MgO_5, and FeO_5 trigonal bipyramids; and AlO_6 octahedra. Vibrations of all functional groups were visible on the Raman spectrum, which could be divided into three regions at 1100–800, 800–400, and 400–100 cm^{-1}. The

Figure 7. The Raman spectrum of a Tranomaro grandidierite sample (blue trace) in the 100–1200 cm^{-1} region is compared to reference spectrum R050196 in the RRUFF database (gray trace), with the approximate wavenumber range of functional groups.

TABLE 1. Chemical composition of grandidierite from southern Madagascar by electron microprobe analysis.[a]
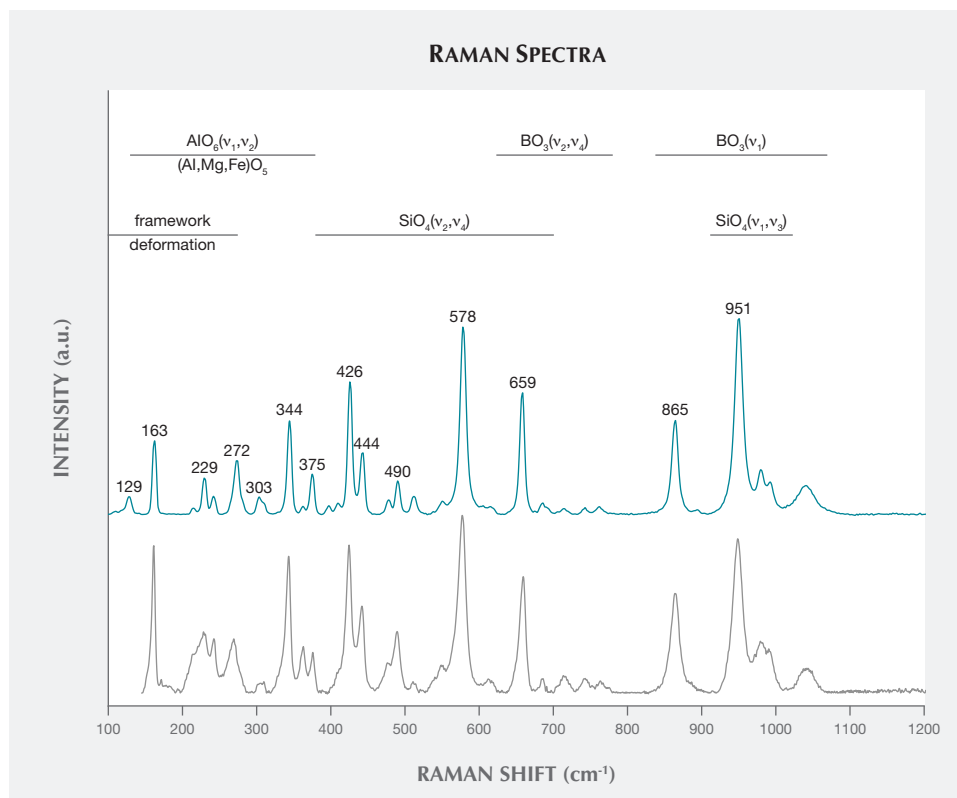
Oxides (wt.%)	Vein 1 Sample 1	Vein 1 Sample 2	Vein 1 Sample 3	Vein 1 Sample 4	Vein 2 Sample 1	Vein 2 Sample 2	Vein 2 Sample 3	Vein 2 Sample 4	Vertriest et al. (2015)[b]
MgO	14.39	14.48	14.17	14.14	14.33	14.29	14.31	14.11	17.01
FeO[c]	0.61	0.51	0.45	0.53	0.53	0.47	0.53	0.56	0.30
Al_2O_3	53.02	52.91	53.12	53.29	53.61	53.25	53.23	52.95	53.89
B_2O_3	12.24	9.92	9.75	11.98	8.89	10.73	9.36	10.22	12.33
SiO_2	20.13	20.24	20.00	20.01	20.47	20.25	20.31	20.56	16.41
Total	100.39	98.05	97.49	99.95	97.83	98.99	97.75	98.40	99.95
apfu[d] O_9									
Mg	1.03	1.07	1.05	1.02	1.07	1.04	1.06	1.04	1.23
Fe	0.02	0.02	0.02	0.02	0.02	0.02	0.02	0.02	0.01
Al	3.00	3.09	3.12	3.03	3.15	3.07	3.12	3.07	3.08
B	1.01	0.85	0.84	1.00	0.77	0.91	0.80	0.87	1.03
Si	0.97	1.00	1.00	0.96	1.02	0.99	1.01	1.01	0.80
Sum of alkalis[e]	1.05	1.09	1.07	1.04	1.09	1.06	1.08	1.06	1.24

[a] Ca, K, Mn, Ti, Th, and U are below detection limit (<300 ppm for K, Ca, and Ti, and <630 ppm for Mn, Th, and U).
[b] Laser ablation–inductively coupled plasma–mass spectrometry (LA-ICP-MS) analysis. MnO and Cr_2O_3 were detected (each 0.01%) but are not included here.
[c] Total iron expressed as FeO.
[d] apfu atoms per formula unit.
[e] Alkalis are Mg and Fe.

1100–800 cm⁻¹ region could be assigned to internal stretching modes of both the planar BO_3 group and the SiO_4 tetrahedron. The Raman band at 1040 cm⁻¹ could be assigned to the B-O stretching vibration of BO_3 units, as with the 1027, 1060, 1086, and 1087 cm⁻¹ bands in other borate minerals (ameghinite, rhodizite, pinakiolite, and takedaite, respectively; see Frost, 2011; Frost and Xi, 2012; Frost et al., 2014a,b). Similarly, the 951 cm⁻¹ band could be assigned to $v_1(BO_3)$, since Ross (1974) mentioned a 910–960 cm⁻¹ range corresponding to this mode for six other (Mg,Fe)-borate minerals. The 800–400 cm⁻¹ region can be assigned to bending vibrations of both BO_3 and SiO_4 units; these modes are commonly reported between 500 and 800 cm⁻¹ for the BO_3 group (Galuskina et al., 2008; Maczka et al., 2010; Frost, 2011; Frost et al., 2013; Frost et al., 2014a). Finally, the region below 400 cm⁻¹ probably corresponds to (Al,Mg,Fe)-O vibrations and framework deformation. The v_1 and v_2 modes of the AlO_6 octahedron, for example, are known as bands in the 150–200 cm⁻¹ range in kaolinite (Frost et al., 1997).

The proposed assignment of Raman peaks to vibrational functional groups must be confirmed by comparison with the mathematical model of the theoretical Raman spectrum for grandidierite.

Chemical Composition. Electron microprobe analyses were performed, and the results are listed in table 1. The mineral's chemical composition was consistent with previously published results and did not vary between the two veins. There were only trace amounts of iron as revealed by the calculated formula $(Mg_{1.02–1.07}Fe_{0.02})Al_{3.00–3.15}(B_{0.77–1.01}O_3)(Si_{0.96–1.02}O_4)O_2$. The samples from near Tranomaro had a low iron content of 0.52% FeO, compared to 0.30% FeO in grandidierite recently reported near Tolanaro (Vertriest et al., 2015) and 0.98%–4.27% FeO from elsewhere (Von Knorring et al., 1969; Black, 1970; Seifert and Olesch, 1977; Farges, 2001). As grandidierite is considered the Mg member of the solid solution with ominelite (its Fe analogue), we can also confirm that grandidierite from Madagascar and Johnsburg, New York, constitute the purest grandidierite, with an Fe/(Mg + Fe) ratio below 0.12 (table 2). The studied samples from Tranomaro, along with the material from Johnsburg, have a ratio of 0.04; the grandidierite recently reported near Tolanaro is the purest ever found, with a ratio of 0.02 (Vertriest et al., 2015).

Compared to the ideal stoichiometric formula for grandidierite, the average Si content was generally consistent, around 1 apfu O_9, while locally Al was higher and B was lower (again, see table 1). Because we are confident of the quality of our microprobe analyses, including for B, substitutions might be involved to explain this balance. The substitution of Si by Al or B is well known in other borosilicate minerals, such

as some tourmalines, but no substitution of B has hitherto been described in the literature. At this point, with no additional investigations, no further assumption can be made.

Mineral Associations. The two veins were composed mainly of plagioclase, phlogopite, enstatite, and diopside, as identified by XRD. Accessory minerals visible with the unaided eye and identified by SEM-EDS were sapphirine (locally forming gem-quality crystals), chlor-fluorapatite, and dravite.

Mineral Inclusions. SEM-EDS observations, confirmed by electron microprobe analyses, also revealed grandidierite crystals hosting Cl-apatite and monazite inclusions of up to a few millimeters long and minute inclusions of zircon (figure 8).

Faceted Stones. Since 2014, a few dozen rough transparent crystals from the Tranomaro deposit have been faceted mainly into round brilliants (again, see figure 1). Some are of gem quality, with transparency and no eye-visible flaws. They display a light blue color in daylight and are trichroic under polarized light (colorless, light blue, and deep greenish blue). Magnification reveals very few flaws. Of these faceted stones, fewer than 10 are above 1 carat. The Tranomaro deposit has produced 800 kg of rough specimens, including about 60 g of eye-clean crystals. The ratio of gem-quality crystals is about 1 in 10,000.

Figure 8. SEM backscattered images of mineral inclusions in grandidierite (mnz = monazite, zrc = zircon). A: A millimeter-length anhedral crystal of monazite. B: A euhedral crystal of zircon. C: A euhedral crystal of Cl-apatite. D: A minute dipyramidal crystal of zircon associated with a bright anhedral crystal of monazite.
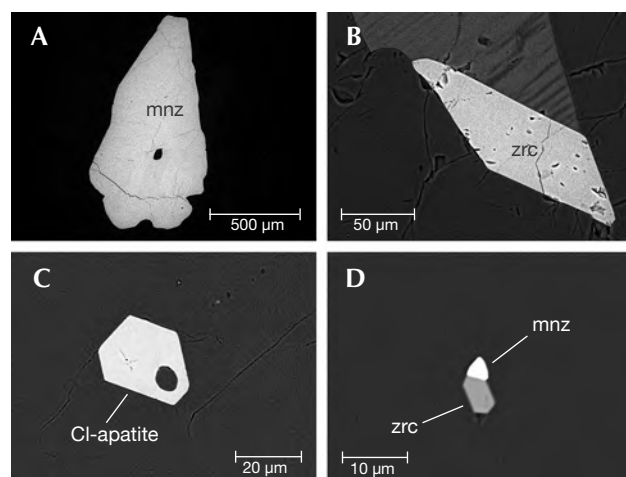

TABLE 2. Fe/Mg ratio of grandidierite samples worldwide.[a]

Locality	Reference	Fe/(Mg + Fe)
Tolanaro, Madagascar	Vertriest et al. (2015)	0.02
Johnsburg, New York	Grew et al. (1991)	0.04
Tranomaro, Madagascar	This study	0.04
Tranomaro, Madagascar	This study	0.05
Tolanaro, Madagascar	Von Knorring et al. (1969)	0.05
Madagascar	Dzikowski et al. (2007)	0.08
Vohibola, Madagascar	Seifert and Olesch (1977)	0.08
Nampoana, Madagascar	Farges (2001)	0.09
Vohibola, Madagascar	Black (1970)	0.09
Vohibola, Madagascar	Razakamanana et al. (2010)	0.10
Sahakondra, Madagascar	Dzikowski et al. (2007)	0.12
Long Lake, Antarctica	Dzikowski et al. (2007)	0.14
Zimbabwe	Dzikowski et al. (2007)	0.14
Faceted gem, Sri Lanka	Schmetzer et al. (2003)	0.15
Andrahomana, Madagascar	Dzikowski et al. (2007)	0.15
Karibe area, Zimbabwe	Dzikowski et al. (2007)	0.17
Almgjotheii, Norway	Dzikowski et al. (2007)	0.18
Andrahomana, Madagascar	Razakamanana et al. (2010)	0.27
Sakatelo, Madagascar	Seifert and Olesch (1977)	0.28
Sakatelo, Madagascar	McKie (1965)	0.28
Tizi-Ouchen, Algeria	Fabriès et al. (1976)	0.29
Nampoana, Madagascar	Seifert and Olesch (1977)	0.33
Nampoana, Madagascar	Farges (2001)	0.33
Landing Bay, New Zealand	Black (1970)	0.34
Pedaru, India	Grew (1983)	0.34
Ampamatoa, Madagascar	Black (1970)	0.36
Maratakka, Suriname	de Roever and Kieft (1976)	0.40
McCarthy Pt., Antarctica	Carson et al. (1995)	0.41
McCarthy Pt., Antarctica	Carson et al. (1995)	0.41
Westport, Ontario, Canada	Grew (1983)	0.42
Blanket Bay, New Zealand	Black (1970)	0.45
Mt. Cimino, Italy	van Bergen (1980)	0.47
Zambia	Seifert and Olesch (1977)	0.48
Vestpolltind, Hinnøy, Norway	Krogh (1975)	0.48
Ihosy, Madagascar	Nicollet (1990)	0.49
Mt. Amiata, Italy	van Bergen (1980)	0.52
Bory Massif, Czech Republic	Cempírek et al. (2010)	0.54
Mchinji, Malawi	Haslam (1980)	0.56
Bory Massif, Czech Republic	Cempírek et al. (2010)	0.57
Mchinji, Malawi	Haslam (1980)	0.59
Ominelite from Japan	Hiroi et al. (2002)	0.95
Ominelite from Japan	Hiroi et al. (2002)	0.95
Ominelite from Japan	Hiroi et al. (2002)	0.96

[a] *Ominelite specimens were added to compare the Fe/Mg ratio with the grandidierite.*

CONCLUSIONS

A new deposit of grandidierite has been discovered in southern Madagascar near Tranomaro, near the now-depleted locality where it was first described. The deposit yields crystals with the same overall properties as those found at the original locality, except that their low iron content and low Fe/(Mg + Fe) ratio make them the purest known grandidierite crystals. The first attempts at faceting provided a few gem-quality stones, including fewer than ten stones above 1 carat. Although modest, this deposit will provide material for museums and collectors in the coming years.

ABOUT THE AUTHORS

Drs. Bruyère, Wille, Maubec, and Lahfid are research scientists in mineralogy and geochemistry at the French Geological Survey (BRGM) in Orléans. Dr. Delor is a geologist and gemologist residing in New Caledonia as head of the local branch of BRGM. Mr. Raoul and Mr. Rakotondranaivo are gemologists and mineral collectors in Madagascar (Beryl International Co.).

REFERENCES

Béhier J. (1960a) Travaux mineralogiques. In H. Besaire, Ed., *Rapport Annuel du Service Geologique pour 1960*. Republique Malgache, pp. 181–199 (in French).

Béhier J. (1960b) Contribution à la minéralogie de Madagascar, *Annales Géologiques de Madagascar*, Imprimerie officielle de Madagascar, Tananarive, Vol. 24 (in French).

van Bergen M.J. (1980) Grandidierite from aluminous metasedimentary xenoliths within acid volcanics, a first record in Italy. *Mineralogical Magazine*, Vol. 43, pp. 651–658, http://dx.doi.org/10.1180/minmag.1980.043.329.15

Black P.M. (1970) Grandidierite from Cuvier Island, New Zealand. *Mineralogical Magazine*, Vol. 37, No. 289, pp. 615–617, http://dx.doi.org/10.1180/minmag.1970.037.289.12

Carson C.J., Hand M., Dirks P.H.G.M. (1995) Stable coexistence of grandidierite and kornerupine during medium pressure granulite facies metamorphism. *Mineralogical Magazine*, Vol. 59, No. 395, pp. 327–339, http://dx.doi.org/10.1180/minmag.1995.059.395.16

Cempírek J., Novák M., Dolnícek Z., Kotková J., Škoda R. (2010) Crystal chemistry and origin of grandidierite, ominelite, boralsilite, and werdingite from the Bory Granulite Massif, Czech Republic. *American Mineralogist*, Vol. 95, No. 10, pp. 1533–1547, http://dx.doi.org/10.2138/am.2010.3480

Dzikowski T.J., Groat L.A., Grew E.S. (2007) The geometric effects of $^{v}Fe^{2+}$ for ^{v}Mg substitution on the crystal structures of the grandidierite-ominelite series. *American Mineralogist*, Vol. 92, No. 5-6, pp. 863–872, http://dx.doi.org/10.2138/am.2007.2275

Fabriès J., Conquéré F., Semroud F. (1976) La grandidiérite de Tizi-Ouchen (Algérie). *Bulletin de la Société Française de Minéralogie et Cristallographie*, Vol. 99, pp. 58–60 (in French).

Farges F. (2001) Crystal chemistry of iron in natural grandidierites: an X-ray absorption fine-structure spectroscopy study. *Physics and Chemistry of Minerals*, Vol. 28, No. 9, pp. 619–629, http://dx.doi.org/10.1007/s002690100170

Frost R.L. (2011) Raman spectroscopy of selected borate minerals of the pinakiolité group. *Journal of Raman Spectroscopy*, Vol. 42, No. 3, pp. 540–543, http://dx.doi.org/10.1002/jrs.2745

Frost R.L., Xi Y. (2012) Raman spectroscopy of the borate mineral ameghinite $NaB_3O_3(OH)_4$. *Spectrochimica Acta Part A: Molecular and Biomolecular Spectroscopy*, Vol. 96, pp. 89–94, http://dx.doi.org/10.1016/j.saa.2012.04.087

Frost R.L., Tran T.H., Kristof J. (1997) The structure of an intercalated ordered kaolinite—a Raman microscopy study. *Clay Minerals*, Vol. 32, No. 4, pp. 587–596, http://dx.doi.org/10.1180/claymin.1997.032.4.09

Frost R.L., Xi Y., Scholz R., Lima R.M.F., Horta L.F.C., Lopez A. (2013) Thermal analysis and vibrational spectroscopic characterization of the boro silicate mineral datolite - $CaBSiO_4(OH)$. *Spectrochimica Acta Part A: Molecular and Biomolecular Spectroscopy*, Vol. 115, pp. 376–381, http://dx.doi.org/10.1016/j.saa.2013.06.012

Frost R.L., López A., Xi Y., Graça L.M., Scholz R. (2014a) A vibrational spectroscopic study of the borate mineral takedaite $Ca_3(BO_3)_2$. *Spectrochimica Acta Part A: Molecular and Biomolecular Spectroscopy*, Vol. 132, pp. 833–837, http://dx.doi.org/10.1016/j.saa.2014.06.004

Frost R.L., López A., Xi Y., Scholz R., Souza L., Lana C. (2014b) The molecular structure of the borate mineral rhodizite (K, $Cs)Al_4Be_4(B, Be)_{12}O_{28}$—A vibrational spectroscopic study. *Spectrochimica Acta Part A: Molecular and Biomolecular Spectroscopy*, Vol. 128, pp. 291–294, http://dx.doi.org/10.1016/j.saa.2014.02.03

Galuskina I.O., Kadiyski M., Armbruster T., Galuskin E.V., Pertsev N.N., Dzierzanowski P., Wrzalik R. (2008) A new natural phase in the system Mg_2SiO_4–Mg_2BO_3F–$Mg_2BO_3(OH)$: composition, paragenesis and structure of OH-dominant pertsevite. *European Journal of Mineralogy*, Vol. 20, No. 5, pp. 951–964, http://dx.doi.org/10.1127/0935-1221/2008/0020-1821

Grew E.S. (1983) A grandidierite-sapphirine association from India. *Mineralogical Magazine*, Vol. 47, pp. 401–403, http://dx.doi.org/10.1180/minmag.1983.047.344.20

Grew E.S., Yates M.G., Swihart G.H., Moore P.B., Marquez N. (1991) The paragenesis of serendibite at Johnsburg, New York, USA: An example of boron enrichment in the granulite facies. In L.L. Perchuk, Ed., *Progress in Metamorphic and Magmatic Petrology. A Memorial Volume in Honour of D.S. Korzhinskiy*. Cambridge University Press, Cambridge, UK, pp. 247–285, http://dx.doi.org/10.1017/CBO9780511564444

Haslam H.W. (1980) Grandidierite from a metamorphic aureole near Mchinji, Malawi. *Mineralogical Magazine*, Vol. 43, pp. 822–823, http://dx.doi.org/10.1180/minmag.1980.043.330.21

Hiroi Y., Grew E.S., Motoyoshi Y., Peacor D.R., Rouse R.C., Matsubara M., Yokoyama K., Miyawaki R., McGee J.J., Su S-C., Hokada T., Furukawa N., Shibasaki H. (2002) Ominelite, (Fe, Mg)Al_3BSiO_9 (Fe^{2+} analogue of grandidierite), a new mineral from porphyritic granite in Japan. *American Mineralogist*, Vol. 87, No. 1, pp. 160–170, http://dx.doi.org/10.2138/am-2002-0117

Krogh E. (1975) The first occurrence of grandidierite in Norway. Contributions to the mineralogy of Norway, No. 59. *Norsk Geologisk Tidsskrift*, Vol. 55, pp. 77–80.

Lacroix A. (1902) Note préliminaire sur une nouvelle espèce minérale. *Bulletin de la Société Française de Minéralogie*, Vol. 25, pp. 85–86 (in French).

——— (1922a) *Minéralogie de Madagascar, Tome I*. Augustin Challamel, Ed., Librairie maritime et coloniale, Paris, 624 pp. (in French).

——— (1922b) *Minéralogie de Madagascar, Tome II*. Augustin Challamel, Ed., Librairie maritime et coloniale, Paris, 694 pp. (in French).

Lonker S.W. (1988) An occurrence of grandidierite, kornerupine, and tourmaline in southeastern Ontario, Canada. *Contributions to Mineralogy and Petrology*, Vol. 98, No. 4, pp. 502–516, http://dx.doi.org/10.1007/BF00372367

Maczka M., Pietraszko A., Hanuza J., Majchrowski A. (2010) Raman and IR spectra of noncentrosymmetric Bi$_{0.21}$La$_{0.91}$Sc$_{2.88}$(BO$_3$)$_4$ single crystal with the huntite-type structure. *Journal of Raman Spectroscopy*, Vol. 41, No. 10, pp. 1297–1301, http://dx.doi.org/10.1002/jrs.2596

Maestrati R. (1989) *Contributions à l'édification du catalogue Raman des gemmes*. Mémoire de diplôme universitaire de gemmologie, Université de Nantes, France (in French).

McKie D. (1965) The magnesium aluminium borosilicates: kornerupine and grandidierite. *Mineralogical Magazine*, Vol. 34, No. 268, pp. 346–357, http://dx.doi.org/10.1180/minmag.1965.034.268.29

Nicollet C. (1990) Occurrences of grandidierite, serendibite and tourmaline near Ihosy, southern Madagascar. *Mineralogical Magazine*, Vol. 54, No. 1, pp. 131–133, http://dx.doi.org/10.1180/minmag.1990.054.374.16

Razakamanana T., Windley B.F., Ackermand D. (2010) Petrology, chemistry and phase relations of borosilicate phases in phlogopite diopsidites and granitic pegmatites from the Tranomaro belt, SE Madagascar; boron-fluid evolution. *Geological Society, London, Special Publications*, Vol. 338, pp. 139–161, http://dx.doi.org/10.1144/SP338.7

de Roever E.W.F., Kieft C. (1976) Grandidierite of contact-metamorphic origin from Maratakka, northwest Surinam. *American Mineralogist*, Vol. 61, No. 3-4, pp. 332–333.

Roig J.-Y., Tucker R., Peters S., Delor C., Théveniaut H. (2012) *Carte géologique de la République de Madagascar à 1/1 000 000*. Ministère des Mines, Antanarivo, République de Madagascar (in French).

Ross S. (1974) Borates. In C. Farmer, Ed., *The Infrared Spectra of Minerals*. The Mineralogical Society, London, pp. 205–226.

Rowley E. (1987) Serendibite, sinhalite, sapphirine, and grandidierite from Johnsburg, NY. *Rocks and Minerals*, Vol. 62, pp. 243–246.

Schmetzer K., Burford M., Kiefert L., Bernhardt H.-J. (2003) The first transparent faceted grandidierite, from Sri Lanka. *G&G*, Vol. 39, No. 1, pp. 32–37, http://dx.doi.org/10.5741/GEMS.39.1.32

Seifert F., Olesch M. (1977) Mössbauer spectroscopy of grandidierite, (Mg,Fe)Al_3BSiO_9. *American Mineralogist*, Vol. 62, No. 5–6, pp. 547–553.

Stephenson D.A., Moore P.B. (1968) The crystal structure of grandidierite, (Mg,Fe)Al_3SiBO_9. *Acta Crystallographica Section B: Structural Science, Crystal Engineering and Materials*, Vol. 24, pp. 1518–1522, http://dx.doi.org/10.1107/S0567740868004577

Tucker R.D., Peters S.G., Roig J., Théveniaut H., Delor C. (2012) *Notice explicative des cartes géologiques et métallogéniques de la République de Madagascar à 1/1 000 000*. Ministère des Mines, Antanarivo, République de Madagascar (in French).

Vertriest W., Detroyat S., Sangsawong S., Raynaud V., Pardieu V. (2015) Gem News International: Grandidierite from Madagascar. *G&G*, Vol. 51, No. 4, pp. 449–450.

Von Knorring O., Sahama Th.G., Lehtinen M. (1969) A note on grandidierite from Fort Dauphin, Madagascar. *Bulletin of the Geological Society of Finland*, Vol. 41, pp. 71–74.

For online access to all issues of GEMS & GEMOLOGY from 1934 to the present, visit:

gia.edu/gems-gemology

PERIDOT FROM THE CENTRAL HIGHLANDS OF VIETNAM: PROPERTIES, ORIGIN, AND FORMATION

Nguyen Thi Minh Thuyet, Christoph Hauzenberger, Nguyen Ngoc Khoi, Cong Thi Diep, Chu Van Lam, Nguyen Thi Minh, Nguyen Hoang, and Tobias Häger

Vietnam is an important source of peridot for the international gem market. Gemological and geo-chemical characteristics of Vietnamese peridot from the Central Highlands are similar to those noted for other localities originating from xeno-liths in alkaline basalts. This peridot was derived from a spinel lherzolite source and appeared to form at temperatures between 910° and 980°C and an assumed pressure of 2.0 ± 0.5 GPa, cor-responding to a depth of around 60 km.

Peridot is a yellowish green to green gem variety of the mineral olivine. It is found as nodules in ig-neous rocks, occasionally as crystals in veins (in Myanmar and Pakistan) or inside meteorites. The main sources are peridotite xenoliths in alkaline basalts and serpentinized dunites (Shen et al., 2011). Commercially important sources are Zabargad, Egypt; San Carlos, Arizona (United States); Myanmar; China; Kohistan, Pakistan; Vietnam; Ethiopia; and Tanzania. Many studies have focused on the charac-teristics of peridot from these sources (Gübelin, 1981; Koivula, 1981; Stockton and Manson, 1983; Koivula and Fryer, 1986; Fuhrbach, 1992; Sinkankas et al., 1992; Nassau, 1994; Kane, 2004; Adamo et al., 2009). Jan and Khan (1996) showed the gemological and chemical properties of peridot from Sapat Valley in Kohistan and suggested that its mineralization is re-lated to post-tectonic hydrothermal activity. Bouilhol et al. (2012) proposed that the mineralization of peri-dot in Kohistan precipitated from subduction-derived fluids. Until now, though, geochemical characteris-tics, genesis, and *P-T* formation conditions of gem-quality peridot have received little attention.

Vietnamese peridot was discovered in the 1990s (Kammerling and Koivula, 1995). Since then, gem-quality material has been mined from three provinces in the Central Highlands: Gia Lai, Dak Nong, and Lam Dong (figure 1). The only active pro-ducer is Gia Lai, where two mines (Ham Rong and Bien Ho) yield more than 100 kg monthly; of that, 15%–20% is of gem quality (Huong et al., 2012). Mining is done mostly on a small scale by independ-ent diggers, who extract the gem material from allu-vial gravels or peridot nodules. In some places miners must dig pits three to five meters deep to reach the peridot-bearing alluvial layers. Jewelry featuring Viet-namese peridot has been on the domestic and inter-national markets for more than a decade (Shigley et al., 2000; Long et al., 2004).

This paper presents gemological and geochemical characteristics of peridot from the Central Highlands. For the present study, the single-grain geothermome-ter used by De Hoog et al. (2010), using Al and Cr in olivine, was used to estimate the origin and *P-T* for-mation conditions. De Hoog et al. (2010) reported that concentrations of Al, Cr, V, Sc, Ca, and Na in

In Brief

- In gemological characteristics and major element com-position, peridot from the Central Highlands of Vietnam is similar to peridot from other localities that originated from xenoliths in alkaline basalts.
- Trace element concentrations corresponded to those of olivine derived from spinel lherzolites.
- The peridot formed at temperatures between 910°C and 980°C and at an assumed pressure of 2.0 ± 0.5 GPa before being carried to the earth's surface by alka-line basalt.

olivine depend mainly upon temperature. The same study presented geothermometers based on the con-centrations in garnet peridotite of Al in olivine, Cr in olivine, and Ca in olivine. They found that the
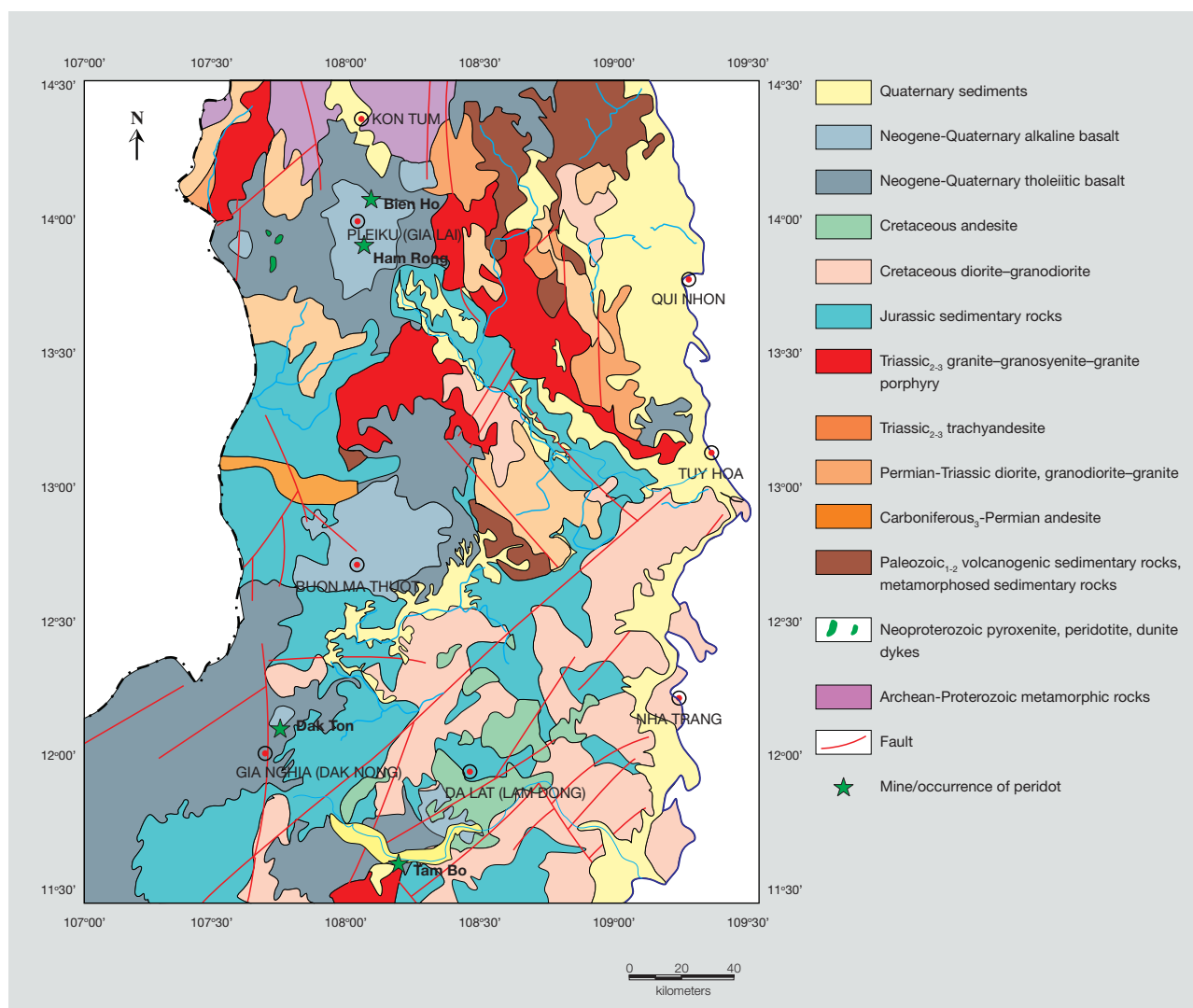
Figure 1. This geological map shows the main rock formations and locations of peridot occurrences in south-central Vietnam (modified after Tinh et al., 1997; Hoa et al., 2005).

most widely applicable of these is Al in olivine for garnet peridotites. Although the thermometers were calibrated with data for garnet peridotites, they also performed well for spinel peridotites.

BACKGROUND

The Central Highlands of Vietnam belong to a large-scale structure of the Truong Son orogenic belt, which is part of the Indochina block (Hoa et al., 2005). This region is composed of Archean-Proterozoic basement rocks and Early to Middle Paleozoic cover rocks. Basement rocks consist of granulite, amphibolite, and greenschist facies metamorphic rocks. Lying on these rocks are volcanogenic sedimentary rocks, metamorphosed sedimentary rocks of greenschist facies, and

also sandstone, siltstone, and shale. Basement and cover rocks were intruded by granite, granodiorite, and granosyenite of Indosinian orogeny association (from Late Paleozoic to Triassic), as well as diorite and granodiorite of Cretaceous orogeny association (related to the Pacific subduction zone). The Early to Middle Paleozoic materials, and Carboniferous to Triassic rocks, were overlain by Jurassic, low-grade metamorphosed terrigenous sedimentary rocks. These older structures were eventually covered by Cenozoic magmatic formations.

Cenozoic magmatic formations belong to a basaltic series distributed in eastern and southeastern Asia, which developed after the end of the East Sea opening in the Middle Miocene (Barr and Mac-
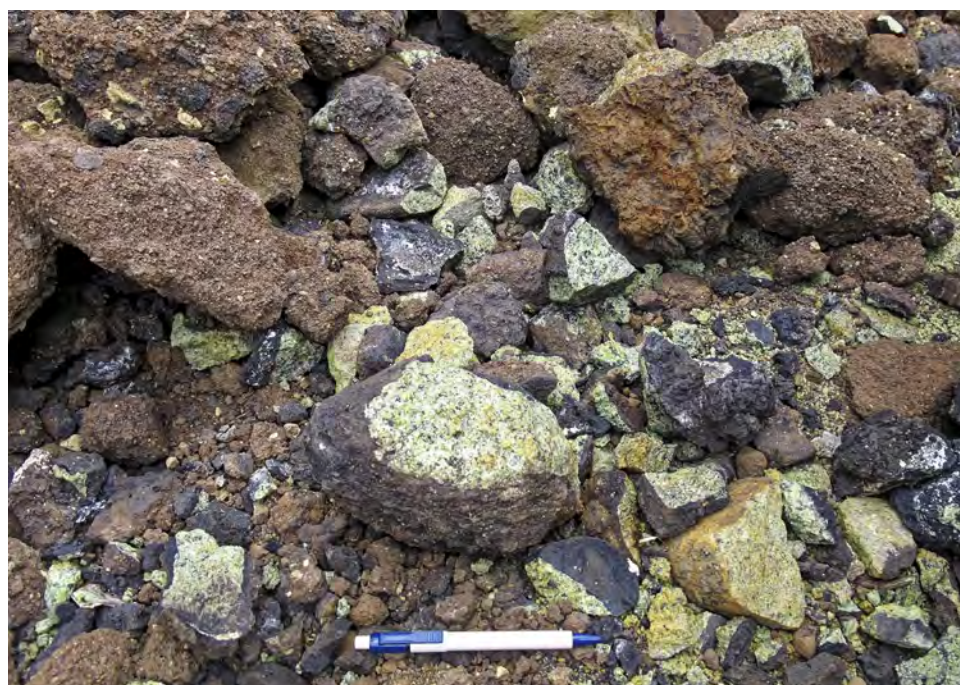
Figure 2. Peridot-bearing nodules are hosted by basalts of Neogene-Quaternary age at the Bien Ho mine. Photo by C. Hauzenberger.

Donald, 1981; Taylor and Hayes, 1983). According to Hoang et al. (1996), basalt formations concentrated in the Central Highlands around several eruptive centers with different ages at Da Lat (13.3–7.9 Ma), Pleiku (<6.3–2.1 Ma), and Buon Ma Thuot (<6.3–1.63 Ma). Most of the centers appear to have developed during two eruptive episodes, separated by paleosol horizons half a meter to five meters in thickness. The early phase consisted of large volumes of quartz and olivine tholeiite flows erupted from extensional fissures. Eruptions of olivine tholeiite, alkaline basalt, and basanite along conjugate strike-slip faults comprised the latter phase. This two-phase pattern was repeated at Da Lat, Pleiku, and Buon Ma Thuot.

Peridot-bearing ultramafic nodules ranging from 5 to 40 cm are found essentially in alkaline basalts in the provinces of Gia Lai, Dak Nong, Lam Dong, and Ba Ria–Vung Tau (Quoc, 1995; Quoc et al. 1995). The peridot-bearing basalts were collected from the Bien Ho and Ham Rong mines in Gia Lai (figure 2). The basalts are dark gray, with phenocrysts in a homogeneous groundmass of acicular crystals. In this study, olivine, plagioclase, and iron hydroxides were found as phenocrysts (figure 3) in a matrix of trachytic texture consisting of plagioclase and iron hydroxides. Silica content was usually less than 52 wt.% and $(Na_2O + K_2O)$ more than 5 wt.%. Also found in the area were some dykes of ultramafic rocks (peridotite, pyroxenite, and dunite) of Neoproterozoic age (Tinh et al., 1997).

MATERIALS AND METHODS

For this study, we examined three gem-quality peridot nodules from the Ham Rong mine in Gia Lai Province (figure 4, left). Fourteen good-quality samples, 20 medium-quality samples, and 11 poor-quality samples were separated from the nodules (figure 4, top right); 15 stones were faceted and examined (figure 4, bottom right). Standard gemological testing was performed at DOJI Institute and Laboratory for Gemology and Jewelry in Hanoi to determine optical properties, hydrostatic specific gravity (SG), UV fluorescence, and microscopic features.

The selected rough stones were divided into three groups on the basis of their color and clarity (figure 4, top right). Nine of the best-quality peridot (from the lot on the left side of the photo), along with nine crystals of medium to good quality (from the middle lot) and two low-quality samples (from the lot on the right), were mounted and embedded in resin, polished, and analyzed by electron microprobe and laser ablation–inductively coupled plasma–mass spectrometry (LA-ICP-MS).

Electron microprobe analysis was performed at the Institute of Earth Sciences, Karl Franzens University of Graz, Austria. We used a JEOL JXA-8200 electron microprobe in wavelength-dispersive mode with an accelerating voltage of 15 kV, a beam current of 15 nA, count times of 60 seconds on peaks and 30 seconds on background, and a beam diameter of approximately 1 µm. The elements analyzed were Si,
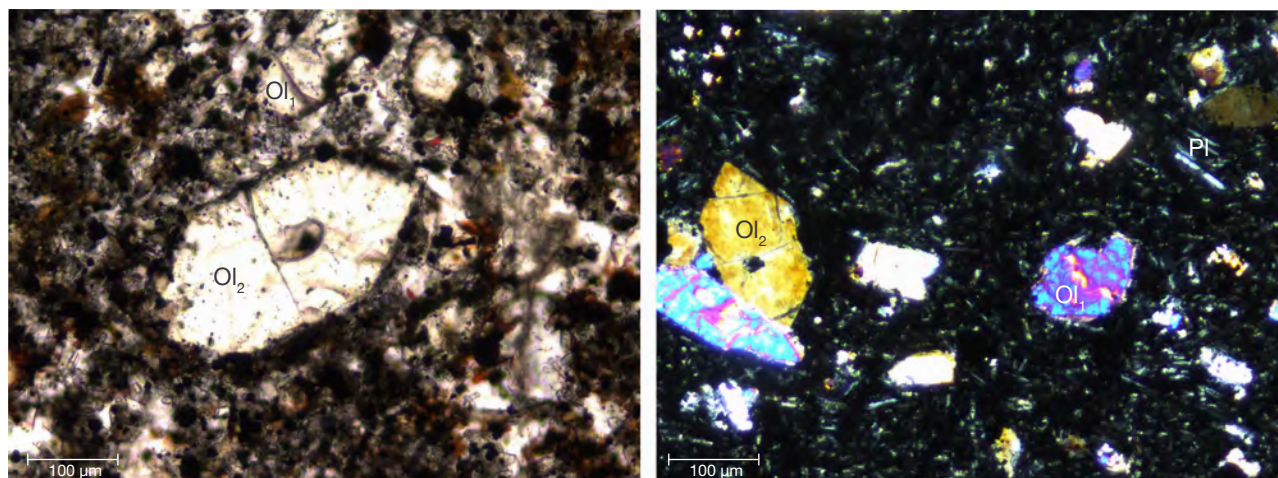
Figure 3. Alkaline basalt from the Bien Ho mine, shown in plane-polarized light (left) and cross-polarized light (right). On the left, the olivine phenocryst (Ol_2) is euhedral and colorless, with high relief; the olivine xenocryst (Ol_1) is colorless and corroded, with a subhedral form. The iron oxides and hydroxides are black. On the right, the Ol_2 phenocryst has a yellow birefringence color; the Ol_1 xenocryst has a high-order birefringence color and is corroded, with a subhedral form. The plagioclase phenocrysts show evident polysynthetic twinning. The groundmass that was crystallized with a subtrachytic texture is composed of plagioclase and sanidine. Photos by N.T.M. Thuyet; field of view 0.7 mm.

Fe, Mn, Mg, Ni, and Ca. Trace element analysis via LA-ICP-MS was carried out at NAWI Graz (a collaborative program jointly run by the University of Graz and Graz University of Technology) using an Agilent 7500 quadrupole coupled with an ESI NWR193 excimer laser source. The material was ablated with a 193 nm laser pulsed at 9 Hz with 75 µm spot size and a laser power corresponding to approximately 7.5

J/cm^2. Helium 5.0 at an approximately 0.6 l/min flow rate was used as a carrier gas for the aerosol produced by laser ablation. Data was acquired in time-resolved analysis mode. The standard glasses NIST610 and NIST612 were routinely analyzed for standardization and drift correction. Standard glasses NIST614 and BCR-2G were analyzed as unknowns and allowed for replication with <10% relative error. Data reduction

Figure 4. Left: Three peridot nodules, collected from the Ham Rong mine in Vietnam's Gia Lai Province, were examined for this study. Top right: The rough stones were sorted by quality into three groups (left to right: good-, medium-, and poor-quality). Bottom right: Fifteen faceted peridot, weighing 0.75–1.41 ct, were cut at DOJI and examined for this study. Photos by N.N. Khoi.
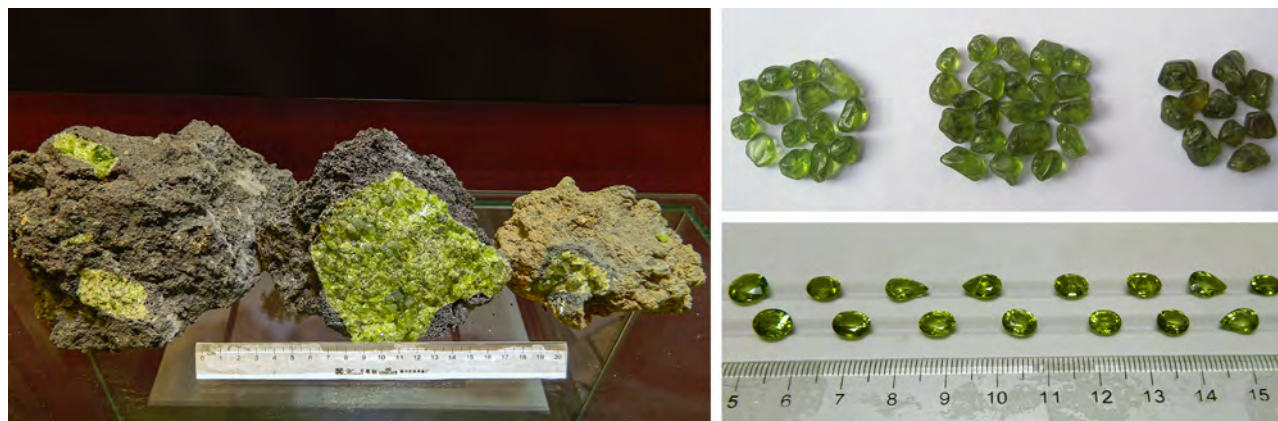
was performed with Glitter software (Macquarie University, Australia) using the concentration values of NIST610 and NIST612 from Jochum et al. (2011). Silicon was used as an internal standard.

Spectroscopy was performed at the Institute of Geosciences, Johannes Gutenberg University in Mainz, Germany. UV-Vis-NIR spectroscopic measurements were taken with a PerkinElmer Lambda 950 spectrophotometer, equipped with an integrating sphere and operating with a spectral resolution of 0.75 nm (for the 200–900 nm range) and 2.8 nm (for the 900–1600 nm range) at a 1 nm/minute scan rate.

RESULTS AND DISCUSSION

Gemological Characteristics. As shown in table 1, the Vietnamese samples showed gemological properties similar to those noted for peridot from other sources found in xenoliths within basalt (Gübelin, 1981; Koivula, 1981; Stockton and Manson, 1983; Koivula and Fryer, 1986; Fuhrbach, 1992; Kane, 2004; Adamo et al., 2009; Huong et al., 2012).

Crystal Morphology. No idiomorphic single crystals of rough peridot have been found in the Central Highlands deposits. Most Vietnamese peridot varies from several millimeters to 1.5 cm in diameter. Pieces as large as 4–6 cm are occasionally discovered (Thuyet et al., 2013).

Figure 5. This light yellowish green (5.09 ct) peridot is from the Bien Ho deposit. Photo by N.T.M. Thuyet.
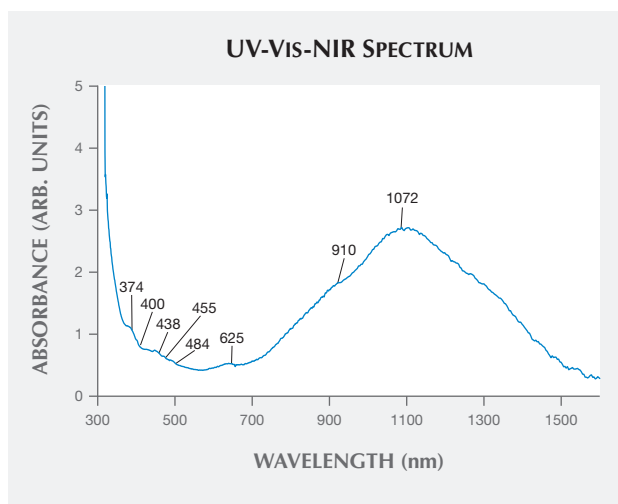

Figure 6. The UV-Vis-NIR spectrum of good-quality peridot from the Central Highlands is characterized by Fe²⁺ absorption features.

Color. The samples ranged from a light yellowish green to a darker, richer yellow green, olive green, and brownish green. Faceted stones had an attractive yellowish green color (figure 4, right, and figure 5). Table 1 shows that the color of Vietnamese peridot is similar to material from Tanzania and Sardinia. In the samples we studied, diaphaneity ranged from translucent (due to high fracturing) to transparent.

Optical Characteristics and Specific Gravity. Testing of the 24 samples indicated that both refractive index (RI) and SG varied slightly with color. The lightest-colored sample's RI was α = 1.650, β = 1.665, and γ = 1.686, with a corresponding birefringence of 0.036. The darkest specimen had RIs of α = 1.667, β = 1.669, and γ = 1.703, with a birefringence of 0.036.

Specific gravity ranged from 3.28 to 3.49; the darker stones generally had a higher SG. The highest reading, 3.49, was obtained from a brownish green sample that contained numerous chromite octahedral inclusions (see figure 8). Chromite, with its SG of 4.50 to 5.09 (4.79 on average), was responsible for the higher than normal reading.

All of the stones were inert to both long- and short-wave UV radiation. To date, cat's-eye and star peridot are not known from the Central Highlands.

The UV-Vis-NIR absorption spectra of five samples were characterized by a broad band at 1072 nm, with a shoulder at approximately 910 nm in the near-IR range, and an increasing absorption toward the UV region (figure 6). Weak bands were also observed at 374, 400, 438, 455, 484, and 625 nm. The bands at

TABLE 1. Gemological properties of peridot from various sources.

| Source	Central Highlands, Vietnam			San Carlos, Arizona	Zabargad, Red Sea	Tanzania	China	Kilbourne Hole, New Mexico	Sardinia, Italy	Kohistan, Pakistan
	Observations from this study	Kammerling and Koivula (1995)	Huong et al. (2012)	Koivula (1981)	Gübelin (1981)	Stockton and Manson (1983)	Koivula and Fryer (1986)	Fuhrbach (1992)	Adamo et al. (2009)	Jan and Khan (1996)
Color	Light yellowish green to a darker, richer yellow-green, olive green, and brownish green	Medium light to medium dark yellowish green to brownish green	Yellowish green to olive green or brownish green	Very dark brown to brownish green to lime green	Dark green, light yellow-green	Light yellowish green	Light yellowish green to a darker yellow-green	Light yellow, light yellowish green, medium yellow to orangy, medium to dark brownish yellow and medium to dark yellowish brown	Yellowish green	Light yellow-green to deep yellow-green, light green, greenish yellow
Diaphaneity	Translucent (due to high fracturing) to transparent	Transparent	Semitransparent to transparent	nr[a]	nr	Transparent	nr	nr	nr	Transparent to translucent and mostly uniform in color, rarely subtranslucent
Pleochroism	Weak to moderate	Weak, brownish to yellowish green	Weak, brownish to yellowish green	nr	Weak but perceptible as pale green along α, green along ß, and light green along γ	nr	nr	nr	Weak to moderate α, ß = green; γ = yellow-green	Thick mineral plates are green and pleochroic with the scheme: ß = yellow-green and α = γ = pale green
Optic character	Biaxial positive	nr	Biaxial negative	Biaxial positive	Biaxial positive	Biaxial positive	nr	nr	Biaxial positive	nr
Refractive indices	n_α = 1.650–1.667	n_α = 1.650	n_α = 1.650–1.652	n_α = 1.649–1.653	n_α = 1.650–1.654	n_α = 1.650	n_α = 1.653	n_α = 1.654–1.673	n_α = 1.650–1.652	n_α = 1.644–1.653
	n_β = 1.665–1.669	n_β = 1.665–1.667	n_β = 1.665–1.669	n_β = 1.665–1.671		n_β = 1.658	n_β = 1.670	n_β = 1.673–1.691	n_β = 1.669–1.670	
	n_γ = 1.686–1.703	n_γ = 1.687–1.688	n_γ = 1.686–1.690	n_γ = 1.686–1.691	n_γ = 1.686–1.690	n_γ = 1.684	n_γ = 1.689	n_γ = 1.691–1.709	n_γ = 1.688–1.690	n_γ = 1.682–1.689
Birefringence	0.036	0.037–0.038	0.036–0.038	0.037–0.038	0.036	nr	0.036	0.036–0.037	0.038	0.036–0.038
Specific gravity	3.28–3.49	3.34 ± 0.01	3.32–3.37	3.28–3.38	3.34	nr	3.36	3.42–3.50	3.32–3.36	3.26–3.44
UV fluorescence Long-wave Short-wave	Inert Inert	nr	Inert Inert	nr	nr	nr	nr	Inert Inert	Inert Inert	nr
Internal features	"Lily pad" inclusions, chromite inclusions, healed secondary fractures and hercynite (rarely)	Chromian spinel(?), biotite mica(?), "lily pads" surrounding negative crystals, smoke-like veils, optically active intergrowth	Spinel, sphalerite, "lily pad" inclusions	Chromite, chromian spinel, negative crystals, "lily pads," cleavages, glass blebs, chrome diopside, biotite, and smoke-like veils	Rounded plate-like, wafer-thin healing seams or residual drops, chromite, "lily pads"	nr	Chromite, biotite, "lily pad," chrome diopside, smoke-like veils	Hercynite, forsterite, diopside, biotite, "lily pad" inclusions	Partially healed fractures, liquid inclusions, "lily pad" inclusions, crystals, growth planes, traces of parallel twinning	nr

[a]nr = not reported
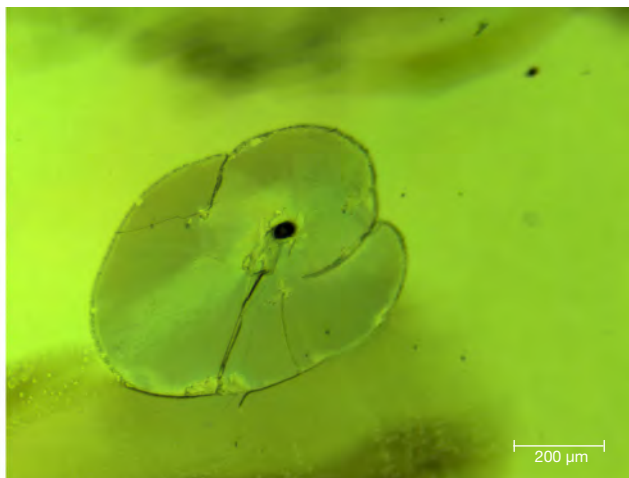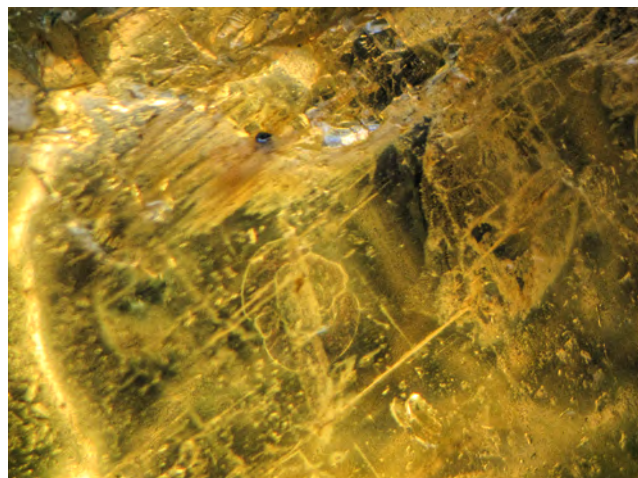
Figure 7. Peridot from the Central Highlands often contains healing planes; the most common inclusions found in the samples were "lily pads." These are cleavage separations produced by the expansion of small fluid-filled negative crystals (left) and a small solid included crystal (right). Photomicrographs by N.N. Khoi (left, field of view 1 mm) and N.T.M. Thuyet (right, field of view 1.4 mm).

455 and 484 nm were visible with a hand spectroscope as well, with total absorption below about 440 nm. This spectral feature is due to the presence of Fe^{2+} (Burns, 1970), confirming that iron is mainly responsible for the coloration.

Internal Features. The internal features of Vietnamese peridot were similar to those found in xenoliths in alkaline basalts elsewhere (again, see table 1).

The most prominent inclusions we observed were round, flat healing planes (disc-like "lily pads") with a small opaque black crystal near the center (figure 7) and black opaque octahedral crystals of chromite surrounded by a tension halo (figure 8, left). Hercynite, a member of the spinel group, was sometimes observed (figure 8, right). This inclusion has only been reported in peridot from Kilbourne Hole, New Mexico (Fuhrbach, 1992). Partially healed secondary

Figure 8. Left: Chromite crystal surrounded by a tension halo. Photomicrograph by N.N. Khoi; field of view 1 mm. Right: Hercynite inclusions were typically surrounded by a tension fracture. Photomicrograph by N.T.M. Thuyet; field of view 1.4 mm.
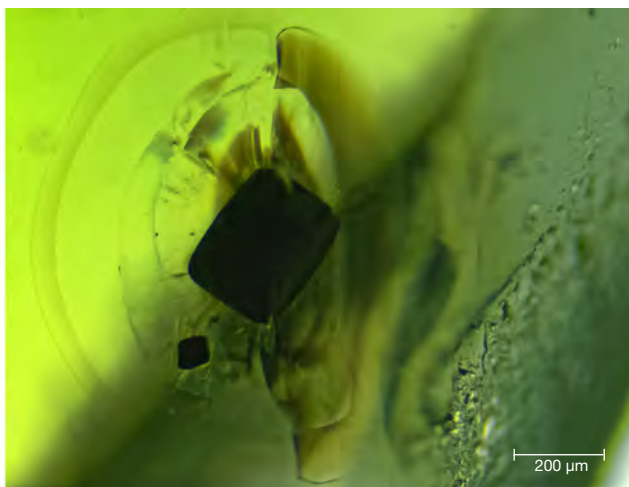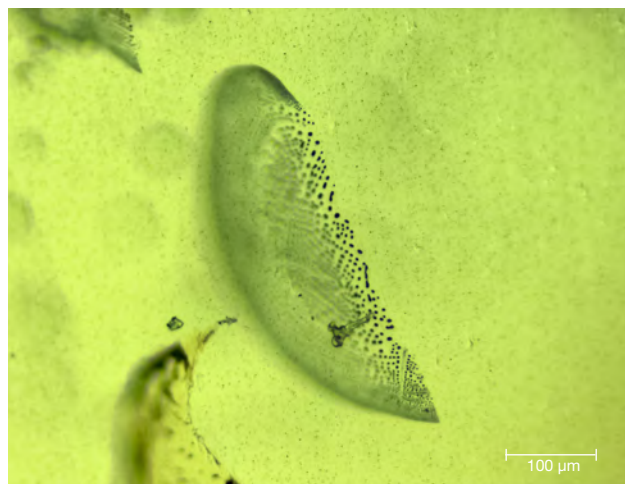
Figure 9. Healed fractures in a peridot from the Central Highlands. Photomicrograph by N.T.M. Thuyet; field of view 0.7 mm.

fractures with iridescence were seen in most of the Vietnamese samples (figure 9).

Chemical Composition. *Major Elements.* The average chemical composition obtained by electron mi-

croprobe is shown in table 2. The samples showed a very narrow range of magnesium content, with forsterite varying from 90.6 to 91.3 mol.%, which is typical for olivine/peridot from mantle sources. Most gem peridot lies within the Fo_{88-93} range (Jan and Khan, 1996) or $Fo_{88.6-96.0}$ range (Shen et al., 2011), while olivine from peridotite xenoliths is in the $Fo_{88.3-92.0}$ range (Embey-Isztin and Dobosi, 2007). Peridot samples from Gia Lai Province did not display the major-element zoning commonly observed in olivine from xenoliths, demonstrating their chemical equilibrium (De Hoog et al., 2010). MgO content varied in a narrow range from 47.22 to 52.25 wt.%, while FeO ranged from 8.24 to 9.90 wt.%, in agreement with data obtained by Huong et al. (2012), Quoc et al. (1995), and Y et al. (2006). Thus, FeO content in Vietnamese peridot was similar to that of samples from Sardinia, Myanmar, and San Carlos, Arizona, but higher than in samples from Tanzania and Zabargad. The FeO content range was not as wide as in samples from Kohistan, which varied from 2.74 to 9.69 wt.% and averaged 6.54 wt.%. The range of SiO_2 content in our samples was similar to that of other peridot localities except Kohistan. There was no substantial difference in any of the remaining main elements (again, see table 2).

TABLE 2. Chemical composition of peridot from Vietnam and other countries by electron microprobe (in wt.%).

Sample	Vietnam: good-quality (46 points/ 9 samples)	Vietnam: medium-quality (45 points/ 9 samples)	Vietnam: poor-quality (15 points/ 2 samples)	Myanmar[a] (4 samples)	Arizona[a] (2 samples)	Sardinia, Italy[b] (2 samples)	Tanzania[a] (1 sample)	Zabargad[a] (2 samples)	Kohistan, Pakistan[c] (7 samples)
SiO_2	40.27–42.64 (41.02)	40.24–41.54 (40.91)	39.82–41.22 (40.52)	40.25–40.81 (40.65)	40.55–40.77	40.69–40.83	40.62	41.03–41.07	38.75–41.57 (40.47)
FeO	8.24–9.90 (8.68)	8.33–8.89 (8.82)	8.40–9.10 (8.74)	8.25–10.16 (9.26)	9.68–9.73	8.77–8.98	7.74	7.95–8.14	2.74–9.69 (6.54)
MnO	0.03–0.24 (0.12)	0.07–0.22 (0.14)	0.07–0.22 (0.15)	0.07–0.15 0.19	0.12–0.17	0.11–0.15	0.12	0.11–0.13	0.06–0.15 (0.11)
MgO	47.22–52.25 (50.36)	49.19–51.04 (50.31)	47.93–50.24 (48.96)	48.9–50.71 (49.85)	48.22–48.98	50.15–50.17	51.26	50.44–50.95	48.52–53.49 (50.80)
NiO	0.24–0.54 (0.36)	0.19–0.55 (0.37)	0.16–0.48 (0.33)	0.31–0.39 (0.35)	0.37–0.39	0.38–0.39	0.39	0.38–0.41	0.17–0.38 (0.26)
CaO	0.03–0.1 (0.06)	0.03–0.08 (0.05)	0.03–0.07 (0.05)	<0.02	0.06–0.11	nr[d]	<0.02	0.03–0.04	0–0.03 (0.01)
Total	99.17–100.99 (100.61)	99.17–100.95 (100.53)	98.15–100.97 (98.75)	99.77–100.8 (100.24)	99.29–99.77	100.12–100.50	100.13	100.18–100.50	97.43–99.38 (98.21)

[a]*Stockton and Manson (1983);* [b]*Adamo et al. (2009);* [c]*Jan and Khan (1996)*
[d]*nr = not reported*

TABLE 3. Trace-element concentration of peridot samples and olivines in spinel and garnet lherzolites by LA-ICP-MS (in ppm).

Sample	Vietnam: good-quality (46 points/ 9 samples)	Vietnam: medium-quality (45 points/ 9 samples)	Vietnam: poor-quality (15 points/ 2 samples)	Sardinia, Italy[a] (2 samples)	Kohistan, Pakistan[b]: gem olivine with no visible solid inclusions	Kohistan, Pakistan[b]: gem olivine with magnetite + serpentine inclusions	Olivine in spinel lherzolite[c] (17 samples)	Olivine in garnet lherzolite[c] (38 samples)
^{60}Ni	2838–3188 (3045)	2602–3062 (2903)	2775–2986 (2855)	3065–2986	2842	2303	2520–3014 (2737)	2232–3307 (2695)
^{55}Mn	919–1016 (966)	869–1121 (952)	924–990 (960)	1162–852	nr[d]	nr	692–1044 (929)	488–851 (646.31)
^{59}Co	139–149 (146)	137–150 (142)	138–149 (145)	213.93–216.77	140.04	146.04	110–132 (124)	104–137 (117.6)
^{65}Cu	1.01–1.84 (1.43)	0.62–1.62 (1.34)	1.27–2.34 (1.55)	nr	0.08	0.09	0.98–1.95 (1.50)	0.54–4.73 (2.19)
^{66}Zn	47.6–63.8 (55.5)	50.4–64.4 (55.0)	48.3–51.8 (51.3)	80.73–73.38	22.5	16.28	20–57.3 (45.0)	37.2–80.8 (49.89)
^{7}Li	1.28–1.93 (1.54)	1.24–1.71 (1.37)	1.22–1.56 (1.43)	2.30–1.99	15.12	1.9	0.96–2.09 (1.70)	1.02–2.38 (1.51)
^{53}Cr	72.4–126 (96)	86.7–124 (103)	99.4–114 (107.84)	157.51–181.35	105.68	4.57	8.71–149.12 (80.25)	25.4–631 (241.46)
^{27}Al	45.7–81.2 (59.3)	46.4–63.3 (53.9)	54–70.5 (57.0)	nr	nr	nr	2.6–164.37 (83.46)	5.5–301 (88.64)
^{51}V	1.70–3.09 (2.51)	1.70–2.58 (2.25)	2.27–2.78 (2.56)	4.18–4.15	1.47	0.35	2.57–3.39 (2.21)	1.3–10.4 (5.71)
^{43}Ca	278–352 (307)	38.6–782 (286)	11.4–13.9 (12.6)	548.50–453.94	13.64	11.42	10.6–523.76 (324.46)	56–632 (227.69)
^{47}Ti	5.55–37.0 (12.9)	7.19–13.5 (11.2)	9.46–10.0 (9.81)	10.51–8.81	2.47	0.81708	3.1–123.68 (21.37)	1.36–287 (89.9)
^{90}Zr	0.036–0.190 (0.090)	0.038–0.147 (0.080)	0.072–0.093 (0.070)	nr	0.0023	0.0011	0.006–0.176 (0.031)	0.006–0.44 (0.156)
^{93}Nb	0.006–0.012 (0.008)	0.005–0.034 (0.010)	0.005–0.009 (0.007)	nr	0.0002	0.0003	0.004–0.017 (0.011)	0.013–1.100 (0.250)
^{172}Yb	0.006–0.031 (0.013)	0.006–0.028 (0.015)	0.009–0.013 (0.010)	nr	0.059	0.013	0.018–0.062 (0.032)	0.002–0.026 (0.006)

[a]*Adamo et al. (2009);* [b]*Bouilhol et al. (2012);* [c]*De Hoog et al. (2010)*
[d]*nr = not reported*

Trace Elements. De Hoog et al. (2010) divided trace elements in olivine into three distinct groups. Ni, Mn, Co, Cu, Zn, and Li, which make up Group I, exhibit small concentration ranges. Olivine is the primary host mineral. Group II, comprised of Cr, Al, V, Sc, Ca, and Na, is strongly concentrated in coexisting mantle minerals (garnet, clinopyroxene, and spinel) and shows a narrow range of bulk rock concentrations. Partition coefficients of Group II elements are highly temperature sensitive. Olivine shows the greatest level of variability, and the elements' concentration ranges are mainly controlled by the host rock's equilibration temperature. The concentration of the Group II elements in olivine allows the appli-

cation of simple geothermometers. The Group III elements (Ti, Zr, Nb, and Y) are strongly dependent on bulk rock contents. These elements show large concentration ranges in olivine as well as in coexisting minerals (garnet, clinopyroxene, and spinel again). The trace-element composition of Vietnamese peridot samples, obtained by LA-ICP-MS analyses, is reported in table 3. In this study, Sc, Na, and Y were not analyzed. For comparison, table 3 also shows the composition of trace elements of Sardinian peridot originating from spinel lherzolite (Adamo, 2009), Kohistan peridot hosted by serpentinized dunites, and olivines from spinel and garnet lherzolite sources. Broadly speaking, the content of most trace elements

in Vietnamese peridot is similar to that of Sardinian peridot and olivine originating from spinel lherzolite but different from that of Kohistan peridot (again, see table 3).

Ni contents ranged from 2602 to 3188 ppm (2934 ppm on average). Concentrations approximated those of peridot from Sardinia and olivine from spinel lherzolite but were higher than those of Kohistan peridot. Furthermore, Ni contents tended to be slightly higher in good-quality peridot than in medium- and poor-quality peridot. Cu concentrations ranged from 0.62 to 2.34 ppm (1.44 ppm on average). These values were typical for peridot from spinel lherzolite but different from those of Kohistan peridot. Li concentrations ranged from 1.22 to 1.93 ppm (1.45 ppm on average) and were similar to those of olivines from spinel and garnet lherzolite, slightly lower than Sardinian material, and much lower than in Kohistan peridot. Cr content varied from 72.4 to 126 ppm (100 ppm on average). This concentration was lower than in Sardinian peridot and olivine from garnet lherzolite sources but higher than in Kohistan peridot or olivine from spinel lherzolite. V ranged from 1.70 to 3.09 ppm (2.41 ppm on average). The samples were similar to olivines from spinel lherzolite sources and lower than the Sardinian peridot and olivine from garnet lherzolite sources but tended to be higher in vanadium content than Kohistan peridot. Ti concentrations ranged from 5.55 up to 37.0 ppm with 11.7 ppm on average. These values were similar to those of Sardinian peridot and lower than those of olivine from spinel and garnet peridotites but slightly higher than in Kohistan peridot. Ca concentration ranged from 11.4 to 782 ppm. The range is similar to olivine derived from spinel and garnet lherzolite. Most of the good- and medium-quality samples analyzed contained approximately 300 ppm of Ca. However, Ca content in the low-quality peridot ranged from 11.4 to 13.9 ppm (12.6 ppm on average), similar to Kohistan peridot.

Source and Formation Conditions. *Lithological Information.* Previous studies based on mineral assemblages coexisting paragenetically, either with olivine in nodules in alkaline basalts or with peridot in placers, have identified the source of Vietnamese peridot as lherzolite xenoliths (Quoc, 1995; Quoc et al., 1995; Toan and Ty, 1995; Long et al., 2004). In those previous works, however, the trace-element composition of minerals and rocks was not used to pinpoint their source. In this study, LA-ICP-MS analysis was used to determine trace elements in Vietnamese peridot. The results indicated that, in terms of trace ele-
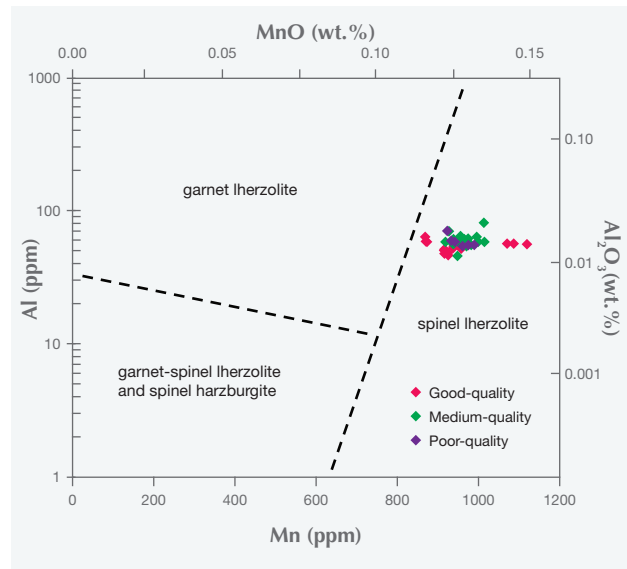

Figure 10. This diagram identifies various mantle lithologies based on Mn vs. log Al in olivine and places Central Highlands peridot in the spinel lherzolite field. The dotted reference lines are after De Hoog (2010).

ments, Vietnamese peridot is similar to peridot and olivine from the spinel lherzolite field. Furthermore, when using Al-Mn discrimination diagrams of De Hoog (2010) for petrological classification of mantle lithologies, Vietnamese peridot always falls into the spinel lherzolite field (figure 10).

P-T Conditions. To demonstrate that olivine's variations in trace elements are determined by temperature (and to some extent pressure), De Hoog (2010) calculated olivine mineral partition coefficients for Group II elements using multiple linear regression analysis. Strong temperature correlations confirmed the temperature-sensitive nature of these elements, as expressed in formulas [1] and [2]:

$$T_{Al=ol}(°C) = \frac{9423 + 51.4P + 1860Cr\#^{ol}}{(13.409 - \ln[Al]^{ol})} - 273 \qquad [1]$$

where [Al]^{ol} is the Al content of olivine in ppm, and Cr#^{ol} is Cr/(Cr + Al) of olivine in atoms.

$$T_{Cr=ol}(°C) = \frac{13444 + 48.5P + 4678Cr\#^{ol}}{(14.53 - \ln[Cr]^{ol})} - 273 \qquad [2]$$

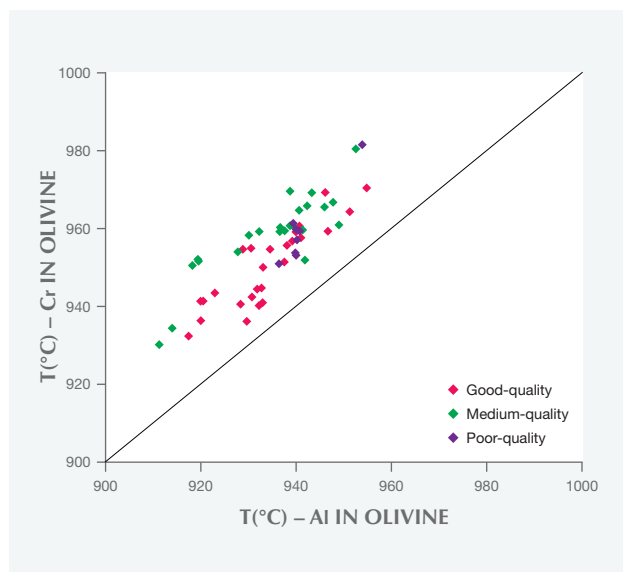where [Cr]^{ol} is the Cr content of olivine in ppm.

Figure 11. Al in olivine and Cr in olivine calculated for 2.0 Gpa. Calculated temperatures are 910 to 980°C; the Cr-in-olivine thermometer consistently gave a temperature higher than the Al in olivine values.

Using the Al [1] and Cr [2] single-grain thermometer from De Hoog et al. (2010), temperature values between 910°C and 980°C can be calculated, assuming a pressure of 2.0 Gpa. This corresponds to a depth of around 60 km and is within the stability field of a spinel lherzolite. The Cr-in-olivine thermometer consistently gave a temperature 14–17°C higher than

the Al in olivine values (figure 11). The average temperatures of good-, medium-, and poor-quality peridot from the Cr and Al single-grain thermometer were calculated as:

	Good-quality	Medium-quality	Poor-quality
Cr	963°C	950°C	957°C
Al	940°C	933°C	940°C

CONCLUSIONS

Chemical analysis demonstrated that the FeO content in Vietnamese peridot is similar to that of peridot from Sardinia, Myanmar, and Arizona, and higher than that of peridot from Tanzania and Zabargad. Pakistani peridot's FeO content was generally lower and more varied. The material's gemological characteristics were similar to those noted for peridot from other localities that originated from xenoliths in alkaline basalts, especially the color of previously studied samples from Tanzania and Italy. Trace-element concentrations corresponded to those of olivine derived from spinel lherzolites. The low-quality Vietnamese samples usually had a lower Ca content than all other Vietnamese peridot.

The results of this study indicate that peridot from the Central Highlands of Vietnam formed at temperatures between 910°C and 980°C and at an assumed pressure of 2.0 ± 0.5 GPa, which corresponds to a depth of around 60 km.

ABOUT THE AUTHORS
Dr. Thuyet (nmthuyet@vnu.edu.vn) is a lecturer in mineralogy at the Hanoi University of Science, Vietnam. Dr. Hauzenberger is an associate professor at the University of Graz, Austria. Dr. Khoi is an associate professor of geology at the Hanoi University of Science and director of DOJI Institute and Laboratory for Gemology and Jewelry. Ms. Diep is a researcher in lithology and petrology, and Dr. Lam is a researcher in mineralogy, at the Vietnam Institute of Geosciences and Mineral Resources in Hanoi. Ms. Minh is a researcher in gemology at DOJI Institute and Laboratory for Gemology and Jewelry. Dr. Hoang is senior scientist at the Institute of Geological Sciences, Vietnam Academy of Science and Technology, also in Hanoi. Dr. Häger is senior scientist at the Centre for Gemstone Research at Johannes Gutenberg University and lecturer in gemstone and jewelry design at the University for Applied Sciences in Idar-Oberstein, Germany.

REFERENCES

Adamo I., Bocchio R., Pavese A., Prosperi L. (2009) Characterization of peridot from Sardinia, Italy. *G&G*, Vol. 45, No. 2, pp. 130–133, http://dx.doi.org/10.5741/GEMS.45.2.130

Barr S.M., MacDonald A.S. (1981) Geochemistry and geochronology of late Cenozoic basalts in Southeast Asia. *Geological Society of America Bulletin*, Vol. 92, No. 8, pp. 1069–1142, http://dx.doi.org/10.1130/GSAB-P2-92-1069

Bouilhol P., Burg J.-P., Bodinier J.L., Schmidt M.W., Bernasconi S.M., Dawood H. (2012) Gem olivine and calcite mineralization precipitated from subduction-derived fluids in the Kohis-

tan arc-mantle (Pakistan). *The Canadian Mineralogist*, Vol. 50, No. 5, pp. 1291–1304, http://dx.doi.org/10.3749/canmin. 50.5.1291

Burns R.G. (1970) Crystal field spectra and evidence of cation ordering in olivine minerals. *American Mineralogist*, Vol. 55, No. 9/10, pp. 1608–1632.

De Hoog J.C.M., Gall L., Cornell D.H. (2010) Trace-element geochemistry of mantle olivine and application to mantle petrogenesis and geothermobarometry. *Chemical Geology*, Vol. 270, Nos. 1–4, pp. pp. 196–215, http://dx.doi.org/10.1016/j.chemgeo. 2009.11.017

Embey-Isztin A., Dobosi G. (2007) Composition of olivines in the young alkali basalts and their peridotite xenoliths from the Pannonian Basin. *Annales historico-naturales musei nationalis hungarici*, Vol. 99, pp. 5–22.

Fuhrbach J.R. (1992) Kilbourne Hole peridot. *G&G*, Vol. 28, No. 1, pp. 16–27, http://dx.doi.org/10.5741/GEMS.28.1.16

Gübelin E. (1981) Zabargad: The ancient peridot island in the Red Sea. *G&G*, Vol. 17, No. 1, pp. 2–8, http://dx.doi.org/10.5741/ GEMS.17.1.2

Hoa T.T., Phuong N.T., Anh T.T., Van V.V., Y N.V., Hoang N., Thanh H.H., Anh P.L., Nien B.A., Hung T.Q., Dung P.T., Lam T.H., Hang H.V., Anh T.V., Chuong V.D., Hung P.V., Quan V.M., Eds. (2005) Study of forming conditions and distribution laws of precious and rare minerals related to magmatic activity in Central Vietnam and Tay Nguyen Highlands. State-level Project, code DTDL-2003/07. Vol. I, 347 pp. (in Vietnamese).

Hoang N., Flower M.F.J., Carlson R.W. (1996) Major, trace element, and isotopic compositions of Vietnamese basalts: Interaction of hydrous EMl-rich asthenosphere with thinned Eurasian lithosphere. *Geochimica et Cosmochimica Acta*, Vol. 60, No. 22, pp. 4329–4351, http://dx.doi.org/10.1016/S0016-7037(96)00247-5

Huong L.T., Häger T., Hofmeister W., Hauzenberger C., Schwarz D., Long P.V., Wehmeister U., Khoi N.N., Nhung N.T. (2012) Gemstones from Vietnam: An update. *G&G*, Vol. 48, No. 3, pp. 158–176, http://dx.doi.org/10.5741/GEMS.48.3.158

Jan M.Q., Khan M.A. (1996) Petrology of gem peridot from Sapat mafic-ultramafic complex, Kohistan, NW Himalaya. *Geological Bulletin, University of Peshawar*, Vol. 29, pp. 17–26.

Jochum K.P., Weis U., Stoll B., Kuzmin D., Yang Q., Raczek I., Jacob D.E., Stracke A., Birbaum K., Frick D.A., Günther D., Enzweiler J. (2011) Determination of reference values for NIST SRM 610–617 glasses following ISO guidelines. *Geostandards and Geoanalytical Research*, Vol. 35, No. 4, pp. 397–429, http://dx.doi.org/10.1111/j.1751-908X.2011.00120.x

Kammerling R.C., Koivula J.I. (1995) A preliminary investigation of peridot from Vietnam. *Journal of Gemmology*, Vol. 24, No. 5, pp. 355–361, http://dx.doi.org/10.15506/JoG.1995.24.5.355

Kane R.E. (2004) The creation of a magnificent suite of peridot jewelry: From the Himalayas to Fifth Avenue. *G&G*, Vol. 40, No.

4, pp. 288–302, http://dx.doi.org/10.5741/GEMS.40.4.288

Koivula J.I. (1981) San Carlos peridot. *G&G*, Vol. 17, No. 4, pp. 205–214, http://dx.doi.org/10.5741/GEMS.17.4.205

Koivula J.I., Fryer C.W. (1986) The gemological characteristics of Chinese peridot. *G&G*, Vol. 22, No. 1, pp. 38–40, http://dx.doi.org/10.5741/GEMS.22.1.38

Long P.V., Giuliani G., Garnier V., Ohnenstetter D. (2004) Gemstones in Vietnam—A review. *Australian Gemmologist*, Vol. 22, No. 4, pp. 162–168.

Nassau K. (1994) Synthetic forsterite and synthetic peridot. *G&G*, Vol. 30, No. 2, pp. 102–108, http://dx.doi.org/10.5741/GEMS. 30.2.102

Quoc N.K. (1995) Origins, distribution rules and assessment of potential of gem and technique stones of Vietnam. State-level Project, code KT-01-09 (in Vietnamese).

Quoc N.K., Hieu H.H., Luong P.T., and Trung N.D. (1995) Gemstones potential of Vietnam. *Proceedings of the National Conference on Geology of Vietnam, Hanoi*, Oct. 4–10, pp. 143–152.

Shen A.H., Koivula J.I., Shigley J.E. (2011) Identification of extraterrestrial peridot by trace elements. *G&G*, Vol. 47, No. 3, pp. 208–213, http://dx.doi.org/10.5741/GEMS.47.3.208

Shigley J.E., Dirlam D.M., Laurs B.M., Boehm E.W., Bosshart G., Larson W.F. (2000) Gem localities of the 1990s. *G&G*, Vol. 36, No. 4, pp. 292–335, http://dx.doi.org/10.5741/GEMS.36.4.292

Sinkankas J., Koivula J.I., Becker G. (1992) Peridot as an interplanetary gemstone. *G&G*, Vol. 28, No. 1, pp. 43–51, http://dx.doi.org/ 10.5741/GEMS.28.1.43

Stockton C.M., Manson D.V. (1983) Peridot from Tanzania. *G&G*, Vol. 19, No. 2, pp. 103–107, http://dx.doi.org/10.5741/GEMS. 19.2.103

Taylor B., Hayes D.E. (1983) Origin and history of the South China Sea Basin. In D.E. Hayes, Ed., *The Tectonic and Geologic Evolution of Southeast Asian Seas and Islands, Part 2*. American Geophysical Union, Geophysical Monograph Series 27, pp. 25–56, http://dx.doi.org/10.1029/GM027p0023

Thuyet N.T.M., Khoi N.N., Hauzenberger C., Hoang N., Tuan D.A. (2013) Some gemmological characteristics of peridot from South Vietnam. *33rd International Gemmological Conference*, Oct. 13–16, Hanoi, pp. 176–178.

Tinh T., Dung L.T., Ty N.H., Lich N.V., Trang N.V., Thuan P.V., Duyen T.D., Nghia T., Vinh V.V. (1997) Geological and Mineral Resources map of Kon Tum, Viet Nam on 1:200.000 (D-48-XVIII).

Toan T.X., Ty N.H. (1995) Geology and gemstones resources in South Vietnam. *Proceedings of the National Conference on Geology of Vietnam, Hanoi*, Oct. 4–10, pp. 153–160.

Y N.V., Phuong N.T., Dung P.T., Lam T.H., Hang H.V. (2006) Forming conditions of basalts on Tay Nguyen Plateau based on the study on features of mineral composition. *Journal of Geology, Vietnam. Series B*, No. 295, pp. 25–38.

BEAD-CULTURED AND NON-BEAD-CULTURED PEARLS FROM LOMBOK, INDONESIA

Nicholas Sturman, Jeffery Bergman, Julie Poli, Artitaya Homkrajae, Areeya Manustrong, and Nanthaporn Somsa-ard

Figure 1. A view of the Lombok farm from the shoreline showing the covered area where the operating and harvesting steps are carried out. Photo by Jeffery Bergman.

Cultured pearls are harvested from wild and hatchery-reared mollusks of various *Pinctada* species in many parts of the world. Today, most of the oysters that form these cultured pearls are raised in hatcheries, and only a few pearl farms still operate using wild oysters. On the Indonesian island of Lom-

bok, the farming procedures follow the industry norm. Some of the authors had the opportunity to visit a Lombok farm (figure 1) in early 2013 to observe the opening and, in some cases, the reseeding/renucleation of numerous *P. maxima* oysters (predominantly gold-lipped). During the one-day visit, we saw a limited number of bead-cultured pearls and even fewer non-bead-cultured pearls ("keshi") recovered from oysters that were opened by the farm owners for the benefit of this research trip. Photos of the recovery and the samples collected, as well as the results of their subsequent analysis, are shared so that
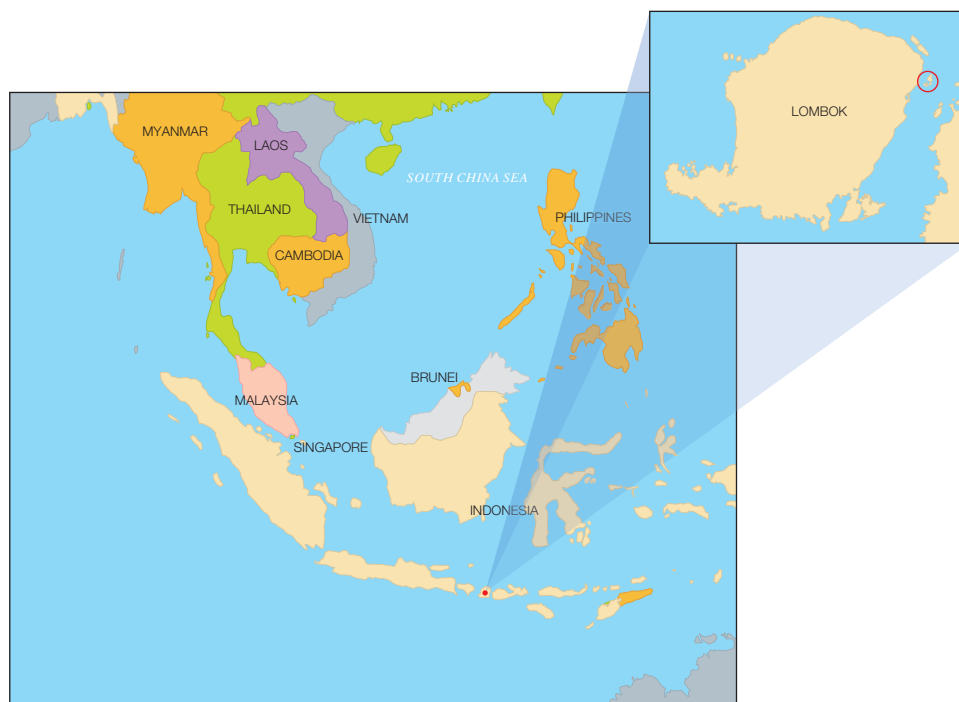
Figure 2. A map of Indonesia and the surrounding region, with Lombok shown in more detail. The red circle indicates the area in which the farm is located.

information on samples of known origin is available in the gemological literature. Analysis of known samples recovered and recorded in this way removes all doubt and gives unequivocal data that can be used with full confidence.

TRIP AND FARM DETAILS

The visit was arranged by author JB, who liaised with Mohamad Irfan Bin Ansori and Wiwi Aswiana, the directors of Jakarta-based Maisya Jewellery. Through their relationship with the owners of the farm, it was possible to visit the operation within a matter of days. The farm itself is located at 8°24′46.33″ S 116°42′45.91″ E (figure 2), off the northeast coast of Lombok, one of the 13,466 islands that make up Indonesia. At an elevation of 3,726 meters, Mount Rinjani is the highest point on Lombok. This active volcano is visible from the farm, though cloud cover obscured the summit on the day of our visit.

The trip from Mataram, Lombok's largest city, took approximately two hours by car—not because of the distance but rather the twisty route through the countryside. The beauty of the sea and the farm's unspoiled environment, both important factors when trying to coax *P. maxima* oysters to produce beautiful pearls, were immediately obvious. The boundaries of the facility were easily within view. Some of the larger Indonesian farms extend for several miles, so this one could be classified as a small-scale operation.

This did not mean that the operation was inferior in any respect, and the authors were impressed by the hatchery in particular.

The most important building on the site was the hatchery, a rather nondescript white structure where all the mollusks used for culturing are raised. While some wild mollusks may have been used to breed offspring for the farm's initial harvests, this does not appear to be the case today. Culturing from farm-raised mollusks seems to be a trend in farms around the world, with the exception of Australia, where a high percentage of wild shells are still used (Marine Stewardship Council, 2015).

During the tour, our hosts were very open and cooperative and allowed us to enter the hatchery and take photographs. The dimly lit interior housed numerous rows of concrete tanks with larvae and spat at various stages of development. In another section of the hatchery, we saw two additional rows of transparent plastic tanks covered with black material to protect the occupants. Finally, in another part of the building we met a young Indonesian biologist who was responsible for ensuring that all the oyster larvae and spat were healthy and eventually able to produce pearls. Shelves in one air-conditioned room of the hatchery were lined with several containers of green, yellow, orange, and colorless liquids (figure 3), a common sight at farm operations today (Cartier et al., 2012). The colored ones contained the various types
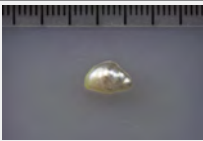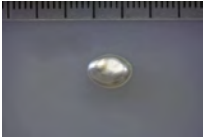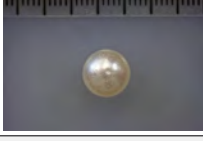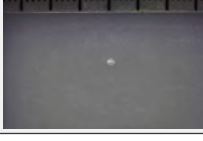
Figure 3. Containers of phytoplankton ready for consumption by hatchery mollusks of various ages. Photo by Nicholas Sturman.

TABLE 1. Pearl samples from Lombok.

Sample number	Photo	Carat weight	Measurements (mm)
0668689302 (NBC)		1.33	8.54 × 6.00 × 4.15
100307378817 (NBC)		1.13	7.82 × 5.79 × 3.74
0668688502 (NBC)		2.48	11.95 × 6.66 × 5.04
100307378805 (bead-cultured)		4.70	8.74 × 8.53
100307378872 ("seed")		0.01	1.38 × 1.02

of phytoplankton at different life stages that were being grown to feed the spat until they were old enough to be moved to the open sea. The role of the marine biologist we met, and others like him throughout pearl farms globally, cannot be underestimated. They are entrusted with making sure that future generations of mollusks thrive and reach an age and size where they can be operated on and produce pearls. Without the knowledge and care of these specialists, the whole concept of pearl farming would not exist.

MATERIALS AND METHODS
The lead author recovered three non-bead-cultured (NBC) pearls directly from the gonad region of their host mollusks and assisted with the removal of some of the nine bead-cultured pearls (including the one shown in table 1) recovered from other mollusks. While some of the bead-cultured pearls were removed from pearl sacs in the gonad region, like the three NBC pearls (table 1), a few were found loose in the hinge area after opening, as they must have fallen out of their sacs during the process. One "seed" pearl was recovered by the lead author during the opening of a shell that also produced a bead-cultured pearl. However, the exact area where the pearl formed within the shell was not clear since it was only found when the organs were being checked for pearls. Those who have searched for pearls in the soft organs of a mollusk know that it is not always easy to find the smaller pearls in field conditions, so the exact formation location of such pearls is rarely recorded.

They are usually found during the final step, when someone meticulously searches the organs. One other shell opened for us was barren. The bead nucleus must have been ejected shortly after insertion, and the mantle implant did not produce a sac in which a pearl could form.

The pearls' internal structures were examined using a Matrix-FocalSpot XT-3 Series real-time X-ray (RTX) machine (90 kV and 5 micron excitation) fitted with a Toshiba image intensifier. A ProCon CT-Mini model X-ray computed microtomography (μ-CT) unit fitted with a Thermo Fisher 8W/90 kV X-ray tube and a Hamamatsu flat-panel sensor detector was used specifically for the three non-bead-cultured pearls and one "seed" pearl. Since all the pearls were white, no Raman or ultraviolet/visible/near-infrared (UV-Vis-NIR) spectra were obtained; these are usually collected on colored pearls. Nor did we record the surface structures or ultraviolet reactions (UV spectroscopy and DiamondView imaging), as the main purpose of this work was to document the internal structures. Even though the pearls were collected from a saltwater environment, their composition was still checked for reference purposes using a Thermo XSeries II laser ablation–inductively coupled plasma–

mass spectrometry (LA-ICP-MS) system equipped with an attached New Wave Research UP-213 nm laser. Microanalytical carbonate standards MACS-1 and MACS-3 from the United States Geological Survey (USGS) were used.

OBTAINING THE SAMPLES

The main purpose of the trip was to observe *Pinctada maxima* samples being opened in field conditions so we could record the positions of the pearls recovered. We ultimately wanted to obtain known examples of non-bead-cultured pearls for further examination in GIA's Bangkok laboratory, as these are the types of pearls most likely to pose identification challenges. Building a reference database of pearls with structures associated with a known provenance is the surest way of solving complex identification issues that may arise. Even though it was not officially harvest time when we visited, our hosts kindly agreed to open a

selection of shells at random to see what they contained (figure 4).

Since the formation of pearls is a purely biological mechanism, it is only through periodic X-ray checks that farms are able to see whether their painstaking work on the mollusks will be rewarded with a pearl. When each mollusk is opened, it is in the hands of fate whether a pearl has actually formed, and whether it is of sufficiently high quality to be considered a gem. Many of the pearls produced on farms around the world are misshapen, blemished, or dull. Because we opened only 13 mollusks, the chances of finding a pearl of any worth were extremely low. The likelihood of finding a non-bead-cultured pearl was even more remote, since the farmers' intent is to produce bead-cultured pearls and not the accidental non-bead-cultured pearls ("keshi") that sometimes occur when beads are ejected from a pearl sac, among other circumstances. While "keshi" might not be the sci-

Figure 4. Of the 13 P. maxima *mollusks opened for us, nine contained a bead-cultured pearl. One was devoid of any type of pearl. Three possessed a non-bead-cultured pearl. Ten of the shells are shown here after opening. Photo by Nicholas Sturman.*

Figure 5. Removal of a bead-cultured pearl (sample 100307378805) from its host mollusk. The pearl sac is clearly visible as a light brown area around the pearl (inset). Photo by Jeffery Bergman.

entifically correct name (Hänni, 2006), the term has become synonymous with pearls that are acciden-

tally formed as a result of bead-culturing in all types of commercially farmed nacreous mollusks (Pteriidae family especially).

Fortune was on our side, as three of the shells opened for us contained a non-bead-cultured pearl in the gonad area. Cultured pearls will only form where the graft is located; nacre-forming epithelial cells are only found in the gonad after the cells have been inserted there during the nucleating process. In unoperated mollusks, these cells are situated only in the mantle tissue that lines both halves of the shell. As with most non-bead-cultured pearls, the samples recovered during this field trip were baroque and exhibited a high luster.

The farm owners were kind enough to allow us to retain the pearls as well as the shells from which they were removed. This allowed us to compare the platy formation of the nacreous pearls and their hosts.

INTERNAL STRUCTURES

Since the purpose of the field trip was to source non-bead-cultured pearls and record their positions in the mollusks, we only detailed the internal features of some of the bead-cultured pearls recovered, one of which is shown being removed from its host in figure 5. Only one (sample no. 100307378805) is included as a representative sample of the typical structure found in such pearls (RTX images only). The one chosen happens to be orientated in a way that clearly shows the banding within the shell nucleus (figure 6) used to instigate the pearl's formation. The banding is visible because of its alignment within the bead nucleus relative to the detector and the X-rays generated from the RTX unit. In some examples, the banding is very distinct in an optimal orientation.

The three NBC pearls (figures 7, 9, and 11) showed structures consisting of void features in a nacreous
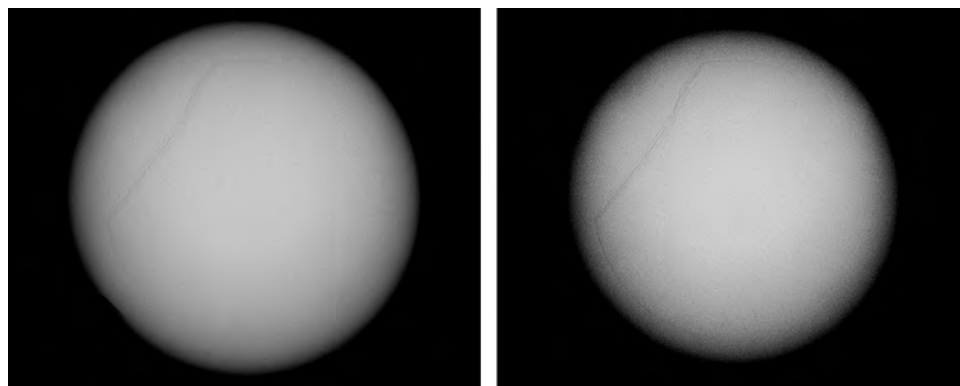

Figure 6. RTX images of the pearl in figure 5 show a fairly large bead nucleus with some banding in one area. The lower-contrast image on the left shows the outline of the bead more clearly. The higher-contrast image on the right shows both the bead's outline and the banding within the bead more clearly.

Figure 7. A non-bead-cultured pearl (sample no. 0668689302) before removal from its host. The pearl is positioned in the gonad region and away from the mantle, where natural pearls are usually recovered. Photo by Nicholas Sturman.

Figure 9. A non-bead-cultured pearl (sample no. 100307378817) still in the light brown pearl sac before removal from its host. Again, the pearl is positioned within the gonad region and away from the mantle. Photo by Nicholas Sturman.

body that lacked distinct concentric rings or surrounding arcs (figures 8 and 10). However, a conchi-olin-rich deposit that followed the outline and hence the shape of the void was present around the voids
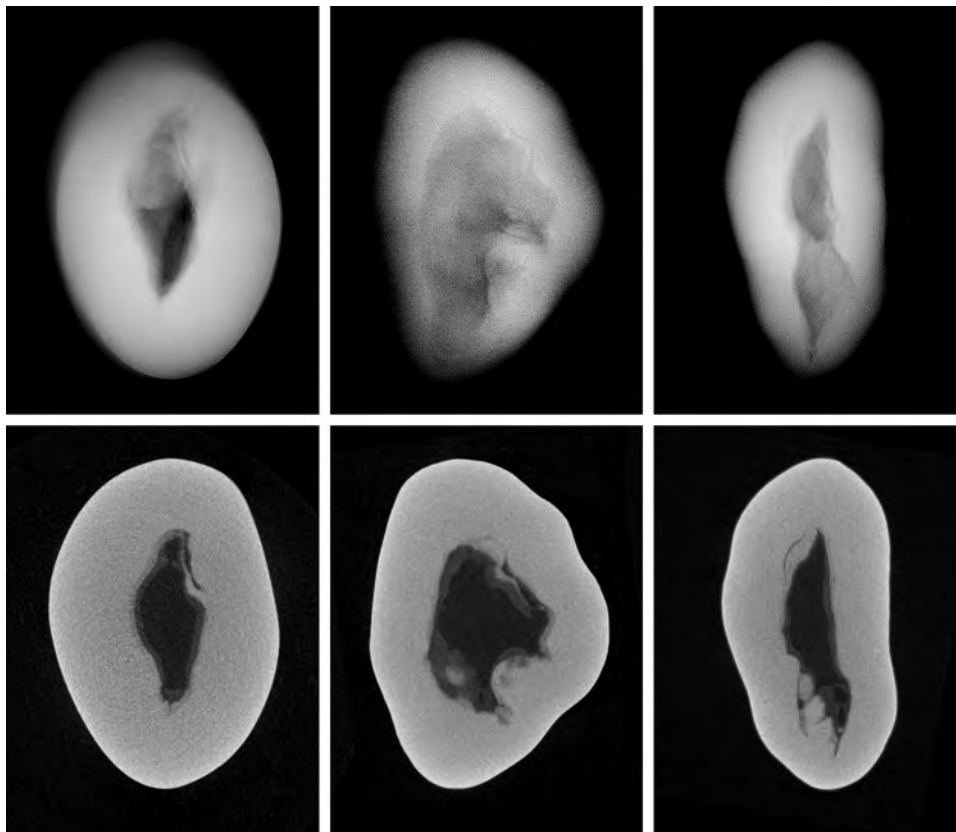

Figure 8. The RTX (top row) and μ-CT (bottom row) images for a non-bead-cultured pearl (sample 0668689302). The RTX images show the whole thickness of the pearl in each orientation, while each μ-CT image shows a micron-thin slice of the structure in each of the directions. This demonstrates the difference between the two types of X-ray techniques.
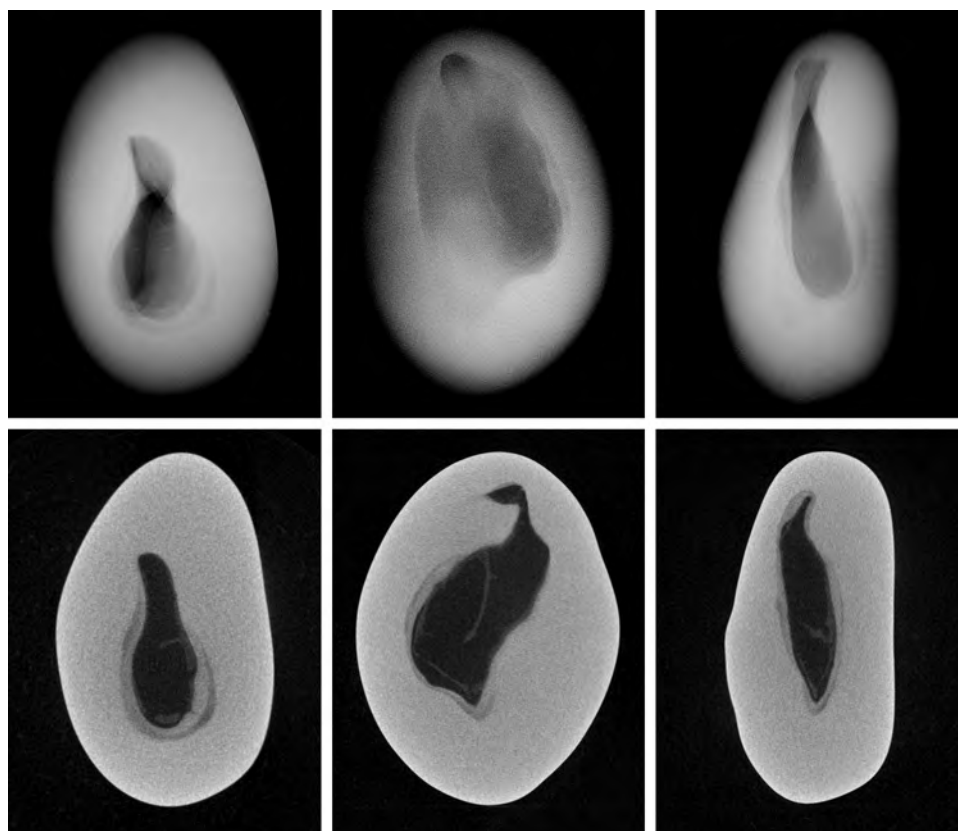
Figure 10. The RTX (top row) and μ-CT (bottom row) images for non-bead-cultured pearl sample 100307378817. The RTX images show the whole thickness of the pearl in each orientation, while each μ-CT image shows a micron-thin slice of the structure in each of the directions.

in all three pearls to varying degrees. This deposition, though not always observed in NBC pearls, is nonetheless a common feature, based on the lead au-

Figure 11. A non-bead-cultured pearl (sample no. 0668688502) positioned near the gonad before removal from its host. Photo by Jeffery Bergman.

thor's experience. Two of the pearls showed one clear central irregular void feature, while the third showed pairs of voids in two separate growth areas. The most common feature of saltwater NBC pearls is a single void (Sturman, 2009). Yet, as the latter example (figure 12) clearly illustrates, two or more voids may also be encountered. Most of the saltwater NBC pearls tested at GIA locations globally show at least one fairly large void or several void features, depending on the shape being examined. The tighter forms showing other features such as linear structures or more natural-looking structures are much less likely to be encountered in a gemological laboratory. But these are the types that can create considerable differences of opinion, which is why collecting known samples on our trip was so important.

Seed pearls like the one found on this trip (figure 13) present their own identification challenges, owing to their small size. Although some show clear natural or NBC structures that prove their origin, many have tight or limited structures that may lead to differences of opinion on their identity. Since the seed pearl we found showed only one weak arc (figure 14), it might be considered more natural by some gemologists. Yet its true classification would be debatable given that it
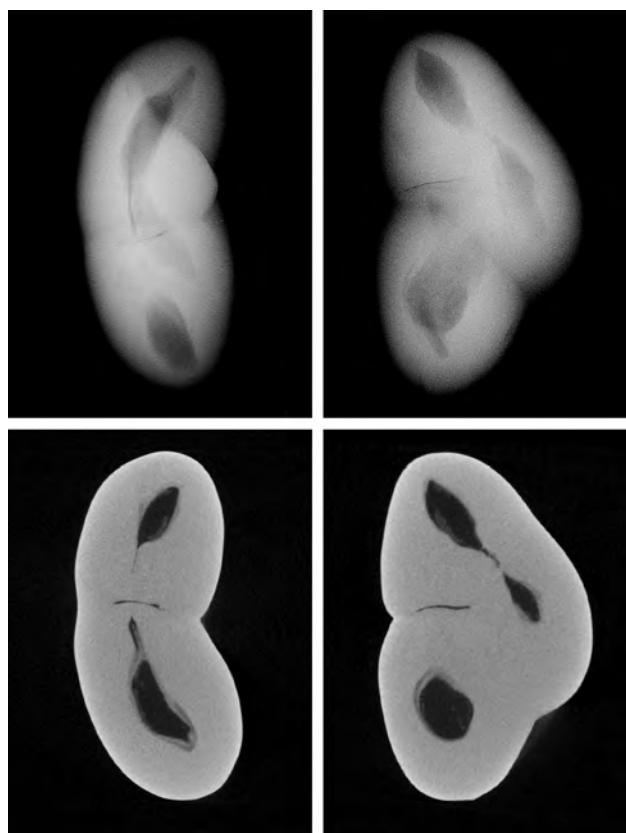
Figure 12. RTX (top row) and μ-CT (bottom row) images of non-bead-cultured pearl sample no. 0668688502 in two orientations. The RTX images show the whole thickness of the pearl in each orientation, while each μ-CT image shows a micron-thin slice of the structure in each of the directions. The thickest orientation was not reproduced here, as the overlapping void features do not provide much insight when examining such multi-structured pearls.

was found in a hatchery shell but likely formed in a pearl sac that was not initiated by humans.

Figure 13. A seed pearl (sample no.100307378872) after discovery in the organs of the same P. maxima shell from which one of the bead-cultured pearls was recovered. Photo by Jeffery Bergman.

CHEMICAL COMPOSITION

Since the pearls are of known saltwater origin, their chemical composition is included purely for academic interest. Work on saltwater pearls from *P. maxima* has already been documented (Scarratt et al., 2012), and our results support the findings of this previous work. The manganese content of saltwater pearls is generally accepted to be much lower than that of freshwater pearls; strontium, gallium, barium,
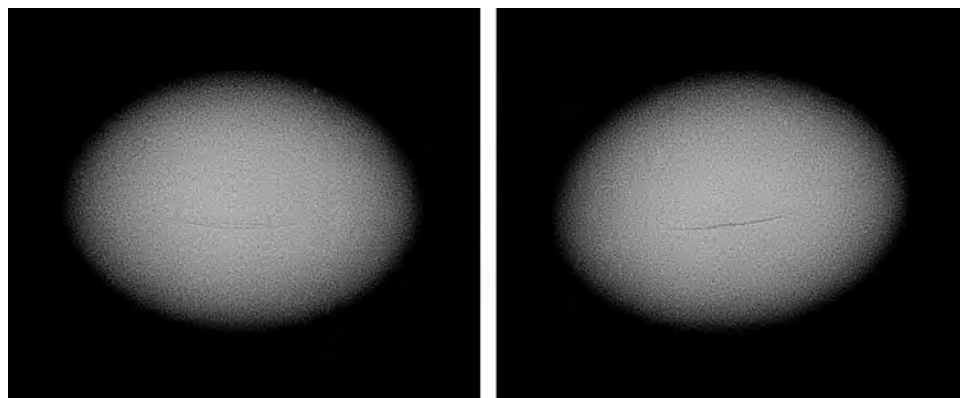

Figure 14. RTX images of the seed pearl (sample no. 100307378872) in two orientations. The RTX images show the whole thickness of the pearl in each orientation; since the linear feature is so fine and the pearl so small, μ-CT analysis did not yield results worth reproducing here.

Sample	^{7}Li	^{11}B	^{23}Na	^{24}Mg	^{31}P	^{39}K	^{45}Sc	^{55}Mn	^{57}Fe	^{66}Zn	^{69}Ga	^{88}Sr	^{137}Ba	^{139}La	^{140}Ce	^{208}Pb	^{209}Bi
0668689302	0.43	16.8	4830	213	bdl	40.1	bdl	23.3	494	bdl	bdl	1050	0.35	0.042	0.04	bdl	bdl
100307378817	0.56	14.0	5210	120	bdl	56.3	bdl	36.1	460	bdl	bdl	860	0.21	0.07	0.038	0.13	bdl
0668688502	0.64	18.1	7530	152	bdl	82.1	bdl	34.0	577	bdl	bdl	1480	0.23	0.042	0.056	0.21	bdl
100307378805	0.51	18.1	6250	111	bdl	138	bdl	12.6	533	bdl	bdl	1420	0.33	0.074	0.078	0.24	bdl
100307378872	0.65	15.8	5820	112	bdl	48.3	bdl	21.6	465	bdl	bdl	1230	0.23	0.075	0.071	0.17	bdl
Detection limit	0.064	1.138	4.679	0.113	91.429	3.889	0.705	0.527	14.609	0.792	0.118	0.003	0.008	0.001	0.001	0.027	0.021

Abbreviation: bdl = below detection limit

and boron levels also differ between saltwater and freshwater mollusks. Table 2 shows the concentration (parts per million) of these and other elements in the samples from this study.

CONCLUSIONS

The three indisputably non-bead-cultured pearls described here, which were removed by the lead author, are just a minute selection of the pearls removed by GIA research staff from shells taken from the open ocean (according to permitted quotas for mother-of-pearl recovery) or from farms around the world. While the structures did not prove to be unusual in any way, and hence fall within those expected for ac-

cidentally formed "keshi" NBC pearls, the recording of their structures should assist those in the trade who deal in or conduct research on examples of such pearls from *known* sources.

Trips to other farms and natural pearl sources worldwide to recover pearls of known origin (figure 15) have helped establish a GIA database of structures, and more visits are planned over the coming months and years. Only by continuing to work with farmers and shell seekers can such a database be accomplished, and only with their cooperation is it possible to accumulate such important samples and knowledge. For that, GIA and the trade cannot be appreciative enough.

Figure 15. A group of bead-cultured pearls of various hues recovered from hatchery-bred Pinctada maxima *oysters on the Lombok farm prior to the authors' visit. Photo by Julie Poli.*

REFERENCES

Cartier L.E, Krzemnicki M.S., Ito M. (2012) Cultured pearl farming and production in the Federated States of Micronesia. *G&G*, Vol. 48, No. 2, pp. 108–122, http://dx.doi.org/10.5741/GEMS.48.2.108

Hänni H.A. (2006) A short review of the use of "keshi" as a term to describe pearls. *Journal of Gemmology*, Vol. 30, Nos. 1–2, pp. 52–58.

Marine Stewardship Council (2015) MSC offers a pearler of an opportunity for gem producers. http://www.wamsc.com.au/news/mediaitem.phtml?MediaID=37

Scarratt K., Bracher P., Bracher M., Attawi A., Safar A., Saeseaw S., Homkrajae A., Sturman N. (2012) Natural pearls from Australian *Pinctada maxima*. *G&G*, Vol. 48, No. 4, pp. 236–261, http://dx.doi.org/10.5741/GEMS.48.4.236

Sturman N. (2009) The microradiographic structures of non bead cultured pearls. http://www.giathai.net/microradiographic-structures-cultured-pearls/

For More on Pearls from Lombok

To view a photo gallery showing pearl farming operations on the Indonesian island of Lombok, please visit www.gia.edu/gems-gemology/fall-2016-bead-cultured-pearls-lombok-Indonesia

G&G Lab Notes

Editors
Thomas M. Moses | Shane F. McClure

DIAMONDS

Evidence of Focused Beam Irradiation In Treated Pink Diamond

A Fancy pink diamond, confirmed as natural-grown, was found to be type IIa and colored by NV^- centers. As part of routine testing, DiamondView fluorescence images were collected to check for synthetic growth features. These images showed unusual patterning in the form of two pink spots near the edge of the table facet (figure 1). Both spots were approximately 0.9 × 0.7 mm, and the table facet was approximately 3.0 mm in diameter. The orange fluorescence throughout most of the table was likely due to NV^0 centers, whereas the pink components were likely due to NV^- centers.

To further investigate the spatial distribution of the $NV^{0/-}$ centers, we acquired a photoluminescence (PL) image of the diamond's table using a 532 nm laser. Figure 2 shows the distribution of the NV^0 and NV^- centers. The distribution of the NV centers confirms the presence of two spots on the table. Figure 3 shows the average PL spectra from inside one of the spots and the average PL spectra from the region outside the spots. Figures 2 and 3 demonstrate that the intensity of the NV centers was greater inside the spots than in the rest of the table. Inside the spots, the average

peak area intensity of the NV^0 center was approximately two times greater and the average peak area intensity of the NV^- centers was approximately three times greater. The spots were comparable in both size and defect concentrations.

To determine the vertical distribution of the NV^- center, a 500 µm PL depth profile was acquired through each spot. This is an automated process the instrument can perform in which a series of spectra are collected along a line spanning the diameter of the spot. The stage is then offset 5 µm in the vertical direction to focus farther into the diamond, and another series of spectra are collected. The process was re-
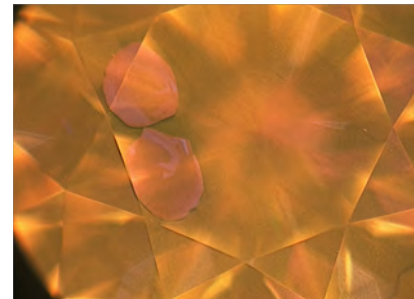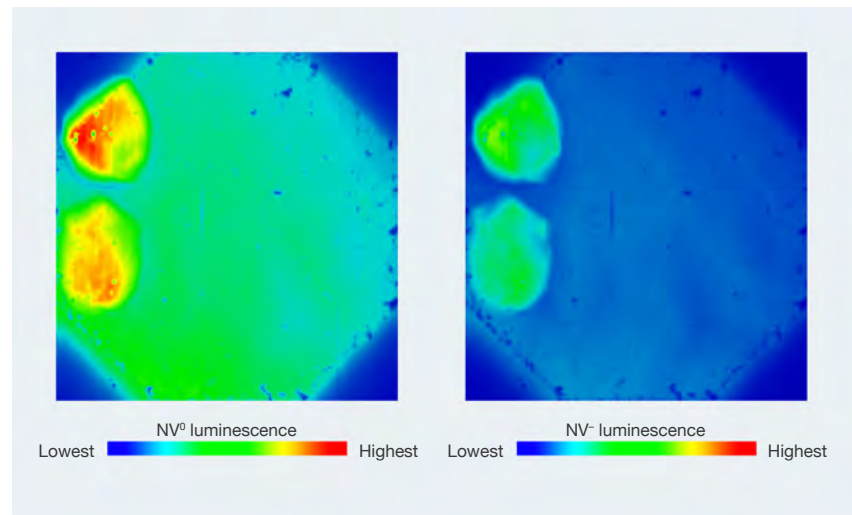

Figure 1. This DiamondView image of the table of a pink diamond shows two distinct pink spots. Field of view approximately 5 mm.

peated 100 times until the target depth of 500 µm was reached. This

Figure 2. Left: A PL map showing the peak area distribution of the NV^0 center. Field of view is approximately 3 mm; scale is relative intensity. Right: A PL map showing the peak area distribution of the NV^- center. Field of view is approximately 3 mm; scale is relative intensity.

NV⁰ luminescence — Lowest … Highest
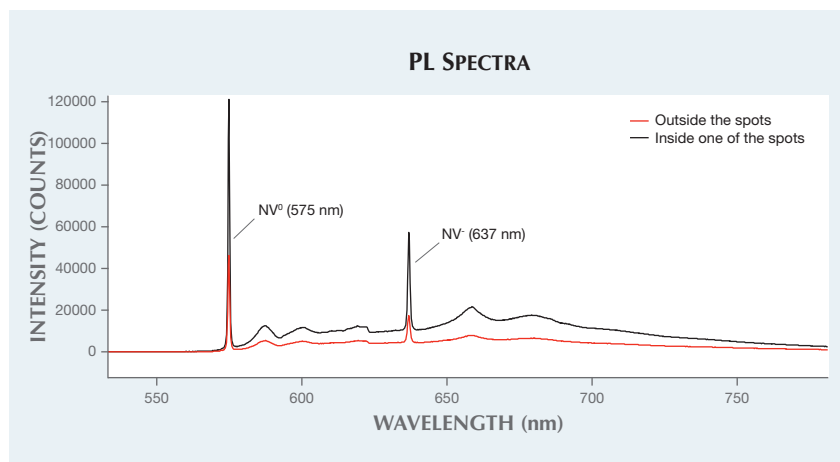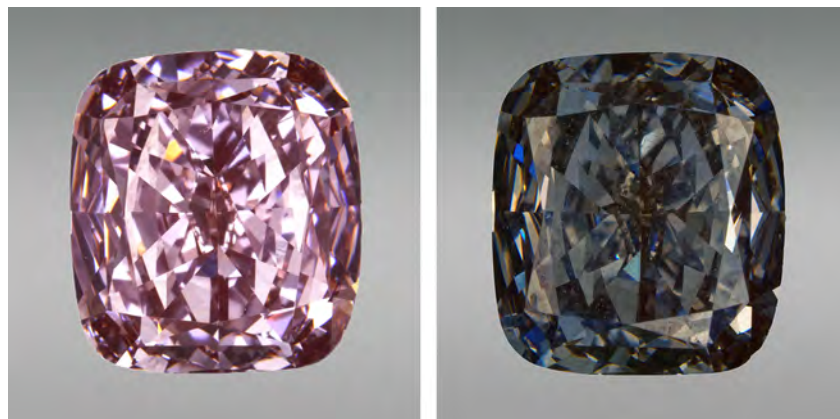
NV⁻ luminescence — Lowest … Highest

PL Spectra

Figure 3. A comparison between average PL spectra from inside one of the spots and the area outside the spots. The y-axis scale is the same for both spectra, so it is apparent that the intensity inside the spot is higher for both NV⁰ and NV⁻ centers.

achieved a depth profile of NV⁻ luminescence, indicating how deeply the irradiation beam had penetrated into the stone. One spot showed an average penetration depth of 100 μm and the other 50 μm. It is important to note that this is axial displacement, which in confocal microscopy is an approximation of the true depth of the illuminated feature. Nevertheless, this demonstrated the shallow penetration of the irradiation beam.

The intensity variation in the NV centers strongly demonstrated that this diamond was HPHT annealed and isolated nitrogen was subsequently introduced due to disaggregation of the A-form nitrogen (pairs of nitrogen atoms) or B-form nitrogen (four nitrogen atoms around a vacancy). It also indicated that this diamond was irradiated by a focused electron beam with relatively low energy (≤ 1 MeV) prior to annealing. These multiple processes introduced high concentrations of NV centers into the localized shallow areas. Furthermore, an increase of electron donor defects at the incident beam area would lead to the observed patterned distribution of the NV⁻ centers. The narrow, focused nature of the electron beam is responsible for the distribution of the defects into the two spots and therefore the reason why the pink spots are observed in the DiamondView image. The two spots may be the result of two separate beams in the irradiation setup. Alternatively, the second spot may be from an additional round of treatment designed to further enhance the color. It is also unusual for the treatment to be done through the table rather than on the culet. It is unknown what benefits the focused beam will have over wide-beam irradiation.

Troy Ardon and Lorne Loudin

Treated Pink Type IIa Diamond Colored by Red Luminescence

Recently, the Carlsbad laboratory received a 4.29 ct type IIa diamond for color origin determination. In daylight-equivalent illumination, the diamond was color graded as Fancy brown-pink, but under incandescent light it appeared Fancy purplish gray (figure 4).

When exposed to long-wave UV light at 365 nm, the diamond exhibited medium orange fluorescence. Based on photoluminescence (PL) spectroscopy, collected using several lasers, it was identified as a treated diamond that had been subjected to high-pressure, high-temperature (HPHT) annealing, irradiation, and subsequent low-pressure annealing. The PL spectra were dominated by the presence of strong NV centers at 575 and 637 nm, along with a strong GR1 peak, confirming the cause of the diamond's luminescence as the NV centers.

UV-Vis-NIR absorption spectra were collected at room temperature (figure 5) and at liquid nitrogen temperature inside an integrating sphere for this diamond (along with a 0.48 ct treated pink CVD synthetic that does not show the pronounced color change, for comparison). At liquid nitrogen temperature with the diamond under incandescent illumination, the

Figure 4. This 4.29 ct type IIa color-treated diamond was graded as Fancy brown-pink under daylight conditions (left) and appeared Fancy purplish gray under incandescent lighting (right). The color change is due to strong NV fluorescence under UV to blue light exposure and irradiation-related GR1 absorption under incandescent illumination.
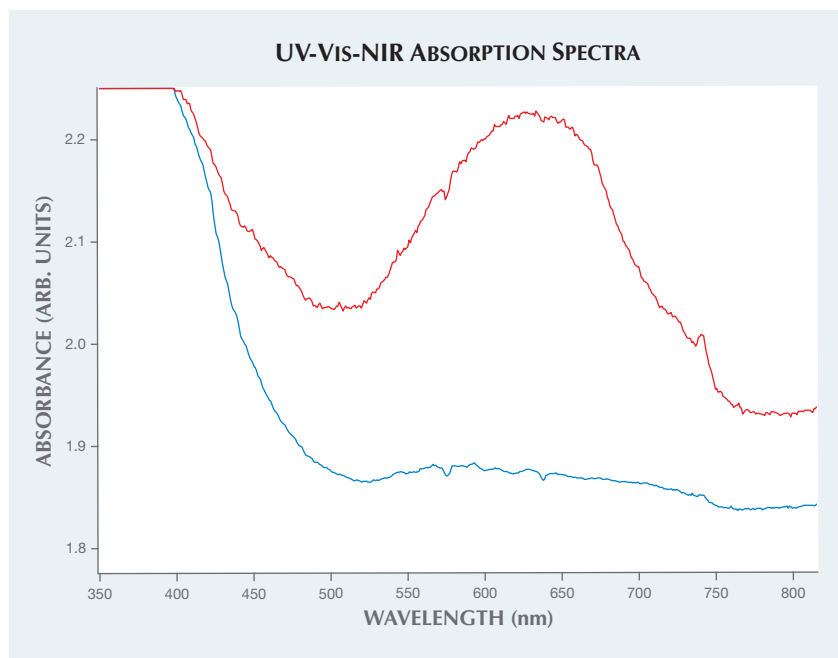
UV-Vis-NIR Absorption Spectra

Figure 5. Room-temperature UV-Vis-NIR absorption spectra were collected on the 4.29 ct treated sample (red trace) and a 0.48 ct treated CVD synthetic (blue trace) with a color grade of Fancy Vivid purplish pink. While NV-related red luminescence caused a pronounced difference in color for the 4.29 ct sample, it only produced a minor change in the treated CVD synthetic. In incandescent light (and with minimal influence of the red luminescence), the synthetic's color shifted slightly to Fancy Deep purplish pink. The pronounced absorption from the GR1 peak (550–750 nm) within the 4.29 ct diamond accounts for the purplish gray color in incandescent lighting.

most prominent feature was the GR1 peak creating the purplish gray coloration, comparable to the blue color generated in many irradiated type IIa diamonds. In daylight-equivalent illumination, the emissions of the NV^0 and NV$^-$ centers were superimposed on the absorption spectrum, thus influencing the diamond's color within the yellow to red region of the visible spectrum. Color grading of diamonds includes the effect of fluorescence, and therefore the reported color was Fancy brown-pink.

While treated diamonds have pronounced UV fluorescence due to NV centers, fluorescence spectra collected at a variety of wavelengths show that the NV luminescence is actually stronger when excitation is from blue light (450–500 nm) than from ultraviolet wavelengths, as in the case of this stone (figure 6). This strong emission stimulated by visible light indicates the diamond is colored by red luminescence in response to blue light and, to a lesser extent, by fluorescence due to the UV component in daylight. Other treated pink diamonds, colored by NV absorption, showed similar excitation spectra (Y. Luo and C.M. Breeding, "Fluorescence produced by optical defects in diamond," Summer 2013 *G&G*, pp. 82–97). This red luminescence due to NV centers is comparable to the more commonly noted green transmission luminescence from the H3 centers seen in some yellow diamonds. Such yellow diamonds receive greenish color grades due to the visible influence of the green emission on the perceived color in daylight conditions.

For most treated pink diamonds, red luminescence corresponds with and enhances the pink bodycolor (Fall 2011 Lab Notes, pp. 228–229), much like chromium-related red fluorescence enhances the color of rubies. Since bodycolor closely corresponds to luminescence color for most treated pink diamonds, the color difference between daylight and incandescent light sources is minimal. For example, the 0.48 ct treated pink CVD synthetic diamond (figure 5, blue trace) was color graded as Fancy Vivid purplish pink using a daylight-equivalent light and as Fancy Deep purplish pink under an incandescent light. The NV-related emission, excited by the UV to blue light, brightened the diamond in that viewing environment.

The purplish gray bodycolor for this 4.29 ct treated diamond seen under incandescent light derived from the strong GR1 absorption induced by irradiation. The GR1 intensity, as measured by 633 nm photoluminescence spectroscopy and normalized using the diamond Raman peak, was compared with 20 other treated pink diamonds that did not show a substantial color shift. The GR1 intensity of this diamond was 8 times greater than the average value of the 20 treated pink diamonds and 3.5 times greater than the highest value. The GR1 intensity of this diamond was comparable to irradiated green to blue diamonds. In incandescent light, the red luminescence appeared to provide a minimal contribution, as the modifying hue was purplish (implying a reddish component) and not bluish as one might reasonably expect for an irradiated diamond.

Other diamonds have shown a shift in color grade due to appreciable fluorescence. Examples include the 56.07 ct Tavernier diamond, which displays a brown to pink color shift (Y. Liu et al., "The alexandrite effect of the Tavernier diamond caused by fluorescence," *Color Research and Application*, Vol. 23, No. 5, 1998, pp. 323–327), and a few type Ib diamonds with a NV-related color shift from greenish brown to orangy brown (Fall 2011 GNI, pp. 234–235).

Some CVD-grown diamonds also have shown a pink to blue color shift,
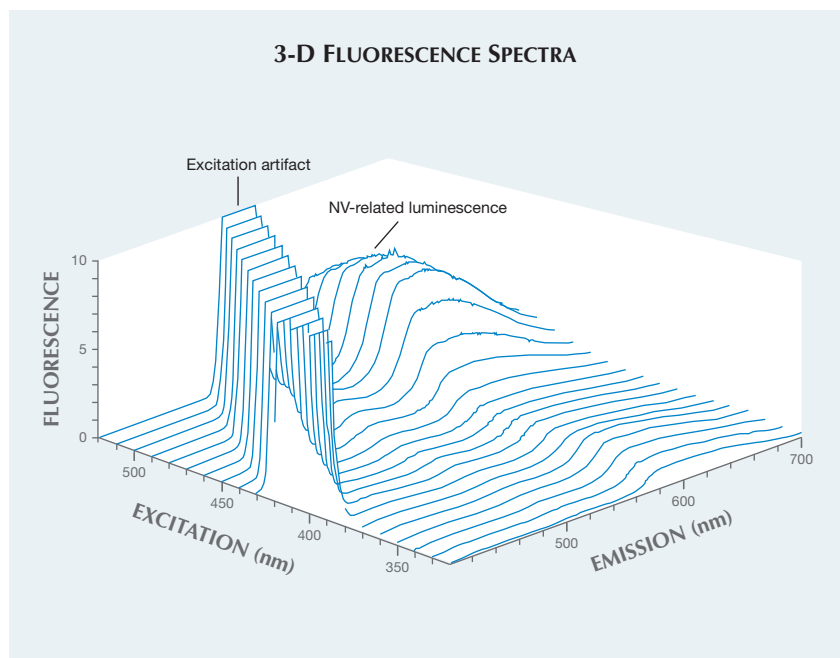
3-D FLUORESCENCE SPECTRA

Figure 6. These 3-D fluorescence spectra were collected using excitation from the UV range through the blue range of visible light (320–520 nm). The corresponding fluorescence spectra show that the relative intensity is much higher when excited by wavelengths within the visible region than in the UV region. This indicates that red luminescence excited by visible light is a greater contributor to the pink color than the UV-activated fluorescence. The 0.48 ct treated CVD synthetic shown in figure 5 demonstrated identical behavior—refer to Luo and Breeding (2016) for comparable spectra—and indicates that NV-related luminescence contributes to the graded color in many pink diamonds that are colored by NV centers. The excitation artifact occurs when the emission spectrometer scans across the excitation wavelength.

anism. In those synthetic diamonds, the color change was caused not by a difference in light sources, but by a temporary charge-transfer effect activated by UV exposure. For those CVD synthetics with a high concentration of silicon impurities, UV exposure precipitated a charge transfer between negative and neutral silicon-vacancy centers. In one CVD specimen, the relative concentrations of SiV⁻ and SiV⁰ were essentially reversed with UV exposure and thus influenced the color change from its stable color of Fancy brown-pink to a temporary Fancy Intense blue (U. D'Haenens-Johansson et al., "CVD synthetic gem diamonds with high silicon-vacancy concentrations," *Conference on New Diamond and Nano Carbons*, May 2015, Shizuoka, Japan).

The 4.29 ct natural diamond noted here was HPHT annealed and irradiated to create the NV centers. It appeared to have been irradiated to a far greater extent than most treated pink diamonds, and as a result it had a significantly higher GR1 intensity (as shown in figure 5 and confirmed with 633 nm PL). This accounts for its purplish gray color in incandescent light. The color change between these two attractive colors, along with its large size, makes this diamond quite unusual and serves to illustrate that the color of treated pink diamonds is assisted by red luminescence. This stone also demonstrates that while multiple treatments can provide for some identification challenges, they can also create some truly intriguing products.

Sally Eaton-Magaña

Very Large Artificially Irradiated Yellow Diamond

Artificial irradiation and annealing to enhance or change color is one of the oldest diamond treatments. English chemist Sir William Crookes first discovered the effects of radiation on a diamond's color, conducting experiments using radium salts in 1904. Today, only a very small percentage of all natural diamonds are irradiated, typically with an electron beam. Because of the risk of damage, diamonds subjected to this treatment are typically under 10 carats.

A 59.88 ct yellow diamond (figure 7) recently examined at the New York laboratory received clarity and color grades of SI₁ and Fancy Vivid yellow. While the face-up color distribution was classified as even, we observed a moderate color concentration along the culet typical of some artificially irradiated diamonds (figure 8). Microscopic examination showed noticeable crystal inclusions at 10× magnification as well as extensive burn marks across the entire surface of the stone. The diamond showed chalky blue fluorescence under longwave UV excitation and medium yellow fluorescence under short-wave UV.

Using a desktop spectroscope, the diamond's visible absorption spec-

Figure 7. This 59.88 ct Fancy Vivid yellow diamond was treated through artificial irradiation and annealing.
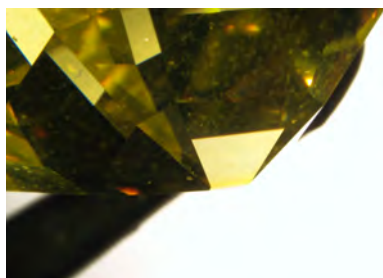
Figure 8. Strong color concentration along the diamond's culet is evidence of artificial irradiation.

trum revealed a series of absorption lines between 415 and 477 nm, indicative of a "cape" diamond. Additionally, an unusually strong peak at 503.2 nm (H3) was noted using a UV-visible spectrometer (figure 9). The enhancement of this H3 center is responsible for the very desirable yellow color. The infrared absorption spectrum showed high concentrations of nitrogen in the one-phonon region, indicating type Ia diamond. Further examination of the infrared region revealed a minor hydrogen de-

fect as well as weak to moderate peaks at approximately 4935 cm^{-1} (H1b) and 5165 cm^{-1} (H1c), further evidence of treatment.

These features led to the conclusion that the diamond was artificially irradiated and annealed (by introducing the H3 defect) to induce a more desirable yellow color. This was by far one of the largest artificially irradiated diamonds identified at GIA, surpassing previous examples by several carats (see Summer 2012 Lab Notes, p. 132; Winter 2014 Lab Notes, p. 295). This diamond reiterates the importance of careful analysis, since even the largest stones may have undergone treatment.

Paul Johnson and
Christopher Vendrell

Unusual Purple Inclusion in EMERALD

Depending on geographic locality, inclusions in emerald are typically similar from one stone to the next. We expect to see classic jagged three-phase inclusions in Colombian emeralds or blocky multiphase inclusions and phlogopite in Zambian emeralds, so it is always interesting for the gemologist to observe something out of the ordinary. The Carlsbad laboratory recently examined a 7.11 ct oval mixed-cut emerald (figure 10), identified by standard gemological testing. Microscopic examination revealed jagged to irregular multiphase inclusions, planes of reflective thin films, clarity-enhanced fractures, and—surprisingly—a fairly large purple inclusion with a subhedral form. Upon closer examination, distinct purple and near-colorless banding was visible (figure 11), and the inclusion proved to be singly refractive when viewed between crossed polarizers. The inclusion was too deep within the stone to confirm its identity with Raman spectroscopy, but its appearance and optic character pointed to fluorite. Based on these characteristics, another possible identity could be halite, but this inclusion strongly resembled a color-banded fluorite inclusion previously reported in emerald by GIA's laboratory in 1969. In that example, the surface-reaching inclusion was identified by scraping a sample and analyzing it with X-ray diffraction

Figure 9. The yellow diamond's Vis-NIR absorption spectrum shows a strong peak corresponding to the H3 defect observed at about 503 nm.

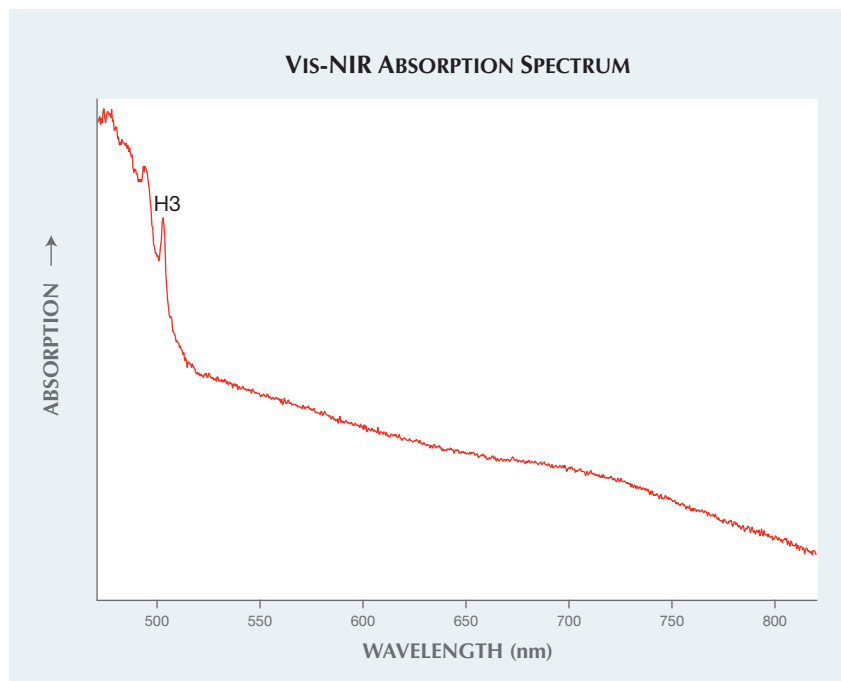**VIS-NIR ABSORPTION SPECTRUM**

Figure 10. This 7.11 ct emerald contains a large purple inclusion visible under the table.
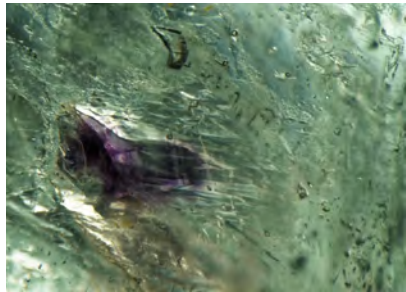
Figure 11. With microscopic examination, clear purple banding is apparent within this fluorite inclusion. Field of view 2.34 mm.

(R.T. Liddicoat, "Developments and highlights at the Gem Trade Lab in Los Angeles," Summer 1969 *G&G*, p. 63).

Fluorite inclusions in emerald have been cited from various localities, as a product of pegmatitic/hydrothermal involvement in formation (E.J. Gübelin and J.I. Koivula, *Photoatlas of Inclusions in Gemstones*, Vol. 3, Opinio Verlag, Basel, Switzerland, 2008, pp. 354–406; D. Schwarz et al., "Emerald and green beryl from Central Nigeria," *The Journal of Gemmology*, Vol. 25, No. 2, 1996, pp. 117–141). These inclusions are usually described as colorless octahedra, although sometimes they are seen as cubes or rounded shapes. Purple banded fluorite is an unusual inclusion in emerald, making this an interesting and unexpected addition to an otherwise typical inclusion scene.

Claire Ito

Non-Nacreous Purple and White PEARLS Reportedly from *Spondylus* Species

The Carlsbad laboratory recently examined three non-nacreous pearls, weighing 7.85 to 9.85 ct and measuring from 10.50 × 10.21 mm to 12.43 × 11.65 × 10.65 mm (figure 12). All three pearls exhibited similar uneven bodycolors and surface characteristics. They displayed purple and white colors with some yellowish brown tints and possessed a porcelaneous surface with mottled to clear fine flames. They were reportedly fished near Ligui, on the eastern coast of the Mexican state of Baja California Sur.

Similar surface structures have been reported in *G&G* (Fall 2014 Lab Notes, pp. 241–242; Winter 2015 Lab Notes, pp. 436–437; Summer 2016 Micro-World, pp. 202–203). A characteristic reflective blue coloration on the base of the 9.85 ct semi-baroque button (figure 13) was clearly visible when the flame structure was illuminated with a fiber-optic light. More-
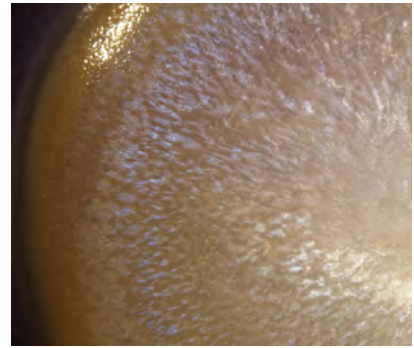

Figure 13. The characteristic reflective blue coloration of Spondylus *pearls was visible within the flame structure of the semi-baroque button pearl when illuminated with a fiber-optic light. Field of view 5.77 mm.*

over, subsurface to surface-reaching acicular inclusions found in most *Spondylus* pearls examined previously were also present in these samples. These inclusions, which appear in the form of tubes or needles, are often associated with the flame structure. At first the inclusions were believed to be parasite channels, which are sometimes observed in shells and pearls of various nacreous and non-nacreous mollusks. But after careful inspection they were seen to be part of the structure, radiating from within and reaching the surface in the same direction and with fairly consistent size and shape—whereas the parasite channels are irregularly shaped and in various sizes, running in random directions and usually crossing over each other.

The pearls' dimpled surface texture appears to be caused by the slightly recessed openings where these inclusions reach the surface. This unique feature is also found on the interior of *Spondylus* shells in GIA's Bangkok laboratory collection (figure 14). The resemblance between a pearl's surface and the interior surface of its host are useful in identifying the mollusk species. Yet many marine gastropods and bivalves pro-

Figure 12. These three purple and white non-nacreous pearls weighing 7.85, 8.37, and 9.85 ct (left to right) are reportedly from Spondylus calcifer.
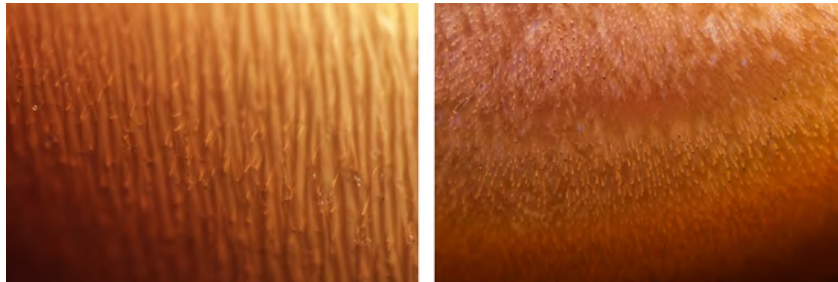
Figure 14. Subsurface to surface-reaching acicular inclusions were found on the interior of a Spondylus shell (left) from the GIA Bangkok reference collection and associated with the flame structure in a Spondylus pearl (right). Fields of view 1.31 mm and 2.37 mm, respectively.

duce non-nacreous pearls, and their similar surface structure and color sometimes make mollusk identification challenging. As with the previously reported *Spondylus* pearls, microradiography of all three pearls revealed tight structures, and no obvious growth arcs were seen.

The *Spondylus* genus (commonly known as "thorny" or "spiny" oyster) consists of about 76 living species distributed in tropical waters around the world. *Spondylus princeps* and *Spondylus calcifer* (also known as *Spondylus limbatus*) are two of the main species on the western coast of the Americas. *S. princeps* is found from the gulf side of Baja California down the Pacific coast of Mexico through Panama to northwest Peru. *S. calcifer* is found in the Sea of Cortez (Mexico) and Ecuador (K. Lamprell, *Spiny Oysters: A Revision of the Living Spondylus Species of the World*, Jean Lamprell, Brisbane, Australia, 2006). Most *Spondylus* pearls examined by GIA are reportedly from *Spondylus princeps*, whose bodycolor is typically white to cream or various saturations of pink, orange, and brown. This is the first time GIA has examined pearls with such a dominant purple hue reported to be from *Spondylus calcifer*. This species has been recorded as producing pearls in Costa Rica (E. Strack, *Pearls*, Ruhle-Diebener-Verlag GmbH & Co., Stuttgart, 2006, p. 59).

Artitaya Homkrajae

Lead Glass–Filled Black Star SAPPHIRE

Fracture and cavity filling of gemstones has been practiced for hundreds of years. In recent times, this treatment has become more sophisticated and widespread, particularly with the use of lead glass, which is most often seen in rubies. The addition of lead oxide (PbO) to silica glass lowers its working temperature and viscosity while raising its refractive index from approximately 1.5 to as high as 1.8. Thus, the filler has an RI that matches many gem materials, making fractures and voids virtually disappear. But the softness and low melting point of the filler create durability issues, especially in low-quality filled rubies (S.F. McClure et al., "Identification and durability of lead glass–filled rubies," Spring 2006 *G&G*, pp. 22–34).

Common inclusion features for lead glass–filled ruby composites include blue flashes from the fractures and trapped gas bubbles. Glass features can also be detected using Fourier-transform infrared (FTIR) spectrometry and energy-dispersive X-ray fluorescence (EDXRF) spectroscopy. But if the ruby has very few areas that are enhanced with lead glass, they may not be obvious under magnification, and FTIR and EDXRF may not detect them. Real-time X-ray (RTX) imaging systems, used by GIA to identify pearl growth features and confirm filling in diamonds, can be

beneficial in differentiating between lead glass and ordinary glass filling in rubies and other gemstones. This is due to opacity differences, as lead glass has a lighter appearance than glass without lead. A combination of X-ray imaging and magnification is also capable of quantifying the extent of lead glass treatment performed on a gemstone.

A 25.10 ct opaque black star sapphire (figure 15) was submitted to the New York laboratory for identification. The stone contained a few hairline fractures and dense golden silk needles. At first glance, the sapphire had a few features that would arouse suspicion for treatment, such as round cavities on the base and a few inconspicuous fractures (figure 16). The sapphire also had a specific gravity of 4.04, which is above the normal range for corundum. Natural black sapphire may have a higher SG due to abundant asterism-causing inclusions of rutile or hematite, both of which are denser than corundum. Because of the stone's opacity, it was difficult to observe internal inclusions under magnification.

Using X-ray imaging analysis (figure 17), it was clear that the fractures and multiple cavities had been filled

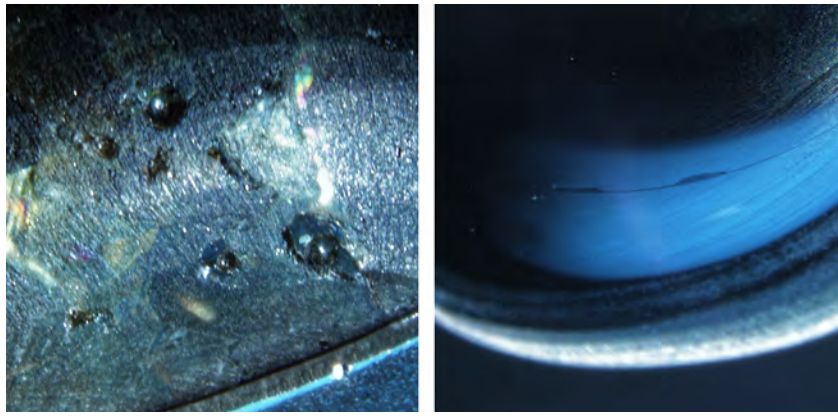Figure 15. This 25.10 ct black star sapphire was enhanced with lead glass.

Figure 16. Gas bubbles visible in the sapphire's cavities (left) and a thin fracture with different surface luster (right) indicate the possibility of lead glass filling. Fields of view 2.10 mm (left) and 3.90 mm (right).

with lead glass, and this finding was confirmed by EDXRF. These properties would have been extremely difficult to see under normal visual magnification.

Figure 17. Face-up (top) and profile (bottom) RTX images of the black star sapphire. The white areas indicate higher opacity in fractures and cavities, evidence of lead glass filling. Noticeable round gas bubbles are trapped in cavity fillings.
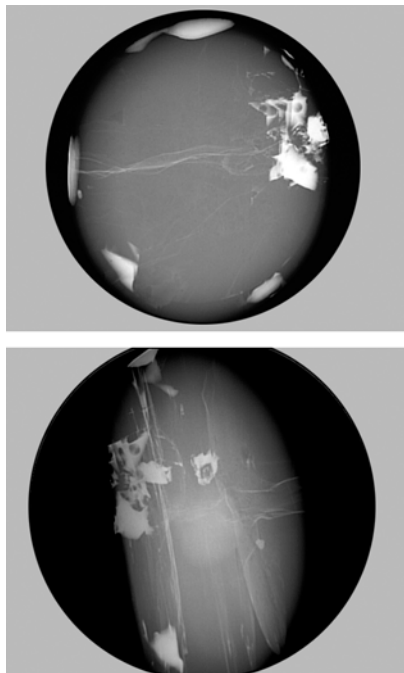
This is the first example of a lead glass–filled black star sapphire examined in the New York laboratory.

Akhil Sehgal

Sapphire Rough Filled with Green Lead Glass

The Carlsbad laboratory recently examined a yellow-green hexagonal prismatic crystal (figure 18, left) that was presented as sapphire. The rough specimen was approximately 11 mm long. The specific gravity was measured as 4.00, and the stone was inert to both long- and short-wave UV. The identity of the rough sapphire was confirmed by Raman spectroscopy.

Microscopic examination revealed that the stone was partially covered by drops of green glassy residue, and numerous fractures throughout it were filled with the same material. Also observed were numerous trapped gas bubbles and a prominent orange flash effect, consistent with a lead-glass filling (figure 18, right). Energy-dispersive X-ray fluorescence (EDXRF) analysis confirmed the presence of lead.

Laser ablation–inductively coupled plasma–quadrupole mass spectrometry (LA-ICP-MS) was used to investigate the chemical composition of the green glassy residue. A line of ablation spots, positioned on one of the flat crystal faces, was designed to cross a large drop of the residue. The oxide weight percent profile (figure 19, left) revealed that the residue contained 9.3 to 9.7 wt.% B_2O_3, 23.7 to 24.9 wt.% Al_2O_3, 12.2 to 12.6 wt.% SiO_2, 3.6 to 4.2 wt.% CuO, 1.2 to 1.3 wt.% CdO, and 45.4 to 47.4 wt.% PbO. The combined oxide weight percent of Li, Na, K, Ca, and Zr was around 1.5 (averaged value). The chemical analysis confirmed that the filler was lead glass.

With such a small amount of Al (2.6 wt.% Al_2O_3) in the lead glass (Z.Q. Zeng and P. Hing, "Preparation and thermal expansion behavior of glass coatings for electronic applications," *Material Chemistry and Physics*, Vol. 75, No. 1–3, 2002, pp. 260–264), the approximate composition of major elements can be obtained by subtracting 24.22 wt.% Al_2O_3 (arising from the host sapphire crystal) from the total chemical composition and renormalizing the sum

Figure 18. Left: This hexagonal green sapphire rough was treated with a green lead-glass filling. Right: Green residue and trapped gas bubbles are seen in the filled fractures; field of view 2.90 mm.
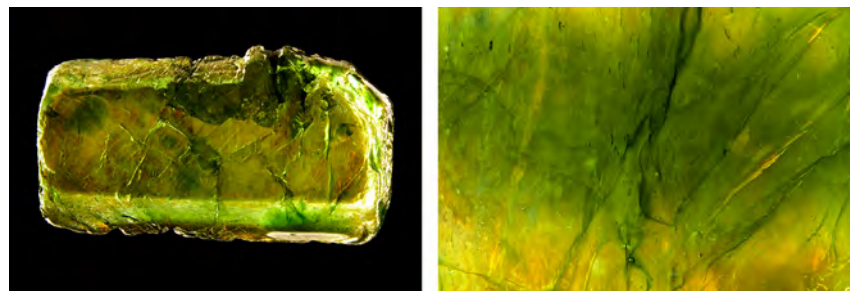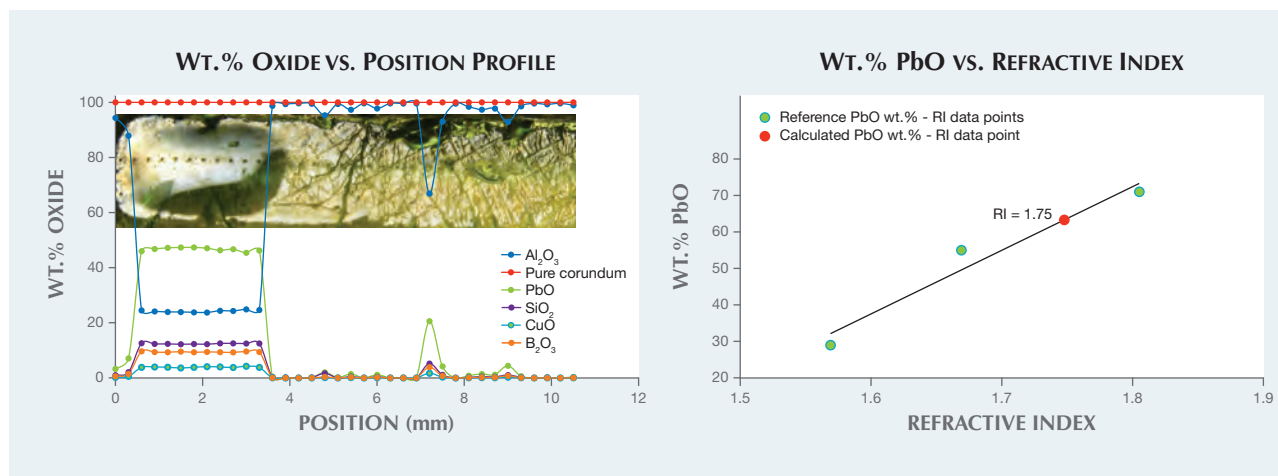
Figure 19. *Left: The wt.% oxide profile shows a strong correlation between the glassy residue and a high Pb concentration. Right: The lead glass shows a refractive index of 1.75 for a PbO content of 63.3 wt.%.*

to 100 wt.% oxide (R. Barbour, *Glass-blowing for Laboratory Technicians*, Wellington, New Zealand, Pergamon Press, 1978, p. 4). The renormalized composition of the lead glass was 63.3 wt.% PbO, 16.9 wt.% SiO_2, 12.8 wt.% B_2O_3, 5.3 wt.% CuO, and 1.7 wt.% CdO. The PbO wt.% was plotted on the Pb wt.% oxide vs. refractive index plot (http://physics.info/refraction) and showed an RI of 1.75, which is very close to corundum's RI of 1.76–1.77 (figure 19, right). The high refractive index of the glass concealed the difference in luster between corundum and filler.

A previous study reported on blue cobalt-colored lead glass–filled sapphires whose color was assigned to the presence of a small amount of cobalt in the filler (T. Leeawatanasuk et al., "Cobalt-doped glass-filled sapphire; an update," *Australian Gemmologist*, Vol. 25, No. 1, 2013, pp. 14–20). The green color of the glass in this specimen was likely caused by the combination of CuO (which causes a greenish blue color in glass) and CdS (which causes a yellow color; see B.H.W.S. De Jong et al., "Glass," in *Ullmann's Encyclopedia of Industrial Chemistry*, Wiley-VCH, 2000, http://dx.doi.org/10.1002/14356007.a12_365). The yellowish appearance and the high levels of Fe (1629 to 2640 ppmw) in the area without filler indi-

cate that the piece might have been a yellow sapphire before being filled. This was the first sapphire with green lead-glass filling examined at the Carlsbad laboratory.

Ziyin Sun and Jonathan Muyal

SYNTHETIC DIAMONDS
Large Crystal Inclusion in CVD Synthetic Diamond

Most inclusions in CVD synthetic diamonds are particulate or needle-like, and they tend to be confined to a plane (Spring 2013 Lab Notes, pp. 47–

Figure 20. *This 302.3 µm graphite inclusion encircled by tension fissures was observed in a CVD synthetic diamond. Subtle iridescent colors resulting from strain were also visible around the inclusion in polarized light. Field of view 1.42 mm.*

49). A previous report covered a case where the inclusions were scattered throughout in a random pattern (Fall 2014 Lab Notes, pp. 238–239), but even these inclusions were flat or pinpoint-sized. A 0.90 ct transparent colorless round brilliant CVD synthetic diamond was found to have an unusually large compact opaque black crystal inclusion. This 302.3 µm inclusion (figures 20 and 21) placed it in the SI clarity range and, as seen in the images, was significant in size in all three dimensions, unlike the usual geometry of CVD growth remnants. The inclusions that exist in a flat plane are thought to be related to imperfections at the growth surface, and the plane of inclusions will generally
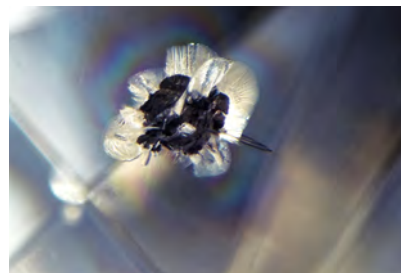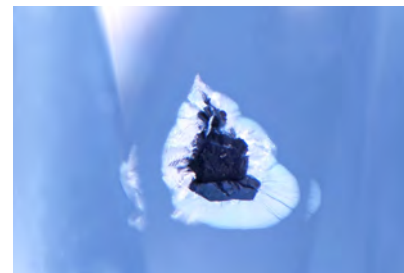
Figure 21. *The large graphite crystal and its radiating tension halo, viewed from the side through the pavilion. Field of view 1.42 mm.*

line up with a growth plane seen in DiamondView images. DiamondView imaging of this specimen showed no growth layers, only the dislocation networks characteristic of CVD synthetic diamonds.

The inclusion was most likely carbon in the form of graphite, although attempting to collect a Raman spectrum on it yielded no results. The inclusion was surrounded by stress fractures; it is unknown whether these were induced during the growth process or resulted from a post-growth treatment. Polarized illumination also revealed some iridescent color due to strain surrounding the inclusion. This sample was graded in the colorless range; this was a sign of post-growth treatment, as most CVD synthetics are brownish from the growth process (the treatment was confirmed by the absence of the 596/597 nm doublet in the photoluminescence spectra).

Under microscopic examination, this inclusion bore a strong resemblance to an inclusion one would find in a natural diamond. Since the size and structure are very different from anything previously seen in a CVD synthetic, identification based on these properties alone could lead to confusion. Luckily, Fourier-transform infrared (FTIR) spectroscopy revealed that the specimen was type IIa, an indication that a diamond may be synthetic (CVD or HPHT). Synthetic origin was proven by DiamondView images revealing growth patterns characteristic of CVD growth and large silicon-vacancy peaks detected by photoluminescence spectroscopy. It is therefore prudent to undertake all testing needed to conclusively separate natural and synthetic diamonds.

Troy Ardon and Jonathan Muyal

Screening of HPHT Synthetic Melee With Natural Diamonds

Significant amounts of melee-size synthetic diamonds produced by both HPHT and CVD technologies are manufactured for the jewelry industry.

The "salting" of natural diamond melee parcels with HPHT-grown synthetic melee is seen more frequently in the trade today. This presents a threat to the integrity of diamond dealers and manufacturers who might unknowingly sell or use synthetic diamonds and represent them as natural. In response, GIA has introduced a melee analysis and screening service aimed at helping the trade combat this problem. The screening is rapid and relatively inexpensive. This service can screen large quantities of diamond melee and separate natural diamond from synthetic material (both HPHT and CVD grown), natural HPHT-processed diamond, and diamond simulants such as cubic zirconia or moissanite. In addition, a color grade within the D–Z range can be assigned to each diamond.

In August 2016, a group of 3,005 melee with a total weight of 70.56 carats (figure 22) was submitted to GIA's New York lab for screening service. Initial testing using our fully automatic screening device, which is based on spectroscopic methods, passed 2,969 (98.7%) of them as natural diamond. Of the remaining 36,

Figure 22. This parcel of 3,005 melee diamonds with a total weight of 70.56 carats was submitted for analysis.

Figure 23. From an initial screening of 3,005 melee diamonds, 24 specimens were referred for further testing. Of these, three were HPHT-grown synthetic diamonds.

12 were subsequently identified as natural material by methods including photoluminescence (PL) spectroscopy, and only 24 were referred for further testing to confirm their identity as natural, treated, or synthetic diamond.

Additional testing with Fourier-transform infrared (FTIR) absorption spectroscopy, Raman PL spectroscopy, and fluorescence imaging techniques identified 21 of these 24 melee as natural diamond. This analysis also confirmed that three (0.1%) of the melee in the parcel were HPHT-grown synthetic diamonds (figure 23).

This highlights the practice of "salting" parcels of natural diamond melee with a small percentage of synthetic diamond melee, and the importance of advanced testing to identify them.

Ivana Petriska Balov and Paul Johnson

Figure 24. These two treated synthetic diamonds, a 0.57 ct Fancy red and a 0.50 ct Fancy Vivid yellowish green, show strikingly vibrant colors rarely found in natural-color diamonds.
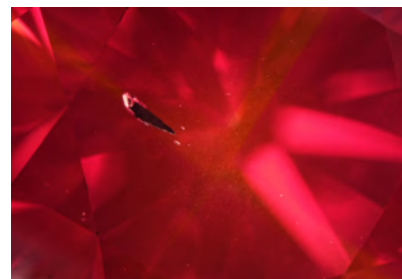

Figure 25. A large metallic inclusion breaks the table of the Fancy red synthetic diamond. This inclusion and the tiny pinpoint clouds in the background are typical identification features of HPHT synthetics. Field of view 2.85 mm.

Treated Red and Green
HPHT SYNTHETIC DIAMONDS

Natural-color red and green diamonds are extremely rare and command some of the highest prices in the market. Only a small number of natural diamonds have ever been graded as Fancy red without any modifying hues such as brownish red or orangy red. A 0.57 ct round brilliant with Fancy red color (figure 24, left) was recently submitted to GIA's New York laboratory for a colored diamond grading report. It showed a heavily saturated and pure red color, without any modifications to the red hue. From another client, we received a 0.50 ct round brilliant graded as Fancy Vivid yellowish green (figure 24, right) for a synthetic colored diamond grading report. The striking features shared by these two specimens caught our attention.

Examination with a standard gemological microscope revealed that both of them contained pinpoint clouds and metallic inclusions (figure 25), a typical feature of synthetic diamonds grown by high pressure and high temperature (HPHT). Mid-FTIR absorption spectra identified both as type Ib, with the relatively high concentration of isolated nitrogen that is responsible for the yellow to brown color typically observed in HPHT synthetics (Winter 2015 Lab Notes, pp. 430–431).

The strong short-wave UV radiation of the DiamondView (figure 26) showed red and yellowish green fluorescence in the red and green samples, respectively. Furthermore, the presence of both cubic {100} and octahedral {111} growth sectors in the DiamondView images suggested that the specimens formed with a relatively high growth rate that facilitated cubic and octahedral development simultaneously, a strong indicator of synthetic origin (Winter 2015 Lab Notes, pp. 429–430).

Diffused lighting showed uneven color zoning in both samples, consisting of their bodycolors and the yellow color from the isolated nitrogen content (figure 27). Spectroscopic analysis revealed that the Fancy red synthetic had an unusually strong peak at 637 nm (NV⁻ center). This peak indicates color alteration by post-growth annealing (T.W. Overton and J.E. Shigley,

Figure 26. DiamondView fluorescence images of the Fancy Vivid yellowish green synthetic diamond (left) and the Fancy red synthetic diamond (center and right) show similar combinations of cubic and octahedral sectors.
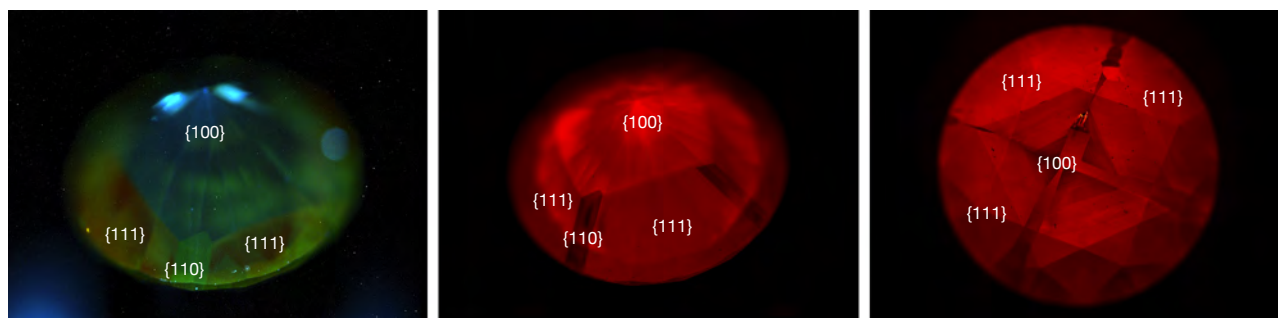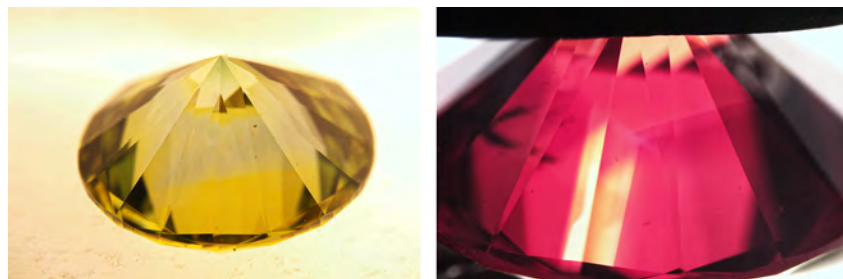
Figure 27. Under polarized light, the Fancy Vivid yellowish green synthetic diamond (left) displays patchy yellow color zoning caused by isolated nitrogen and a green color concentration on the culet caused by post-growth artificial irradiation treatment. The Fancy red sample (right) shows yellow to near-colorless zones following the cubic growth sectors, with the red color caused by post-growth annealing. Fields of view 7.19 mm (left) and 4.79 mm (right).

lowish green hues. While the yellowish green round brilliant received a synthetic colored diamond report, the undisclosed nature of the Fancy red's growth required the lab to issue an identification report to properly disclose its synthetic origin.

Yixin (Jessie) Zhou and
Paul Johnson

"A history of diamond treatments," Spring 2008 *G&G*, pp. 33–55). In the Fancy Vivid yellowish green synthetic, a concentration of green color on the culet area indicates that artificial irradiation was applied to alter the as-grown yellow color to vivid green.

Both synthetic diamonds underwent post-growth treatment to change their color to the desirable red and yel-

For online access to all issues of GEMS & GEMOLOGY from 1934 to the present, visit:

gia.edu/gems-gemology

Andradite in Andradite

Recently we had the opportunity to examine a dramatic iridescent andradite fashioned by Falk Burger (Hard Works, Tucson, Arizona) from a crystal originating from the Tenkawa area of Nara Prefecture in Japan. Known as "rainbow" andradite, this material was previously reported in *Gems & Gemology* (T. Hainschwang and F. Notari, "The cause of iridescence in rainbow andradite from Nara, Japan," Winter 2006, pp. 248–258). The specimen was unique for its genesis and optical phenomenon.

Weighing 16.79 ct and measuring 15.41 × 13.86 × 10.49 mm, the andradite was very large for its species and local-ity, but size was not what made it special. As shown in figure 1, close examination of one of the polished crystal faces revealed a bright reddish orange "hot spot" in the center, caused by an iridescent inclusion of andradite with a different crystallographic orientation than its host. As seen in figure 2, the inclusion's different orientation caused the iridescence of the rhomb-shaped "hot spot" to appear and disappear as the light source was passed over the crystal's surface. To see the iridescence from both the host and inclusion at the same time, two light sources from opposite directions must be used due to the different crystallographic orientation of the host and inclusion. This elusive optical phenomenon made this Japanese andradite crystal extremely interesting for any aspiring inclusionist.

John I. Koivula
GIA, Carlsbad

Unusual Growth Zoning in Beryl

An aquamarine crystal from Pakistan recently examined by the authors showed a rather dramatic inclusion scene in which several cracks were lined with a vivid blue coloration. We theorize that this relatively pale blue aquamarine developed cracks while in the growth environment. Subsequently, the nutrient solution may have shifted out of equilibrium with the beryl crystal, resulting in a rela-

Figure 1. This 16.79 ct Japanese andradite garnet exhibits a very unusual rhomb-shaped "hot spot" below the surface of one crystal face. Photo by Kevin Schumacher.
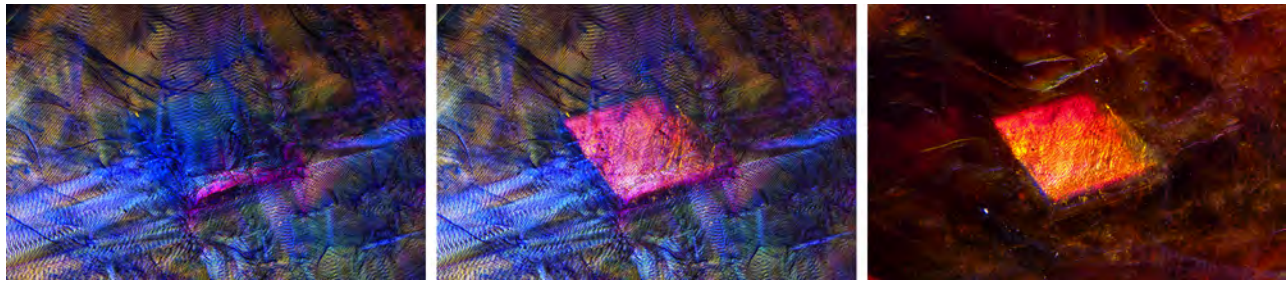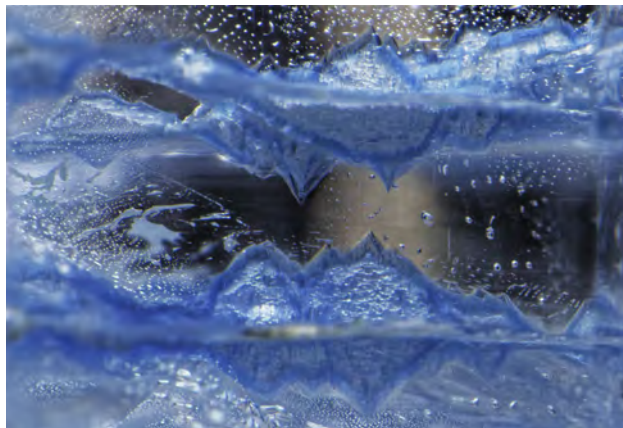
Figure 2. Using two oblique fiber-optic light sources from opposing directions, the iridescent surface of the host crystal and inclusion can be seen at the same time (center). Viewed with only one fiber-optic light, the iridescence on either the host or the inclusion alone can be seen because of their different crystallographic orientations. Photomicrographs by Nathan Renfro; field of view 5.11 mm.

tively quick dissolution along the cracks. After some period of time, there appears to have been a modification of the nutrient solution and/or growth conditions in which precipitation of beryl became favorable once again. This second generation of growth had a distinctly different trace element composition, resulting in a strongly saturated blue coloration (figure 3) that made the boundary between the primary and secondary growth layers readily apparent (for previously documented examples of second-generation growth, see E. J. Gübelin and J. I. Koivula, *Photoatlas of Inclusions in Gemstones*, Vol. 2, Opinio Verlag, Basel, Switzerland, 2005, pp. 249–250). Chemical analysis by laser ablation–inductively coupled plasma–mass spectrometry (LA-ICP-MS) confirmed that both zones were in fact beryl and revealed elevated levels of iron in the dark blue layers, which accounts for their darker color (G.R. Rossman, "Color in gems: The new technologies," Summer 1981 *G&G*, pp. 60–71). The trace elements Na, Mg, Sc, Ti, V, and Mn were also elevated in the dark blue areas. This dramatic

change in chemical composition further supports our theory that there was a significant modification of the nutrient solution in the crystal's growth environment. This striking specimen shows how complex and dynamic the "birthplaces" of gems can be.

Nathan Renfro and Ziyin Sun
GIA, Carlsbad

Growth Blockages in Cat's-Eye Beryllonite

The sodium beryllium phosphate mineral beryllonite $(NaBePO_4)$ is a rare gem coveted by collectors. The material is typically fashioned as a transparent colorless faceted stone but occasionally as a cat's-eye cabochon (figure 4). Recently, an interesting colorless rough specimen studied at GIA's Carlsbad laboratory exhibited an unusually sharp, obvious separation between two regions. One area contained a high density of hollow tubes, while the other was clean and transparent.

Figure 3. This aquamarine, shown in plane-polarized light, has a dramatic secondary growth layer that is much more saturated in color than the crystal's primary growth. Photomicrograph by Nathan Renfro; field of view 2.45 mm.

Figure 4. Left to right: a cat's-eye beryllonite cabochon, two faceted transparent colorless samples, and a partially polished specimen with clean areas and growth tubes. The larger faceted stone in the center weighs 1.90 ct. The rough on the far right is the specimen from this study. Photo by Kevin Schumacher.

Figure 5. Two-phase inclusions and parallel tubes in a colorless beryllonite are the result of growth blockages created by tiny crystal inclusions, shown in diffused transmitted lighting. Photomicrograph by Jonathan Muyal; field of view 2.88 mm.

Chatoyant beryllonite gems have been reported previously (Spring 1991 GNI, pp. 47–48), but this peculiar specimen offers a clue to the mechanism that gives rise to the chatoyant phenomenon. The answer lies in the separation between the two regions, which is where minute inclusions (figure 5) were deposited during growth of the crystal. This created a localized blockage of necessary nutrients, preventing growth of the host mineral and leaving behind the parallel tubes (Summer 2010 Lab Notes, pp. 55–56).

This collector's cat's-eye beryllonite, with its beautiful contrasting black-and-white inclusion scene, furthers our understanding of chatoyancy in this mineral.

Jonathan Muyal and Ziyin Sun
GIA, Carlsbad

Iridescent Inclusion in Tanzanite

Gemmy blue zoisite, more commonly known as tanzanite, is valued for its pleasing violet to blue hue. One tanzanite specimen from Merelani, Tanzania, was purchased by the author for an entirely different aesthetic feature: its well-defined, minimally damaged crystal faces. Microscopic observation uncovered a hidden bounty of color just below the surface, particularly when subjected to metal halide oblique lighting. Crystallographically aligned, vividly iridescent colors resulting from fine separations along the stone's cleavage planes (figure 6) were visible using fiber-optic light.

Photographing inclusions can be challenging, to say the least. When light enters the host material, each delicately nuanced feature is affected in unpredictable ways. Documenting surface textures or crystal faces is equally difficult; the challenges are manifold when attempting to photograph both simultaneously. Knowledge of lighting techniques is useful in such situations (N. Renfro, "Digital photomicrography for gemologists," Summer 2015 *G&G*, pp. 144–150). In this instance, a combination of diffused lighting and direct pinpoint lighting was used to illuminate both features. Low-intensity diffused light was reflected from the surface of the stone so as to illuminate the crystal faces without overpowering the iridescent colors brought from below. Once lit, a
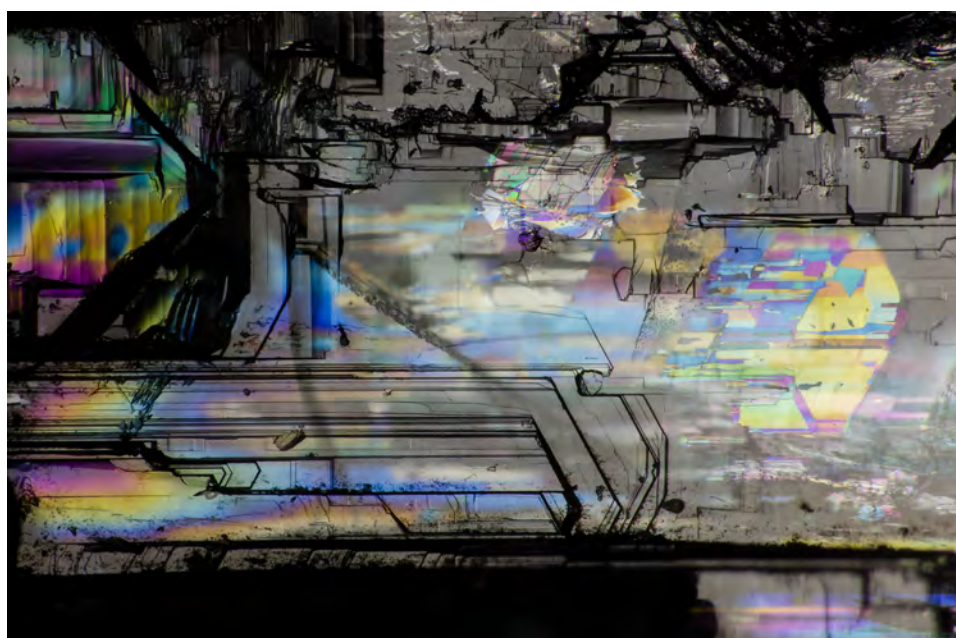

Figure 6. The iridescence in this tanzanite hints at the complex and dynamic world just below the surface, in the form of crystallographically aligned iridescent cleavage. Photomicrograph by Danny Sanchez; field of view 3 mm.
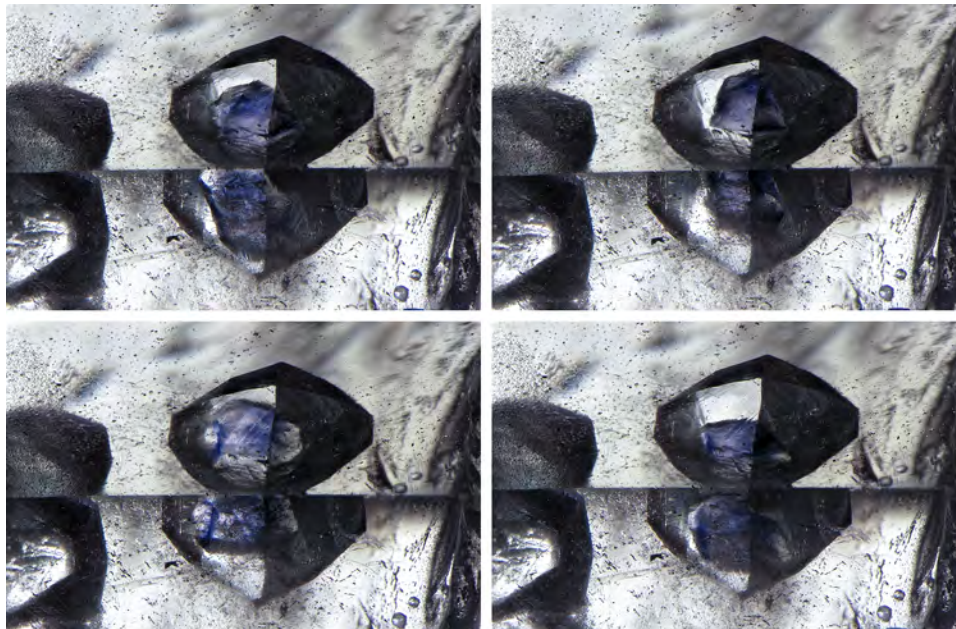
Figure 7. This violet-colored fluorite crystal was free to move in its octahedral void, as seen in four different positions. Photomicrographs by Nathan Renfro; field of view 7.18 mm.

short "stack" of images captured the appropriate amount of depth into the stone.

Danny Sanchez
Los Angeles

Mobile Fluorite in Quartz

In 2005, a deposit in Madagascar yielded quartz that showed beautiful blue to purple octahedral fluorite crystal inclusions (Summer 2005 GNI, pp. 180–181). This author recently examined a unique example of this material in which a fluorite crystal was much smaller than the cavity it occupied (figure 7). The difference in size allowed the fluorite to move freely within the void. Also present in the void and surrounding the fluorite crystal were an aqueous liquid and a small gas bubble. Because the cavity was an octahedron, a shape not related to quartz morphology, it is assumed that the fluorite was originally much larger and defined the shape of the void while in that larger state. Also observed was a secondary healed crack that broke from the surface of the quartz to the void while it was still in the growth environment. This crack allowed fluids that were not in equilibrium with the fluorite to partially dissolve it before the crack healed, trapping the much smaller fluorite remnant in the void. Mobile inclusions in gems such as this example are rare and fascinating to observe.

Nathan Renfro

Etch Marks, Negative Crystals, and Etch Tubes in Spinel from Madagascar

During a recent study of blue sapphires from the Ilakaka region in Madagascar, the authors discovered a stone with an unusual appearance. Mixed in a parcel of blue sapphires

purchased from Malagasy sapphire miner Nirina Rakoto-saona was a 2.18 ct blue pebble (figure 8). RI (1.718) and SG (3.62) measurements identified it as a spinel. Mr. Rakoto-saona had mined these stones near Antsoa village, along the Taheza River. Magnification revealed numerous triangular etch marks on the surface, which is not uncommon for spinel (Summer 2004 Lab Notes, p. 168). The frosted surface of the stone made it difficult to study its internal features, so we polished a window in order to observe them.

What we found was a spectacular internal world, with several well-developed negative crystals associated with etch tubes (figure 9). These etch features were characterized by a narrowing of the tubes toward the center of the

Figure 8. The multitude of negative crystals and growth tubes in the 2.18 ct spinel pebble are exposed under fiber-optic light. Photo by Victoria Raynaud; field of view 13.11 mm.
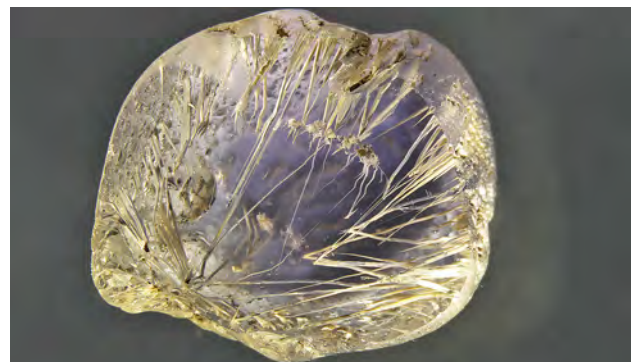
Figure 9. Negative crystals with stubby etching and very long etch tubes within the spinel. The triangular etch marks are visible in the background. The image was taken using a combination of brightfield and fiber-optic lighting. Photomicrograph by Victoria Raynaud; field of view 2.67 mm.

crystal, indicating that they were produced by dissolution of spinel after the crystal had formed. This preferential dissolution was located at weaker structural zones in the spinel, which might be related to the presence of the negative crystals.

While all the negative crystals were aligned and had the overall classic octahedral form for spinel, they also showed modifications such as twinning and short stubby etching (figure 10). The etch tubes radiated outward from these negative inclusions or passed through them. Etch tubes are well known in sapphires from Madagascar, but this stone shows they can also be found in blue spinels from the island. It was this etching that made for one of the most interesting inclusion scenes the authors have encountered.

Victoria Raynaud and Wim Vertriest
GIA, Bangkok

Figure 10. Octagonal negative crystals associated with slender etch tubes, seen under a fiber-optic light. Photomicrograph by Victoria Raynaud; field of view 1.44 mm.

Sphalerite in Topaz

A 6.54 ct colorless topaz specimen hosting eye-visible dark crystals was examined at GIA's Carlsbad laboratory. The crystals exhibited a submetallic luster and showed isometric morphology with step-like growth (figure 11). Some also displayed slightly corroded rounded edges with a reflective iridescent interface. The corroded appearance suggested that these dark crystals are protogenetic inclusions that were present in the growth environment before the topaz began to form. Raman spectrometry and LA-ICP-MS analysis confirmed that the inclusions were sphalerite, a zinc-iron sulfide with the formula $(Zn,Fe)S$. Fluid inclusions were also observed in this topaz.

Sphalerite has been described in the literature as a collector's gem for its rarity and beautiful luster (Summer 1992 Gem News, p. 202). This is the first documented example of sphalerite as a crystal inclusion in colorless topaz, making it an unusual collector's gemstone.

Jonathan Muyal, Ziyin Sun, and Nathan Renfro
GIA, Carlsbad

Aaron Palke
University of Queensland and Queensland Museum
Brisbane, Australia

Tourmaline Termination

Depending on their size, large tourmaline crystals are known as "hand" or "cabinet" mineral specimens. To be used in jewelry, specimens of sufficient quality must be cut to a suitable size. This generally results in all of the natural surfaces being ground off and polished away. On occasion, however, a natural surface on a crystal is so in-

Figure 11. Oblique diffuse illumination reveals the scene within a colorless topaz. Its sphalerite inclusions all feature an isometric crystal habit, metallic luster reflections, and subtle iridescent interface colors. Photomicrograph by Jonathan Muyal; field of view 4.79 mm.
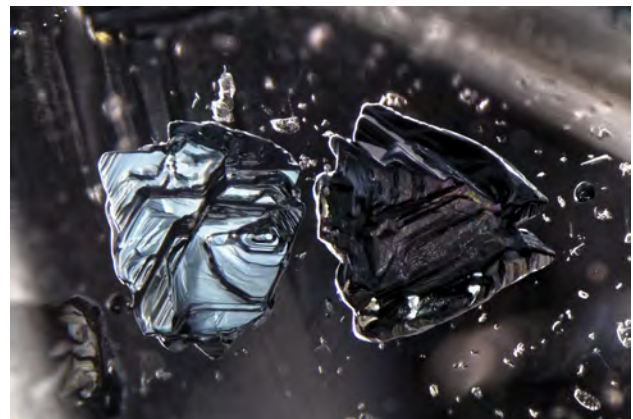
Figure 12. Highlighted by blue and pink color accents, trigonal growth features are clearly visible on the surface of this 42.78 ct polished tourmaline termination. Photo by Kevin Schumacher.

teresting that it is preserved and used as a gem in its own right. Such was the case with a blue cap elbaite tourmaline (figure 12) from Fianarantsoa, Madagascar.

During the cutting of this tourmaline, gem artist Falk Burger (Hard Works, Tucson, Arizona) saved the blue cap termination by sawing it off into a thin plate and mirror-polishing the sawn surface, thereby accentuating its remarkable trigonal growth features and pink and blue color zoning (figure 13, left). This resulted in the beautiful and unique designer gem seen in figure 12, which weighed 42.78 ct and measured 37.23 × 31.97 × 3.60 mm.

This gem was also very interesting when examined through a microscope (figure 13, right). In crossed polarizers, while looking perpendicular to the polished plate, interference colors were clearly visible, accentuating the growth of the tourmaline.

John I. Koivula

Quarterly Crystal: Quartz with Axinite

In their September-October 1982 *Mineralogical Record* article, D. Pohl et al. described a discovery of ferroaxinite from New Melones Dam in Calaveras County, California. There was a very brief mention of ferroaxinite inclusions in quartz, but no illustrations of the inclusions were provided. Recent exploration of the Calaveras County locality by one of the authors (JM) led to the discovery of a large pocket that produced some beautiful axinite and quartz specimens (figure 14) containing bladed inclusions of ferroaxinite.

This new mineralized pocket was situated on the edge of a ledge and had a different geological appearance than the surrounding area. Successive layers within the pocket, 6–12 cm in thickness, were composed of metagabbro and crushed coarse rock crystal quartz that contained well-developed single quartz crystals measuring up to 9 cm in length and 6 cm in diameter. These crystals displayed both long and short columnar habits. Also found within them were crushed coarse crystalline axinite and mats of small

Figure 13. Left: Using diffused transmitted light, contrasting pink and blue color zoning is seen. Right: Viewing the tourmaline through crossed polarizers and looking perpendicular to the polished plate, interference colors were clearly visible. Photomicrographs by Nathan Renfro; field of view 23.95 mm.
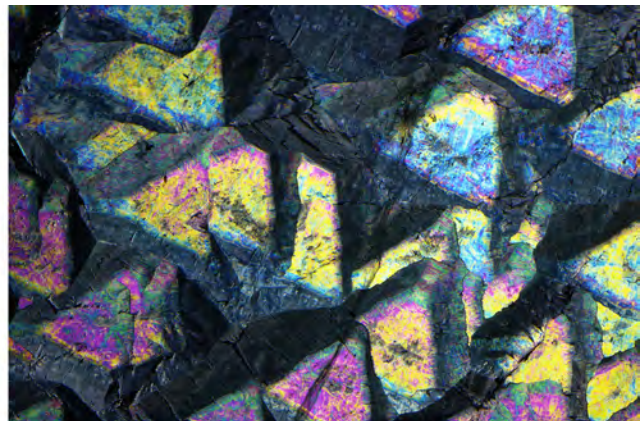
epidote needles. Cracks in the crystals allowed quartz-forming fluids to seep through and crystallize on the surface of the metagabbro, often surrounding both the epidote matting and a mixed layer consisting of chlorite/axinite/epidote.

The large pocket, measuring approximately 7 feet deep, 4 feet wide, and 6 feet long, produced almost 2,000 pounds of quartz. The specimens ranged from translucent to extremely clear and varied in size from 1 to 18 cm. Some of them contained axinite or chlorite phantoms as well as full and partial inclusions of bladed axinite floater crystals. This huge pocket also produced several spectacular plates of axinite, with individual crystals measuring up to 8 cm long, along with floater crystals of similar dimensions.

The axinite inclusions themselves displayed the typical bladed habit expected for this mineral. When examined with polarized light, they also showed pronounced pleochroism, from a light brown (figure 15, left) to a more intense pinkish purple (figure 15, right). This represents the first visual record of axinite inclusions in quartz published in the gemological and mineralogical literature.

John Miatech
Kelseyville, California

John I. Koivula
GIA, Carlsbad

Figure 14. Two examples of quartz with inclusions of ferroaxinite from the New Melones Dam in Calaveras County, California. The larger specimen measures 65.28 mm tall. Photo by Kevin Schumacher.

Figure 15. With plane-polarized light, the axinite inclusions in quartz show very distinct pleochroism. Both of these images were taken with the polarizer rotated at approximately 90 degrees from each other. Photomicrographs by John I. Koivula; field of view 9.0 mm.

COLORED STONES AND ORGANIC MATERIALS

Aquamarine from a new primary deposit in Mexico. Scientists still have not adequately surveyed Mexico from a mineralogical or gemological point of view. But recent finds of amazonite, jadeite, topazolite, demantoid, and labradorite demonstrate the importance of systematic research of the Mexican subsoil, which may lead to the discovery of other gemstones and gem localities (M. Ostrooumov, "Gemstones from Mexico—A review," Summer 2011 *G&G*, p. 141).

Recently, the author discovered transparent blue crystals with hexagonal-prismatic habit in a granitic pluton in the hills of Guadalcázar municipality, San Luis Potosí State, in north-central Mexico. These crystals, the largest of which measured $12.04 \times 5.68 \times 4.57$ mm, were embedded in a single quartz vein in association with muscovite (figure 1). All observed aquamarine crystals were generally characterized by a lighter blue tone, lacking visible inclusions. The samples were submitted for identification at the Institute of Earth Sciences at the University of Michoacan in Morelia, Mexico.

Standard gemological testing yielded the following properties: refractive index (RI)—n_o=1.582–1.587 and n_e=1.575–1.580; pleochroism—strong blue and near-colorless; birefringence—0.007, with a uniaxial negative optic sign; hydrostatic specific gravity (SG)—2.70–2.71; fluorescence—inert to both long- and short-wave UV radiation. These properties suggested beryl, which we later confirmed with UV-Vis-NIR and infrared reflection spectroscopy and Raman microprobe.

UV-Vis-NIR spectroscopy showed absorption bands at 428, 452, 575, 630, and 805–815 nm. Narrow, weak absorption lines at 428 and 452 nm are attributed to the spin-forbidden transition of six-coordinated Fe^{3+}. A broad intense band at 575 nm and a much weaker line at 630 nm, which are responsible for the aquamarine color, are assigned to an Fe^{2+}-O-Fe^{3+} intervalence charge transfer transition (A.S. Marfunin, *Advanced Mineralogy*, Vol. 2, Springer-Verlag, Berlin, 1995, pp. 113–114). Finally, an intense broad band at approximately 805–815 nm is attributed to spin-allowed transitions of Fe^{2+}.

Infrared reflection spectroscopy and Raman microprobe are methods of "fingerprinting," and a combination of

Figure 1. Aquamarine was recently discovered in San Luis Potosí State in north-central Mexico. Here the aquamarine is shown in association with muscovite and quartz. The approximate size of the visible aquamarine crystal is $12.04 \times 5.68 \times 4.57$ mm. Photo by M. Ostrooumov.

IR Spectrum {1010}
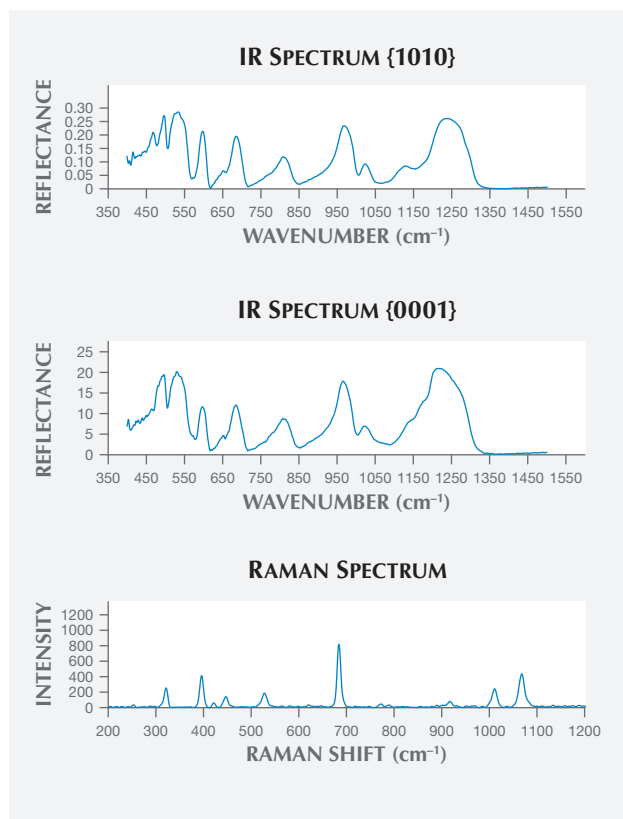

IR Spectrum {0001}

Raman Spectrum

Figure 2. Infrared reflection spectra and Raman microprobe results of the samples confirm their aquamarine identity. The IR spectrum at the top is from the {1010} orientation, while the middle spectrum shows the {0001} orientation. The bottom plot shows the unoriented Raman microprobe results, with principal peaks at 322, 396, 447, 528, 684, 773, 916, 1011, and 1068 cm⁻¹.

these techniques permits the user to identify a wide range of mineralogical, gemological, and archaeological objects (M. Ostrooumov, "Infrared reflection spectrometry analysis as a non-destructive method of characterizing minerals and stone materials in geoarchaeological and archaeometric applications," *Geoarchaeology*, Vol. 24, No. 5, 2009, pp. 619–637).

This study confirmed that the crystals belonged to the beryl group (http://rruff.info). The infrared reflection spectra were obtained on oriented crystal faces {0001} and {1010} in order to take into account the effect of orientation (figure 2, top and middle). These results indicate the presence of the typical Be-O band vibrations at 743–807 cm⁻¹ and 1215–1276 cm⁻¹. The infrared absorption spectra showed the presence of hydroxyl groups with a prominent band at 3450 cm⁻¹ and a secondary band at about 3558 cm⁻¹ due to the fundamental OH stretching vibration of water molecules, as well as the water-bending vibration at approximately 1630 cm⁻¹. The Raman microprobe spectra (figure 2, bottom) showed excellent agreement with a reference spec-

trum for aquamarine from Ilmen, Russia, in the author's FT-Raman database (http://www.mineralog.net). The Raman spectra of aquamarine in the water range from 3700 to 3500 cm⁻¹ using 532 nm excitation wavelength showed two Raman bands at 3608 and 3598 cm⁻¹ with different intensities. Water molecules in the channels are classified as type I or type II according to their orientation to the beryl structure. The Raman band at 3608 cm⁻¹ is assigned to the vibration of type I water, and the Raman band at 3598 cm⁻¹ is ascribed to the vibration of type II water molecules. UV-Vis-NIR, infrared reflection, and Raman microprobe techniques, as well as standard gemological testing, confirmed the discovery of aquamarine in the Guadalcázar granitoid deposits of San Luis Potosí State.

The recent discovery of *in situ* aquamarine in Mexico has renewed interest in the geology and mineralogy of gem deposits in that country. More discoveries are anticipated with further exploration in the region.

Mikhail Ostrooumov (ostroum@ umich.mx)
University of Michoacan, Institute of Earth Sciences
Morelia, Michoacan, Mexico

Update on colored gemstone mining in Tanzania. A team of GIA field gemologists visited Tanzanian mines in the summer of 2016 to collect ruby and sapphire for GIA's reference collection and explore new sources of colored stones. The field expedition, led by these authors, visited many known Tanzanian gem localities as well as new deposits at Loolera, Kibuko (figure 3), Lutela, Amani Makoro, and Ngapa. The trip was made possible by the support of Mark Saul of Swala Gem Traders (Arusha, Tanzania), Tanzanian gem broker Justin Mmbaga, and several regional mining officers. We found that the most active colored gemstone mining area is still Merelani, which produces tanzanite and green grossular garnet. Ruby and sapphire output has been relatively low since the 2009 discovery of the ruby deposit in Montepuez, Mozambique, as confirmed by our Tanzanian sources.

Tanzanian miners supply stones to licensed brokers, who are allowed to buy and transport gems within the country. These brokers sell to licensed master dealers, who are allowed to export internationally. These master dealers are mainly located in Dar es Salaam and Arusha. While we met Thai and Sri Lankan buyers in Mahenge, Songea, and Tunduru, foreigners must have approval from regional mining officers and possess a proper business visa to visit the deposits. This is particularly enforced in southern Tanzania; around Songea, we met immigration officers who were "hunting for foreigners."

Our journey started in Longido, where rubies were discovered about 100 years ago (D. Dirlam et al., "Gem wealth of Tanzania," Summer 1992 *G&G*, pp. 80–102). The main operation in the Longido area is the Mundarara ruby mine, currently Tanzania's largest, with a workforce of 78 people. The gems are extracted from an underground tunnel about 200 meters deep crossed by several horizontal tunnels that

Figure 3. A view of the pink sapphire mining pit at Kibuko, in the Uluguru Mountains of Tanzania. Photo by Vincent Pardieu/GIA.

host most of the production. The mine yields ruby in zoisite (suitable for carving), as well as some cabochon- and facet-grade material of a very deep red color. The color is reminiscent of rubies from Mozambique.

We continued to the Umba River, where Tanzanian sapphire production began after World War II and a ruby-bearing area was discovered by Georges "Papas" Papaeliopoulos in the 1950s (again, see Dirlam et al., 1992). The situation has changed significantly since author VP visited in 2005 and 2009. At the time there was a dispute between the company working the deposit, called "Amazon," and local communities. The dispute ended with the government revoking Amazon's license. During our 2016 expedition, we witnessed about 40 small-scale local miners using hand tools to work the primary deposit discovered by Pa-

paeliopoulos, as well as secondary deposits scattered along the banks of the Umba. Most of the production is traded each evening around the Mississippi Hotel in Umba.

In the Kilindi area, about halfway between Umba and Winza, a new ruby deposit has been discovered near the Maasai village of Loolera. This site, located atop a hill, produces gems very similar to those found near Winza in 2007. We visited the area with the support of the village leader, who said the first rubies were found about 10 years ago, but the quality of the stones was low. A few miners were working the deposit sporadically using hand tools. But in April 2016, some good-quality material was found in amphibole matrix, attracting considerable interest. About 25 mining licenses were issued during the summer of 2016, but there is a sense that the area is under the control of a few major players.

The deposit where the first rubies at Loolera were found is owned by a miner called Dr. Ozu. The mining pit appeared to be about 90 meters deep, but we could not inspect the tunnel as Dr. Ozu was not present. We studied the entrance and looked through the tailings near the pit. In these rejects we found many small fragments of rubies associated with garnets, amphibole, mica, and feldspar. Although the material we saw resembled Winza ruby, the stones contained minute particles that gave them a milky aspect.

Our next stop was Winza, where an important gem rush occurred in 2007–2008 (D. Schwarz et al., "Rubies and sapphires from Winza, central Tanzania," Winter 2008 *G&G*, pp. 322–347; V. Pardieu, "The Winza ruby and sapphire mining area, Mpwapwa district, Dodoma province, Tanzania," www.fieldgemology.org, 2009). The main mining area at Mtakanini was nearly deserted. An old rusted washing plant was visible, but due to mechanical problems it had not washed any stones in more than a year. We estimated that a handful of people were still mining around Mtakanini, mainly at primary deposits in underground tunnels, some of which were over 100 meters deep. Working conditions are difficult, as the rock is hard and the tunnels are prone to flooding. We learned that several brief ruby rushes occurred nearby at Godegode, Makutop, Magaseni, Singonali, and Berega. In Morogoro Province, two ruby and spinel mining areas have been exploited since the 1980s. One is located just east of Morogoro in the Uluguru Mountains, and the second is about 150 km south near Mahenge. Most of the gem trade in the Uluguru Mountain region is in Mkuyuni, while the mining takes place near Matombo, Ngongolo, Mwaraze, and Kibuko. In Matombo we witnessed about 30 people retrieving pink spinel and rubies from a secondary deposit near Kiswila. Near

Figure 4. Pink sapphires from the new deposit near Kibuko. Photo by Vincent Pardieu/GIA.

Figure 5. This garnet was mined from the new deposit in Lutela, Tanzania. Photo by Vincent Pardieu/GIA.

Ngongolo, we visited four small-scale operations where locals with hand tools were mining small rubies in marble associated with pyrite, graphite, and mica.

Near Kibuko, a new pink sapphire deposit was worked by about 10 miners on a site owned by Luciano Kipanzi, who took over the area in 2015. Pink sapphires up to 100 carats are associated with carbonates and pyrite in a primary deposit (figure 4). Most of the stones were the milky "geuda" type, but there was some transparent facet-grade material with very fine crystallization. The mine had evidently yielded about 20 kg of sapphire, from cabochon- to facet-grade, during the previous six months. Nearby, three groups of small-scale miners were uncovering a limited amount of similar stones from secondary deposits.

The Mahenge district, known for spinel and ruby, is the second most active gemstone mining area in Tanzania. Recent discoveries of graphite near Ipanko and garnet near Lutela (the latter in February 2016) have kindled interest in the area. The new alluvial deposit produces an interesting range of attractive garnets (figure 5), from light "champagne" to deeper saturated rhodolite, including some color-shifting stones. We saw some clean stones weighing up to 20 ct and heard about others as large as 60 ct. About 100 miners were still working the alluvial deposit. Activity was already slowing; we were told that a few months earlier, up to 300 miners were in the valley. This secondary deposit is rapidly depleting, and so far no primary deposit has been located.

Ipanko is still the main spinel deposit in the region. Author VP noticed that the pits were much larger than in 2012, meaning that the area had been mined since then. Nevertheless, the activity seemed slow compared to 2012: Several excavators were working secondary deposits, whereas small-scale miners once worked individual plots, called "boxes" by the locals. The nearby primary spinel deposit was still active, with about 400 people mining red spinel and only a few working on rubies. We then visited several small-scale ruby deposits along the Lukande River, including three operations working either primary or sec-

Figure 6. This blue sapphire rough, weighing about 7 ct, is from the new deposit at Ngapa, near Tunduru. Photo by Vincent Pardieu/GIA.

ondary deposits. As in the Uluguru Mountains, the rubies from these areas come from marble-type deposits. We saw about 50 miners working around Lukande, Kwam Somali, Mayote, Chipa, Ibogoma, Gombe, and Kitonga during the dry season, retrieving cabochon-grade rubies along with smaller facet-grade material. During the rainy season, these workers focus on gold mining or farming.

Our last visit was the region around Songea and Tunduru, where sapphire production began in the 1990s. The Songea deposit, discovered in 1992, was quite productive until the discovery of fine blue, yellow, and pink sapphires near Tunduru in 1994. The deposit was nearly inactive until the early 2000s, when the newly developed beryllium diffusion treatment was able to turn Songea's muddy green and brownish purple stones into attractive yellow to orange sapphires. In Songea, we heard of a new discovery at Amani Makoro, close to the old diggings around Ngembambili and Masuguru. In Amani Makoro, we witnessed about 200 miners in a swampy area using hand tools. The aspect and quality of the stones was similar to those from Ngembambili and Masuguru. Overall, about 300 people are still mining or trading gems around Songea. According to the regional mining officer, nine Thai merchants are registered buyers here. Songea still seems to be Tanzania's most active sapphire mining area.

The region east of Tunduru, located along the Muhuwesi, Lumesule, and Ruvuma rivers and up through Ngapa and Kitowelo, is known to produce blue, yellow, green, pink, and purple sapphires, and rarely rubies. The deposits, discovered by Swiss gem merchant Werner Spaltenstein in 1994, were very active until 1999, when buyers left Tunduru for the newly discovered sapphire deposits of Ilakaka, Madagascar.

A paved road linking Tunduru to the coast and then Songea should be finished in 2017, making these areas much less isolated. Around Tunduru, a new environmental law that forbids mining within 60 meters of a stream or a river is creating issues, as most of the mining there takes place in riverbeds. Last year Mr. Spaltenstein had to stop his mechanized operation because of that law, though local authorities seem to be more tolerant of small-scale miners. While the area is much less active than when VP visited in 2005 and 2008, we estimate that about 400 to 500 miners are working around Tunduru. In the town, we found 10 Sri Lankan and three Thai buying offices. In the main gem-producing area there was a small rush in Ngapa, near Kitowelo and the area known as the "DSM Box" (figure 6). We were told the area produces some good blue, pink, and purple sapphire rough weighing up to 50 ct; fine sapphire of this size was previously unknown in Tunduru. The second most active place was Muhuwesi, where several groups of small-scale miners are reportedly working.

The post-2009 downturn of Tanzania's ruby and sapphire mining was not unexpected, because many of the corundum discoveries triggered rushes that were exploited for short-term gain. Tanzania also faces competition from the world-class ruby deposit in Montepuez. Nevertheless, recent colored stone discoveries point to the vast potential of gem mining in Tanzania.

Vincent Pardieu and Wim Vertriest
GIA, Bangkok

Purple pyrope-almandine garnet from Mozambique. In early 2016, attractive purple garnets from East Africa started to appear in the Bangkok market (T. Sripoonjan and T. Leelawatanasuk, "Preliminary investigation of purple garnet from a new deposit in Mozambique," *GIT Gemstone Update*, 2016, pp. 1–6). Author VP purchased 17 samples (figure 7) at the Bangkok Gem Fair and inquired about their origin. Mark Saul of Swala Gem Traders (Arusha, Tanzania) informed him that the source was a very unstable area of Manica Province in central

Figure 7. These purple pyrope-almandine garnets are from Manica Province of Mozambique. The rough specimens weigh (clockwise from left) 1.49, 1.14, 1.11, and 1.77 ct, while the faceted stone in the center weighs 2.34 ct. Photo by Lhapsin Nillapat.
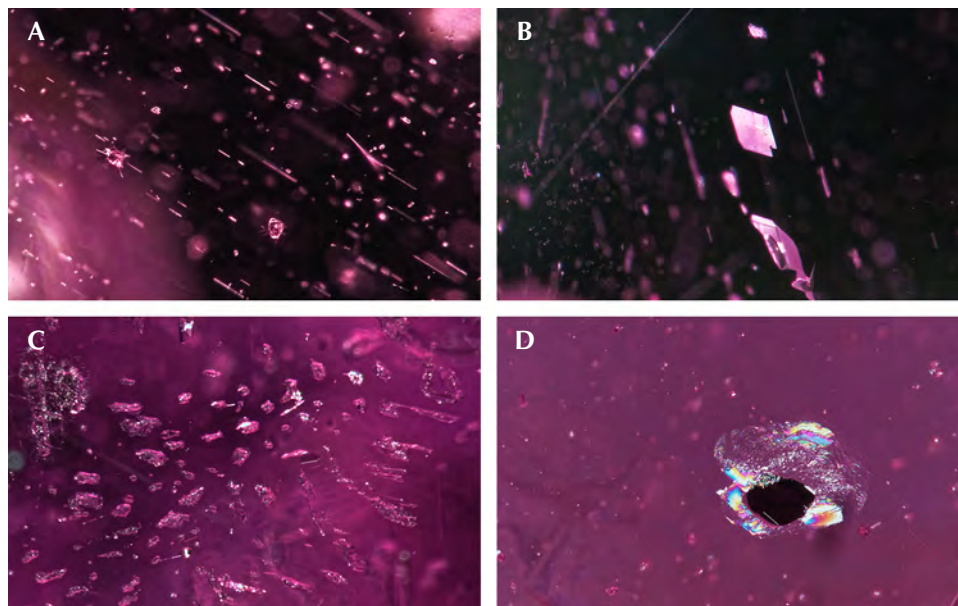
Figure 8. Magnification of the pyrope-almandine garnets revealed several internal features: (A) zircon inclusions with stress halos and needles, field of view 1.4 mm; (B) thin films, field of view 3.5 mm; (C) groups of colorless quartz, field of view 1.8 mm; and (D) a platelet of black graphite, field of view 1.8 mm. Photomicrographs by Victoria Raynaud.

Mozambique. Ameen Ikram, a gem merchant from Sri Lanka, confirmed this after managing to visit the mining site in June 2016. The deposit is located about 60 km northeast of Chimoio, near Gorongosa National Park. The area is under the control of the Mozambican National Resistance (RENAMO), an armed rebel group.

The stones exhibited a vitreous luster. Standard gemological testing yielded an isotropic RI reading of 1.767 ± 0.003 and an SG value of 3.87 ± 0.02. An isotropic reaction with anomalous double refraction (ADR) was observed through the polariscope. The samples were inert when exposed to both long-wave and short-wave UV radiation. Examination with a gemological microscope revealed several internal features (figure 8), including individual and clus-

tered zircon crystals, zircons with stress halos, black platelets of graphite, groups of colorless quartz crystals, thin films, needles, tubes, and iron stains in tubes. Raman spectroscopy was used to identify the mineral inclusions.

Advanced analytical techniques, including UV-Vis-NIR and Fourier-transform infrared (FTIR) spectroscopy and laser ablation–inductively coupled plasma–mass spectrometry (LA-ICP-MS), were used to collect additional information. The UV-Vis-NIR spectrum (figure 9, left) indicated electronic transitions of specific Fe and very weak Mn transition metal ions, as described in the literature (K. Krambrock et al., "Purplish-red almandine garnets with alexandrite-like effect: Causes of colors and color-enhancing treatments," *Physics and Chemistry of Minerals*, Vol. 40, No. 7, 2013, pp.

Figure 9. Left: The purple garnet's UV-Vis-NIR spectrum shows weak absorption bands attributed to Fe^{3+} (337, 367, and 424 nm) and Mn^{2+} (408 nm). The remaining peaks in the visible region (400, 461, 504, 523, 575, 619, and 698 nm) can be assigned to Fe^{2+}. Right: The FTIR spectrum reveals Fe^{2+} bands at 5820 and 4450 cm^{-1}, hydroxyl group features at 3552 and 3525 cm^{-1}, and CO_2 peaks at 2360 and 2341 cm^{-1}. The very small peak at 2627 cm^{-1} may be caused by the samples' numerous inclusions.
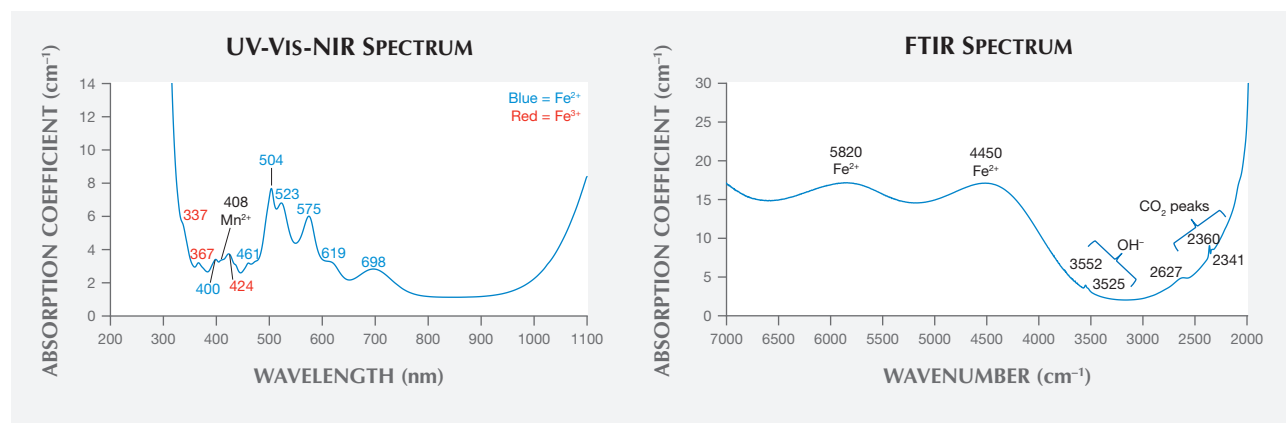
Oxide	Weight (%) ± SD (n = 5)
SiO_2	42.34 ± 0.33
Al_2O_3	25.41 ± 0.22
FeO	17.93 ± 1.31
MgO	13.16 ± 1.19
CaO	0.94 ± 0.20
MnO	0.22 ± 0.02
V_2O_3	0.002 ± 0.001
Cr_2O_3	bdl
TiO_2	bdl

n: number of studied samples
bdl: below detection limit
SD: standard deviation

555–562). All of the samples showed an iron spectrum including Fe^{2+} and Fe^{3+}, and a weak absorption peak at 408 nm was assigned to Mn^{2+}. The FTIR spectrum (figure 9, right) showed Fe^{2+} peaks at 4450 and 5820 cm^{-1} (R.G. Burns, *Mineralogical Applications of Crystal Field Theory*, Vol. 5, Cambridge University Press, Cambridge, UK, 1993, pp. 155–158), hydroxyl group features at around 3500–3600 cm^{-1} (G.R. Rossman et al., "Quantitative analysis of trace OH in garnet and pyroxenes," *American Mineralogist*, Vol. 80, No. 5–6, 1995, pp. 465–474), and CO_2 peaks at 2340–2360 cm^{-1}. A minor FTIR peak at 2627 cm^{-1} might have resulted from the numerous inclusions in the samples. LA-ICP-MS analysis (table 1) revealed major amounts of Si, Al, Fe, and Mg, as well as minor amounts of Ca and Mn. Vanadium was also detected in very low concentrations, while titanium and chromium were below the detection limits. The LA-ICP-MS data confirmed the material's identification as pyrope-almandine garnet with the following chemical components: 48.8–59.5% pyrope, 37.9–47.6% almandine, 2.0–3.5% grossular, and 0.5–0.6% spessartine.

The UV-Vis-NIR spectrum explains the purple color of the samples. Since the main absorption bands dominate the green-yellow regions of the visible spectrum, two strong blue and red transmission regions combine to produce an eye-visible purple color. These samples can be classified as pyrope-almandine garnet, commonly referred to as "rhodolite" garnet.

Supharart Sangsawong, Victoria Raynaud, and
Vincent Pardieu
GIA, Bangkok

Trapiche rhodochrosite. It is not often that a very old locality produces a gem material previously unrecorded in the literature. Yet the Capillitas mine in Argentina's Catamarca Province, once mined by the Incas and long known for its fine rhodochrosite stalactites, has yielded two trapiche-like rhodochrosite gemstones, first observed by the author in August 2014.

The stalactite that produced these two slices was reportedly found in the 1980s. The smaller of the two specimens, a 30 mm round weighing 35 ct (figure 10, left), is a symmetrical example of this rhodochrosite's cogwheel habit. The 40 mm oval, which weighs 56 ct (figure 10, right), was cut from the same stalactite; it is the only other example of this formation the author could locate.

Rhodochrosite from the Capillitas mine typically consists of minute crystalline grains. These two examples, however, are very coarsely crystalline and are quite possibly twinned, which would explain both the unusually large size of these crystals and their obvious symmetry.

Dr. Carl Francis, former curator of the Mineralogical Museum of Harvard University, points out that stalactites of calcite, which are chemically and structurally similar to rhodochrosite, rarely exhibit this type of growth (pers. comm., 2014). The floral pattern of these red gemstones makes them beautiful and incredibly rare.

Russell E. Behnke
Meriden, Connecticut

Figure 10. The trapiche-like rhodochrosite "flower" on the left, measuring 30 mm across and weighing 35 ct, is from Argentina's Capillitas mine. This piece appears to be formed by the intersection of three crystals, with 60° of separation. The 56 ct rhodochrosite specimen on the right, also from the Capillitas mine, measures 40 mm across. Photos by Russell E. Behnke; from the author's collection.

Preliminary study on rubies reportedly from Pokot, Kenya.
In July 2016, Christine Muthama and David Pkosing from Pokot Gems Ltd. in Nairobi submitted eight faceted rubies (figure 11) to GIA's Bangkok laboratory. The material came from a new operation in the Pokot area, a marble-type deposit in western Kenya that has been largely inactive since the 1960s. This new production could prove to be an interesting source of cabochon- and facet-grade rubies from East Africa.

The submitted rubies ranged from 0.36 to 4.38 ct and were semitransparent to translucent, with a very fine, milky appearance. Their gemological properties were consistent with ruby from marble-type deposits. The samples displayed strong red fluorescence under long-wave UV radiation and a medium red reaction under short-wave UV. They contained unhealed fractures, planes of negative crystals, fingerprints, and different mineral inclusions such as apatite, calcite, orange and black rutile, chlorite, pyrite, zircon, and amphibole (figure 12), the last of which is uncommon in marble-hosted rubies. Short needles, boehmite, and clouds of reflective particles were also observed.

Since the samples had inclusion features similar to those seen in marble-hosted rubies from Myanmar or Luc Yen, Vietnam, this interesting new Kenyan material could present a challenge in future origin determination studies. Nevertheless, spectroscopy and chemical composition analysis can be used to separate rubies from these deposits. FTIR spectroscopy of all eight samples from Pokot showed the presence of boehmite. LA-ICP-MS analysis revealed a distinguishing trace element composition. The rubies from

Figure 11. These eight rubies (0.36–4.38 ct) are reportedly from Pokot, Kenya. Photo by Lhapsin Nillapat.

Pokot had low Fe content (60–252 ppma), along with the following trace element contents: V: 6–11 ppma; Ga: 5–10 ppma; Ti: 29–135 ppma; and Cr: 678–1773 ppma. This combination is quite different from that of known Vietnamese rubies, showing once again that trace element composition is a useful tool for determining the origin of rubies.

Sudarat Saeseaw, Charuwan Khowpong, and
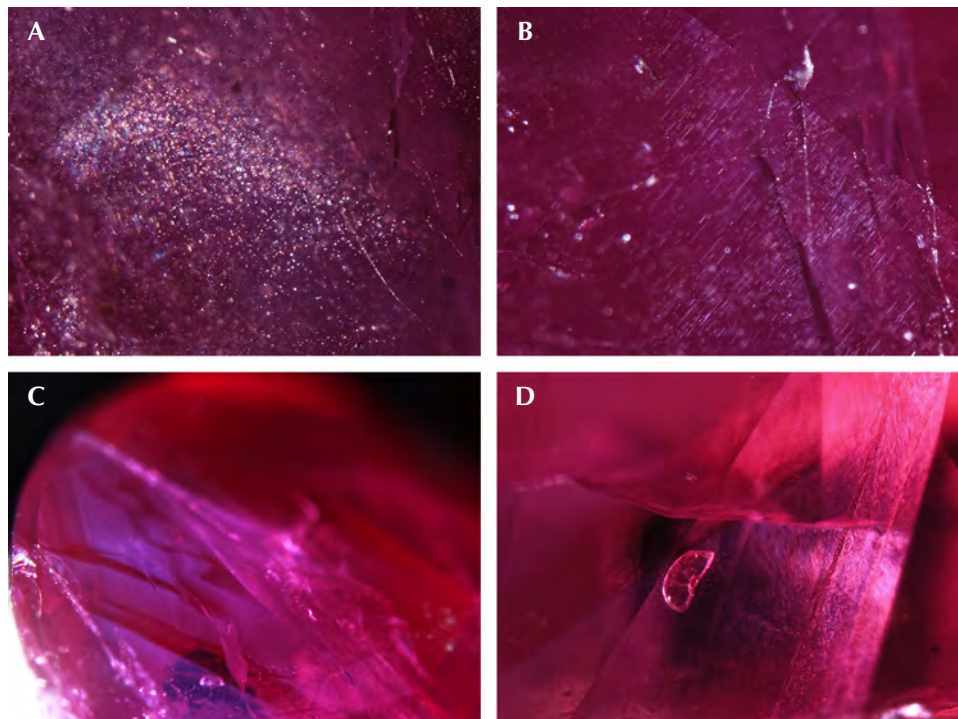*Vincent Pardieu*
GIA, Bangkok

Figure 12. The rubies reportedly from Pokot contained a variety of internal features, including (A) reflective particles, field of view 2.4 mm; (B) very fine short needles, field of view 1.3 mm; (C) very fine milky bands, field of view 4 mm; and (D) an amphibole crystal, field of view 1.3 mm. Photomicrographs by Charuwan Khowpong.

Blue sapphire reportedly from Badakhshan, Afghanistan. Recently, Habib Khan (Royal Gems Stone, Bangkok) donated a parcel of more than 40 rough sapphires to the GIA laboratory in Bangkok. Mr. Khan reported that they were mined from a new deposit in Badakhshan Province of northeastern Afghanistan. A few days later, Kamran Wahidy from the city of Fayzabad informed author VP of a new sapphire deposit near Khash in Badakhshan. This site produces material similar to the stones presented by Mr. Khan. Previous discoveries of corundum around Khash have been reported (Fall 2007 GNI, pp. 263–265; Winter 2010 GNI, pp. 319–320).

The samples (see figure 13) were blue, purplish, or near-colorless. The rough sapphires ranged from 0.9 to 19.6 ct and were transparent to translucent. Standard gemological testing revealed an RI of 1.760–1.768 and an SG of 3.71–3.98. The wide range in SG can be explained by the large pieces of lighter matrix attached to some of the corundum samples. The stones displayed weak orange to inert fluorescence under long-wave UV and were inert under short-wave UV.

All samples were originally covered with a thick, dark greenish black skin that was removed to reveal the blue sapphire inside. Most samples still had some of this skin attached. The skin contained dark green spinel, phlogopite, chlorite, feldspar, amphibole, and tourmaline, which were identified by Raman spectroscopy.

Flat negative crystal fingerprints were commonly seen; some contained CO_2 bubbles and diaspore fibers that became visible at 60× magnification. The samples displayed ladder- or dust-like inclusions similar to those seen in sapphires from Kashmir (figure 14; see H.A. Hänni, "A contribution to distinguishing characteristics of sapphire from
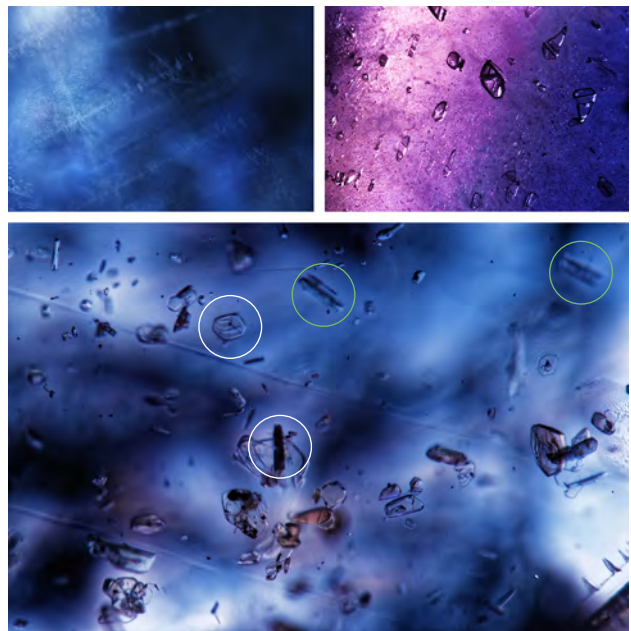

Figure 14. Inclusion scenes in the Badakhshan sapphire. Left: Ladder-like inclusions under darkfield illumination; field of view 2.7 mm. Right: Negative crystals with CO_2 bubbles; field of view 1.8 mm. Bottom: Crystal inclusions of amphibole (green circles) and mica (white circles); field of view 2.4 mm. Photomicrographs by Charuwan Khowpong (left) and Victoria Raynaud (right and bottom).

Kashmir," *Journal of Gemmology*, Vol. 22, No. 2, 1990, pp. 67–75).

Crystal inclusions were identified (using Raman spectroscopy and the RRUFF reference database) as apatite, amphibole, mica, diaspore, chlorite, tourmaline, feldspar, and spinel. We also observed unidentified clusters of tiny black crystals and crystals that might have been epidote or allanite. FTIR spectroscopy revealed the presence of boehmite, kaolinite, and a peak at 3161 cm^{-1}. LA-ICP-MS showed an iron content between 154 and 402 ppma, while gallium ranged from 7 to 11 ppma.

If confirmed, the discovery of a new blue sapphire deposit near Khash could be interesting for the gem trade in Afghanistan. However, this new material represents a true challenge for gemologists working on origin determination, as its inclusion scene is, in some aspects, very similar to those in sapphires from Kashmir.

Wim Vertriest, Ungkhana Atikarnsakul, Victoria Raynaud, Charuwan Khowpong, and Vincent Pardieu
GIA, Bangkok

"Punsiri"-type FTIR spectral features in natural yellow sapphires. Recently, a yellow sapphire from Chanthaburi, Thailand, showed a spectrum associated with "Punsiri" high-temperature heat treatment of blue sapphire. In response, GIA's Bangkok lab performed FTIR spectroscopy

Figure 13. These blue and purplish sapphires are reportedly from a new deposit near Khash in Badakhshan Province, Afghanistan. The largest stone weighs 19.6 ct and measures 19.2 × 13.9 mm. Photo by Lhapsin Nillapat.

Figure 15. Ten of the 38 basalt-related yellow sapphires from this study. The specimens on the left, weighing 0.22–0.41 ct, are from the Anakie area in Queensland, Australia. The material on the right, ranging from 0.41 to 1.40 ct, comes from the Khao Ploi Waen area of Chanthaburi, Thailand. Photo by Nuttapol Kitdee.

on 38 untreated natural basalt-related yellow sapphires (figure 15). Twenty-two of the samples were from the Anakie Gem Fields area in Queensland, Australia, and the remaining 16 from the Khao Ploi Waen area of Chanthaburi. All were collected from the mines by GIA field gemologists.

Standard gemological testing of the Australian sapphires showed RI (n_ω) = 1.774 ± 0.001 and RI (n_ε) = 1.765 ± 0.001, with a birefringence of 0.009 ± 0.001. For the Thai sapphires, RI (n_ω) = 1.773 ± 0.001 and RI (n_ε) = 1.764 ± 0.001, with a birefringence of 0.009 ± 0.001. All the stones were inert under long-wave and short-wave UV radiation due to their very high iron content.

Most of the Australian sapphires were yellow, whereas the Thai sapphires appeared greenish yellow. Only homogeneous yellow areas were analyzed by FTIR. Many of the stones (about 45% of the Australian stones and about 38% of the Thai stones) showed a characteristic Punsiri FTIR spectrum, consisting of a multiple band structure positioned around 2000–3300 cm^{-1} with peaks at 2025, 2137, 2258, 2413, 2463, 2627, 2990, 3032, and 3220 cm^{-1} (figure 16). These features have traditionally been considered indicative of heat treatment, since this pattern has only been observed in Punsiri-type heated blue sapphires (G. DuToit et al., "Beryllium treated blue sapphires: continuing market observations and update including the emergence of larger size stones," *GIA Research News*, June 2009) that display multiband FTIR spectra around 3000 cm^{-1}. This FTIR feature is attributed to the stretching vibration of the OH bond formed by the incorporation of hydrogen and host oxide ion in a publication about "magnesium-doped α-alumina" grown by the Verneuil method, where the IR absorption results are affected by the incorporation of hydrogen into a Mg-doped α-alumina (N. Fukatsu et al., "Incorporation of hydrogen into magnesium-doped α-alumina," *Solid State Ionics*, Vol. 162, 2003, pp. 147–159). Since the samples were all collected in the field, it is extremely interesting to document that Punsiri-type FTIR spectra may be found in natural unheated yellow sapphires.

LA-ICP-MS showed trace elements of Mg, Ti, V, and Ga, with very high ppm levels of Fe (3000 ppma on average). Mg content (about 23 ppma) was higher than Ti content (approximately 16 ppma); thus, blue coloration is not seen in these stones. Since Be was not detected, there are no concerns about beryllium diffusion treatment, which is not surprising since these specimens were collected in the field.

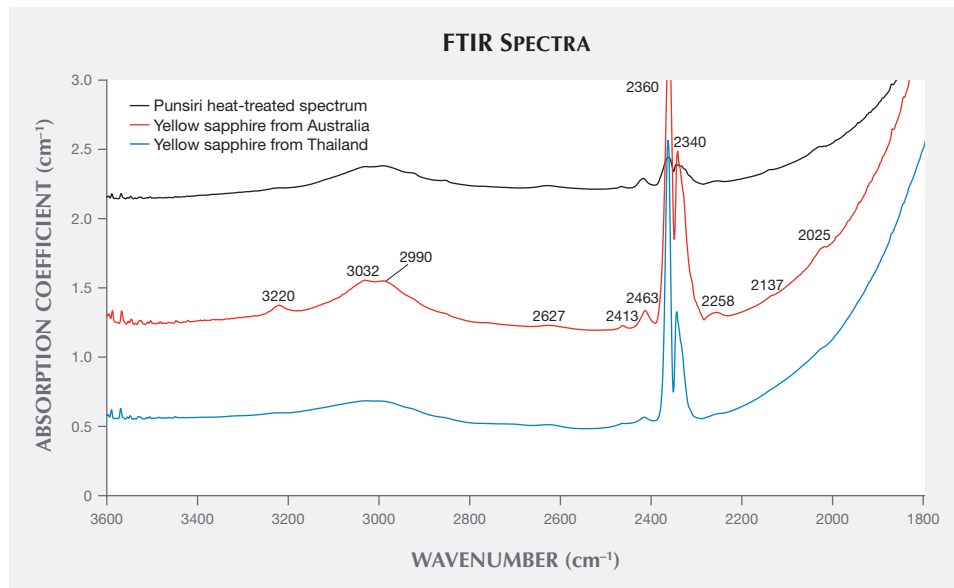Figure 16. FTIR spectra of natural yellow sapphires from Australia and Thailand in the 1800–3600 cm^{-1} range. The peaks shown here are similar to those observed in Punsiri heat-treated blue sapphire (black spectrum). Peaks at 2360 and 2340 cm^{-1} are related to CO_2. Please note that the absorption coefficient of the Punsiri heat-treated blue sapphire (black spectrum) at the y-axis was divided by two.

Figure 17. This 15.54 ct triangular modified brilliant faceted amethyst (left) features a large aqueous primary fluid inclusion (right; field of view 7.19 mm). Photos by Jonathan Muyal.

It appears as though the incorporation of hydrogen in corundum may form characteristic Punsiri-like FTIR features. Since these features were observed in natural basalt-related yellow sapphires from Australia and Thailand, careful consideration must be exercised when using FTIR to identify heat treatment in corundum.

Supharart Sangsawong, Vincent Pardieu,
Victoria Raynaud, and Sasithorn Engniwat
GIA, Bangkok

Large aqueous primary fluid inclusion in amethyst. A triangular modified brilliant was submitted to GIA's Carlsbad laboratory by L. Allen Brown (All That Glitters, Methuen, Massachusetts) for scientific examination. The 15.54 ct stone (figure 17, left) was presented as a Moroccan amethyst. Standard gemological testing established the following properties: RI—1.544–1.553; birefringence—0.009; optic sign—uniaxial positive; pleochroism—moderate purplish blue to purple; SG—2.65; fluorescence reaction—inert to long- and short-wave UV radiation. All of these properties were consistent with amethyst. What made this example notable was a strikingly large primary fluid inclusion under the table facet, which is easily seen with the unaided eye and confirms the natural origin of this stone (figure 17, right). The gas bubble in the fluid inclusion moves freely when the stone is turned slightly. No magnification is needed to reveal the beauty of this interactive inclusion, which can be easily enjoyed by rocking and tilting the stone.

Ziyin Sun and Jonathan Muyal
*GIA, Carlsbad*

TREATMENTS

Application of the DiamondView in separating impregnated jadeite. Infrared and Raman spectroscopy are frequently used to separate impregnated jadeite jade from untreated material. Recent trials show that the DiamondView instrument provides reliable results in detecting impregnated material, offering gemologists a new identification method.

The Lai Tai-An Gem Lab in Taipei analyzed two client-submitted jadeite samples (figure 18): a 4.91 ct oval measuring approximately 19.64 × 11.78 × 2.62 mm and a 0.32 ct

pear-shaped drop measuring 7.77 × 5.91 × 0.95 mm. The oval possessed a mottled dark and light green bodycolor, while the pear shape exhibited a more uniform, lighter green bodycolor. Both pieces were translucent. Standard gemological testing showed spot RIs of 1.66 and SGs of 3.30 for the oval and 3.24 for the pear. A handheld spectroscope revealed lines at 630, 655, and 691 nm, indicative of naturally colored jadeite; both samples were inert to long-wave and short-wave UV fluorescence. Microscopic observation revealed fine surface-reaching networks of cracks and uncovered the "cobweb-like" features characteristic of bleached jadeite. However, DiamondView imaging produced striking blue reactions (figure 19), clearly indicating that both jadeites had been impregnated.

We confirmed that the samples were impregnated jadeite using the advanced methods commonly applied in such cases. FTIR spectroscopy revealed absorptions at 3061, 3037, 2965, 2925, and 2874 cm^{-1} (figure 20), while Raman spectroscopy using a 532 nm laser showed peaks at 638, 1112, 1608, and 3066 cm^{-1}. Both offered proof that an epoxy was used as the impregnation material.

Figure 18. The two jadeite samples exhibited a mottled dark and light green bodycolor (left, 4.91 ct oval) and a uniform lighter green bodycolor (right, 0.32 ct pear). Photos by Lai Tai-An Gem Lab.
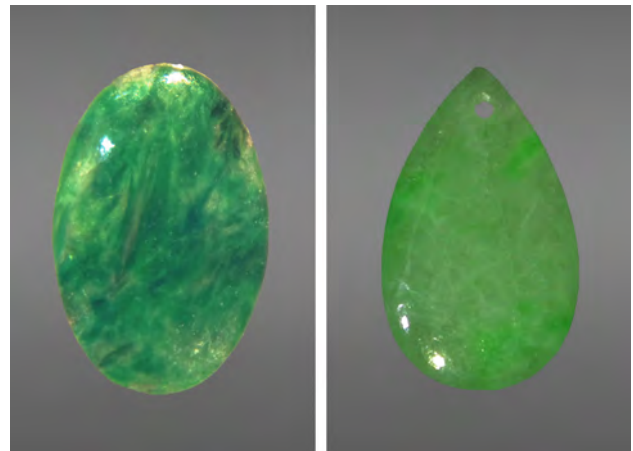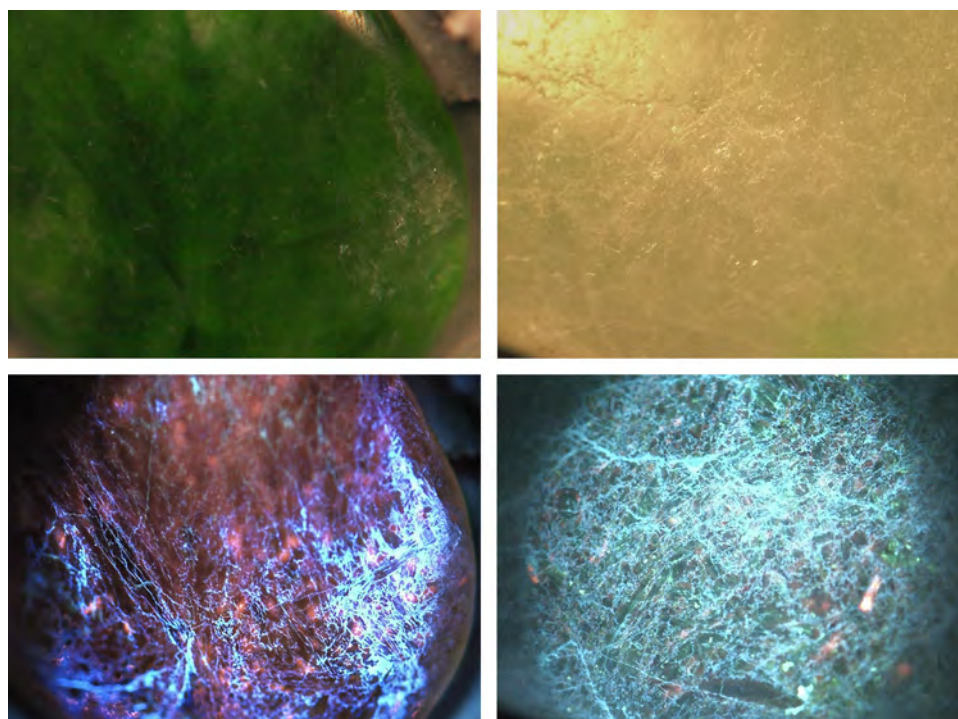
Figure 19. Diamond-View imaging of the jadeite samples. Top: Both the oval (left) and the pear shape (right) displayed the "cob-web" feature under visible light. Bottom: The DiamondView's UV light produced striking blue reactions in the cobweb structure, indicating impregnation in both jadeites. Images by Lai Tai-An Gem Lab.

DiamondView imaging is effective in alerting gemologists to possible impregnation in jadeite. While more samples need to be examined, this technique could be a simple and effective way to identify impregnation treatment.

Larry Tai-An Lai (service@laitaian.com.tw)
Lai Tai-An Gem Laboratory, Taipei

Figure 20. Peaks in the jadeite sample's FTIR spectrum at 3061, 3037, 2965, 2925, and 2874 cm⁻¹ proved that an epoxy was used as the impregnation material.
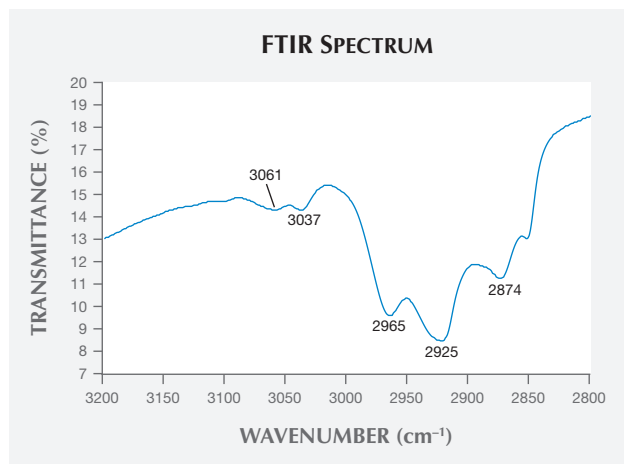
CONFERENCE REPORTS

Gem Materials at the Second European Mineralogical Conference (emc2016). The European Mineralogical Conference, organized by the Italian Society of Mineralogy and Petrology (SIMP) and the Universities of Ferrara and Padova, was held in Rimini, Italy, September 11–15. Among the event's 28 sessions was "Gem Materials," chaired by **this contributor**, **Lee Groat** (University of British Columbia, Vancouver, Canada), **Federico Pezzotta** (Museum of Natural History, Milan), and **David Turner** (University of British Columbia). "Gem Materials" yielded both an oral and a poster session.

The poster session, held September 13, covered topics such as worldwide emerald sources; red beryl; demantoid from Madagascar; turquoise from the collections of the Royal Mineralogical Museum of Naples; epidote from Val Malenco, Italy; and rhodonite from the Swiss Alps. There was also a review of colored gems in art and gemology, as well as experimental work applied to gems from miarolitic pegmatites.

The September 15 oral session featured 14 presentations. **Dan Marshall** (Simon Fraser University, Burnaby, Canada) opened with a keynote address on a reclassification of emerald deposit formation models based on tectonic and metamorphic conditions. **Emmanuel Fritsch** (Institut des Matériaux, Jean Rouxel, University of Nantes, France) posed the question of why some minerals are gem quality, using crystal growth as a consideration.

Peter Bačik (Comenius University, Bratislava, Slovakia) began the presentations on Cr- and V-bearing minerals with spectrometric characterizations of ruby, spinel, chrysoberyl, diopside, garnet, zoisite, emerald, and tourmaline. **Isabella**

Pignatelli (French National Center of Research, Vandœuvre) studied the Cr- and V-bearing euclase from the Gachala mining district of Colombia, focusing on atypical texture formed by solid inclusions trapped along crystallographic axes. Her presentation opened a discussion of trapiche vs. trapiche-like textures. **Dan Marshall** spoke again, this time on fluid inclusions and stable isotope data from emerald in Western Australia's Poona deposit, showing multiple generations of emerald combined with metamorphic and magmatic fluid circulations. **This contributor** demonstrated that it was possible to decipher the geographic origin of pink and red spinel through oxygen isotopes and trace-element data on pink and red spinels in marble, with a special focus on the Kul-i-Lal mine in Tajikistan. **Stefanos Karampelas** (GemResearch Swisslab, Adligenswil, Switzerland) offered new insights on detection of heat treatment of tanzanite, indicating that this form of treatment can only be identified under very specific circumstances.

Aaron C. Palke (University of Queensland and Queensland Museum, Brisbane, Australia) presented on melt inclusions in sapphires from Montana's Yogo deposit, which are similar in composition and mineralogy to the ocelli observed in the Yogo lamprophyres. **David Turner** offered new mineralogical insights from near-field hyperspectral imaging of sapphire-bearing marble at Baffin Island, Canada.

The silica family was covered in three presentations. **Benjamin Rondeau** (University of Nantes) related the presence of numerous minerals (including an unknown type) from the lazulite-bearing blue quartzite from Itremo, Madagascar. **Ilaria Adamo** (Italian Gemological Institute, Milan) characterized blue and white banded chalcedony (agate) from Yozgat Province in Turkey. The agate formed from mixture of quartz and moganite, but the origin of the blue color is unknown, since iron content at approximately 10 ppm is constant in all the banding. **Boris Chauviré** (University of Nantes) explained a model for the formation of precious opal from Wegel Tena, Ethiopia. The model suggests a paleotopographic control on the location of the deposits and the repetition of the soil formation process in space and time.

Special topics related to gem museums and historical writings were also covered. **William B. "Skip" Simmons** (Maine Mineral and Gem Museum, Bethel) retraced the state's recent and historical gem production and the museum's acquisitions from Maine pegmatites. **Ann C. Pizzorusso** (Naples, Italy) tackled the gems of Dante's *Divine Comedy*, discussing the gemological knowledge of the late Middle Ages and the meanings associated with precious metals, pearls, rubies, diamonds, and other gems.

Details from the European Mineralogical Conference are available at http://emc2016.socminpet.it. The next conference will take place in 2020 at a site to be determined.

Gaston Giuliani
Institute for Research and Development
Toulouse, France
French National Center of Research, Vandœuvre

GSA 2016 annual meeting. The Geological Society of America (GSA) held its annual meeting September 25–28 in Denver, Colorado. This was the fourth meeting in which GIA hosted gemological technical sessions. In the oral and poster sessions, gemologists, geoscientists, and students from all over the world came together to present their research and discuss advanced topics.

Invited speaker **Jeffrey Post** (Smithsonian Institution, Washington DC) presented detailed studies on a selection of significant fancy-color diamonds, including blue, pink, and chameleon stones. Among these, the researchers applied time-of-flight secondary ion mass spectrometry (ToF-SIMS) analysis to the Hope diamond, which allowed the measurement of total boron concentration; the results revealed strong zoning from this chromophore in many blue diamonds. **Graham Pearson** (University of Alberta, Canada) reported on his study of the saline fluid inclusions preserved in some diamonds from the Ekati and Diavik mines and pointed out that alkali- and Cl-rich fluids play a key role in diamond formation. Invited speaker **Emmanuel Fritsch** (University of Nantes, France) discussed the state of synthetic diamond identification. He also noted the advantages and limitations of some of the most commonly used sorting methods.

GIA researchers shared their results on several diamond-related projects. **Christopher M. Breeding** showed the fluorescence colors and patterns that diamonds can display when exposed to ultraviolet light. In addition to their beauty, these colors and patterns are important in diamond formation studies and the identification of natural, treated, and synthetic material. **Karen Smit** presented new data on a suite of canary diamonds from Sierra Leone. This will allow researchers to further specify the source fluids and color-forming defects of these yellow diamonds and better correlate their features to the unusual geological formation history of the Zimmi diamond deposit. **Evan Smith** reported his findings on inclusions in thousands of high-quality type II polished diamonds and trimmed-off portions. The recurring set of inclusions in many stones includes a metallic multi-phase assemblage and retrogressed former perovskite phases. Together, the two inclusion types revealed a unique paragenesis for these large, top-quality diamonds.

Presentations on colored gemstone research revealed a variety of studies on important gem species and collector stones. **Mandy Krebs** (University of Alberta) reported on Pb-Pb geochronology of rubies and the first-ever radiometric age determination of ruby. This new method allows dating to be done directly on the ruby itself rather than on inclusions such as zircon. This dramatically broadens the application of geochronology in ruby provenance determination. **Jullieta Lum** (University of Johannesburg) presented major and trace element composition of emerald and aquamarine collected from central Namibia and South Africa. **Peter Heaney** (Penn State University) revealed the cause of iridescence in metamorphic hematite from Minas Gerais, Brazil. The study by Dr. Heaney and his former student Xiayang Lin found that this phenomenon is caused by a framework of well-oriented

hematite nanorods. **Raquel Alonso-Perez** (Harvard University) presented preliminary results on the geochemistry of emeralds from the Irondro deposit in Madagascar.

Important research on gemstone formation was also delivered. **Yury Klyukin** (Virginia Tech) addressed the valuable information that fluid and melt inclusion studies can provide in solving gem formation problems, using diamond, emerald, and corundum as examples. Invited speaker **David London** (University of Oklahoma) discussed the different mechanisms that caused zonation within pegmatites. Understanding of mineral segregation within pegmatites is critical for gem exploration.

The poster session presenters included two graduate students from the China University of Geosciences (Wuhan). **Chengsi Wang** proved the robustness of photoluminescence (PL) spectroscopy in treated and synthetic spinel identification through a series of heating and annealing experiments. **Yuan Zheng** applied linear discriminant analysis (LDA) in separating hundreds of turquoise samples from three different sources after analyzing their trace elements using ICP-MS.

GIA staff also presented interesting discoveries in the poster session. **Wuyi Wang** studied the distribution of the SiV^- defect and found that it has a dramatically different correlation with Ni_i^+ between natural and HPHT synthetic diamonds. **Paul Johnson** demonstrated that hydrogen-rich diamonds with intensive inclusions and fractures can be heated to generate a more uniform black color. Based on his experience, microscopic observation remains the most powerful tool in identifying this treatment. **Troy Ardon** and **Sally Eaton-Magaña** conducted a series of annealing experiments at different temperatures with two hydrogen-rich Zimbabwe diamond plates. They evaluated the effect of high temperature on the diamonds' spectroscopic features and inclusions. **Rose Tozer** examined one of the rarest publications in the GIA library collection: *Russia's Treasure of Diamonds and Precious Stones*. Edited by the well-known mineralogist A.E. Fersman, this book documents Russia's regalia and crown jewels at the time of the February Revolution in 1917. The volume has been digitized as part of GIA's project to digitize items from its rare book collection and can be accessed free of charge at https://archive.org/details/gialibrary.

Abstracts from the two gemological sessions can be found at https://gsa.confex.com/gsa/2016AM/webprogram/Session40327.html (oral) and https://gsa.confex.com/gsa/2016AM/webprogram/Session41331.html (poster). The 2017 meeting will be held October 22–25 in Seattle.

Tao Hsu, Jim Shigley, and Dona Dirlam
GIA, Carlsbad

IN MEMORIAM

Fred Ward (1935–2016). *Gems & Gemology* mourns the loss of acclaimed photographer and gemologist Fred Ward, who died July 19 at the age of 81. Mr. Ward was known for capturing iconic images of celebrities and for his work with *National Geographic* magazine, which sparked his gemological pursuits.

Mr. Ward was born in Huntsville, Alabama, and grew up in Miami. His passion for photography blossomed in high school, when he decided to turn his extracurricular activity into a career. He earned a master's degree in journalism from the University of Florida in 1959.

Well known for his shots of President John F. Kennedy's funeral in November 1963 and the Beatles' first American performance (1964), he photographed Gerald Ford for *Portrait of a President* (1975). Mr. Ward's work can be found in collections owned by the Metropolitan Museum of Art and the Library of Congress, among others. Mr. Ward became interested in gemology as a freelance photographer for *National Geographic*, where he worked on several assignments related to gems. He went on to publish the highly influential nine-volume Fred Ward Gem Book Series. He earned his Graduate Gemologist diploma from GIA in 1990 and was a member of the Washington, DC chapter of the GIA Alumni Association. He was a coauthor of *G&G*'s Spring 2000 article "Burmese Jade: The Inscrutable Gem."

Fred Ward is survived by his wife of 58 years and frequent collaborator Charlotte Mayes Ward, four children, and four grandchildren. We extend our deepest condolences to his family and friends.

ERRATA

1. In the Summer 2016 field report retracing Peter Rainier's time in Chivor, Colombia, the publication date of Fritz Klein's *Smaragde unter dem Urwald* was incorrectly listed as 1925 (p. 175). The correct date for the first edition is 1941.

2. The Summer 2016 Chivor field report also stated that Klein first returned to Germany from Colombia in 1914 (p. 176). However, Klein's own book states that he left Colombia in January 1915. It was impossible for him to have worked for Francisco Restrepo on his return from Germany after World War I in 1919, as Restrepo had died in 1914 at the mine. The authors thank Dr. Karl Schmetzer for bringing these errata to our attention.

G&G
Lab Notes

Editors
Thomas M. Moses | Shane F. McClure

DIAMONDS

Evidence of Focused Beam Irradiation In Treated Pink Diamond

A Fancy pink diamond, confirmed as natural-grown, was found to be type IIa and colored by NV^- centers. As part of routine testing, DiamondView fluorescence images were collected to check for synthetic growth features. These images showed unusual patterning in the form of two pink spots near the edge of the table facet (figure 1). Both spots were approximately 0.9×0.7 mm, and the table facet was approximately 3.0 mm in diameter. The orange fluorescence throughout most of the table was likely due to NV^0 centers, whereas the pink components were likely due to NV^- centers.

To further investigate the spatial distribution of the $NV^{0/-}$ centers, we acquired a photoluminescence (PL) image of the diamond's table using a 532 nm laser. Figure 2 shows the distribution of the NV^0 and NV^- centers. The distribution of the NV centers confirms the presence of two spots on the table. Figure 3 shows the average PL spectra from inside one of the spots and the average PL spectra from the region outside the spots. Figures 2 and 3 demonstrate that the intensity of the NV centers was greater inside the spots than in the rest of the table. Inside the spots, the average

peak area intensity of the NV^0 center was approximately two times greater and the average peak area intensity of the NV^- centers was approximately three times greater. The spots were comparable in both size and defect concentrations.

To determine the vertical distribution of the NV^- center, a 500 μm PL depth profile was acquired through each spot. This is an automated process the instrument can perform in which a series of spectra are collected along a line spanning the diameter of the spot. The stage is then offset 5 μm in the vertical direction to focus farther into the diamond, and another series of spectra are collected. The process was re-
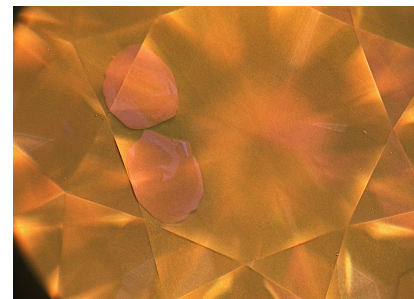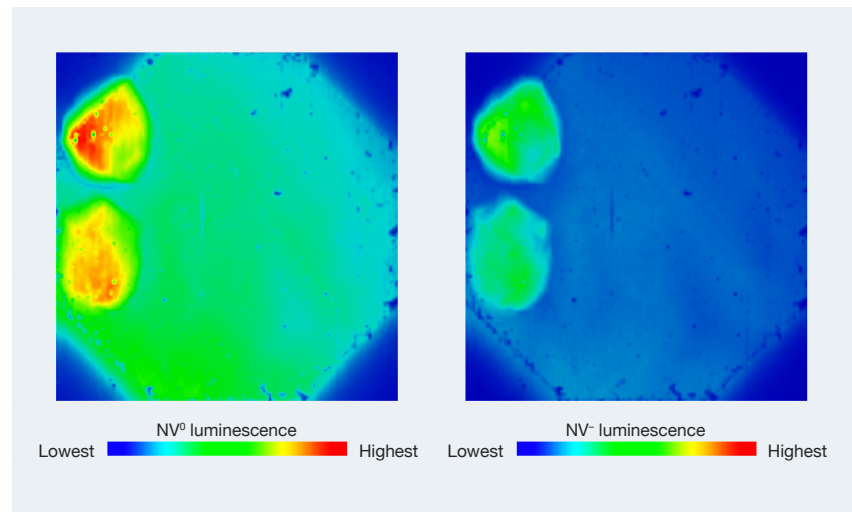

Figure 1. This DiamondView image of the table of a pink diamond shows two distinct pink spots. Field of view approximately 5 mm.

peated 100 times until the target depth of 500 μm was reached. This

Figure 2. Left: A PL map showing the peak area distribution of the NV^0 center. Field of view is approximately 3 mm; scale is relative intensity. Right: A PL map showing the peak area distribution of the NV^- center. Field of view is approximately 3 mm; scale is relative intensity.

NV⁰ luminescence
Lowest ▬▬▬ Highest

NV⁻ luminescence
Lowest ▬▬▬ Highest